ADVANCED FUNCTIONAL MATERIALS
www.afm-journal.de

Solid-State Electrolytes for Lithium Metal Batteries: State-of-the-Art and Perspectives

*Jun Huang, Chen Li, Dongkai Jiang, Jingyi Gao, Lei Cheng, Guocheng Li, Hang Luo, Zheng-Long Xu, Dong-Myeong Shin, Yanming Wang, Yingying Lu, and Yoonseob Kim**

The use of all-solid-state lithium metal batteries (ASSLMBs) has garnered significant attention as a promising solution for advanced energy storage systems. By employing non-flammable solid electrolytes in ASSLMBs, their safety profile is enhanced, and the use of lithium metal as the anode allows for higher energy density compared to traditional lithium-ion batteries. To fully realize the potential of ASSLMBs, solid-state electrolytes (SSEs) must meet several requirements. These include high ionic conductivity and Li^+ transference number, smooth interfacial contact between SSEs and electrodes, low manufacturing cost, excellent electrochemical stability, and effective suppression of dendrite formation. This paper delves into the essential requirements of SSEs to enable the successful implementation of ASSLMBs. Additionally, the representative state-of-the-art examples of SSEs developed in the past 5 years, showcasing the latest advancements in SSE materials and highlighting their unique properties are discussed. Finally, the paper provides an outlook on achieving balanced and improved SSEs for ASSLMBs, addressing failure mechanisms and solutions, highlighting critical challenges such as the reversibility of Li plating/stripping and thermal runaway, advanced characterization techniques, composite SSEs, computational studies, and potential and challenges of ASS lithium–sulfur and lithium–oxygen batteries. With this consideration, balanced and improved SSEs for ASSLMBs can be realized.

1. Introduction

1.1. Lithium (Li)-Based Batteries

Energy is a crucial topic in modern societies for creating a sustainable environment. Developing energy storage devices is an effective way to widely deliver power sources as needed. Among current energy storage devices and technologies, Li-based rechargeable batteries, that utilize lithium ions (Li^+) as the primary charge carrier, have gained significant attention since their commercialization in the 1990s. They are considered important milestones in the development of the energy industry,[1,2] and have become the dominant energy storage sources in numerous devices that we use daily, including portable electronic devices, electric vehicles, unmanned aerial vehicles, and renewable energy storage systems.[3] The fundamental principle behind Li-based batteries lies in the transport of Li^+ between two electrodes during the charging and discharging processes. These electrodes are typically made of materials capable of hosting Li^+, such as lithium cobalt

J. Huang, C. Li, H. Luo, Y. Kim
Department of Chemical and Biological Engineering
The Hong Kong University of Science and Technology
Hong Kong SAR 999077, China
E-mail: yoonseobkim@ust.hk

D. Jiang, L. Cheng, Y. Wang
University of Michigan – Shanghai Jiao Tong University Joint Institute
Shanghai Jiao Tong University
Shanghai 200240, P. R. China

J. Gao, D.-M. Shin
Department of Mechanical Engineering
the University of Hong Kong
Pokfulam, Hong Kong SAR 999077, China

The ORCID identification number(s) for the author(s) of this article can be found under https://doi.org/10.1002/adfm.202411171

DOI: 10.1002/adfm.202411171

G. Li, Z.-L. Xu
Department of Industrial and Systems Engineering
Research Centre for Deep Space Engineering
The Hong Kong Polytechnic University
Hong Hum, Hong Kong SAR 999077, China

Y. Lu
State Key Laboratory of Chemical Engineering
Institute of Pharmaceutical Engineering
College of Chemical and Biological Engineering
Zhejiang University
Hangzhou 310027, China

Y. Lu
ZJU-Hangzhou Global Scientific and Technological Innovation Center
Zhejiang University
Hangzhou 311215, China

Y. Lu
Institute of Wenzhou
Zhejiang University
Wenzhou 325006, China

oxide ($LiCoO_2$; LCO) or lithium iron phosphate ($LiFePO_4$; LFP), serving as the positive electrode, cathode, and graphite or alloys, serving as the negative electrode, anode.[4] During charging, a voltage is applied to the battery, driving Li^+ to migrate from the positive electrode through an electrolyte to the negative electrode. This voltage-governed process draws electrons and Li^+ from the cathode and stores them in the anode. Conversely, the stored Li^+ is released back to the cathode during discharging, sending electrons to power external devices. Li-based batteries offer several advantages over other rechargeable battery technologies such as nickel metal hydride (Ni–MH), nickel–cadmium (Ni–Cd), and lead-acid. First, they exhibit a high-energy-density, meaning they can store much electrical energy in a compact and lightweight package. This characteristic makes them ideal for portable electronics, where battery size and weight are crucial considerations. Second, Li-based batteries have a relatively low self-discharge rate, <5% per month,[5] meaning they can retain their stored energy for extended periods without significant loss. This feature makes them suitable for applications where the battery may not be used for a while, such as emergency backup systems or intermittent renewable energy sources.[6] Moreover, Li-based batteries have a high cell voltage of 3.7 volts (V), which is higher than most other rechargeable battery chemistries, such as Ni–MH, Ni–Cd, and lead–acid batteries, where the nominal cell voltages are 1.2, 1.2, and 2.0 V, respectively.[7] This higher voltage allows for greater power output and efficiency, enabling faster charging and discharging rates, e.g., 2 C (1 C equals the current density for full charging or discharging in 1 h).

Despite their numerous advantages, Li-based batteries have limitations. One notable concern is safety, as they are susceptible to thermal runaway and potential fires if mishandled or exposed to extreme conditions, particularly in the case of batteries exhibiting higher energy density, >400 Wh kg^{-1} and >800 Wh L^{-1},[8] there is an augmented level of safety risk. Although battery management systems and safety features have been developed to mitigate these risks and ensure safe operation, batteries with flammable liquid electrolytes still have a potential hazard of explosion.[9,10] Another major concern is the cell capacity. The typical Li-ion batteries (LIBs) can achieve a gravimetric energy density of 150–250 Wh kg^{-1}, which is not ideal for large-scale grid and transportation applications (**Figure 1**). This issue of limited energy density can be solved by using Li metal as anode; thus Li metal batteries (LMBs) or Li–sulfur batteries (Li–S).

We compared gravimetric and volumetric energy density among conventional LIBs, LMBs, and Li–S (Figure 1). Those two metrics serve as crucial parameters for assessing various battery technologies' practical performance and energy storage capacity.[19] Presently, commercially available classical LIBs with various cathode materials such as LFP, LCO, $LiNi_xCo_yAl_{1-x-y}O_2$ (NCA), $LiNi_xMn_yCo_{1-x-y}O_2$ (NCM), and $LiMn_2O_4$ (LMO), are manufactured by LG, Panasonic, Samsung, and CATL. These batteries offer a gravimetric energy density of up to 250 Wh kg^{-1}, meeting the power requirements of most small electronic devices. However, such a capacity is insufficient to meet electric vehicles' demand with extended driving ranges or large grid systems.[20] This limitation stems from the relatively modest theoretical capacity of graphite, which stands at 372 mAh g^{-1}.[21] Electric vehicles with current LIBs need to recharge every 300–600 km due to the capacity limitation.[22,23] To address those concerns and to enhance performance, research and development efforts are continuously underway. New electrode materials, electrolytes, and cell configurations are being explored to increase energy density, extend cycle life, and reduce manufacturing costs.[24–26] One of the breakthroughs and most promising ways can be found in Li metal anodes with solid-state electrolytes (SSEs).[27–29]

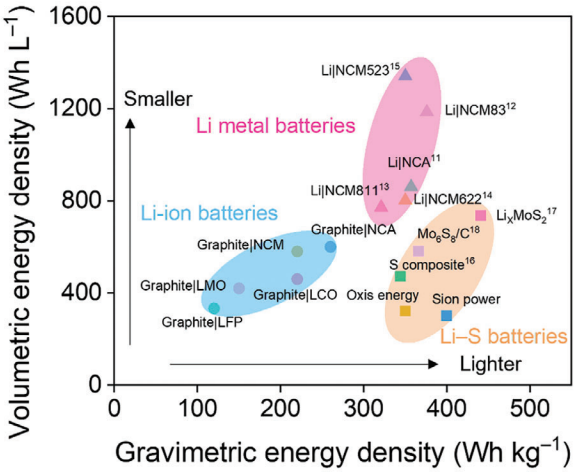

Figure 1. Comparison of gravimetric energy density and volumetric energy density of Li-ion batteries (LIBs), Li metal batteries (LMBs), and Li–sulfur batteries (Li–S). Commercial classical LIBs with $LiFePO_4$ (LFP), $LiCoO_2$ (LCO), $LiNi_xCo_yAl_{1-x-y}O_2$ (NCA), $LiNi_xMn_yCo_{1-x-y}O_2$ (NCM), and $LiMn_2O_4$ (LMO) cathodes are fabricated by LG, Panasonic, Samsung, and CATL. LMBs with $LiNi_{0.8}Co_{0.15}Al_{0.05}O_2$ (NCA),[11] $LiNi_{0.83}Mn_{0.06}Co_{0.11}O_2$ (NCM83),[12] $LiNi_{0.8}Co_{0.1}Mn_{0.1}O_2$ (NCM811),[13] $LiNi_{0.6}Mn_{0.2}Co_{0.2}O_2$ (NCM622),[14] and $LiNi_{0.5}Co_{0.2}Mn_{0.3}O_2$ (NCM523)[15] cathode are reported. Li–S batteries with S composite,[16] Li_xMoS_2,[17] and Mo_6S_8/C[18] cathodes are reported. Commercial Li–S batteries are fabricated by Oxis Energy and Sion Power.

1.2. LMBs and Li–S, Equipped with Li Metal Anode

High-capacity electrodes are crucial in pursuing high-energy density in Li-based batteries and are relatively simple to manufacture.[30] Li metal anode is a particularly attractive choice among anode materials due to their ultra-high theoretical specific capacity of 3860 mAh g^{-1}, which is more than ten times higher than the capacity of commonly used graphite anode-based LIBs; and the lowest electrochemical potential of −3.04 V to the standard hydrogen electrode, which could result in higher cell voltage and energy efficiency.[31] Thus, LMBs represent a promising next-generation energy storage technology that can take over conventional LIBs. The core principle behind LMBs involves the reversible plating and stripping of Li metal during the charging and discharging processes.[32] During charging, the oxidation reaction separates Li^+ and electrons at the cathode and sends them to the anode to deposit metallic Li on the surface of the anode. This process is reversed during discharging, where the Li metal

Y. Kim
Energy Institute
The Hong Kong University of Science and Technology
Hong Kong SAR 999077, China

is stripped from the anode to be ionized.[33] Here, we briefly summarize the recent examples of high-performance LMBs. In 2019, Liu's group reported a Li metal pouch cell with a specific energy density of 300 Wh kg^{-1}, accomplished by implementing $LiNi_{0.6}Mn_{0.2}Co_{0.2}O_2$ as the cathode.[34] Subsequently, in 2021, Liu's group investigated the competing degradation mechanisms observed in 350 Wh kg^{-1} Li metal pouch cells. The optimal anode-to-cathode capacity ratio of 1:1 and the utilization of ultra-thin Li, 20 µm, achieved a long cycle life of 600 cycles and high capacity retention of 76%.[14] However, attaining the desired high specific energy of over 500 Wh kg^{-1} in LMBs requires cathode materials with several critical characteristics, such as a high capacity, exceptional cycling stability with sustained structural integrity, rapid kinetics, and cost-effectiveness.[35] For this purpose, Ni-rich NCM, with Ni content >60 mol%, cathode materials are receiving attention, although their structural stability during the cyclic charge-discharge process needs to be improved.[36] Consequently, identifying suitable cathode materials also remains crucial to achieving high-performance LMBs.

Accordingly, Li–S batteries, which utilize sulfur-based cathodes and Li metal anodes, have received attention, as sulfur-based cathode can theoretically show a capacity of 2,567 Wh kg^{-1} with a minimum of 600 Wh kg^{-1} for full-cell configurations due to the redox activities of the sulfur cathode.[22] However, when deployed for practical uses, the energy density of Li–S batteries is usually lower than 600 Wh kg^{-1} due to the insufficient utilization of S cathode and polysulfides' shuttling effects.[37] Examples include the Li group's Li–S pouch cells with a gravimetric energy density of 366 Wh kg^{-1} and a volumetric energy density of 581 Wh L^{-1}, realized through the implementation of a hybrid cathode composed of Mo_6S_8 and carbon,[18] and a study by Chhowalla's group reported that Li–S pouch cells with Li_xMoS_2 cathode demonstrated a high gravimetric energy density of 441 Wh kg^{-1} and a volumetric energy density of 735 Wh L^{-1}.[17]

Overall, LIBs have unsatisfactory gravimetric energy density for emerging energy storage applications, but both LMBs and Li–S batteries have significantly improved the gravimetric energy density of Li-based battery chemistry. However, the Li–S batteries show low volumetric energy density due to the low packing density of the sulfur-based cathode materials and suffer from polysulfide shuttling (Figure 1).[38] Therefore, LMBs exhibit significant promise as the next-generation, high-performance energy storage devices, particularly for electric vehicles requiring extended driving ranges. Although LMBs have made notable advancements, the pursuit of achieving a gravimetric energy density exceeding 500 Wh kg^{-1} and a volumetric energy density surpassing 1500 Wh L^{-1} remains a primary focus in state-of-the-art LMB research. Furthermore, ensuring high-safety standards and achieving a low cost below \$100 kWh^{-1} are crucial factors enabling the widespread adoption of LMBs.[39] These considerations emphasize the importance of concurrently addressing safety, cost, and energy density targets to facilitate the broad application of LMB technology.

1.3. Electrolytes for LMBs

In LMBs, carbonate-based liquid electrolytes are the most commonly used, as they can show high ionic conductivity (σ) at room temperature (r.t.), ranging from 10^{-3} to 10^{-2} S cm^{-1}.[40] In addition, liquid electrolytes possess the advantage of establishing exceptional interfacial contact with electrodes due to their solid–liquid interaction. Consequently, the interfacial resistance is minimal, ensuring swift transport of Li^+ between the anode and cathode during battery charging and discharging. This characteristic is crucial to ensure the efficient operation of the batteries,[41] and the fluid nature offers design flexibility, thereby improving the adaptability of the energy storage systems in complex shapes.[42] However, liquid electrolytes commonly exhibit limitations in the form of a low Li^+ transference number (t_{Li+}) ranging from 0.2 to 0.4, high cost, and a narrow electrochemical window. For example, the anodic stability of the commercial ethylene carbonate-based liquid electrolyte is ≈4.3 V (vs Li^+/Li).[43–45] The liquid electrolytes with low boiling points are also associated with a limited operating temperature range.[46] Furthermore, using organic solvents in liquid electrolytes can decrease the stability of the Li metal electrode, leading to an increased amount of dead Li and the growth of dendrites.[47] The presence of Li dendrites not only affects battery performance but also poses safety hazards, limiting their widespread commercialization (**Figure 2a**).[48]

Quasi-solid-state electrolytes (QSSEs), consisting of solid ion conductors and 10–30% of liquid components, are also gaining attention due to their intermediate σ between liquid electrolytes and SSEs and their ability to achieve smooth interfacial contact with electrodes.[49] QSSEs offer much improved interfacial contact between the electrolyte and electrodes, attributed to their compositional properties, which surpass those of all-solid-state electrolytes (ASSEs). Thus, QSSEs can achieve fast ion conduction. For example, gel-based QSSEs typically show σ exceeding 10^{-3} S cm^{-1} at r.t., meeting the conductivity requirements for LMBs.[50] QSSEs-based LMBs provide improved safety advantages compared to their liquid electrolyte counterparts.[51] This is due to the increased resistance to leakage and reduced susceptibility to thermal runaway. Furthermore, the utilization of QSSEs in LMBs leads to improved mechanical properties, which inhibit the growth of Li dendrites to a certain extent.[52] Nevertheless, QSSEs are not without their limitations. The presence of liquid components in QSSEs still poses a potential safety risk due to the flammability of organic solvents (Figure 2b).[53] Additionally, QSSEs exhibit lower thermal stability compared to their ASSEs counterparts. Furthermore, QSSEs may still face challenges regarding mechanical properties, particularly in gel electrolytes that contain a significant proportion of solvents.[54] This deficiency in mechanical properties can result in the potential failure of LMB cells during prolonged operations. In light of the increasing demand for high-safety and high-energy-density in applications such as electric vehicles, ASSEs hold greater promise for the future.[55] As a result, our work primarily focuses on all-solid-state electrolytes. Interested readers seeking information specifically on QSSE electrolytes in the context of LMBs are recommended to refer to the cited papers.[56–58]

To overcome these limitations, extensive research and development efforts are focused on developing advanced materials, electrolyte formulations, and cell designs.[59–61] Strategies such as the use of ASSEs, protective coatings, and modified Li metal deposition techniques are being explored to mitigate dendrite formation and enhance battery safety. In the past three decades of Li-based battery development, there has been a tremendous development

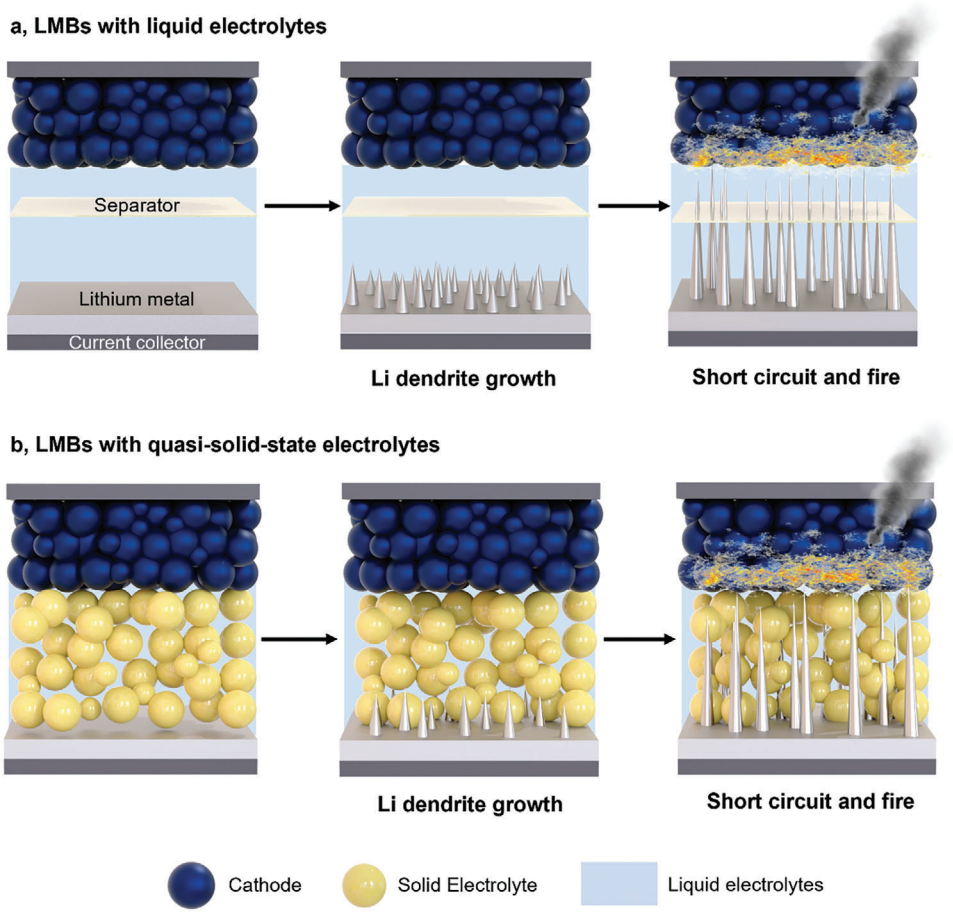

Figure 2. Limitations of liquid electrolytes and quasi-solid-state electrolytes. Upon cyclic operations of charging and discharging Li dendrites grow on Li metal's surface and, the dendrites penetrate through the separator (a) and grow through the voids of quasi-solid-state electrolyte (b). Eventually, the dendrites touch the cathode and current collectors to cause short circuits and fire.

and focus on electrode materials for both the anode and cathode, interfacial issues, and characterization techniques. Here, we list some notable review papers. Chen's group reported emerging strategies to enhance Li metal anodes' safety in LMBs.[62] This review encompassed interfacial chemistry, rational design of the host materials, and novel electrolytes. Furthermore, they offered insights and perspectives on the future development of Li metal anodes for high-energy-density LMBs. However, their review was primarily centered on the Li metal anode and did not extensively cover other aspects of LMBs. Meng's group reviewed the characteristics and properties of interfaces and interphases in solid-state LMBs, focusing on achieving stable interfaces between inorganic SSEs and electrodes.[63] The review provided insights into addressing interface challenges and offered strategies for enhancing stability. Furthermore, the paper examined characterization techniques to enable a better understanding of the interface and interphase detection, as well as the dynamic behavior and failure mechanisms associated with these interfaces. However, this review primarily focused on the interfaces and interphases in ASSLMBs employing inorganic SSEs. The discussion regarding the challenges and strategies associated with interfaces and interphases in solid-state LMBs using organic SSEs is lacking. In another review conducted by Meng's group examined the current advanced characterization techniques, shedding light on the nanoscale phenomena occurring within the interfaces of solid-state LMBs.[64] The review provided valuable insights into exploring and understanding unstable solid-solid interfaces through in situ techniques.

However, relatively little attention has been paid to the electrolyte until the last five years, even though electrolyte is a key component in realizing high-performing and safe LMBs.[65–67] Regarding ASSEs for LMBs, some review papers have been published in the past five years. However, most of the reviews concentrate on a specific type of SSEs. For example, Ding et al. reviewed the advancements in polymer SSEs and the design strategies employed to enhance their performance by manipulating functional units.[68] Wu et al. provided an overview of solid-state LMBs based on sulfides. Their work specifically focused on the compatibility of sulfide SSEs with oxide cathodes.[69] Kim et al. analyzed the stability of both sulfide and oxide SSEs, including mechanical, chemical, and electrochemical stability.[70] They also discussed the challenges associated with these SSEs, particularly interface issues. Nan's group reviewed a specific type of oxide SSEs known as garnet-type SSEs, particularly interfacial challenges involving Li metal anodes, oxide cathodes, and moisture.[71] Tuo et al. covered halide-based SSEs, describing their synthetic developments,

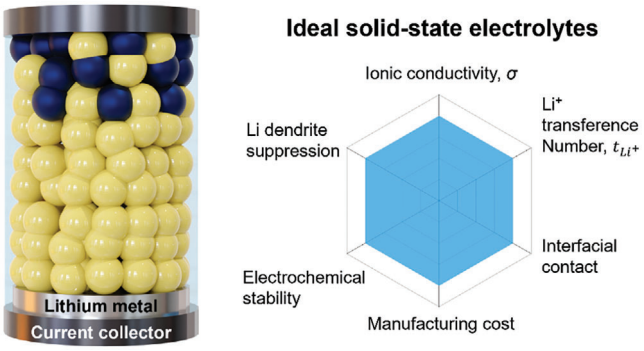

Figure 3. Requirements of SSEs for high-performing and safe LMBs. High ionic conductivity (σ), high Li^+ transference number (t_{Li^+}), good interfacial contact, low manufacturing cost, high electrochemical stability, and strong Li dendrite suppression need to be achieved simultaneously in a balanced manner.

chemical stability, and future challenges.[72] The authors also addressed the cost considerations and scalable production capabilities associated with the practical application of halide SSEs in solid-state LMBs. Overall, there are many high-quality review papers on specific topics of SSEs for LMBs. However, an extensive report on the development of SSEs for LMBs in the past five years is lacking. Thus, we provide a comprehensive analysis and discussion on developing SSEs for LMBs and the next directions. We begin by providing a concise introduction to the development of SSEs. Subsequently, we analyze the advantages and disadvantages of different types of solid electrolytes, including traditional polymer electrolytes, ceramic-based electrolytes, emerging materials, and their composites, considering multiple aspects such as Li^+ conduction, suppression of Li dendrite formation, interfacial contact, electrochemical stability, and manufacturing cost. In the last chapter, we present discussions on failure mechanisms in achieving both high-energy-density and high-safety in ASSLMBs and the solutions, use of composite SSEs for achieving balanced and enhanced SSEs for LMBs, the employment of advanced characterization techniques to visualize the interfaces between the electrolyte and electrodes, SSEs' integrations in devices, and utilization of computational studies to better understand the transport of ions and mechanisms. Since our focus is all-solid-state systems, SSEs hereinafter mean all-solid-state electrolytes.

2. Requirements of SSEs for LMBs

As a first step to understanding the SSEs for LMBs, we analyze the electrolyte requirements for LMBs. Then, we move on to the specific cases of SSEs of LMBs. Performance and safety are the two most important criteria for recognizing ASSLMBs.[66] Thus, to meet the requirements of two goals of the battery cells, the electrolytes must ensure to achieve high σ, high t_{Li^+}, good interfacial contact, low manufacturing cost, high electrochemical stability, and strong Li dendrite suppression (**Figure 3**).

Along with those six criteria, we analyze six types of SSEs, polymers, oxides, sulfides, metal–organic frameworks (MOFs), covalent organic frameworks (COFs), and composites, and their practical applications in LMBs (**Figure 4**). Polyethylene oxide (PEO) stands out as one of the extensively studied polymer SSEs as its processibility can ensure the formation of working cells (Figure 4a). However, PEO-based SSEs typically exhibit a relatively low σ ranging from 10^{-8} to 10^{-5} S cm^{-1} at r.t.[73] Furthermore, PEO-based SSEs demonstrate electrochemical stability windows (ESWs) of up to 3.9 V (vs. Li^+/Li), which renders them unsuitable for use in LMBs equipped with cathodes operating at high cut-off voltages exceeding 4.2 V, such as LCO.[74] Consequently, this limitation restricts the energy density of PEO-based ASSLMBs. Poly(vinylidene fluoride) (PVDF)-based SSEs are promising candidates due to their superior mechanical properties and excellent electrochemical stability, which significantly surpass those of PEO-based SSEs.[75] Moreover, PVDF facilitates the dissociation of Li salts, thereby enhancing Li^+ transport. However, PVDF SSEs still encounter challenges related to low σ (typically $< 10^{-4}$ S cm^{-1} at r.t.) and exhibit poor compatibility with Li metals compared to PEO-based SSEs. In situ polymerized materials, such as poly(1,3-dioxolane) (PDOL), exhibit significant potential as high-performance polymer-based electrolytes.[76] This is attributed to their exceptional σ, exceeding 10^{-3} S cm^{-1}, and their excellent compatibility with Li metals, which results from the in situ ring-opening polymerization of dioxolane.[77] For instance, Archer's group reported a PDOL-based electrolyte that achieves a σ exceeding 10^{-3} S cm^{-1} with an optimized initiator concentration.[78] However, PDOL demonstrates poor thermal stability, decomposing at temperatures above 110 °C, which raises concerns regarding potential thermal runaway when used in LMBs.[79] To enhance the thermal stability of PDOL, Huang's group proposed a strategy involving the incorporation of 1,3,5-tri glycidyl isocyanurate as a cross-linking agent, resulting in a new material referred to as TPDOL.[80] The TPDOL electrolyte exhibits an impressive σ of 5.5×10^{-3} S cm^{-1}. Furthermore, the improved thermal stability of TPDOL mitigates the risk of thermal runaway, allowing LMBs to operate safely at temperatures up to 130 °C. It is important to note that achieving a polymerization degree of 100% in PDOL is challenging. The presence of unreacted dioxolane monomers may pose potential safety issues, particularly when compared to fully polymerized all-solid-state counterparts. Two primary categories of inorganic ceramic SSEs are oxides and sulfides. Oxide-based SSEs exhibit promise due to their high σ, wide electrochemical window, exceptional chemical stability, and robust mechanical strength.[81] Among various oxides, a particular representative garnet-type oxide, $Li_7La_3Zr_2O_{12}$ (LLZO) exhibited the highest σ, reaching 10^{-3} S cm^{-1} at r.t. (Figure 4b).[82] In addition to garnet-type LLZO oxides, NASICON-type oxide-based SSEs, particularly LATP (a compound with a general composition of $Li_{1+x}Al_xTi_{2-x}(PO_4)_3$) and LAGP (a compound with a general composition of $Li_{1+x}Al_xGe_{2-x}(PO_4)_3$), have garnered increasing attention due to their high σ (exceeding 10^{-3} S cm^{-1} at r.t.), wide ESWs, and excellent chemical stability against air and moisture.[83] For example, Wang et al. reported the development of a LATP-based oxide SSE utilizing a co-doping strategy with B^{3+} and In^{3+}. The optimized SSE, with a composition of $Li_{1.3}Al_{0.21}B_{0.08}In_{0.01}Ti_{1.7}(PO_4)_3$, exhibited a maximum relative density of 98.2%, which resulted in a high σ of 1.1×10^{-3} S cm^{-1} at r.t. LAGP exhibits an impressive ESW of 6 V (vs. Li^+/Li), which holds significant promise for applications in high-voltage LMBs.[84] However, NASICON-type oxide-based SSEs exhibit limited compatibility with Li metals. For instance, when LATP

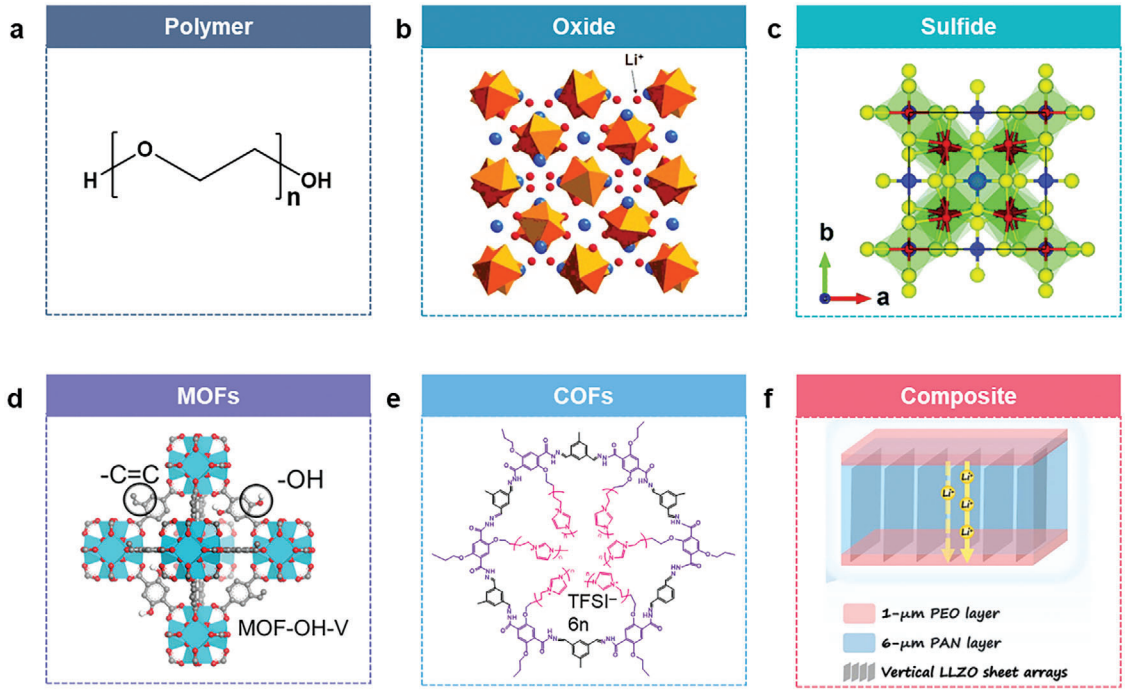

Figure 4. Representative SSEs. a) Chemical structure of polyethylene oxide (PEO). b) Schematic diagram of the crystal structure of $Li_7La_3Zr_2O_{12}$ (LLZO). Reproduced with permission.[82] Copyright 2007, Wiley-VCH Verlag GmbH & Co. KGaA. c) Schematic diagram of the crystal structure of $Li_{10}GeP_2S_{12}$ (LGPS). Reproduced with permission.[91] Copyright 2021, Royal Society of Chemistry. d) Structural illustration of MOF-OH-V (UiO-66 type). Reproduced with permission.[96] Copyright 2023, Wiley-VCH Verlag GmbH & Co. KGaA. e) Chemical structure of COF-MCMC (iCOFs with multicationic molecular chains).[99] f) Structural illustration of the LLZO/PAN/PEO composite. Reproduced with permission.[101] Copyright 2022, Elsevier.

comes into contact with Li metal, Ti^{4+} can be reduced to Ti^{3+}, leading to the formation of an insulating interfacial layer.[85] This layer has low σ, which increases interfacial resistance and promotes the formation of Li dendrites, ultimately resulting in significant capacity decay in the cells. The instability at the interface between LATP and Li metal further restricts its broader practical applications. Sulfides, another important class of ceramics SSEs, have garnered significant attention due to their outstanding σ. Various sulfide-based SSEs have been developed, based on their crystalline states, they can classify three major types: glass (e.g., $Li_2S{-}SiS_2$), glass-ceramic (e.g., $Li_2S{-}P_2S_5$), and crystalline (e.g., Li_6PS_5Cl).[86] Among them, a family of sulfide SSEs, lithium argyrodites Li_6PS_5X (X = Cl, Br), are attracting more attention due to high σ, easy processability, high thermostability, and relatively good compatibility with cathodes in LMBs.[87,88] For example, wang et al. reported a Li_6PS_5Cl SSE through the sintering at 550 °C for 10 minutes, which exhibit a high σ of 3.2×10^{-3} S cm^{-1} at r.t.[89] However, the undesired reaction between Li_6PS_5Cl and Li metal lead to the decomposition of Li_6PS_5Cl, the decomposition product Li_3P and Li_2S with low σ will hinder the Li^+ transport, resulting in diminished cell performance.[90] Following the discovery of $Li_{10}GeP_2S_{12}$ (LGPS, Figure 4c)[91] superionic conductor by Kanno's group in 2011,[92] sulfides have been recognized as promising SSEs with exceptional σ. Notably, LGPS exhibits a high σ of 1.2×10^{-2} S cm^{-1} at r.t. Several other Li superionic conductors have been reported to exhibit exceptional σ. For instance, $Li_{9.54}Si_{1.74}P_{1.44}S_{11.7}Cl_{0.3}$ and LSiGePSBrO demonstrate record-high σ of 2.5×10^{-2} and 3.2×10^{-2} S cm^{-1} at r.t., respectively.[93,94] The exceptional performance of sulfides has positioned them as SSEs capable of replacing liquid electrolytes. However, their weak chemical stability against moisture and high contact resistances remain critical issues. Porous crystalline polymers (PCPs) have gained widespread usage in energy devices due to their high porosity and highly defined ion channels, which facilitate efficient ion conduction. Among these materials, MOFs and COFs are particularly prominent. MOF-based SSEs have attracted considerable attention in LMBs due to their high surface area, significant Li^+ transport capability, and chemical and electrochemical stability.[95] A notable MOF-based SSE features customized bilayer zwitterionic nanochannels (Figure 4d), exhibiting a remarkable σ exceeding 10^{-4} S cm^{-1} at 30 °C, indicating efficient transport of Li^+ within the MOFs.[96] Yang et al. reported the development of an anionic MOF-based SSE with Li^+ as the sole mobile charge carriers. This SSE demonstrated a high t_{Li^+} of 0.90 and a σ of 6.0×10^{-4} S cm^{-1} at 25 °C.[97] COFs, porous crystalline materials synthesized through stable covalent bonds, represent another class of materials with significant potential. Among them, ionic covalent organic frameworks (iCOFs), where ion groups attached to the COFs' backbone, are distinct. iCOFs demonstrate great promise as SSEs in LMBs due to their highly ordered nanochannels that facilitate the transport of Li^+.[98] Huang's group reported an SSE constructed from iCOFs containing multicationic molecular chains for gate-mechanism-controlled ion transport, attaining high Li^+ conductivity (Figure 4e).[99] Li et al. presented an SSE based on an azanide-based anionic COF, which exhibited an outstanding t_{Li^+} of 0.93, an exceptional ESW of up to 5.6 V (Li^+/Li), and a σ of 1.3×10^{-5} S cm^{-1} at r.t.[100]

These results highlight the significant potential of iCOFs as SSE materials capable of facilitating rapid conduction of Li^+. However, achieving σ exceeding 10^{-3} S cm^{-1} at r.t. remains a significant challenge for MOF- or COF-based SSEs. Composite SSEs hold immense potential for next-generation high-performance LMBs due to their balanced properties. Among the various types of composites, ceramic/polymer composites have garnered significant attention owing to their high σ, high t_{Li^+}, excellent interfacial contact, and good chemical, thermal, and electrochemical stability.[10] For example, Wang et al. reported an oxide/polymer SSE composite consisting of well-ordered vertical LLZO sheet arrays, PEO, and polyacrylonitrile (PAN) (Figure 4f).[101] The composite SSE demonstrated an impressive σ of 2.6×10^{-4} S cm^{-1} at 30 °C. Incorporating LLZO contributes to the mechanical strength of the composite, while the trilayer polymer structure ensures excellent interfacial contact between the SSE and the electrodes. Additionally, the composite SSE exhibited an excellent ESW of 5.1 V (vs. Li^+/Li). Hu et al. proposed an ultrathin composite SSE composed of $Li_{6.75}La_3Zr_{1.75}Ta_{0.25}O_{12}$, poly(vinylene carbonate), and succinonitrile. This composite SSE exhibited a σ of 6.5×10^{-4} S cm^{-1} and a t_{Li^+} of 0.71 at r.t., along with a wide ESW of ≈5.0 V (vs Li^+/Li).[102] Our group proposed a novel composite SSE consisting of COF integrated with a charged polymer matrix.[103] This composite exhibited an exceptional σ exceeding 10^{-3} S cm^{-1} at r.t., along with a high t_{Li^+} greater than 0.80.

2.1. Ionic Conductivity and Li^+ Transference Number

σ and t_{Li^+} are the first steps to check when evaluating SSEs for LMBs. σ refers to the ability of an electrolyte to conduct ions. It is a measure of how rapidly ions can move through electrolytes. High σ in electrolytes is desirable because it enables efficient and rapid transport Li^+, facilitating high-energy-density output and fast charging/discharging.[104] Additionally, high σ reduces the battery's internal resistance, which helps minimize energy losses during the operation. t_{Li^+} is a measure of the fraction of total current carried by Li^+ compared to all other ions present in the electrolyte. Thus, it represents the electrolyte's selectivity on ions for transporting through it. It is important to note that cations and anions can participate in ion conduction and ideally, electrolytes should have a high t_{Li^+} to ensure that most of the current is carried by Li^+, to avoid undesired reactions on the surface of electrodes. This selective transport can not only inhibit parasitic reactions at the interface between Li anode and electrolytes, but also enables fast charging/discharging over 4 C.[25]

We assessed σ and t_{Li^+} values of different SSEs, with liquid electrolytes serving as a benchmark for comparison (**Figure 5**). Please note that this assessment only includes all-solid-state electrolytes. Samples containing fractions of organic solvents or plasticizers etc. are not included. As mentioned, liquid electrolytes exhibit a notable advantage in their high σ, ranging from 10^{-3} to 10^{-2} S cm^{-1}.[105] Achieving such a level of conductivity has been a target for most SSEs. However, liquid electrolytes exhibit a low t_{Li^+}, typically below 0.4.[106] The t_{Li^+} lower than 0.4 means that the total ionic conductivity mainly was contributed by anions, due to a less effective mobility of Li^+ and preferential solvation exhibited by Li^+ in comparison to its counterion. This leads to the formation of a voluminous solvation shell surrounding Li^+, contrasting with the solvation shells typically found around ordinary anions. Conventional polymer SSEs typically exhibit t_{Li^+} values ranging from 0.2 to 0.6.[10,107] For instance, SSEs based on PEO typically have t_{Li^+} values within the range of 0.2 to 0.4.[108] Thus, research on single-ion conductive, high t_{Li^+} exceeding 0.9, polymer SSEs have been the main focus in recent years. Gao et al. reported an impressive case for this, where a borate polymer SSE was crosslinked to show an exceptional t_{Li^+} of 0.98, approaching unity.[109] Furthermore, the researchers were able to achieve tunable σ by manipulating the segmental mobilities of the polymers used in the electrolyte system. Typically, polymer SSEs exhibit ionic conductivities in the range of 10^{-7} to 10^{-4} S cm^{-1} at r.t.[110] Such lower σ in polymer SSEs can be attributed to the existence of multiple ions in the system and ill-defined conducting pathways in an amorphous network. Recently, Han et al. reported a single-ion polymer SSE, which exhibited a σ of 4.2×10^{-5} S cm^{-1} at 30 °C, accompanied by a single-ion conductive t_{Li^+} of 0.93.[111] The efficient distribution of Li^+ throughout the material and facilitated site-to-site ion migration were achieved through the

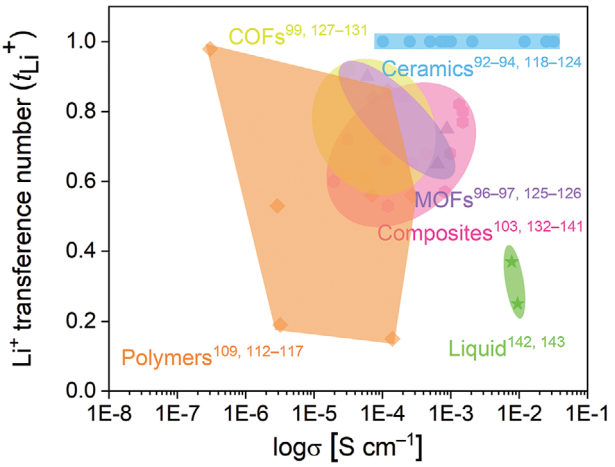

Figure 5. σ and t_{Li^+} of various SSEs. Polymer SSEs data include PDADMA FSI-LiFSI (80°C),[113] xPTHF10 and xPEO10 (30 and 70 °C for σ and t_{Li^+}, respectively.),[112] HPCPEG (85 °C),[114] P(IL-PEGDA) (30 and 25 °C for σ and t_{Li^+}, respectively.),[115] ANP–BEG7,[109] PEO_8–LiPCSI (60 °C),[116] and PTT-SPE.[117] Ceramic SSEs data include LGPS,[92] $Li_{9.54}Si_{1.74}P_{1.44}S_{11.7}Cl_{0.3}$,[93] LiF modified $Li_{0.35}La_{0.55}TiO_3$ (LLTO, a compound with a general composition of $Li_{3x}La_{2/3-x}TiO_3$),[118] $Li_{1.3}Al_{0.3}Ti_{1.7}(PO_4)_3$ (LATP),[119] $Li_7La_3ZrNb_{0.5}Y_{0.5}O_{12}$ (30°C)[120] LSiGePSBrO,[94] $Li_{6.25}Al_{0.25}La_3Zr_2O_{12}$[121] $Li_{6.55}Ga_{0.15}La_3Zr_2O_{12}$,[122] $Li_{6.65}Ga_{0.05}La_{2.95}Ba_{0.05}Zr_{1.75}Ta_{0.25}O_{12}$,[123] and Li_6PS_5I.[124] Metal–organic frameworks (MOF) SSEs data include UiOLiTFSI with Lithium bis(trifluoromethanesulfonyl)imide (LiTFSI, 25°C),[125] MOF-BZN (30 °C),[96] UiO-66-LiSS,[97] and UIO-67-Li.[126] Covalent organic frameworks (COF) SSEs data include TpPa-SO_3Li,[127] Li-CON-TFSI (30 °C),[128] COF-MCMC (30 °C),[99] dCOF-ImTFSI-60@Li (30 °C),[129] Li-CON-3 (20 °C),[130] and Im-COF-TFSI@Li (30 °C).[131] Composite SSEs data include TpPa-SO_3Li with Li DMA@LiTFSI (23°C),[132] $Li_{6.4}La_3Zr_{1.4}Ta_{0.6}O_{12}$/polyacrylonitrile (60 °C),[133] LLTO/$BiTiO_3$/PVDF (25 °C),[134] $Li_{6.75}La_3Zr_{1.75}Ta_{0.2}O_{12}$/polytetrafluoroethylene,[135] PEO/CMOF,[136] PEO-PVDF/LATP (25 °C),[137] LLZO/hybrid polymer (25 °C),[138] COFs/PEG (30 °C),[139] $Li_{6.4}La_3Zr_{1.4}Ta_{0.6}O_{12}$/PEO (60 °C),[140] PEO-PEG/LGPS,[141] and PIL/iCOFs.[103] Liquid electrolyte data.[142,143] The temperatures noted in the parenthesis are test conditions. If not mentioned, tested at r.t.

precise arrangement of designed repeating units within alternating polymer sequences. This structural design enhanced σ, enabling fast Li^+ transport within the SSE. Another type of polymer SSEs is a dual-ion conductive system, where Li^+ and anionic species exist within the polymer matrix. In these SSEs, the mobility of Li^+ is typically lower compared to the anionic counterparts. This reduced mobility can be attributed to the interactions between Li^+ and Lewis basic sites present in the polymer matrix. As a result, dual-ion conducting polymer SSEs often exhibit lower values of t_{Li^+}, typically below 0.5.[107] Zhenan Bao's group reported a crosslinked PEO polymer SSE, which exhibited a t_{Li^+} of 0.19, along with a σ of 3.2×10^{-6} S cm^{-1} at 30 °C.[112]

Ceramic SSEs are known for their high σ, which typically range from 10^{-4} to 10^{-2} S cm^{-1} at r.t. In some instances, the σ of ceramic SSEs can be comparable to or surpassing that of liquid electrolytes. Kanno's group reported a representative sulfide SSE with the compound formula $Li_{9.54}Si_{1.74}P_{1.44}S_{11.7}Cl_{0.3}$ in 2016, which exhibited an ultra-high σ of 2.5×10^{-2} S cm^{-1} at r.t.[93] This exceptional conductivity was attributed to the presence of 3D Li^+ pathways within the structure of the sulfide crystal lattices. According to the ion transport mechanism observed in ceramic SSEs, the t_{Li^+} of ceramic SSEs is generally unity, indicating that the Li^+ have predominant mobility within these materials.[65] Waetzig et al. reported an SSE based on a sodium (Na) superionic conductor (NASICON)-type oxide, specifically LATP, with the composition $Li_{1.3}Al_{0.3}Ti_{1.7}(PO_4)_3$.[119] The SSE exhibited an impressive σ of 1.0×10^{-3} S cm^{-1} at r.t., and the remarkable conductivity was attributed to the reduction in impurity concentration and the absence of secondary phases achieved through the implementation of sol-gel synthesis. Ceramic SSEs are by far the highest performers in terms of σ and t_{Li^+}; however, high interfacial contacts among the particles and questionable chemical stability are considered weak points.

We also include a class of emerging materials, such as MOFs and COFs. These materials exhibit great promise as SSEs for LMBs due to their highly crystalline porous structures, which facilitate efficient conduction of Li^+.[144] MOF SSEs typically showed σ ranging from 10^{-5} to 10^{-4} S cm^{-1} without any liquid components such as organic solvents or plasticizers. Zhu et al. demonstrated SSEs utilizing anionic MOFs combined with Li salt to show a high σ of 2.1×10^{-4} S cm^{-1} at 25 °C, along with a t_{Li^+} of 0.84.[125] SSEs based on single-ion MOFs have demonstrated the ability to achieve a high t_{Li^+} of 0.9, indicating their significant potential in facilitating efficient Li^+ conduction.[97] iCOFs, COFs having ionic groups installed, have attracted considerable attention as well,[98] as they can show single-ion conduction behavior, $t_{Li^+} > 0.9$ and high σ. This notable performance can be attributed to the direct installation of anionic groups onto the COF backbone, which effectively ensures that Li^+ are the exclusive mobile species within the material. The σ of COF SSEs ranges from 10^{-5} to 10^{-4} S cm^{-1}, without including any liquid components such as organic solvents or plasticizers. For instance, Li et al. developed a hydrazone-based iCOF, denoted as Li-CON-3, with a high t_{Li^+} of 0.92 and a σ of 3.2×10^{-5} S cm^{-1} at 20 °C.[130] To ensure the high performance of the battery cells, it is desirable for SSEs to have a t_{Li^+} of at least 0.8, although a value above 0.9, indicating single-ion conduction, is ideal. Achieving such high t_{Li^+} is not difficult for most SSEs, as anionic groups are typically immobilized on solid substrates. However, in practice, simultaneously achieving both exceptional σ and t_{Li^+} is challenging for many types of SSEs. Electrolyte formulations may prioritize one parameter over the other, depending on the specific requirements of the battery application. Thus, researchers and battery developers are continuously working on this point to enhance the performance and safety of the LMBs. Composite SSEs are practically the most preferred direction as they combine the advantages of both the fillers—conduction property—and the matrix—improved surface contacts and stability. Liu et al. reported a single-ion conducting polymer-modified garnet-type $Li_{6.4}La_3Zr_{1.4}Ta_{0.6}O_{12}$ (LLZTO) composite SSE, which exhibited both a high σ of 1.5×10^{-3} S cm^{-1} and a t_{Li^+} of 0.77 at 60 °C.[140] In section 3, we will discuss the detailed pros and cons of various SSEs.[145]

2.2. Interfacial Contact

The interfacial contact resistance between SSEs and electrodes is critical for solid-state batteries. Thus, researchers have developed strategies to minimize such contact resistance. Here, we classified the design of SSEs and cathode assembly, thereby interfacial resistances, into five primary classes (**Figure 6**). The first type is pure solid electrolytes (Figure 6a). This classification encompasses inorganic SSEs, or SSEs composed of highly rigid particles, such as MOFs and COFs, as pure composition. In these instances, voids arise unavoidably when it is unfeasible to attain the highest packing density, resulting in certain limitations concerning interfacial contact resistances.[63] The existence of voids within the interfacial contact between solid particles impedes ions' diffusion and hinders efficient charge transfer. Furthermore, Li dendrites can grow through the voids.[104] Although SSEs containing voids may possess a high t_{Li^+}, they usually result in reduced σ. This is mainly attributed to the inadequate pathways created by the presence of voids. An illustrative example is the sulfonate TpPa-SO_3Li COFs pellet, fabricated using a cold-pressing method and demonstrated a σ of 2.7×10^{-5} S cm^{-1} at r.t.[127] Another example is LLZO, a representative oxide SSE known for its wide ESW and excellent chemical stability against Li metal.[146] However, the resulting lithiophobic surface of LLZO caused significant interfacial resistance, limiting the electrochemical performance of the electrolyte and battery cells. In particular, the interfacial resistance between Li metal and LLZTO can reach 1789 Ω cm^2.[147]

Numerous studies have been conducted to reduce the interfacial contact resistances among the SSEs, and between SSEs and electrodes. One approach that has been widely investigated is using liquid solvents as plasticizers (Figure 6b), which results in the classification of these SSEs as QSSEs. Li et al. reported a TpPa-SO_3Li COF that was synthesized by a pre-synthesis approach.[148] To reduce the contact resistances and improve the σ of the electrolytes, a plasticizer of 10 µL of ethylene carbonate/dimethyl carbonate was introduced. The resulting TpPa-SO_3Li COF QSSE pellet demonstrated an impressive σ of 1.6×10^{-3} S cm^{-1} at 20 °C, surpassing the conductivity of solvent-free TpPa-SO_3Li COF.[127] The presence of plasticizers has significantly impacted the σ of the COF- or MOF-based SSEs. The incorporation of plasticizers in SSEs serves multiple functions. Plasticizers can dissociate Li^+

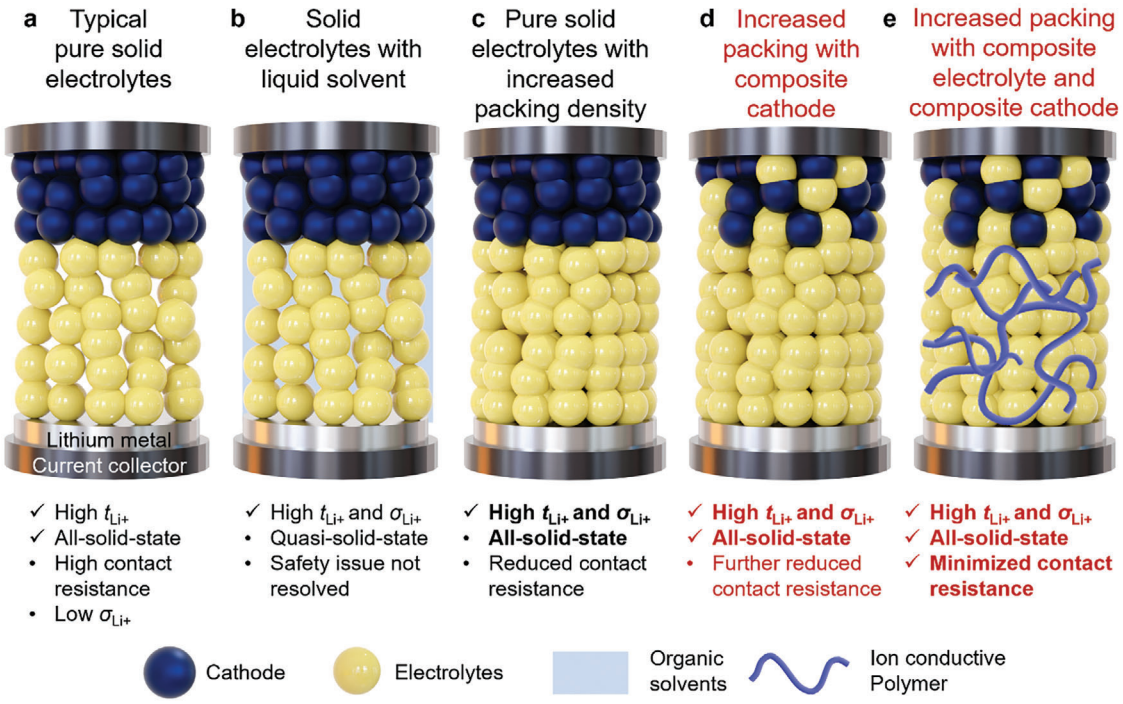

Figure 6. Five types of SSEs and cathode designs and their resulting contact resistances and electrochemical properties. a) Typical pure solid electrolytes. b) Solid electrolytes with liquid solvent as the plasticizer. c) Pure solid electrolytes with increased packing density. d) Increased SSE packing with composite cathode design. e) Increased SSE packing with composite electrolytes and composite cathode design.

within the porous structure of SSEs, thereby promoting their efficient transport through their highly organized ionic channels.[149] Additionally, plasticizers aid in mitigating the adverse effects of reduced ion transport caused by the presence of voids in SSEs. Hu's group implemented a strategy to improve the interfacial resistance between the garnet-type $Li_7La_{2.75}Ca_{0.25}Zr_{1.75}Nb_{0.25}O_{12}$ (LLCZN) SSE and $Li_2FeMn_3O_8$ cathode by incorporating a small amount of liquid organic electrolyte.[150] The liquid organic electrolyte consisted of a mixture of fluoroethylene carbonate, 3,3,3-fluoroethylmethyl carbonate, and 1,1,2,2-tetrafluoroethyl-2,2,2-trifluoroethyl ether in a volumetric ratio of 20:60:20, with a $LiPF_6$ concentration of 1 M. However, it is important to note that using liquid solvents in SSEs can raise safety concerns, especially in extreme operating conditions.

On the other hand, enhancing the packing density within the SSEs can lead to decreased interfacial contact between SSEs and electrodes (Figure 6c). In a study conducted by Wen's group, a sintering process was employed to fabricate highly dense LLZO SSEs with relative densities ranging from 97% to 98%.[151] The sintering process involved the manipulation of the Li_2O atmosphere. The resulting LLZO SSE exhibited improved interfacial contact with Li metal, leading to a critical current density of 0.9 mA cm^{-2}. Meng's group also conducted a study in which the interfacial contact between a Li anode and Li_6PS_5Cl SSE decreased by applying pressure at 25 MPa.[152] The Li_6PS_5Cl pellet with a relative density of 87% was prepared using a cold-pressing technique. Applying external pressure represents a straightforward and efficient approach to enhance the interfacial contact between SSEs and electrodes, resulting in improved cyclability of the batteries.[153] However, it should be noted that the practicality of applying external pressure in real-world applications would be limited.[59] Incorporating solid ionic conductors as catholytes within composite cathodes offers an advanced approach to reduce further interfacial resistance between SSEs and cathode materials (Figure 6d). Composite cathodes are fabricated by blending active cathode materials with SSEs. Additionally, an electronically conductive additive is included in the composite cathode formulation. This ionic conductive binder facilitates improved ion transport, thus promoting efficient electrochemical reactions and reducing interfacial resistance.[63] Rupp's group synthesized an LCO cathode by directly infiltrating metal salts within a porous LLZO scaffold at a relatively low processing temperature of 700 °C.[154] This process led to the forming of a composite cathode, specifically LCO/LLZO, on the surface of a dense LLZO SSE. The resulting composite cathode exhibited a low interfacial resistance of 62 Ω cm2 when in contact with a Li anode. This method is important in developing LLZO SSEs for high-performance ASSLMBs.

The most sophisticated method is to introduce ion conductive polymer to the packed SSEs while having a catholyte design (Figure 6e). This setup can facilitate high σ, increased t_{Li^+}, and minimized contact resistance. Sun's group investigated composite systems integrating PEO and ceramic components.[155] The performance of a composite SSE comprising 20 vol.% of 200 nm LLZTO particles was examined, revealing a notable σ of 1.6×10^{-4} S cm^{-1} at 30 °C. Additionally, an evaluation was conducted on a composite SSE comprising 80 vol.% of 5 μm LLZTO particles, revealing a notable tensile strength of 12.7 MPa. To overcome challenges related to dendrite

suppression and achieving optimal interfacial contact with Li metal, a sandwich-type composite SSE was developed. This innovative design incorporated hierarchical garnet particles, with a 5 µm particle layer strategically positioned between two layers of 200 nm particles. As a result, the sandwich-type composite SSE successfully mitigated dendrite formation and established superior interfacial contact with Li metal. Fan's group presented a 3D composite SSE consisting of $Li_{6.75}La_3Zr_{1.75}Ta_{0.25}O_{12}$, succinonitrile, and polytetrafluoroethylene (PTFE) binder.[135] With 80.4 wt.% garnet ceramic, this SSE film exhibited excellent heat resistance, nonflammability, and high processability. It featured a wide electrochemical stability window of 4.8 V (vs. Li^+/Li), making it suitable for high-voltage ASSLMBs. Our group reported a solvent- and plasticizer-free composite SSE composed of iCOFs and poly(ionic liquid) (PIL).[103] The composite SSE, incorporating silicate COFs, demonstrated an exceptional σ of 1.5×10^{-3} S cm^{-1} and a t_{Li^+} of 0.8 at r.t. Moreover, it exhibited excellent compatibility with a Li metal anode. To mitigate the interfacial resistance between the composite SSE and the cathode, a composite cathode was prepared by blending SSEs with LFP. As a result, the Li|SSE|LFP coin cell exhibited an initial discharge capacity of 141.5 mAh g^{-1} at 1 C and r.t., and maintained a high capacity of over 87% after 800 cycles.

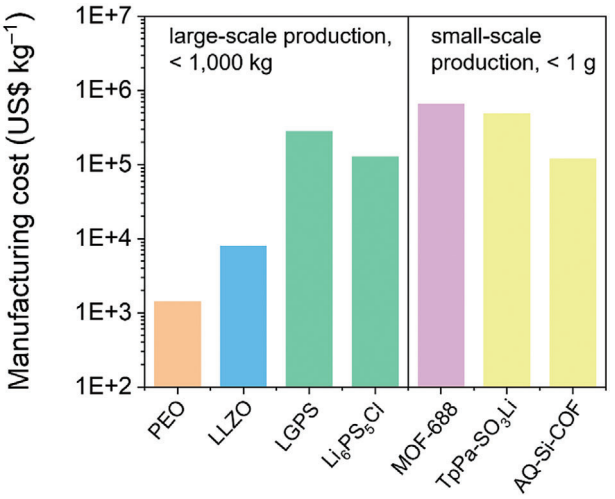

Figure 7. Manufacturing costs of various SSEs. Estimated costs for PEO, LLZO, LGPS, Li_6PS_5Cl, MOF-688, TpPa-SO_3Li, and AQ-Si-COF are \$1420, \$8000, \$278 000, \$128 000, \$655 055, \$490 808, and \$119 539 kg^{-1}, respectively.

2.3. Manufacturing Cost

The manufacturing cost of SSEs is crucial for determining whether the commercialization of ASSLMBs can successfully replace traditional LIBs. These costs include mainly the expenses associated with raw materials and processing. Processing costs primarily include investment in production equipment and processes, labor, and energy consumption. Liquid electrolytes and separators used in current commercial LIBs range from ≈\$12–20 kg^{-1}.[156,157] To ensure the competitiveness of ASSLMBs against the currently available commercial LIBs in the market, it is crucial to keep the material cost of SSEs below \$50 kg^{-1}, although we note that large-scale production with such low cost and high yield would remain a formidable challenge.[158] We note that commercialization of the SSEs is still in its infancy, and cost analyses based on current state-of-the-art technology would be helpful to foresee and design the next steps.

Here, we analyze the manufacturing cost of different SSEs – large-scale production for polymers and ceramics <1000 kg, and small-scale for MOFs and COFs <1 g (**Figure 7**). PEO is the most widely used polymer matrix as they are easy to synthesize and process. PEO-based SSEs mainly consist of PEO and Li salt, such as the commonly used Lithium bis(trifluoromethanesulfonyl)imide (LiTFSI). Therefore, the manufacturing cost of PEO-based SSEs is quite low, estimated to be around \$1,420 kg^{-1}.[159] Ceramics, including oxides and sulfides, generally have higher material costs than PEO-based SSEs. For instance, the cost of LLZO is estimated to be around \$2000 kg^{-1}.[55] However, sulfide-based SSEs tend to have even higher materials costs than LLZO due to the inclusion of expensive metal elements such as Germanium (Ge). For example, LGPS and Li_6PS_5Cl are around \$69 500 and \$32 000 kg^{-1}, respectively.[160] When fabricating energy devices, it is generally applicable that the processing cost is approximately three times higher than the materials cost.[161] Due to the various processing methods employed for oxides and sulfides, it is impossible to evaluate their processing costs using a single parameter accurately. Still following the above general practice, the estimated manufacturing costs for LLZO, LGPS, and Li_6PS_5Cl are ≈\$8 000 kg^{-1}, \$278 000 kg^{-1}, and \$128 000 kg^{-1}, respectively.

Currently, the mass production (kilogram scale) of MOFs and COFs has not been achieved, as those emerging materials are still laboratory-level research. Thus, we need to rely on small-scale laboratory preparation methods (starting monomers, <100 mg, and solvent, <300 mL) when assessing the manufacturing cost of MOF- or COF-based SSEs, meaning that the manufacturing cost primarily involves the procurement cost of starting monomers and bases, cost of laboratory equipment, electricity, and human resource. Let's take a representative from the Yaghi's group, MOF-688.[162] When we factored in the prices of commercial raw materials from chemical vendors, such as Sigma-Aldrich and TCI Co., Ltd, and associated electricity and labor during the synthesis process, the calculated manufacturing cost for this MOF electrolyte is \$655 055 kg^{-1}, far surpassing the cost of LGPS. Again, please note that this is a synthetic cost in small lab-scale, <1 g. The production cost could go lower upon successful mass production. When we applied the same assessment method, the production cost of the sulfonate COFs, TpPa-SO_3Li, from Lee's group[127] is ≈\$490 808 kg^{-1}, slightly lower than the cost of MOF-688 SSEs. Our group reported anthraquinone-based silicate COFs with a remarkable σ of 9.8×10^{-3} S cm^{-1} at r.t. and a t_{Li^+} of 0.92.[163] When applying the same calculation method, the production cost of the anthraquinone-based silicate COFs turned out to be \$119 539 kg^{-1}. Notably, the manufacturing costs associated with those emerging SSEs exhibit significant heterogeneity owing to many determinants, such as types of monomers used and synthetic procedures, which indicate a long way ahead for mass production.

2.4. Electrochemical Stability

The electrochemical stability of SSEs is a critical characteristic that determines their capacity to function and endure electrochemical conditions without undergoing undesirable chemical or structural alterations. This property ensures solid-state batteries' optimal performance and long-term stability.[63] Before exploring compatible cathode and anode materials, it is essential to identify the electrochemical window ranges of the SSEs to ensure compatibility and optimal performance in battery devices. The electrochemical stability of SSEs under equilibrium conditions is often evaluated using the grand potential diagram by varying the chemical potential of Li.[164] Some factors can influence the chemical potential of Li in SSEs, including the composition of the SSE, doping with specific elements or ions, temperature, pressure, surface effect, and electrode materials. Comprehending the influence of these factors on the chemical potential of Li in SSEs is essential for the design and optimization of SSE materials and their interfaces in electrochemical devices.[165] Here, we summarize the experimental electrochemical window ranges for various SSEs, including polymers, oxides, sulfides, MOFs, COFs, and composites (**Figure 8**).

Typically, most polymer-based SSEs exhibit an ESW within the 4–5 V (vs Li^+/Li). Notably, SSEs based on PEO have demonstrated an ESW of up to 3.9 V.[74] However, in practical applications of ASSLMBs, an ESW surpassing 4.2 V is highly desirable. Notably, carbonate-based polymer SSEs, owing to their higher dielectric constants, exhibit higher ESWs than PEO-based SSEs.[187] For instance, Shan et al. reported poly(vinyl ethylene carbonate)-based SSEs synthesized via in situ copolymerization, which showcased an impressive ESW of up to 5 V (vs Li^+/Li).[167] This observation underscores the potential of carbonate-based polymer SSEs for utilization in high-voltage ASSLMBs.

Oxide-based SSEs generally exhibit superior electrochemical stability. The oxidation stability of oxide-based SSEs is indeed influenced by the release of $O2^-/O_2$ gas, which is closely related to the oxygen atom bonding environment with neighboring atoms. For instance, two commonly studied oxide-based SSEs, garnet-type LLZO and perovskite-type LLTO (a compound with a general composition of $Li_{3x}La_{2/3-x}TiO_3$), exhibit different oxygen atom bonding environments and exhibit different oxidation stabilities. Among oxide-based SSEs, garnet-type LLZO, is known for its excellent chemical stability and a wide electrochemical window of 0–6 V (vs. Li^+/Li), making it a promising candidate for applications that require demanding long-term operations compared with LLTO.[146] The oxygen atoms in LLZO are bonded to Zr atoms to form a highly stable ZrO_6 octahedral configuration. This strong bond prevents the release of $O2^-/O_2$ gas and enhances the oxidation stability of the material. This way, LLZO can withstand high-voltage operation and is compatible with Li metal anodes. However, LLTO is more prone to oxidation than LLZO. The oxygen atoms in LLTO are bonded to Ti atoms, and this bonding environment is less stable than the ZrO_6 octahedral configuration in LLZO. Consequently, LLTO can release $O2^-/O_2$ gas under certain conditions, leading to material degradation and reduced stability. A notable example is the work conducted by Hu's group, which investigated a Ca^{2+} and Nb^{5+} substituted LLZO, known as LLCZN.[150] LLCZN exhibited an exceptional ESW of up to 6 V (vs Li^+/Li). Furthermore, the reduction potential of SSE is determined by its cation framework, particularly the lower oxidation states accessible to the cation and its thermodynamic reduction potential. SSEs with cations with lower oxidation states and lower thermodynamic reduction potentials generally exhibit lower reduction potentials. In these garnet-type LLZO SSEs, reduction reactions can occur, involving the reduction of cations like Zr^{4+} to lower oxidation states, such as Zr^{3+}, or even to the metallic form.[174] Due to its low decomposition energy, LLZO may undergo reduction decomposition reactions when the voltage falls below 0.05 V (vs Li^+/Li). The reduction may generate products such as Li_2O, Zr_3O, and La_2O_3.[174] It is widely acknowledged that the electrochemical window of SSEs is defined by their oxidation voltage and reduction potential. Specifically, the oxidation voltage establishes the upper limit of the electrochemical window, while the reduction potential determines the lower limit. Therefore, when designing and utilizing electrolytes, careful consideration of voltage selection is needed to avoid escaping its stability range.[188] A NASICON-type oxide-based SSE, LATP can undergo reduction reactions as well.[173] The Ti cations in LATP can be reduced from Ti^{4+} to Ti^{3+} or even further to the metallic form. A study conducted by Zhou's group investigated an ultra-fine surface LAGP SSE with the specific composition $Li_{1.5}Al_{0.5}Ge_{1.5}P_3O_{12}$, which belongs to the NASICON-type oxide family.[84] The LAGP SSEs exhibited a wide electrochemical window ranging from 0.5 V to 6 V (vs Li^+/Li).

Among the ceramic SSEs, sulfides exhibit relatively poor electrochemical stability and thus come with narrower electrochemical windows. For example, Li_2S is stable within the voltage range of 0–2.01 V, and one of the notable sulfide SSEs, LGPS, undergoes lithiation and reduction starting at 1.71 V.[189] The anionic framework within their structure strongly influences the oxidation stability of SSEs. The onset oxidation potential of sulfide SSEs is highly dependent on factors such as the electronegativity of the anion and its charge density. These properties directly impact the ability of SSEs to withstand oxidation processes. SSEs with highly electronegative anions and high charge density exhibit greater oxidation stability.[190] Fluorides, the most electronegative atoms, can be incorporated into SSEs to enhance their oxidation stability, although fluoride-based SSEs generally exhibit lower ionic conductivity.[191,192] The electrochemical stability of sulfide-based SSEs is also known to be influenced by their structural properties. Theoretical calculations have predicted an electrochemical window of 0.6–3.7 V (vs Li^+/Li) for Li_3PS_4 (LPS) SSE.[193] However, experimental results on nanostructured β-LPS SSE, as reported by Liu et al., have demonstrated stability within a wider voltage range of 0–5 V (vs Li^+/Li).[176] This underscores the importance of considering both theoretical calculations and experimental design to improve the electrochemical stability of SSEs.

Emerging PCPs demonstrated wide ESWs comparable to those of sulfides. For MOFs, choosing metal centers and organic linkers is important for their electrochemical behavior and, consequently, their electrochemical windows.[194,195] Different metal centers can exhibit varying redox potentials, affecting the upper and lower voltage limits of the electrochemical window. Similarly, the organic linkers' nature and stability determine the MOF structure's overall electrochemical stability. A representative example is the use of single-ion conducting UiO-66 MOF.[97] This SSE is synthesized by covalently immobilizing anions onto the

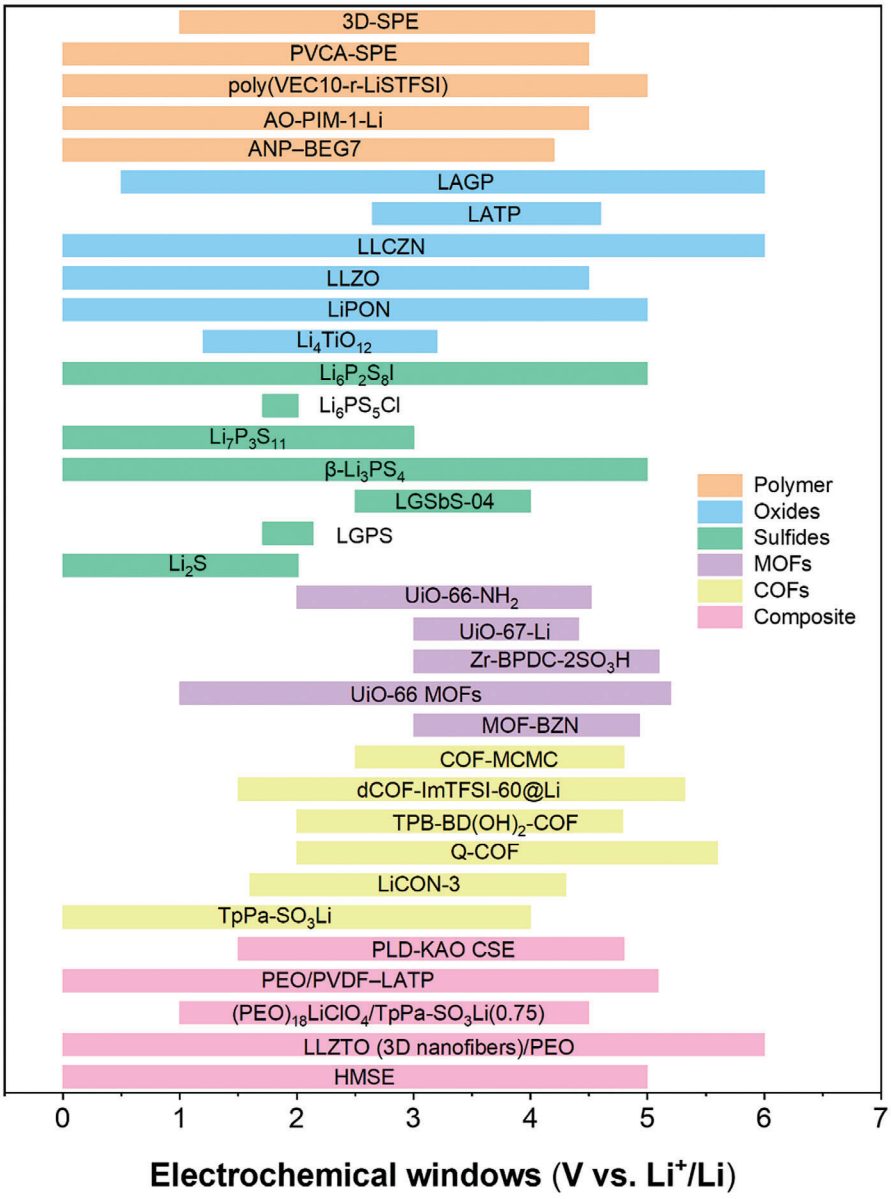

Figure 8. Experimental electrochemical windows of various SSEs. Polymer SSEs include ANP–BEG7,[109] AO-PIM-1-Li,[166] poly(VEC10-r-LiSTFSI),[167] PVCA-SPE,[168] and 3D-SPE.[169] Oxide SSEs include Li_4TiO_{12},[170] LiPON,[171] LLZO,[172] $Li_7La_{2.75}Ca_{0.25}Zr_{1.75}Nb_{0.25}O_{12}$ (LLCZN),[150] LATP,[173] LAGP.[84] Sulfide SSEs include Li_2S,[85] LGPS,[174] LGSbS-04,[175] β-Li_3PS_4 (LPS),[176] $Li_7P_3S_{11}$,[177] Li_6PS_5Cl,[178] and $Li_6P_2S_8I$.[179] MOF SSEs include MOF-BZN,[96] UiO-66 MOFs,[97] Zr-BPDC-2SO_3H,[180] UiO-67-Li,[126] and UiO-66-NH_2.[125] COF SSEs include TpPa-SO_3Li,[127] LiCON-3,[130] Q-COF,[181] TPB-BD$(OH)_2$-COF,[182] dCOF-ImTFSI-60@Li,[129] and COF-MCMC.[99] Composite SSEs include HMSE,[183] and LLZO (3D nanofibers)/PEO,[184] $(PEO)_{18}LiClO_4$/TpPa-SO_3Li(0.75),[185] PEO/PVDF–LATP,[137] and PLD-KAO CSE.[186]

MOF structure's skeleton, which exhibited a wide electrochemical window of ≈1–5.2 V (vs. Li^+/Li). Zeng et al. reported an SSE incorporating cross-linked MOF chains, and this SSE displayed an ESW of 5.1 V (vs Li^+/Li).[180] Regarding the electrochemical stability of COFs, various factors, including the nature of the organic linkers and the presence of functional groups, can impact their electrochemical stability.[196] Understanding and optimizing these factors can help enhance the electrochemical stability of COFs, making them more suitable for LMBs. Researchers have developed COFs with enhanced stability and wider electrochemical windows by designing chemically robust linkages and optimizing the pore structures.[197] The sulfonate COFs, TpPa-SO_3Li, exhibited an electrochemical window of 0–4 V (vs Li^+/Li).[127] To enhance the stability and performance of COF-based SSEs, researchers have employed ingenious post-functionalization strategies. These strategies aimed to improve the oxidation resistance of the COF skeleton, enabling it to withstand harsh electrochemical conditions. After post-functionalization, quinolyl-linked COF SSEs demonstrated improved oxidation resistance, better compatibility with high-voltage NCM811 cathodes, and an

expanded ESW of up to 5.6 V (vs Li^+/Li).[181] The high-voltage tolerance was attributed to the incorporation of stable electron-withdrawing triazine and polyfluorobenzene groups into the skeleton of the imine-linked COF. Furthermore, the Povarov reaction was utilized to convert the reversible imine linkage into more stable quinoline aromatic ring linkages. It served as the first example of high-voltage tolerant COF-based SSEs, and displayed the highest oxidation voltage. Another noteworthy example is the utilization of defective 2D COFs functionalized with imidazolium groups, dCOF-ImTFSI-60-based SSE.[129] This COF SSE demonstrated a remarkable ESW of up to 5.3 V (vs Li^+/Li). These findings suggest that MOFs and COFs have the potential to serve as high-voltage SSEs for ASSLMBs.

Addressing the inherent limitations associated with the narrow ESWs of SSEs, especially the sulfide-based materials, can be achieved by implementing a composite approach. For example, a composite SSE, PEO/PEG-3LGPS, was developed by integrating LGPS fillers within a polymer matrix consisting of PEO and polyethylene glycol (PEG).[141] Notably, this composite SSE exhibited an exceptional ESW surpassing 5.1 V (vs Li^+/Li). A noteworthy example from Hu's group involves the development of an oxide/polymer composite utilizing 3D garnet-type $Li_{6.4}La_3Zr_2Al_{0.2}O_{12}$ nanofibers as fillers and PEO as the matrix material.[184] This composite exhibited an impressive ESW of 0–6 V (vs Li^+/Li). In addition, investigations have been conducted on the ESWs of composite systems comprising PCPs and polymers. For example, the composite $(PEO)_{18}LiClO_4$/TpPa-SO_3Li(0.75), which combined a PEO polymer matrix with TpPa-SO_3Li iCOFs powder fillers, exhibited an enhanced ESW of 4.5 V (vs Li^+/Li), surpassing the ESW of 4 V observed from TpPa-SO_3Li alone.[185] These results highlight the effectiveness of making the composite in achieving a wide ESW and, thus, high-performance ASSLMBs.

2.5. Dendrite Suppression

Currently, LIBs utilizing flammable liquid electrolytes suffer from safety issues caused by the formation and growth of Li dendrites.[198,199] These dendrites can penetrate the porous separator and create internal short circuits, leading to cell ignition and posing significant safety concerns. The same issues exist in the LMBs and are even worsened to the extent that LMBs have highly reactive Li metal as anode. Thus, the broader adoption of LMBs depends on safety management related to dendrite growth. In this context, SSEs are desirable for LMBs, as SSEs are non-flammable and mechanically strong, effectively blocking the penetration of Li dendrites, and electrochemically stable compared to liquid electrolytes.[200,201]

While polymer SSEs offer advantages such as flexibility and ease of processing, the soft nature of polymers is often considered a crucial factor contributing to dendrite penetration.[202] Most polymer SSEs demonstrate a low shear modulus, which renders the electrolyte vulnerable to the growth of sharp dendritic structures. According to the Monroe and Newman model, dendrite growth can theoretically be suppressed if the shear modulus of SSEs is greater than 1.8 times the shear modulus of Li metal, which is ≈2–4 GPa.[203,204] Various strategies are being explored to address the issue of dendrite penetration in polymer SSEs. These efforts involve the development of electrolyte additives or modifications that aim to enhance the mechanical properties of polymer SSEs. These additives, often called fillers, can be incorporated into the electrolyte system to improve mechanical properties, enhance thermal stability, provide structural support, or achieve specific functionalities.[155] In addition, methods to increase the stiffness of the polymer SSEs are being explored as an effective means of suppressing dendrite growth.[205] For example, Yang et al. introduced a polymer SSE that utilized an in situ cross-linking approach of PEO in the presence of a woven glass fiber.[206] The resulting polymer SSE exhibited a significantly high elastic modulus of up to 2.5 GPa, surpassing PEO/LiTFSI's modulus of ≈0.1 MPa.[207] The substantial elevation of the elastic modulus indicates heightened mechanical robustness, thereby suppressing dendrite formation.

Inorganic ceramic SSEs demonstrate significantly higher shear modulus than soft polymer SSEs, making it easier to satisfy the shear modulus criterion. For example, the garnet-type LLZO exhibits an exceptionally high shear modulus of 100 GPa.[208] This high mechanical strength can easily suppress the formation and growth of Li dendrites. Indeed, it has been widely believed that inorganic SSEs possess a rigid nature that should inherently restrict the growth and spread of Li dendrites within these materials.[209] However, as research progressed, it became apparent that the rigidity of inorganic SSEs alone is insufficient to prevent the formation and propagation of Li dendrites, mainly when higher current density is applied.[210] Several factors can contribute to this, including defects or imperfections in the SSEs, the interface between the SSEs and the electrodes, and the influence of external operating conditions.[211,212] This phenomenon has been observed in different material systems, such as LLZO,[213] Li_6PS_5Cl,[214] and $Li_2S-P_2S_5$.[215] To address this challenge, researchers are exploring additional strategies beyond rigidity alone, including developing SSEs with minimized defects, optimizing interface design to enhance adhesion, and uniaxial cold or hot pressing to suppress dendrite growth.[202,216] For example, Wang's group incorporated LiI, a material with high σ but electronic insulation properties, into the $Li_2S-P_2S_5$ SSE to significantly enhance the suppression of dendrite formation.[217] The resulting Li|SSE|Li symmetric cell demonstrated excellent cycling performance, maintaining stable operation for 200 h at a current density of 1.5 mA cm^{-2} and 100 °C. This highlights the need for a comprehensive understanding of the interplay between material properties, interface interactions, and operating conditions to effectively mitigate dendrite formation and ensure solid-state battery systems' long-term stability and safety.[218]

PCPs, such as MOFs and COFs, have been increasingly investigated as potential protective coatings for Li metal anodes to mitigate dendrite growth.[219,220] These materials exhibit unique properties, including designable structures, high rigidity and stability, and versatile functionality. As an example, Guo's group introduced a zirconium-based MOF layer into the Li metal anode.[221] The incorporation of this MOF layer facilitated uniform transport of Li^+ and exhibited significant mechanical strength. The MOF materials employed in this study demonstrate a considerably high Young's modulus of approximately 32 GPa, resulting in an effective restriction of dendrite propagation. Single-ion conducting PCP SSEs exhibit significant potential in suppressing dendrite formation, effectively promoting uniform Li

deposition. For instance, the UiO-66 MOFs SSE, with a high t_{Li^+} of 0.9, promoted the dense growth of Li deposits, resulting in effective dendrite suppression.[97] Yue et al. reported triazine-based COFs highly enriched in nitrogen, with a nitrogen content of 47.04 at%.[220] The COFs prepared in this work possess a remarkable Young's modulus of 3.51 GPa, effectively impeding the formation of Li dendrites. Arumugam Manthiram's group reported COFs, synthesized via co-condensation reaction of diboronic acid and hexahydroxytriphenylene, to show a high Young's modulus of 15–20 GPa.[222] The substantial strength of this COF was sufficient to inhibit the growth of Li dendrites. Recently, Zheng's group reported an exciting breakthrough regarding the remarkable mechanical strength of single-crystal 2D COF films.[223] These elastic COF films exhibit an exceptional Young's modulus, with the highest value reported at 73.4 ± 11.6 GPa. This outstanding mechanical strength of COF film-based materials renders them highly promising for utilization as SSEs in battery applications. Notably, iCOFs, exhibiting both rapid Li^+ conduction and suppression of Li dendrites, are promising as solid electrolyte interphase (SEI) materials and SSEs. Notably, a study by Xu's group introduced 3D anionic COF SSEs called CD-COF-Li.[224] The unique characteristic of single-ion conductivity in iCOFs contributes to the superior ability of this type of COF SSE to inhibit the growth of Li dendrites. The Li|CD-COF-Li|Li configuration demonstrated stable cycling at a current density of 0.2 mA cm^{-2} for over 800 h. Further investigation is required to gain a deeper understanding of the factors influencing the growth of Li dendrites in SSEs based on MOFs and COFs. This area of research necessitates additional research efforts to delve into the underlying mechanisms and explore potential strategies for dendrite suppression.

Composite materials consisting of both soft and rigid components have been designed to address the trade-offs between Young's modulus and interfacial contact in SSEs. Guo's group developed polymer/polymer composite SSEs using an interpenetrating poly(ether-acrylate) structure.[225] These SSEs were synthesized by photopolymerizing ion-conductive PEO and branched acrylate. The rigid and flexible structure of this SSE offered several advantages. It exhibits a high σ of 2.2×10^{-4} S cm^{-1} at r.t. Furthermore, it possesses sufficient mechanical strength, with a value of ≈12 GPa, effectively impeding the Li dendrites growth. He et al. presented a 3D composite SSE consisting of LLZO and poly(vinylidene fluoride-co-hexafluoropropylene), and this composite architecture synergistically combines high-rigidity ceramics with soft polymers.[226] The resulting composite SSEs demonstrated both high mechanical strength and uniform deposition of Li^+, thus effectively impeding the growth of Li dendrites. As a result, the Li|SSE|Li symmetric cell utilizing this composite SSE, when subjected to a current density of 0.2 mA cm^{-2}, could operate continuously for up to 1500 h. Guo's group reported the development of a thin-film LLZTO/PAN composite SSE, where PEO SSE was applied on the surface of LLZTO/PAN to prevent the reactivity between PAN and Li metal.[133] The LLZTO/PAN/PEO sheet exhibited Young's modulus of ≈9.7 GPa, which provides the ability to effectively suppress the formation of Li dendrites. Consequently, the Li|SSE|Li symmetric cell, utilizing the thin-film LLZTO/PAN composite SSE sandwiched between two Li foils coated with PEO SSE, demonstrated stable Li plating and stripping behavior for 300 h at a current density of 0.1 mA cm^{-2} and 60 °C. Manthiram's group also published a study on a polymer/iCOFs composite SSE synthesized through in situ polymerization called DMA@LiTFSI-mediated COF (DLC).[132] The SSE exhibited a dual SEI structure on its surface, composed of an inorganic inner layer and an organic outer layer. The high mechanical strength of the inner layer, with Young's modulus of ≈9 GPa, effectively suppressed the growth of Li dendrites. Meanwhile, the soft top layer, with Young's modulus of ≈4 GPa resulting from the DLC electrolyte, facilitates the maintenance of electrode|electrolyte contact during Li stripping and deposition. Overall, incorporating both soft and rigid materials in composite structures offers the potential for enhanced mechanical properties, including an improved Young's modulus, while concurrently ensuring favorable interfacial contact with the electrodes. This approach enables superior ion transport, reduced interfacial resistance, and overall enhanced performance of the SSEs.

Now we summarize the above discussion about the properties of different SSE types based on the six parameters in the radar charts (**Figure 9**). Among various electrolytes, liquid electrolytes demonstrate the highest levels of σ and exhibit exceptional interfacial contact with electrodes.[227] As a result, most commercial LIBs employ liquid electrolytes. However, their low electrochemical stability and vulnerability to dendrite growth make people find alternatives for LMB applications.[228] Within the SSEs, inorganic ceramics, PCPs (MOFs and COFs), and composites demonstrate higher σ relative to conventional polymers. Inorganic ceramics, MOFs, COFs, and composites demonstrate better suppression of Li dendrites compared to conventional polymers, owing to their improved mechanical properties and higher t_{Li^+}.[44] However, conventional polymers possess better interfacial contact than other types of SSEs characterized by high rigidity, such as inorganic ceramics, MOFs, and COFs. Composites can make good interfacial contacts as well. Regarding electrochemical stability, conventional polymers, and inorganic ceramics do not exhibit significant improvements compared to liquid electrolytes. However, MOFs, COFs, and composite SSEs demonstrate high levels of electrochemical stability among different types of electrolytes. Among the various types of electrolytes, the manufacturing cost for inorganic ceramic and PCPs stands out as the two most expensive options. The elevated manufacturing cost of inorganic ceramics can be attributed to the high cost of raw materials and the substantial processing expenses associated with high-temperature sintering procedures.[229,230] PCPs have the highest manufacturing costs, primarily due to the intricate and energy-intensive nature of the synthesis process and expensive small-scale production.[231,232] However, costs are expected to decrease when the scaled-up production is successful. We also summarized this information on various SSE's significant advantages/disadvantages (**Table 1**).

3. State-of-the-Art Examples of SSEs in the Past 5 Years

Over the past 15 years, there has been a significant increase in publications related to SSEs for LMBs (**Figure 10**). The total number of publications increased almost exponentially to become 509, 619, and 648 in 2021, 2022, and 2023, respectively (Note that

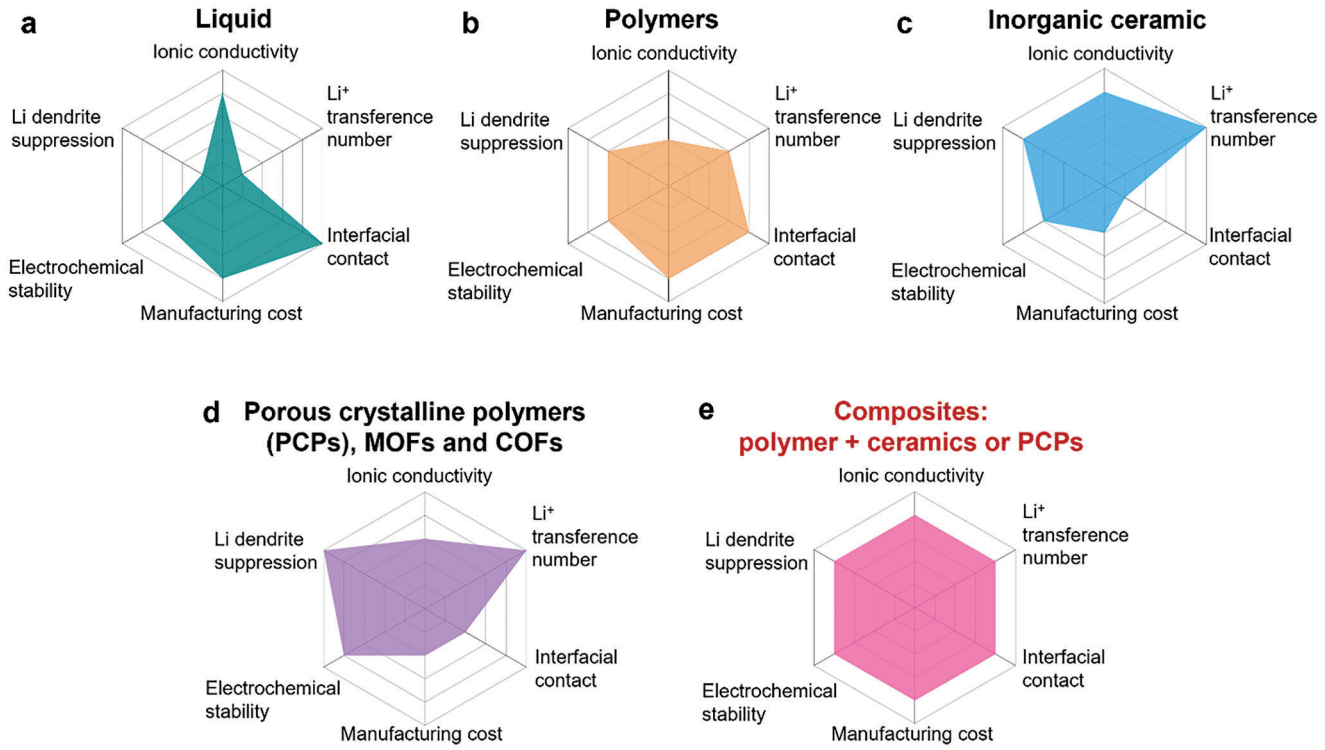

Figure 9. Analysis of electrolytes for LMBs. a) Liquid. b) Polymers. c) Inorganic ceramic. d) Porous crystalline polymers (PCPs), MOFs, and COFs. e) Composites: polymer + ceramics or PCPs. Balanced properties from composite SSEs seem to be ideal for practical ASSLMB applications.

we only included all-solid-state cases. The QSSEs cases are excluded). The publication in polymer is the major part, taking 47.7, 49.1, and 52.1% in 2021, 2022, and 2023, respectively. Composites take the second largest portion to be 33.4, 29.9, and 24.3% in 2021, 2022, and 2023, respectively. Pure ceramics account for a smaller portion, with 9.8, 10.5, and 10.7% in 2021, 2022, and 2023, respectively, several times less than polymer and composite SSEs. Pure MOF and COF SSEs have the smallest shares. MOFs take up 7.5, 8.6, and 9.5% in 2021, 2022, and 2023, respectively, remaining below 10%. Although publications on COFs are minimal, they exhibit a gradual upward trend, comprising 1.6%, 1.9%, and 3.4% in 2021, 2022, and 2023, respectively. Composite SSEs can be classified into four main categories based on the type of fillers used in conjunction with a polymer matrix: polymer composites, ceramic composites, MOFs composites, and COFs composites. Ceramic composites hold the majority share among the total composites, accounting for 60.6, 53.5, and 41.5% in 2021, 2022, and 2023, respectively. The total polymer shares, including pure polymer and composite, dominate the research and comprise more than half of the SSE research. This dominance stems from the benefits of decent yet efficient Li^+ transport, high flexibility, processability, favorable interfacial contact with electrodes, and wide ESWs.[107] Other than polymer and ceramics composites, composites with filler materials, such as COFs, are still being explored and in their infancy, with a percentage remaining around or less than 10%. Thus, we expect to see more contributions from these areas. In the following section, we analyze the features and pros and cons of each SSE sector, polymers, oxides, sulfides, MOFs, COFs, and their composites, and provide a comparison table of the σ, t_{Li^+}, and ESW (vs Li^+/Li) of representative SSEs, as well as LMB performance utilizing these SSEs at the end of the section to understand recent trends in SSE research from an overarching view.

3.1. Conventional Materials: Polymer

Polymer SSEs, consisting of a polymer host and Li salts such as LiTFSI and lithium bis(fluorosulfonyl)imide (LiFSI), hold great promise for solid electrolytes due to their ease of processing, flexibility, low cost, good interfacial contact with electrodes, and excellent mechanical properties.[110] The first polymer SSE reported was PEO. In 1973, Wright et al. discovered that blending PEO with alkali metal salts showed noticeable ion conduction.[233] In 1979, Armand et al. validated Wright's discovery and suggested that the PEO/Li salt system has the potential to be used as electrolytes for LIBs.[234] Their discovery opened a new era of polymer electrolytes used in metal-ion batteries, mainly in lithium-ion and sodium-ion batteries. However, the σ of PEO-based SSEs at r.t. was quite low, remaining in the range of 10^{-8}–10^{-5} S cm^{-1}, which is far below the performance requirements for practical applications, 10^{-4}–10^{-3} S cm^{-1}.[73] The low σ observed in PEO/Li salt electrolytes can be attributed to the constrained motion of the polymer segments within the crystalline region. Thus, elevated temperatures, typically exceeding 60 °C, are often required to enhance the mobility of PEO polymer segments, thereby improving Li^+ conduction. One approach to enhance the σ of PEO/Li salt electrolytes involves reducing the crystallinity content. The

Table 1. Comparison of the significant advantages and disadvantages of various SSEs.

Type	σ at r.t. [S cm^{-1}]	t_{Li^+}	Advantages	Disadvantages
Polymer	10^{-7}–10^{-4}	0.2–0.9	• High compatibility with Li • Excellent interfacial contact with electrodes • Easy for large-scale production • Excellent flexibility	• Low ionic conductivity • Poor thermal stability
Sulfide	10^{-3}–10^{-2}	≈1	• Excellent ionic conductivity • High mechanical strength • and good flexibility • Good thermal stability	• Poor compatibility with electrodes • Poor chemical and electrochemical stability
Oxide	10^{-4}–10^{-3}	≈ < 1	• High mechanical strength • Excellent thermal stability • High chemical and electrochemical stability	• Poor flexibility • Difficulty in large-scale production • Poor interfacial functionality
MOFs	10^{-5}–10^{-4}	0.6–0.9	• Excellent porosity for ion transport • High mechanical strength • High chemical and electrochemical stability • Excellent versatility and functionality	• Very high manufacturing cost • Poor interfacial contact with electrodes • Moderate ionic conductivity
COFs	10^{-5}–10^{-4}	0.6–0.9	• High porosity for ion transport • Excellent mechanical strength • Excellent chemical and electrochemical stability • Excellent versatility and functionality	• High manufacturing cost • Poor interfacial contact with electrodes • Moderate ionic conductivity
Composite	10^{-4}–10^{-3}	0.5–0.8	• High ionic conductivity • Good flexibility • Good interfacial contact with electrodes	• Complicated preparation method • Complicated ion transport mechanism

incorporation of plasticizers has shown promise in significantly enhancing the σ of PEO/Li salt electrolytes to levels surpassing 10^{-4} S cm^{-1} at r.t., primarily by reducing the content of the crystalline phase.[235] However, it is important to note that most plasticizers utilized are liquid-based materials, including ethylene carbonate-based organic solvents and ionic liquids. Consequently, such electrolyte formulations cannot be classified as SSEs.

Since the pioneering discovery of PEO as SSEs, extensive research has been conducted to explore the suitability of various polymer hosts, such as polycarbonate,[236] polyester,[237] PVDF,[75] and its copolymers.[238] Among the polymer SSEs, PEO mixed with Li salts such as LiTFSI is the typical type of polymer electrolyte.[239] For example, Butzelaar et al. reported a styrene-based PEO side-chain copolymer by mixing them with LiTFSI, which exhibited a σ of 1.6×10^{-5} S cm^{-1} at 25 °C.[240] The fabricated full cell with Li|SSE|NMC622 configuration showed a high initial discharge capacity of approximately 175 mAh g^{-1} and a capacity retention of 57% after 100 cycles at 0.1 C at 60 °C. Zhang et al. prepared LiFSI/PEO polymer SSEs, yielding SSE membranes with specific molar ratios (**Figure 11**a,b).[241] The resulting LiFSI/PEO SSE demonstrated a σ of 3.3×10^{-4} S cm^{-1} at 60 °C, when the EO/Li$^+$ molar ratio was 20 (Figure 11c). In comparison, the LiTFSI/PEO SSE exhibited a higher σ of 4.7×10^{-4} S cm^{-1} at 60 °C under the same EO/Li$^+$ molar ratio. Moreover, the Li|LiFSI/PEO|LFP cell utilizing this LiFSI/PEO SSE exhibited stable cycling performance at 0.2 C and 80 °C, delivering an initial discharge capacity of 146 mAh g^{-1} and maintaining a capacity of 144 mAh g^{-1} after 20 cycle (Figure 11d).

Some strategies can be employed to improve the t_{Li^+} of PEO-based SSEs, leading to enhanced cycling stability when used in ASSLMBs. One such strategy is the addition of fillers. For instance, Li et al. prepared a hexagonal boron nitride (h-BN)-PEO composite polymer electrolyte where h-BN was used as the filler.[242] They showed the presence of BN inhibited anions movement and improved the selectivity of Li$^+$ transport. The

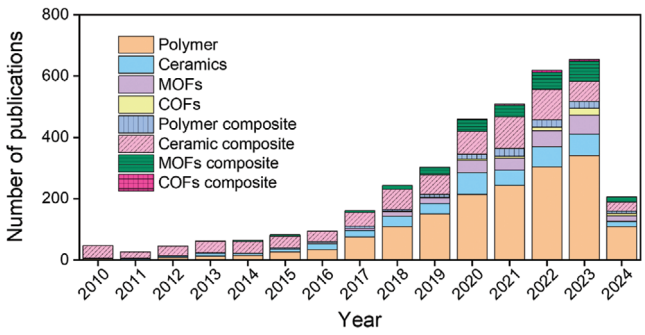

Figure 10. Publication trends on LMBs with different types of SSEs. Search data was updated in May 2024. Source: Web of Science.

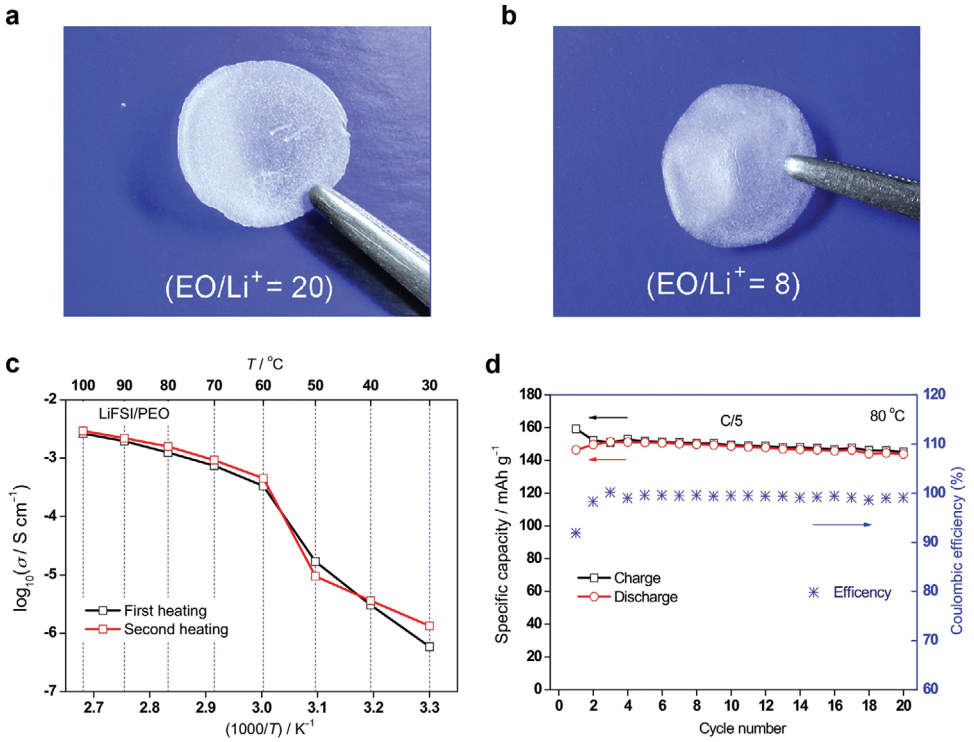

Figure 11. PEO SSE for ASSLMBs. a,b) Digital images of LiFSI/PEO SSE membrane with EO/Li^+ molar ratios of 20 (a) and 8 (b). c) Arrhenius plot of the σ of LiFSI/PEO SSE. d) The cycling performance of a Li|LiFSI/PEO|LFP cell at 0.2 C and 80 °C. Reproduced with permission.[241] Copyright 2014, Elsevier.

composite SSE achieved a maximum t_{Li^+} of 0.56, surpassing the t_{Li^+} value of 0.25 observed in the PEO/LiTFSI SSE. The improvement in t_{Li^+} contributes to enhanced Li^+ transport and helps suppress the formation of Li dendrites. In line with these findings, the Li|SSE|Li symmetric cell, utilizing the h-BN/PEO/LiTFSI composite SSE, demonstrated an extended cycle time of 430 h when operated at a current density of 0.2 mA cm^{-2}. Additionally, the Li|SSE|LFP cell exhibited an initial discharge capacity of 144 mAh g^{-1} and a capacity retention of 93% after 140 cycles at 0.2 C and 60 °C.

PVDF-based SSEs generally exhibit σ below 10^{-4} S cm^{-1} at r.t. The copolymer poly(vinylidene-co-hexafluoropropylene) (PVDF-HFP) can be employed to enhance the σ of PVDF SSEs. In this formulation, the incorporation of hexafluoropropylene segments facilitates partial amorphization, which boosts Li^+ conduction.[243] At the same time, the crystalline regions retained in the structure contribute to maintaining essential mechanical strength. Furthermore, the σ of PVDF-based electrolytes can be significantly enhanced by developing gel-based formulations. For instance, Jie et al. demonstrated the creation of a PVDF-HFP gel polymer by incorporating N-methyl-2-pyrrolidone as a solvent.[244] This approach resulted in an impressive σ of 7.2×10^{-4} S cm^{-1} at 70 °C, alongside an ESW of 5.2 V and a t_{Li^+} of 0.57. However, it is important to note that gel-based electrolytes should be categorized as QSSE.

Poly(ionic liquid)s (PILs), having charges on the backbones, have emerged as highly promising candidates for polymer SSEs and have garnered increasing attention. This is primarily attributed to their distinct properties when compared to neutral polymers. PILs offer several advantageous characteristics, including exceptional chemical stability, wide ESWs that can exceed 5 V (vs Li^+/Li), non-flammability, excellent thermal stability exceeding 300 °C, and diverse structural variations.[245] These unique attributes make PILs attractive for SSEs in advanced energy storage systems. PILs refer to a class of ionic liquid polymers with anionic and cationic groups on repeating units, which are produced by the polymerization of ionic liquid monomers and have both properties of ionic liquids and polymers. σ is a fundamentally important property of PILs as it arises from the presence of ion species that are incorporated into the polymer backbone.[246–248] In the solid-state near r.t., most reported PIL SSEs exhibit a behavior where only the counter ions act as charge carriers, while the movement of the ionic backbone is minimal, contributing high σ and t_{Li^+}. PILs offer the advantage of tunable σ through three key aspects: the glass transition temperature, polymer architecture, and molecular weight. By adjusting these parameters, the σ of PILs can be tailored to meet specific requirements, making them versatile materials for SSEs.[249] It is noteworthy that PILs possess the remarkable ability to facilitate the transport of Li^+ even in the absence of additional Li salt additives. Furthermore, PILs can also serve as effective hosts for Li salt incorporation as SSEs. This unique characteristic positions PILs as highly promising candidates for SSEs in the context of LMBs. The dual capability of PILs to transport Li^+ without Li salt and accommodate Li salt as SSEs highlights their potential for enabling advanced LMB technologies.[250]

Dong et al. presented a study on a cross-linked SSE comprising polytetramethylene ether glycol and 1-vinyl-3-butylimidazole

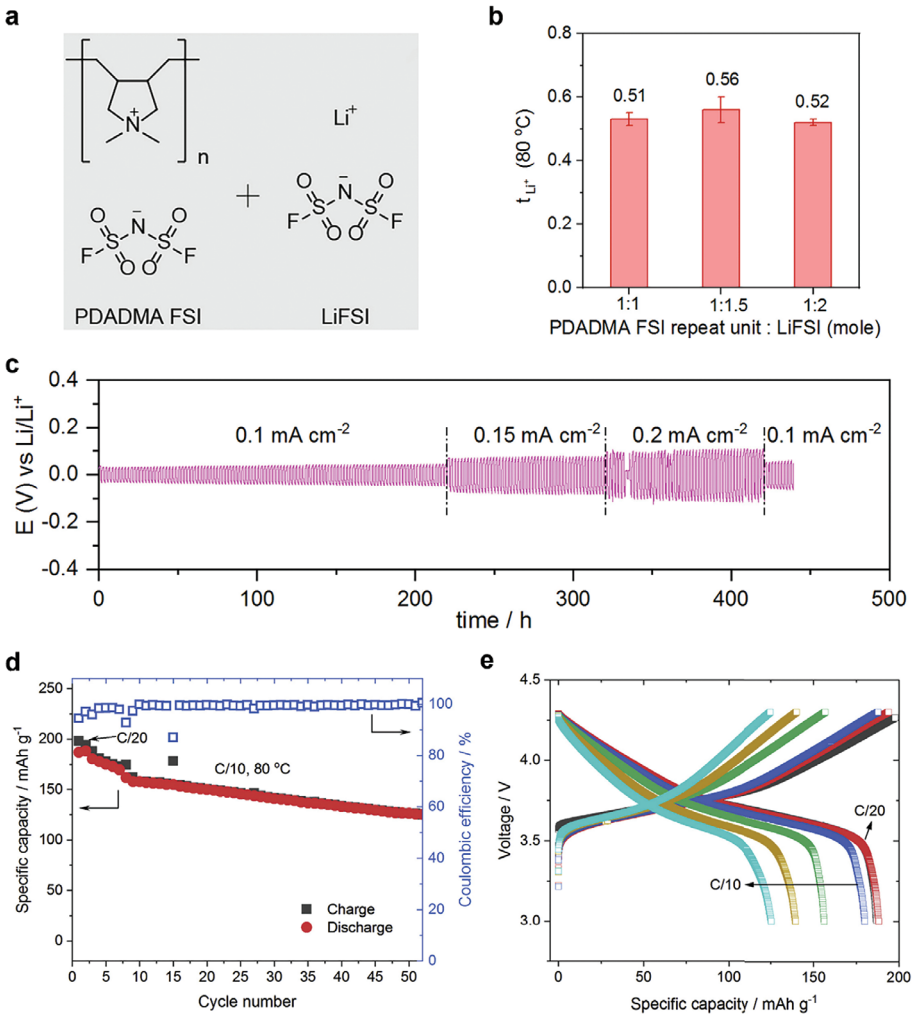

Figure 12. PIL-based SSE demonstrated fast Li+ transport facilitated by forming a co-coordination structure. a) Chemical structures of PIL (PDADMA FSI) and LiFSI salt. b) t_{Li^+} of PDADMA FSI/LiFSI SSEs with varying compositions at 80 °C. c) The cycling performance of Li|PDADMA FSI/LiFSI|Li symmetric cell at different current densities. d) The cycling performance of the Li|PDADMA FSI/LiFSI|NMC cell at 0.1 C and 80 °C, the first two cycles were operated at 0.05 C. e) The charge and discharge profiles of the Li|PDADMA FSI/LiFSI|NMC cell. Reproduced with permission.[113] Copyright 2019, Elsevier.

bis(trifluoromethylsulfonyl)imide ionic liquid. The SSE demonstrated a σ of 3.2×10^{-5} S cm^{-1}, with a t_{Li^+} of 0.47 at r.t.[251] The enhanced σ in this SSE was attributed to the favorable loose coordination between the polymer chain and Li^+, a characteristic that distinguishes it from PEO-based SSEs. The Li|SSE|LFP cell using the PIL SSE showed excellent cycling stability, with an initial discharge capacity of 155 mAh g^{-1} and 99.5% capacity retention after 100 cycles at 0.1 C and r.t. In 2019, Forsyth's group proposed improving Li^+ transport by designing a co-coordination structure in a PIL-in-salt electrolytes system (**Figure 12**).[113] The PIL employed was poly(diallyldimethylammonium) bis(fluorosulfonyl)imide, denoted as PDADMA FSI (Figure 12a). PIL-in-salt SSE enhanced Li^+ transport, achieving a σ of 7.0×10^{-5} S cm^{-1} at 80 °C with a PIL to LiFSI molar ratio of 1:1.5, while maintaining a t_{Li^+} of 0.56 even at high Li salt content (Figure 12b). The Li|PDADMA FSI/LiFSI|Li symmetric cell exhibited stable cycling performance, sustaining a current density of up to 0.2 mA cm^{-2} (Figure 12c). When $Li_{1/3}Ni_{1/3}Mn_{1/3}CoO_2$ (NMC) is utilized as the cathode material, the Li|PDADMA FSI/LiFSI|NMC cell demonstrated excellent cycling performance at 80 °C, delivering an initial discharge capacity of 188 mAh g^{-1} and a capacity retention of 67.6% after 50 cycles (the cell was operated at 0.05 C for the first 2 cycles, then at 0.1 C) (Figure 12d,e). This strategy can be extended to SSEs that facilitate the conduction of other ions such as K^+, Na^+, and OH^-.[252,253] However, the limitation of low σ at r.t. hampers the full realization of their potential in ASSLMBs. Addressing this challenge is crucial to further exploit the advantages of PIL-in-salt SSEs in practical LMB applications.

3.2. Recent Trends

In the realm of SSEs, inorganic ceramic SSEs exhibit the highest σ, and t_{Li^+} approaching near unity. These characteristics make them highly desirable for advanced energy storage

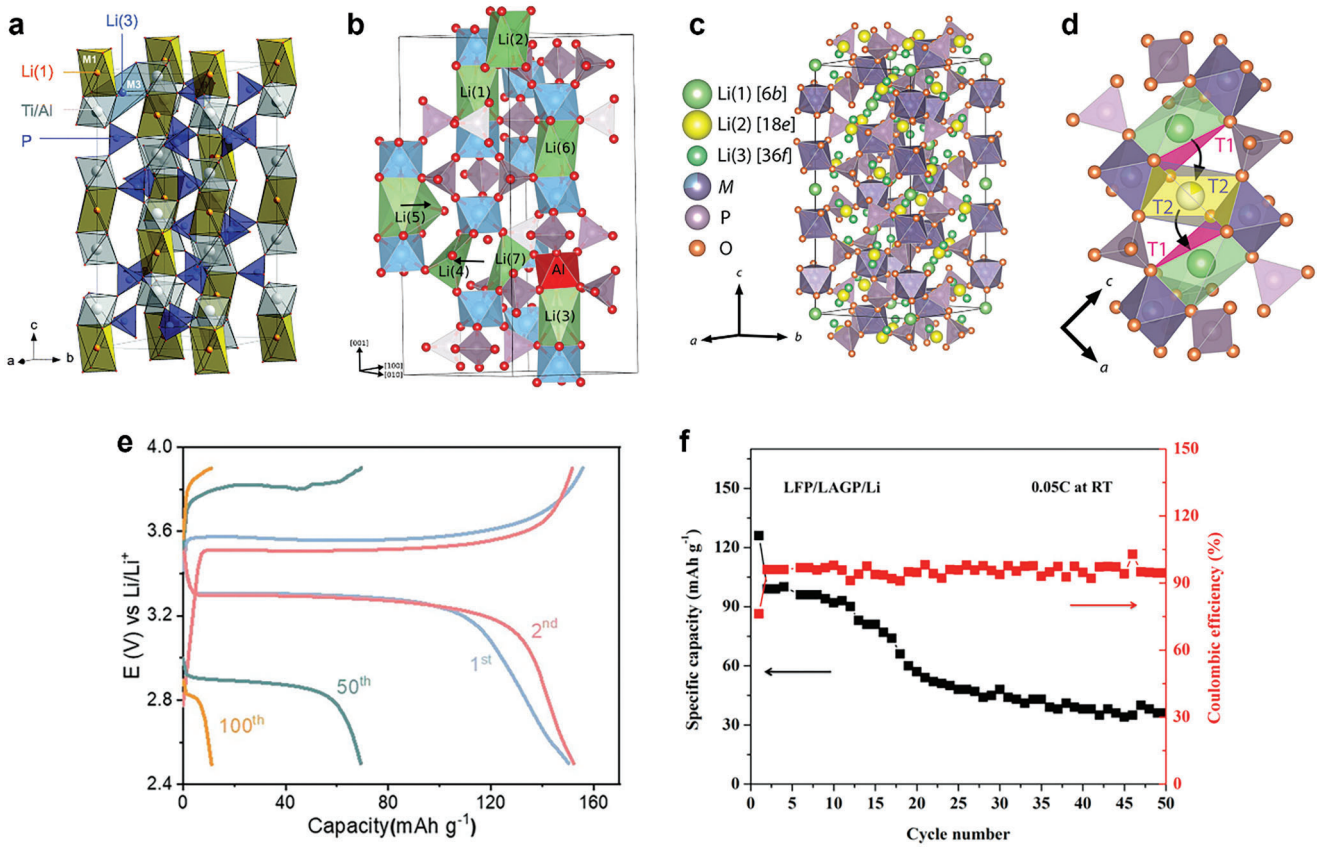

Figure 13. Representative oxides SSEs (LATP and LAGP) for ASSLMBs. a) The crystal structure of LATP. Reproduced with permission.[262] Copyright 2015, Royal Society of Chemistry. b) The Li migration pathway in LATP. Reproduced with permission.[263] Copyright 2015, American Chemical Society. c) The crystal structure of LAGP. d) The Li^+ hopping pathway in LAGP. Reproduced with permission.[264] Copyright 2018, American Chemical Society. e) The voltage profiles of Li|LATP|LFP cell at 1.5 C and various cycles. Reproduced with permission.[265] Copyright 2020, Wiley-VCH Verlag GmbH & Co. KgaA. f)The cycling performance of Li|LAGP|LFP cell at 0.05 C and r.t. Reproduced with permission.[266] Copyright 2018, American Chemical Society.

applications. However, as discussed earlier, one critical challenge associated with inorganic ceramic SSEs is the issue of interfacial contact. The interface between the ceramic electrolyte and electrode materials can be unstable, causing overall performance degradation.[63,254,255] To address this challenge, current research trends focus on developing inorganic ceramic SSE composites with polymer materials.[256] By incorporating polymers into ceramic electrolytes, the interfacial resistances can be reduced. This section provides a detailed analysis of inorganic ceramic SSEs and their composites, exploring their properties, design strategies, and performance as SSEs for ASSLMBs.

3.2.1. Inorganic Ceramic

The field of inorganic SSEs for LIBs has a long and rich history, and a significant milestone was achieved in 1992 with the fabrication of a thin-film type lithium phosphorus oxynitride (LiPON) material as an SSE.[257,258] Since then, inorganic SSEs have garnered widespread attention and have been extensively studied for their potential applications in LIBs. Based on the crystal structures, the exploration of inorganic SSEs for solid-state batteries primarily focuses on several types of materials: perovskite-type, NASICON-type, Li superionic conductor (LISICON)-type, garnet-type, and sulfide-type. These conductors can be broadly classified into two categories: oxides and sulfides. The section will delve into a detailed discussion of oxides and sulfides, exploring their characteristics, properties, and applications as solid Li^+ conductors. Furthermore, halides have garnered significant attention over the past five years; this review will also explore halide-based SSEs.

The perovskite-type LLTO was first reported in 1993 as oxide-based SSE, demonstrating a remarkable σ of 2.0×10^{-5} S cm^{-1} at r.t.[259] In 1997, the first NASICON-type oxide-based SSEs, LATP and LAGP were reported by Jie Fu, showing σ of 1.3×10^{-3} S cm^{-1} and 4.0×10^{-4} S cm^{-1} at r.t., respectively.[260,261] **Figure 13**a,b illustrates the crystal structure and Li migration pathway of LATP, respectively.[262,263] Similarly, the crystal structure and Li^+ hopping pathway of LAGP are depicted in Figure 13c,d, respectively.[264] The Li|LATP|LFP and Li|LAGP|LFP cells exhibited satisfactory initial discharge capacities (Figure 13e,f).[265,266] However, their cycling performance was compromised due to the elevated internal resistance resulting from the reduction reaction between the Li metal anode and the pristine LATP or LAGP SSEs. The Li|LATP|LFP cell displayed an initial specific capacity of 150 mAh g^{-1} and a low capacity of retention of 7.4% after 100 cycles

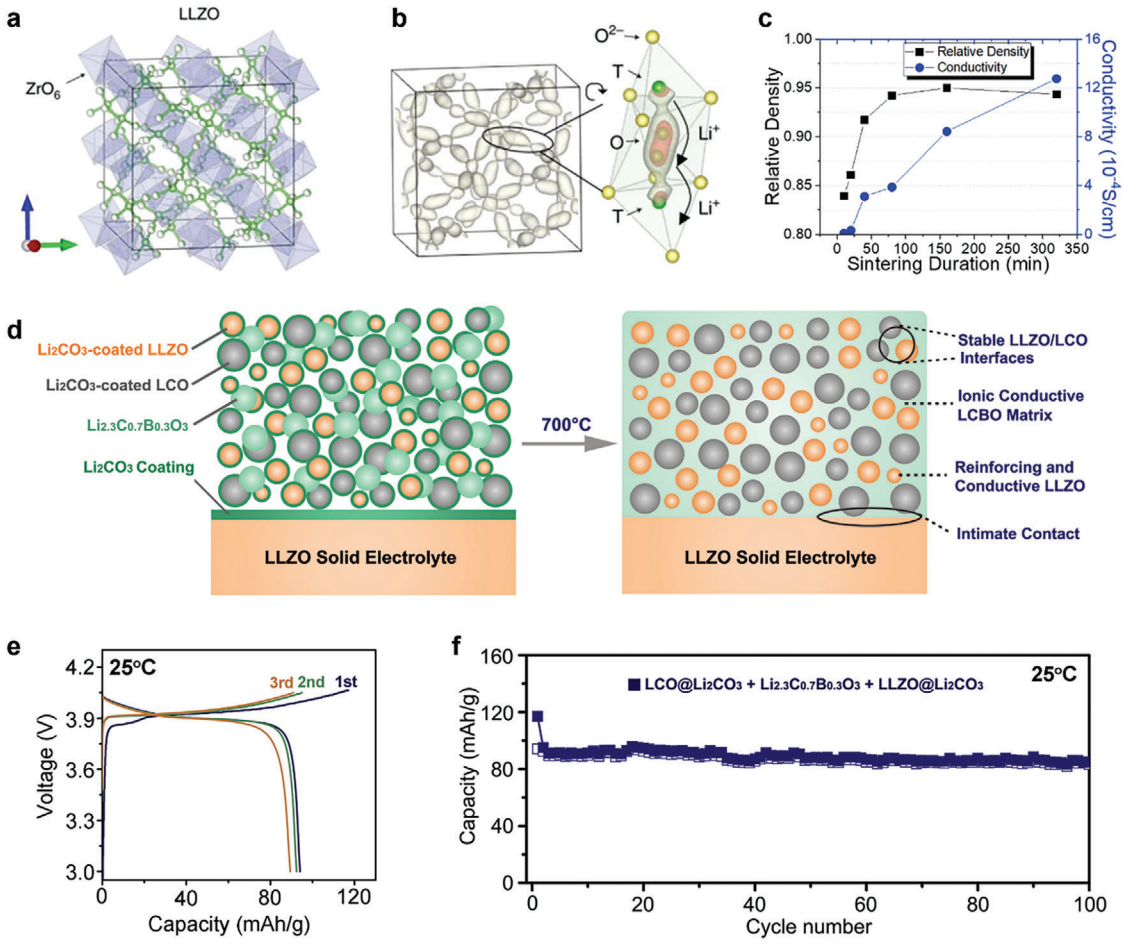

Figure 14. Representative oxides SSEs (LLZO) for ASSLMBs. a) The crystal structure of LLZO. b) The Li^+ migration pathway in LLZO. Reproduced with permission.[267] Copyright 2017, Springer Nature. c) σ at 25 °C and relative densities of the Ga-doped LLZO SSEs as a function of sintering time at 1100 °C. Reproduced with permission.[268] Copyright 2020, Elsevier. d) The schematic diagrams of the interphase-engineered all-ceramic LCO/LLZO cathode/electrolyte system. e) The voltage profiles of the interphase-engineered all-ceramic Li|LLZO|LCO cell at 0.05 C and 25 °C. f) The cycling performance of the interphase-engineered all-ceramic Li|LLZO|LCO cell at 0.05 C and 25 °C. Reproduced with permission.[270] Copyright 2018, Elsevier.

at 1.5 C and r.t. Similarly, the Li|LAGP|LFP cell demonstrated an initial capacity of 96 mAh g^{-1} and a low capacity of retention of 37.5% after 50 cycles at 0.05 C and r.t.

In 2007, a significant development was made by Murugan et al., where the authors developed a garnet-type oxide SSE known as LLZO, and this SSE exhibited exceptional chemical and thermal stability and demonstrated a high σ of 3.0×10^{-4} S cm^{-1} at 25°C.[82] This breakthrough opened up new possibilities for utilizing LLZO as a promising SSE material in solid-state batteries, offering enhanced safety and performance characteristics. In recent years, oxide SSEs have gained more and more interest owing to high σ, 10^{-4}–10^{-3} S cm^{-1}, wide ESWs, excellent chemical stability, and high mechanical properties.[10] Some garnet-type LLZO SSEs have achieved even higher σ, over 10^{-3} S cm^{-1} at r.t.[71] The crystal structure and Li^+ migration pathway through LLZO can be found in **Figure** 14a,b, respectively.[267] In a study by Huang et al., a Ga-doped LLZO SSE was synthesized by sintering the powder at 1,100 °C for 320 minutes (Figure 14c).[268] The resulting sintered material exhibited relative densities exceeding 94% and conductivities higher than 1.2×10^{-3} S cm^{-1} at 25 °C. However, to attain dense ceramics exhibiting high σ within the range of 10^{-4}–10^{-3} S cm^{-1} at r.t., sintering at over 1000 °C is typically required. Furthermore, oxide SSEs often lack flexibility due to their inherent rigidity, which presents challenges in accommodating volume changes of electrode materials during cycling.[269] Consequently, this can lead to compromised contact between oxide SSEs and electrodes. Wang's group introduced an innovative approach to address the interfacial resistance between LLZO and LCO through interphase engineering.[270] Specifically, they employed thermal soldering to join LCO and LLZO using the $Li_{2.3-x}C_{0.7+x}B_{0.3-x}O_3$ SEI, which forms through the reaction between $Li_{2.3}C_{0.7}B_{0.3}O_3$ solder and Li_2CO_3 coatings on both LLZO and LCO (Figure 14d). The resulting superior interface between LCO and LLZO enabled an all-ceramic Li|LLZO|LCO cell to exhibit stable cycling performance at 0.05 C and 25 °C, with the capacity stabilizing at approximately 83 mAh g^{-1} over 100 cycles (Figure 14e,f). However, considering the need for high-temperature processing and the rigid nature of LLZO-based materials, large-scale production becomes cost-prohibitive.

Inorganic oxide-based SSEs have been studied widely, such as superionic conductor NASICON type, e.g., LAGP, Perovskite type, e.g., LLTO, and garnet type, e.g., LLZO. As mentioned, they show a range of σ from 10^{-4} to 10^{-3} S cm^{-1} at r.t. and possess excellent mechanical strength. However, their applications are limited due to challenges such as poor flexibility, inadequate interfacial functionality, and high production costs, particularly for large-scale manufacturing.[269,271] Most of the full cells using ceramics have carefully addressed those issues. For example, Zheng et al. employed an in situ grain boundary modification approach by leveraging the reaction between Li_2TiO_3 (LTO) and a tantalum (Ta)-substituted garnet-type electrolyte (referred to as LLZT).[272] This method resulted in an SSE with a σ of $\approx 5.0 \times 10^{-4}$ S cm^{-1} at r.t. The Li|SSE|Li symmetric cell, utilizing the LLZT/LTO composite SSE, demonstrated a remarkably high critical current density of up to 1.8 mA cm^{-2}. Furthermore, the symmetric cell exhibited excellent cycling stability, maintaining stable performance for over 2000 h at a current density of 0.3 mA cm^{-2}. Furthermore, upon integration of the LLZT/LTO composite SSE into a full cell configuration, with NCM622@UiO66 serving as the cathode, the full cell demonstrated an impressive capacity retention of 86.3% after undergoing 200 cycles at a rate of 0.2 C. This corresponded to a maintained capacity of 149.3 mAh g^{-1}. Additionally, incorporating dopants is another method that can be employed to enhance electrolyte performance and address interface issues. Kim et al. presented a novel methodology wherein they customized garnet-type LLZO SSE by manipulating bulk dopant concentrations and applying dopant-specific interfacial modification methods utilizing protonation/etching techniques.[273] The Ta-doped LLZO (Ta-LLZO) SSE demonstrated a σ of 5.1×10^{-4} S cm^{-1} at 25 °C. Furthermore, the Ta-LLZO SSE exhibited a stable EIS spectrum for 72 h, enabling the Li|SSE|Li symmetric cell to sustain continuous operation for more than 160 h at a current density of 0.2 mA cm^{-2} and 60°C. Additionally, when the protonated Ta-LLZO SSE was employed in the Li|SSE|NCM111 full-cell configuration, it displayed an initial areal capacity of 3.2 mAh cm^{-2} and a capacity retention of 95% after 1000 cycles at a rate of 0.5 C and 60 °C.

Sulfide SSEs have garnered significant attention due to their high σ, up to 10^{-2} S cm^{-1} at r.t., surpassing that of certain commercial liquid electrolytes, which attracted many researchers into the field. Also, sulfide SSEs exhibit favorable mechanical strength and flexibility. Notably, these materials can be processed at lower temperatures than oxide SSEs, offering potential advantages in terms of manufacturing and scalability.[274] However, these sulfide SSEs have limitations, including relatively narrow ESWs, poor chemical compatibility with electrodes, and the propensity to form Li dendrites within the electrolyte.[275,276] Thio-LISICON, which is derived from a LISICON-type γ-Li_3PO_4 SSE through the substitution of oxygen with sulfur, has shown promising performance in addressing most of the limitations.[277] Thio-LISICON SSEs generally exhibit higher σ compared to their oxide counterparts. This is attributed to the lower electronegativity of S compared to O, which decreases the binding energy between Li^+ and the electrolyte, consequently facilitating enhanced ion migration channels and promoting the movement of Li^+ within the electrolyte.[278] In 2011, Kanno's group made a groundbreaking achievement by introducing a LISICON known as LGPS (**Figure 15a–c**).[92] This material possesses a 3D crystal structure with the general configuration $Li_{11-x}M_{2-x}P_{1+x}S_{12}$, where M represents a metal cation, such as Ge, Si, or Sn, and demonstrates an exceptional σ of 1.2×10^{-2} S cm^{-1} at r.t. (Figure 15e). Notably, this σ level is the highest among all SSEs at that time. Kuhn et al. employed a range of techniques, including impedance spectroscopy, electron diffraction, XRD,[7]Li nuclear magnetic resonance (NMR),[31]P magic angle spinning (MAS) NMR, and others, to investigate the Li^+ kinetics of LGPS.[279] In their study, they discovered that the primary reason for the high σ observed in LGPS is the isotropic movement of Li^+ within the bulk lattice. This finding suggests that the rapid jumping of Li^+ contributes significantly to the overall σ of the LGPS electrolyte. This successful fabrication of the LGPS SSE represented a significant milestone in developing sulfide SSEs, contributing to the advancement of high-performance Li-based batteries. However, the Li|LGPS|LFP cell displayed a quite low initial capacity of 22 mAh g^{-1} and substantial polarization at 0.1 C (Figure 15g).[280] Furthermore, the Li|LGPS|LFP cell exhibited poor cycling stability, with the capacity dropping to zero after 60 cycles (Figure 15h). In comparison, the Li|PCE-LGPS-PCE|LFP cell with a plastic crystal electrolyte (donated as PCE, was made of 5 mol% LiTFSI in succinonitrile) interlayer between Li metal and LGPS demonstrated much better electrochemical performance due to the interlayer effectively mitigated the interfacial reactions between LGPS and Li metal. It demonstrated a notable higher initial capacity of 131 mAh g^{-1} at 0.5 C, and a capacity retention of 91.6% after 120 cycles. These unfavorable electrochemical performances in LGPS-based ASSLMBs are primarily attributed to severe interfacial resistances and side reactions between LGPS and Li metal anode, as well as suboptimal solid-solid contact between LGPS and LFP cathode.[281] These findings showed that interface engineering is critical in enabling the widespread application of LGPS-based ASSLMBs. In 2013, Seino's group achieved another notable advancement in sulfide SSEs by developing a Li_2S–P_2S_5 glass-ceramic Li^+ conductor with a high σ of 1.7×10^{-2} S cm^{-1} at r.t. as well as a low conduction activation energy of 17 kJ mol^{-1}.[282] This substantial increase in conductivity can be attributed to two key factors: the reduction in grain boundary resistance and the diminished impact of voids, both arising from the heat treatment process. Building upon their previous work on LGPS SSE, Kanno's group developed an outstanding LISICON with a composition of $Li_{9.54}Si_{1.74}P_{1.44}S_{11.7}Cl_{0.3}$ in 2016 (Figure 15d).[93] This new sulfide SSE exhibited an extraordinarily high σ of 2.5×10^{-2} S cm^{-1} at r.t. due to the 3D Li^+ pathways (Figure 15f), which is double of the LGPS's conductivity and set a record at that time. Notably, this SSE does not contain the expensive element Ge, making it even more promising for developing high-performance and cost-effective SSEs in next-generation advanced ASSLMBs.

Nazar's group has developed a scalable and solution-engineered strategy for sulfide materials, which includes synthesizing a novel argyrodite solid solution phase called $Li_{6-\gamma}PS_{5-\gamma}Cl_{1+\gamma}$ (γ = 0–0.5). The resulting SSE obtained through this method exhibited an exceptionally high σ of 3.9×10^{-3} S cm^{-1} at r.t. while displaying negligible electronic conductivities. Moreover, this group fabricated a $Li_{11}Sn_6|Li_6PS_5Cl|TiS_2$ cell using this electrolyte, which demonstrated a theoretical capacity of 239 mAh g^{-1} at a rate of 0.11 C. Notably, this cell exhibited no discernible difference in performance compared to the one utilizing

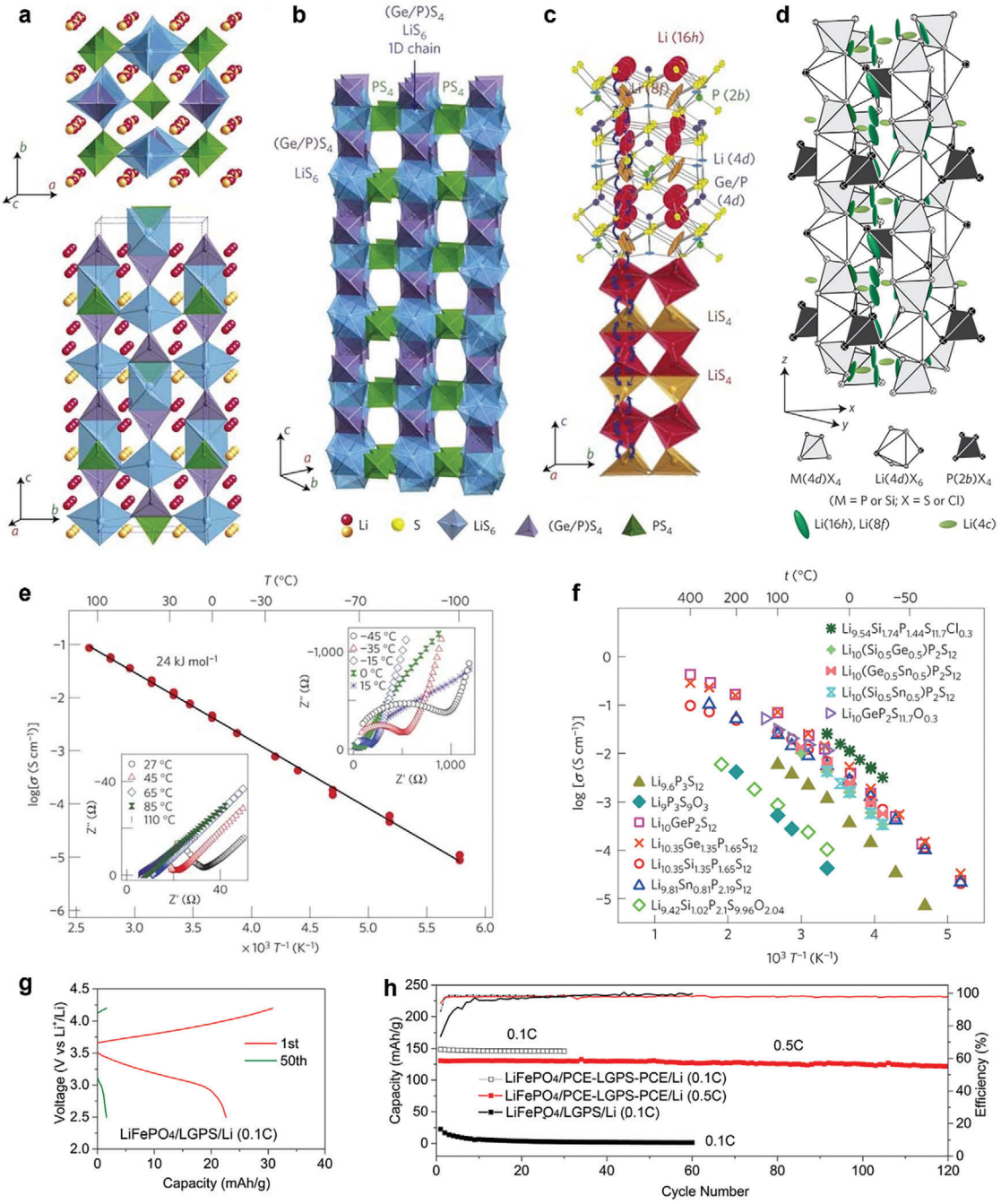

Figure 15. Representative sulfide SSEs (LGPS) for ASSLMBs. a) The ionic conduction in LGPS involves the participation of Li^+ within its framework structure. b) The crystal structure of LGPS. c) Li^+ migration pathway in LGPS. Reproduced with permission.[92] Copyright 2011, Springer Nature. d) The crystal structure of $Li_{9.54}Si_{1.74}P_{1.44}S_{11.7}Cl_{0.3}$. Reproduced with permission.[93] Copyright 2016, Springer Nature. e) σ of LGPS SSE as a function of temperature. Reproduced with permission.[92] Copyright 2011, Springer Nature. f) Arrhenius plot of the σ of $Li_{9.54}Si_{1.74}P_{1.44}S_{11.7}Cl_{0.3}$ SSE, LGPS family, and $Li_{9.6}P_3S_{12}$ SSEs were also compared. Reproduced with permission.[93] Copyright 2016, Springer Nature. g) The voltage profiles of the Li|LGPS|LFP cell at 0.1 C and r.t. h) The cycling performance of the Li|LGPS|LFP and Li|PCE-LGPS-PCE|LFP cells at r.t. Reproduced with permission.[280] Copyright 2019, Wiley-VCH.

a solid-state-derived electrolyte. This observation suggests that any minor impurities formed during the solution-engineered process have minimal impact on the overall cell performance.[283] To address the issues of poor compatibility between sulfide-based SSEs and Li metal, as well as the sensitivity to air, Sun's group introduced a novel approach by substituting Sn (IV) for P (V) in the argyrodite sulfide Li_6PS_5I (LPSI), resulting in the development of LPSI-*x*Sn SSEs where "*x*" represents the Sn substitution percentage. Among these SSEs, LPSI-20Sn, with a Sn substitution percentage of 20%, exhibited a σ of 3.5×10^{-4} S cm^{-1} at 25 °C.

Notably, this value is 125 times higher than that of the original LPSI SSE, demonstrating the significant improvement achieved through Sn substitution.[284] The high σ exhibited by LPSI-20Sn allowed the I-containing electrolyte to function as a stable interlayer, effectively mitigating the reactivity between the electrolyte and Li metal in sulfide-based symmetric cells and ASSLMBs. This enhanced interlayer stability contributed to the batteries' exceptional cycling stability and rate capability. Consequently, in the Li|LPSI-20Sn|Li symmetric cell, stable Li plating and stripping behavior were observed for an extended period. Specifically, the cell exhibited stable performance for over 700 h (equivalent to 350 cycles) at a current density of 0.1 mA cm^{-2} (the cut-off capacity was 0.1 mAh cm^{-2}) and r.t. Additionally, even under the demanding conditions of a high current density of 1.26 mA cm^{-2} and a cut-off capacity of 1 mAh cm^{-2}, the cell maintained stable Li plating and stripping profile for ≈200 h (corresponding to 125 cycles). To showcase the practical application of the LPSI-20Sn SSE in ASSLMBs, Sun's group incorporated the LPSI-20Sn SSE as the interlayer between the Li metal and LGPS electrolyte. They utilized a LiNbO*x*-coated LCO (LCO@LNO) cathode in their setup. As a result, the Li|LGPS/LPSI-20Sn|LCO@LNO cell exhibited an initial specific capacity of ≈113 mAh cm^{-1} at a rate of 0.1 C (where 1 C corresponds to 140 mA g_{LCO}^{-1}) and r.t. After 50 cycles, the cell achieved a capacity retention of 88.5%. Furthermore, the Li|LGPS/LPSI-20Sn|LCO@LNO cell demonstrated excellent rate performance, reaching a capacity of 93.8 mAh cm^{-1} at a rate of 1 C and r.t. These results highlight the favorable electrochemical characteristics and potential of the LPSI-20Sn SSE for ASSLMBs, showcasing its ability to support high-capacity and stable cycling performance even under demanding operating conditions. In addition, various doping materials are employed to enhance the σ of sulfide-based SSEs and improve their interfacial stability with the electrodes. In 2022, Zhang et al. conducted a study where they introduced rare earth oxide La_2O_3 as a doping component for LPS sulfide SSEs, demonstrating improved performance for the first time.[285] They generated a range of sulfide-based SSEs with a formula of (100-*x*)(LPS)-*x*La_2O_3, where x represents different doping levels, including 0, 1, 2, and 3. Among the synthesized (100-*x*)(LPS)-*x*La_2O_3 SSEs, the 98(LPS)-2La_2O_3 SSE exhibited the highest σ of 2.4×10^{-4} S cm^{-1} at r.t. Furthermore, it displayed a wide ESW of up to 5.0 V (vs Li^+/Li). The interfacial compatibility between the 98(LPS)-2La_2O_3 SSE and Li metal anode was found to be significantly superior compared to that between LPS SSE and Li anode. As a result, Li|98(LPS)-2La_2O_3|Li symmetric cell exhibited stable cycling for 250 h at a current density of 0.1 mA cm^{-2}, with a polarization voltage of 100 mV after the cycling test. In contrast, Li|LPS|Li cells demonstrated a high polarization voltage of 1.25 V, while both cells started with an initial polarization voltage of 50 mV. Furthermore, a double-layer sulfide SSE configuration consisting of LGPS and 98(LPS)-2La_2O_3 was employed to investigate the applicability of the sulfide-based SSE in ASSLMBs with a cathode of LCO. The Li|LGPS/98(LPS)-2La_2O_3|LCO cell exhibited an initial specific capacity of 118.5 mAh g^{-1} and maintained 75.8% capacity retention after 100 cycles at 0.1 C. Similarly, Fan's group prepared a range of novel $Li_{3+2x}P_{1-x}Bi_xS_{4-1.5x}O_{1.5x}$ ($x = 0.02, 0.04, 0.06, 0.08$) SSEs through the process of co-doping LPS with Bi and O.[286] The co-doped $Li_{3.12}P_{0.94}Bi_{0.06}S_{3.91}O_{0.09}$ SSE demonstrated a σ nine times higher than LPS, reaching 2.8×10^{-3} S cm^{-1} at r.t., indicating improved conductivity, as well as enhanced air-stability. It is noteworthy that the Li|$Li_{3.12}P_{0.94}Bi_{0.06}S_{3.91}O_{0.09}$|Li symmetric cell exhibited remarkable stability, remaining stable for a duration of 400 h even when subjected to a high current density of 1 mA cm^{-2} and 25 °C. Furthermore, the Li|$Li_{3.12}P_{0.94}Bi_{0.06}S_{3.91}O_{0.09}$|$LiNbO_3$ coated NCM523 cell exhibited 83.2% discharge capacity retention after 50 cycles at 0.1 C and 25 °C, corresponding to a capacity of 106.1 mAh g^{-1}. These findings indicate the potential of the co-doped sulfide-based SSEs in enabling stable and high-performance ASSLMBs.

In 2023, Kanno's group published a significant advancement in LISICON-type SSE.[94] They modified the existing LGPS framework to alter its compositional complexity by employing a high-entropy material design. This modified SSE, denoted as LSiGePSBrO (**Figure 16a**), exhibited increased compositional complexity to eliminate ion migration barriers while maintaining the structural framework necessary for efficient ion conduction. Notably, the bulk σ of this SSE reached an impressive value of 3.2×10^{-2} S cm^{-1} (Figure 16b), which stands as the highest reported σ among SSEs to date. Moreover, the Li|$Li_{10.25}P_3S_{12.25}I_{0.75}$|LSiGePSBrO/$LiNbO_3$-coated LCO ASSLMB cell ultilizing LSiGePSBrO as the catholyte, demonstrated outstanding rate performance at 60 °C. It achieved discharge areal capacities of 14 mAh cm^{-2} and 11 mAh cm^{-2} at 0.025 C and 1 C, respectively (Figure 16c). This breakthrough holds great promise for the development of advanced SSEs, also emphasizes the importance of achieving high σ for the electrochemical performance of ASSLMBs employing a thick cathode configuration. Nevertheless, sulfide SSEs do have certain drawbacks. First, sulfides are highly sensitive to moisture and can react with moisture in the air, leading to the generation of H_2S gas, which can degrade and compromise the electrolyte.[287] Additionally, most sulfide SSEs are susceptible to reduction at low potentials when in contact with Li metal and oxidation at moderate potentials.[288] Furthermore, sulfide SSEs often exhibit poor compatibility with cathode materials.[289]

Before 2018, halide SSEs received limited attention primarily due to their low σ ($<10^{-3}$ S cm^{-1}) at r.t., compared to oxides and sulfides.[290] A significant breakthrough occurred in 2018 when Asano et al. successfully synthesized Li_3YCl_6 and Li_3YBr_6, achieving high σ exceeding 10^{-3} S cm^{-1} at r.t. by employing high-energy ball milling followed by high-temperature annealing.[291] This milestone spurred rapid progress in developing halide SSEs for LMBs. In particular, ternary halide SSEs with the general formula Li_3MX_6, where M denotes metal elements such as Y, Er, In, or Sc, and X signifies halide elements such as Cl, Br, or I, have attracted significant attention for their ability to achieve σ in the range of 10^{-3} S cm^{-1} at r.t.[292] In 2020, Sun's group reported the development of highly conductive monoclinic halide SSEs with the formula Li_3ScCl_6, achieved by optimizing the occupancy of Li and Sc sites.[293] This Li_3ScCl_6 SSE, prepared using a cold-pressing method, demonstrated a remarkable σ of 3.0×10^{-3} S cm^{-1} at r.t. Furthermore, the Li_3ScCl_6 SSE exhibited a wide electrochemical window ranging from 0.9 to 4.3 V (vs Li^+/Li) and good compatibility with both bare Li metals and LCO cathodes. In 2021, Liu et al. reported halide SSEs consisting of $Li_3Y(Br_3Cl_3)$, which exhibited a record σ of 7.2×10^{-3} S cm^{-1} at r.t.[294] This remarkable conductivity was attained through hot pressing at 170 °C under a pressure of 294 MPa. In a notable study published in 2023,

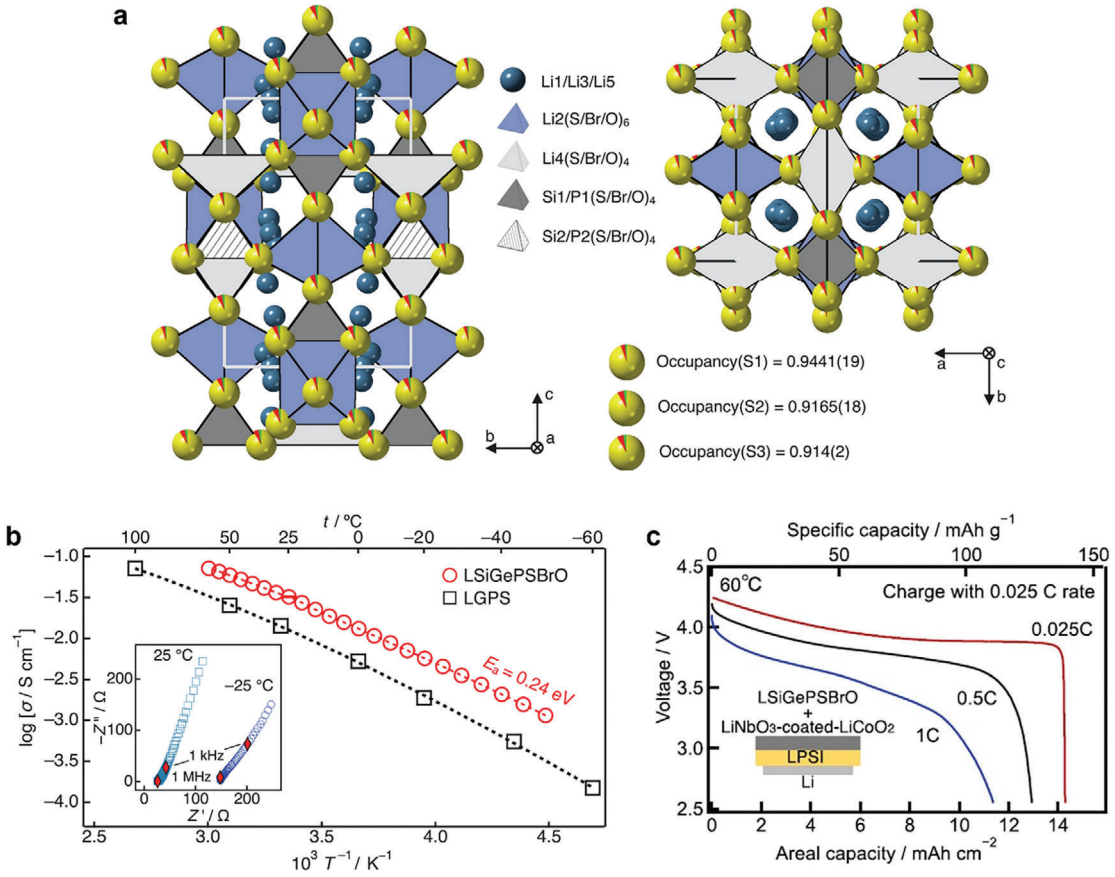

Figure 16. Representative sulfide SSE (LSiGePSBrO) and its application for ASSLMBs. a) The crystal structure of LSiPSBrO, and the occupancy of the S, Br, and O atoms at the S sites are visually represented in the illustration using yellow, green, and red colors, respectively. b) Arrhenius plot of the σ of LSiGePSBrO SSE, LGPS was also evaluated for comparison. c) Rate performance of the Li|$Li_{10.25}P_3S_{12.25}I_{0.75}$|LSiGePSBrO/$LiNbO_3$-coated LCO ASSLMB cell at 60 °C. Reproduced with permission.[94] Copyright 2023, American Association for the Advancement of Science.

Yin et al. presented a lanthanide metal chloride SSE with the optimized composition of $Li_{0.388}Ta_{0.238}La_{0.475}Cl_3$.[295] This electrolyte demonstrated a high σ of 3.0×10^{-3} S cm^{-1} at 30 °C showed strong compatibility at the interface with Li metals. The ASSLMB full cell equipped with an NMC523 cathode exhibited an initial discharge capacity of 163.96 mAh g^{-1} at 30 °C and demonstrated a capacity retention of 81.6% after 100 cycles. Although halide SSEs have made significant progress in achieving σ exceeding 10^{-3} S cm^{-1} at r.t, most halide SSEs still face challenges in attaining ESWs above 4.5 V (vs Li^+/Li) while maintaining this level of σ. Recently, Ye et al. reported a Li_3InCl_6-based SSE enhanced by Ta^{5+} doping.[296] The optimized $Li_{2.6}In_{0.8}Ta_{0.2}Cl_6$ SSE exhibited an exceptional σ of up to 4.5×10^{-3} S cm^{-1} at 30 °C and a wide ESW of 5.1 V (vs Li^+/Li). Currently, halide SSEs have gained increased attention due to several advantages, including high σ, stability with Li metals, and favorable mechanical properties.[297] In comparison to oxide SSEs, halide SSEs can achieve high σ exceeding 10^{-3} S cm^{-1} at r.t. without requiring high-temperature sintering processes. Additionally, halide SSEs provide greater mechanical flexibility than oxide SSEs, facilitating a more straightforward preparation process. Specifically, halide pellets can be produced using cold pressing methods.[72] While halide SSEs exhibit high sensitivity to moisture, they present a more environmentally friendly option than sulfide SSEs, as they do not release toxic gases upon moisture exposure.[298] Furthermore, halide SSEs generally possess wider ESWs compared to sulfide SSEs.[299] Therefore, it is worth noting that halide SSEs are also considered promising materials and have been the subject of significant research. Interested readers can refer to the cited papers for more information and an in-depth analysis on halide SSEs and their potential applications in solid-state batteries.[290,300,301]

3.2.2. Ceramic Composites

Despite their high σ and nearly unit t_{Li^+}, inorganic ceramic SSEs, such as oxides and sulfides, face practical limitations due to their intrinsic brittleness and the challenges associated with achieving effective electrode/electrolyte contact. These factors continue to impede their widespread application in practical settings.[302,303] By contrast, polymer SSEs, e.g., PEO, PAN, PVDF, and poly (methyl methacrylate) (PMMA), usually demonstrate excellent flexibility, good interfacial contact towards electrodes, and easy to produce a large-area membrane.[304,305] However, insufficient σ at r.t. and limited thermal stability make the solo use of polymer SSEs difficult to satisfy the stringent demands of ASSLMBs.[207]

One notable type of composite electrolytes, which has been extensively studied, involves the integration of inorganic ceramic fillers into a flexible solid polymer host. This approach has shown great promise in meeting the various requirements for implementing ASSLMBs.[306,307] The inorganic fillers used in composite electrolytes can be classified into two categories based on their functional mechanisms: conductive and nonconductive.[308] Nonconductive ceramics (e.g., SiO_2, ZrO_2, $BaTiO_3$, Al_2O_3, and TiO_2) primarily enhance the σ of composite SSEs by reducing the crystallinity of the polymer matrices.[309] It is widely acknowledged that ion transport within polymer matrices predominantly occurs in the amorphous regions. These regions, characterized by a lack of long-range order, facilitate the necessary mobility for ions to traverse the material.[310] In recent years, there has been significant research interest in utilizing garnet-structured, sulfide-structured, NASICON, and perovskite ceramics as fillers in solid composite SSEs. These ceramic materials have drawn attention due to their excellent thermal and chemical stability and wide electrochemical windows. These desirable properties make them promising candidates for enhancing the performance and stability of composite SSEs in battery applications.[311,312] Remarkably, conductive ceramics fillers with inherent Li^+ conductivity offer a dual advantage in composite SSEs. First, they can effectively reduce the crystallinity of the polymer matrices. Secondly, these conductive ceramics serve as a conductive framework within the polymer matrix, facilitating the transport of ions. Additionally, they enable rapid ion transport on their surfaces, further enhancing the overall conductivity of the composite electrolyte system.[313]

PEO is often used as a substrate in ceramic composites to allow the addition of fillers to improve ion transport. Song et al. reported the pioneering use of garnet nanosheets to create interconnected pathways for Li^+ transport within a PEO matrix.[314] The composite SSE, prepared by incorporating 15 wt% garnet-type $Li_{6.5}La_3Zr_{1.5}Nb_{0.5}O_{12}$ nanosheets into a PEO matrix, demonstrated a practically useful σ of 3.6×10^{-4} S cm^{-1} at r.t. This high σ enabled the Li|SSE|Li symmetric cells fabricated with this electrolyte to exhibit stable cycling for 200 h at a current density of 0.1 mA cm^{-2}. The Li|SSE|LFP cell, utilizing this composite SSE, displayed an initial specific capacity of 98.1 mAh g^{-1} and maintained a capacity retention of 97.5% after 30 cycles when operated at 0.05 C and 40°C. LLTO is an SSE of ABO_3-type perovskite with a cubic phase structure. In theory, LLTO has high σ, but due to the barrier effect of grain boundaries, the σ of LLTO is significantly lower than that of single crystal materials.[269] Liu et al. developed a flexible composite SSE comprising a combination of PEO and perovskite-type LLTO (with a specific composition of $Li_{0.33}La_{0.557}TiO_3$).[315] Additionally, the composite SSE featured PEO layers on both sides. The PEO on both sides formed an excellent interface and buffered the volume change of electrolytes during cycling. As a result, the fabricated PEO/LLTO SSE exhibited a σ of 1.6×10^{-4} S cm^{-1} at 24 °C. Moreover, the Li|SSE|Li symmetric cell employing this PEO/LLTO composite SSE maintained stability for 400 h of operation at a current density of 0.3 mA cm^{-2} and 60 °C. The Li|SSE|LFP full cell demonstrated exceptional rate performance, achieving a specific capacity of 135 mAh g^{-1} at a rate of 2 C and 60 °C. Additionally, this cell exhibited excellent cycling stability, with a capacity retention of 79% after 300 cycles at 2 C and 60 °C, corresponding to a 106.6 mAh g^{-1} capacity. Wang et al. reported the development of an oxide/polymer composite SSE by blending a high ion-conductive vertical LAGP with the mechanically flexible PEO.[316] The composite SSE displayed a high σ of 1.7×10^{-4} S cm^{-1} at r.t. and a t_{Li^+} of 0.56. When incorporated into a Li|LAGP/PEO|LFP full cell configuration, the cell exhibited excellent cycling stability over 300 cycles. It displayed an initial discharge capacity of 148.7 mAh g^{-1} and a remarkable capacity retention of 93.3% at 0.3 C and 60 °C.

PVDF is another polymer that is frequently utilized as a substrate in various applications due to its high polarization and dielectric constant due to fluorine's strong electron-withdrawing nature.[317] These characteristics make PVDF well-suited for effectively separating Li salts, thereby improving Li^+ transport.[318,319] Additionally, PVDF demonstrates excellent thermal and electrochemical stability, further enhancing its suitability for use in various applications, including battery systems.[320] As a notable example, Kang's group reported a composite SSE that exhibited both high conductivity and dielectric properties. The composite was made of a PVDF matrix and $BaTiO_3$–LLTO nanowires arranged in a side-by-side heterojunction structure. This LLTO/$BaTiO_3$/PVDF composite SSE demonstrated a high ionic conductivity of 8.2×10^{-4} S cm^{-1}, along with a t_{Li^+} of 0.57 at 25 °C. The fast Li^+ transport was attributed to two key aspects: First, the dielectric $BaTiO_3$ facilitated the dissociation of the Li salt, resulting in more free-moving Li^+ ions. These Li^+ could then spontaneously transfer across the interface to the coupled LLTO phase, enabling highly efficient transport. Secondly, the $BaTiO_3$–LLTO nanowires suppressed the formation of the space charge layer between PVDF matrix and the inorganic fillers, thereby promoting the transport of the dissociated Li^+. Furthermore, the SSE demonstrated a wide ESW of 4.8 V (vs Li^+/Li), making it highly compatible with high-voltage nickel-based cathodes. In addition, the LLTO/$BaTiO_3$/PVDF composite SSE exhibited excellent interfacial stability with both the NCM811 cathode and the Li metal anode. When assembling a Li|LLTO/$BaTiO_3$/PVDF|NCM811 cell utilizing this composite SSE, the cell delivered an initial specific capacity of 172.1 mAh g^{-1} and a capacity retention of 57.1% after 1500 cycles at 1 C and 25 °C.

Bruce's group have developed a ceramic/polymer composite SSE featuring a 3D-ordered bicontinuous structure composed of ceramic and polymer microchannels.[321] This composite SSE incorporates LAGP along with non-conducting polymers such as polypropylene and epoxy. Leveraging the capabilities of 3D printing, precise microstructural designs in cubic, gyroidal, and diamond configurations are achieved, allowing for accurate control of the ceramic-to-polymer ratio. The preparation process of the composite SSEs involves fabricating a 3D printed template, filling the template with LAGP powders, forming a structured LAGP scaffold through calcination and sintering, and subsequently filling the scaffold with polymers followed by polishing (**Figure 17a,b**). The composite SSE exhibited a σ of 1.6×10^{-4} S cm^{-1} at r.t., which is lower than that of a dense ceramic pellet with a σ of 2.8×10^{-4} S cm^{-1} (Figure 17c). This decrease in σ can be solely attributed to the volume fraction of space occupied by the non-conducting polymer. In the study, a detailed analysis of the Nyquist plots via electrochemical impedance spectroscopy (EIS) measurements of the composite SSE was conducted at −30 °C (Figure 17d). The Nyquist plots displayed two semicircles, which can be attributed to the intragrain and

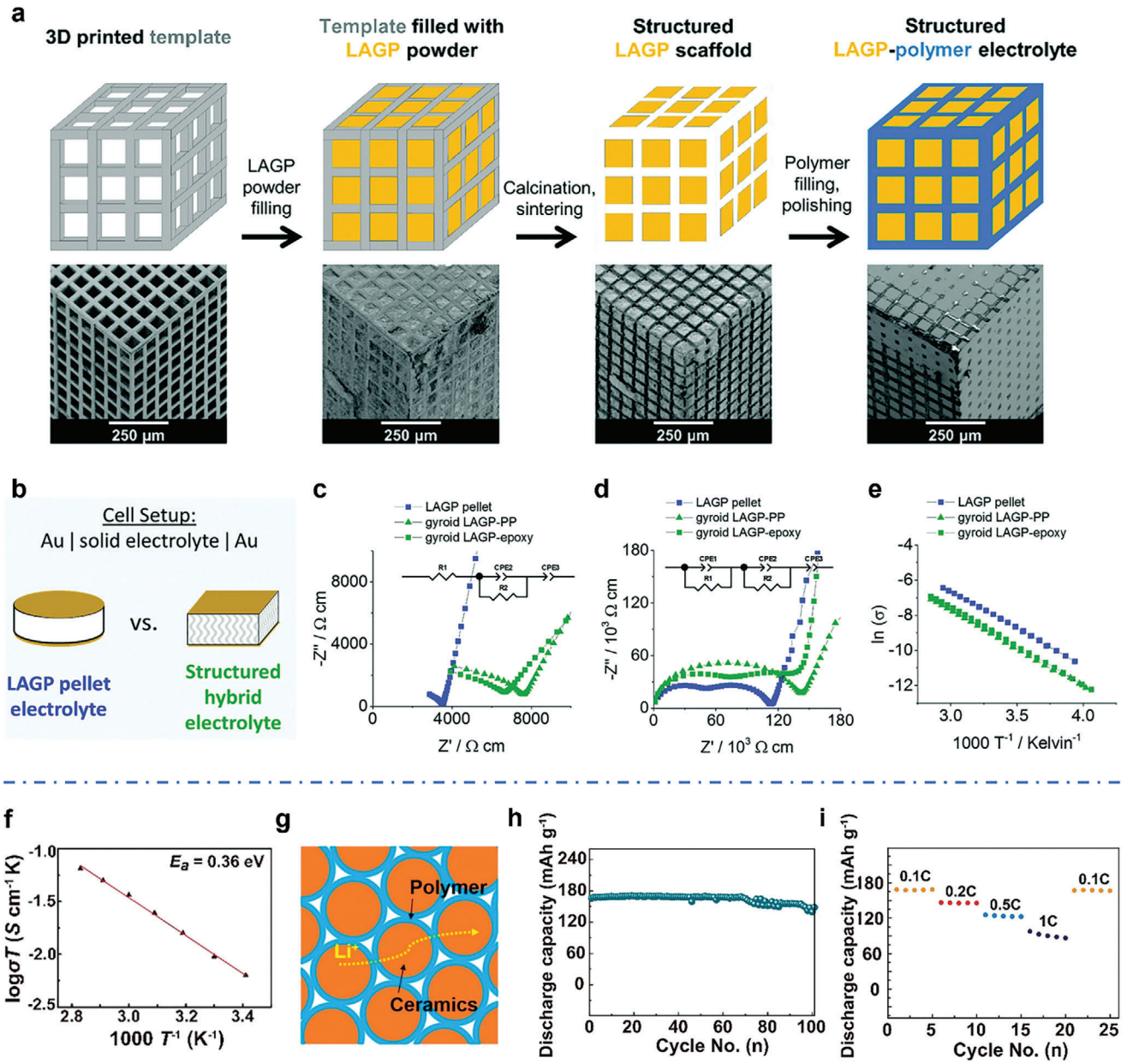

Figure 17. Representative oxide/polymer composite SSEs. a–e) The 3D LAGP/polymer composite SSE. a, The fabrication process of LAGP/polymer composite SSE and scanning electron microscopy (SEM) images capturing each step of the fabrication process. b) The cell setup for σ measurement. c,d) Nyquist plots of EIS measurements for the LAGP and LAGP/polymer composite SSEs at r.t. and −30 °C, respectively. e) Arrhenius plots of LAGP and LAGP/polymer composite SSEs. Reproduced with permission.[321] Copyright 2018, Royal Society of Chemistry. f–i) LLZTO/PAN composite SSE. f) Arrhenius plots of the σ of LLZTO/PAN composite SSE. g) The schematic diagram of the interparticle Li^+ transport within the LLZTO/PAN composite SSE. h) Cycling performance of the Li|LLZTO/PAN|LFP cell at 0.1 C and 60 °C. i) Rate performance of the Li|LLZTO/PAN|LFP cell at 60 °C. Reproduced with permission. Copyright 2021, American Chemical Society.

intergrain Li^+ transport within the LAGP phase observed in both the LAGP pellet and structured LAGP/polymer composite. Furthermore, the σ of the composite SSEs were investigated at various temperatures ranging from −20 °C to 75 °C (Figure 17e). It is worth noting that the introduction of polymers enhances the mechanical properties of the composite SSE, rendering it less susceptible to fracture compared to the LAGP pellet. This improvement is attributed to the polymer's ability to alleviate the inherent brittleness of the ceramic material. By employing 3D printing, the composite SSE achieves excellent mechanical properties while maintaining a favorable level of σ. The diverse structural designs also enable tunable SSE performance, thus offering a promising avenue for developing high-performance ASSLMBs. Guo's group reported the fabrication of an LLZTO/PAN composite SSE by coating PAN onto the surface of LLZTO particles.[133] The resulting LLZTO/PAN

composite SSE pellet exhibited a σ of 1.1×10^{-4} S cm^{-1} at 60 °C (Figure 17f), significantly higher than that of the cold-pressed LLZTO pellet (2.0×10^{-7} S cm^{-1}). This enhancement in conductivity was attributed to the uniform conjugated PAN nanocoating, which provided pathways for Li^+ conduction between adjacent particles in the unsintered ceramics (Figure 17g). The LLZTO/PAN composite SSE also displayed a t_{Li^+} of 0.66 and a wide ESW of up to 4.4 V (vs Li^+/Li). Moreover, the composite SSE could be tape-casted into a thin film with a thickness of less than 10 µm, enabling high energy density in ASSLMBs. In order to prevent parasitic reactions between PAN polymer and the Li metal anode, a layer of PEO-based SSE with a thickness of ≈1 µm was applied onto the LLZTO/PAN composite SSE layer, establishing direct contact with the Li anode. In a Li|LLZTO/PAN|LFP cell utilizing the LLZTO/PAN thin-film SSE, excellent cycling stability and rate performance were achieved at 60 °C. The cell exhibited an initial discharge capacity of 167 mAh g^{-1} at 0.1 C, with a capacity retention of 89.6% after 100 cycles (Figure 17h). Furthermore, the Li|LLZTO/PAN|LFP cell demonstrated capacities of 146, 135, and 98 mAh g^{-1} at 0.2 C, 0.5 C, and 1 C, respectively (Figure 17i). The oxide/polymer composite SSEs, which exhibit fast Li^+ transport and excellent mechanical performance, hold significant potential for use in high-energy-density ASSLMBs.

Zhang's group reported a sulfide/polymer composite SSE consisting of LGPS and a blend of PEO and PEG with the addition of Li salt (**Figure 18a**).[141] This composite SSE exhibited a high σ of 9.8×10^{-4} S cm^{-1} at r.t. (Figure 18b), and a t_{Li^+} of 0.68. Furthermore, this composite SSE demonstrated remarkable electrochemical stability, as evidenced by its ESW of 5.1 V vs Li^+/Li (Figure 18c). Additionally, due to its high t_{Li^+} and the formation of a dense protective layer via an in situ coupling reaction with a well-organized molecular arrangement, the composite SSE exhibited exceptional Li dendrite suppression ability. This characteristic resulted in sustained electrochemical performance of the cell when employing LFP as the cathode material. The Li|PEO/PEG-3LGPS|LFP cell demonstrated an initial discharge capacity of 164 mAh g^{-1} at 0.05 C and 60 °C and exhibited a capacity retention of 91% after 150 cycles when operated at 0.5 C, with a corresponding capacity of 143 mAh g^{-1} (Figure 18d,e). Overall, the strategy of making ceramic/polymer composite SSE represents a promising approach for developing SSEs with high σ, favorable t_{Li^+}, and enhanced safety features through dendrite suppression. Overall, ceramic composites are promising as SSEs for addressing interface challenges and instabilities commonly observed in pure ceramic SSEs.[63,322,323] This is primarily due to the utilization of polymer materials, which provide improved interface contact. By incorporating polymers into ceramic composites, the resulting SSEs can effectively mitigate interface issues and enhance stability, thereby offering a potential solution to the limitations associated with traditional ceramic SSEs.

3.3. Emerging Materials

Considerable efforts have been dedicated to advancing SSEs, and the discovery of emerging materials has garnered significant interest. These emerging materials encompass a range of substances, including MOFs, COFs, porous polymers, and crystalline polymer composites. These materials exhibit substantial potential in the development of high-performing SSEs, characterized by a high σ and t_{Li^+}, exceptional thermal/chemical/electrochemical stability, and cost-effectiveness for large-scale production.[324] In this section, we delve into a comprehensive discussion of these emerging materials as SSEs. This entails exploring their distinctive features, properties, and performance in the context of applications for ASSLMBs.

3.3.1. MOFs

MOFs are a class of porous materials composed of metal ions or clusters connected by organic ligands, and they are renowned for their exceptional structural diversity, high functional tunability, and extraordinarily high surface areas.[325] The metal ions in MOFs can range from transition metals like copper, zinc, or iron to rare earth metals. On the other hand, ligands are typically organic molecules with functional groups capable of forming coordination bonds with the metal ions, typically carboxylic acids. The distinctive coordination bonds between metal ions and organic ligands in MOFs impart exceptional design flexibility and functional versatility.[326] This unique combination enables MOFs to exhibit various properties and find applications in energy storage fields.[327–329] In recent years, there has been a surge of interest in utilizing MOFs as SSEs in battery applications.[330–333] This interest is driven by the exceptional intrinsic characteristics displayed by MOFs, which include their unique pore structures with high surface areas that facilitate rapid ion transport.

Dincă's group has developed a series of high-performing electrolytes with a copper-azolate MOFs host.[334] The copper-azolate MOF electrolytes exhibited tunable σ depending on the Li salt used. Specifically, the highest recorded σ achieved at r.t. was 1.1×10^{-4} S cm^{-1} when LiI was used as the Li salt and washed by propylene carbonate (PC), while the highest t_{Li^+} of 0.69 was achieved with LiCl as the Li salt. These findings highlight the potential of copper-azolate MOFs as electrolytes in LMBs. Nevertheless, the inclusion of PC in electrolytes still categorizes them as QSSEs, which can pose potential safety issues when applied in practical LMBs. Single-ion conductors exhibit a notable characteristic of a high t_{Li^+} owing to their distinctive ion transport properties. In order to fulfill the practical requirement of Li^+ conduction, researchers have installed ionic groups on the MOFs' backbones, specifically ionic MOFs.[335,336] Yang et al. reported a single Li^+ conductor based on UiO-66 MOFs.[97] The SSE named UiO-66-LiSS was initially synthesized through a solvothermal method using $ZrCl_4$ and 2-bromoterephthalic acid reagents. Afterward, a Mizoroki-Heck coupling reaction was employed to covalently link sulfonated side chains and sodium *p*-styrenesulfonate to the MOF skeleton. Finally, the Na^+ within the SSE was replaced with Li^+ through an ion exchange process. The resulting UiO-66-LiSS SSE exhibited a σ of 6.0×10^{-5} S cm^{-1} and a high t_{Li^+} of 0.90 at 25 °C without the use of plasticizers. The SSE also demonstrated a wide ESW of 5.2 V (vs Li^+/Li). When the UiO-66-LiSS SSE was integrated into ASSLMBs, specifically in the Li|UiO-66-LiSS|LFP full-cell configuration, excellent cycling stability was observed. The full cell exhibited an initial discharge capacity of 127 mAh g^{-1} and capacity retention of 88.1% after 100 cycles at a rate of 0.2 C and 25 °C. Furthermore, the Li|UiO-66-LiSS|LFP cell

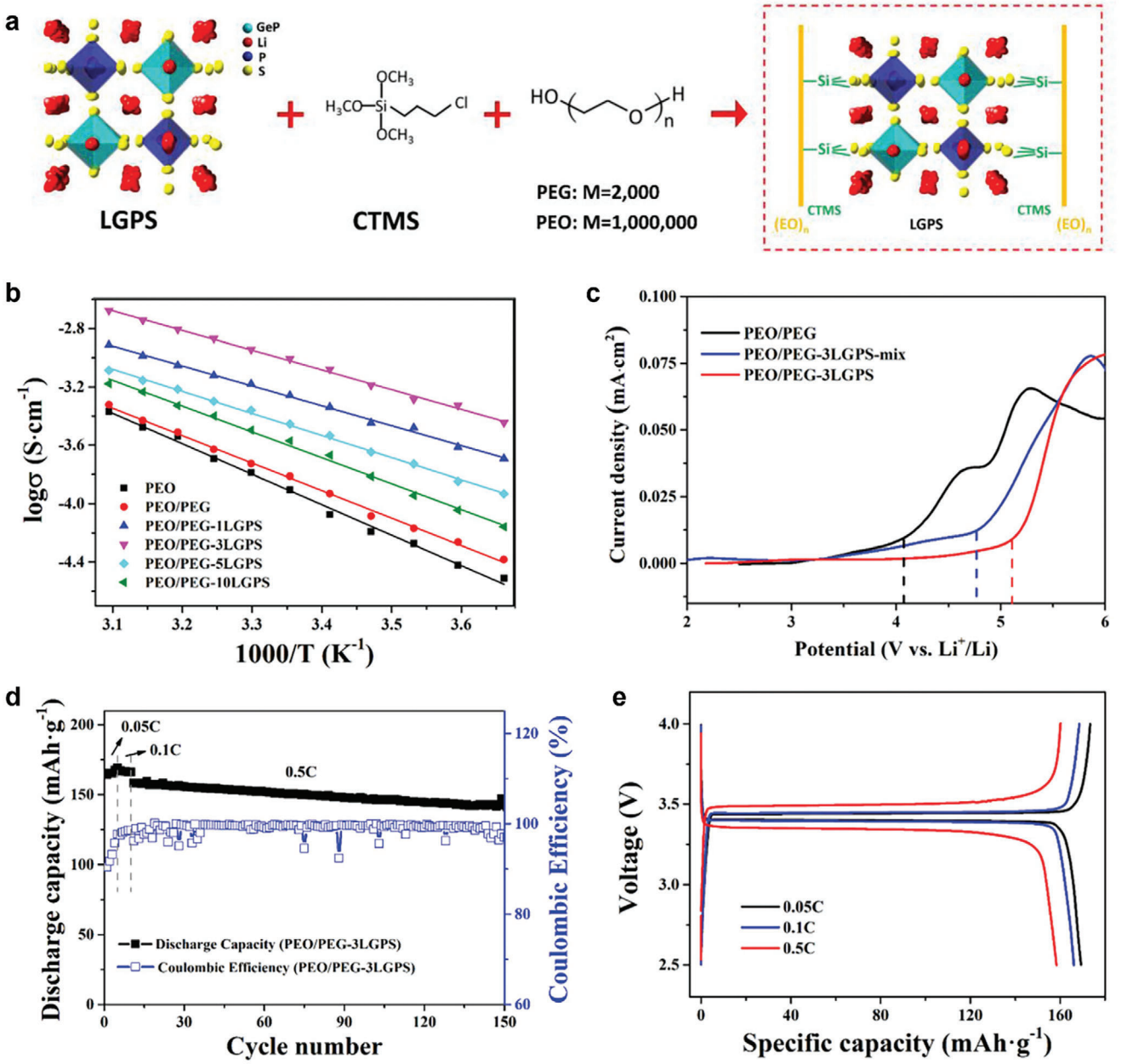

Figure 18. A sulfide/polymer composite SSE, denoted as PEO/PEG-LGPS. a) The composition of the PEO/PEG-LGPS SSE. b) Arrhenius plot of the σ of PEO, PEO/PEG, and PEO/PEG-LGPS SSEs. c) ESW of the PEO/PEG, PEO/PEG-3LGPS (mechanical mixture), and PEO/PEG-3LGPS SSE. d, The cycling performance of the Li|PEO/PEG-3LGPS|LFP cells at rates of 0.05 C, 0.1 C, and 0.5 C at 60 °C. e) The voltage profiles of the Li|PEO/PEG-3LGPS|LFP cells at different rates and 60 °C. Reproduced with permission.[141] Copyright 2020, Wiley-VCH Verlag GmbH & Co. KgaA.

demonstrated exceptional rate capability, achieving a discharge capacity of 150 mAh g^{-1} at 0.1 C and a capacity of 88 mAh g^{-1} at a high rate of 2 C. Shang et al. reported a SSE based on UiO-66-type MOFs with immobilized anions.[337] This MOFs-based SSE was synthesized by copolymerizing diallyl decarbonate and introducing a double bond onto UiO-66-NH_2 MOFs. The optimized SSE exhibited a σ of 5.1×10^{-4} S cm^{-1} at 25 °C, a t_{Li^+} of 0.65, and a wide ESW of 5.4 V (vs Li^+/Li). This approach not only mitigated the agglomeration issue resulting from the direct physical introduction of MOFs but also effectively immobilized $TFSI^-$ by leveraging the abundant coordinated unsaturated cation sites presented on the MOFs-based SSE. According to the space charge theory, the coordination of anions within the SSE acts as an effective strategy to prevent the formation of Li dendrites. When this MOFs-based SSE was utilized, the Li|SSE|Li symmetric cell demonstrated stable Li plating and stripping behavior for 300 h at a current density of 0.5 mA cm^{-2}. Furthermore, during cycling stability testing at a rate of 0.2 C and r.t., the Li|SSE|LFP cell achieved the highest specific capacity of 154.6 mAh g^{-1}, along with a capacity retention of 95.75% after 200 cycles.

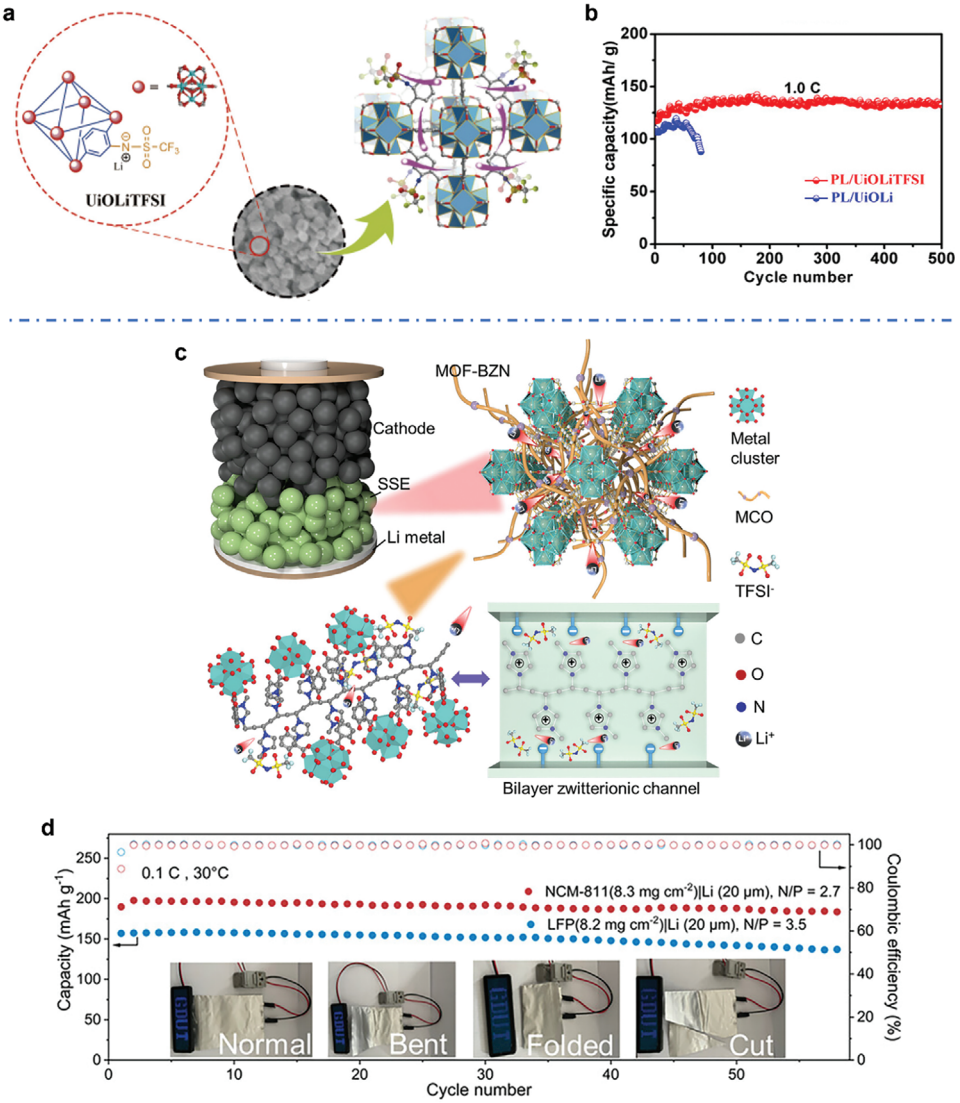

Figure 19. Representative MOFs SSEs for ASSLMBs. a,b) UiOLiTFSI. a) The structure of UiOLiTFSI SSE. b) The cycling performance of the Li|PL/UiOLiTFSI|LFP cell at 1 C. Reproduced with permission.[125] Copyright 2019, American Chemical Society. c,d) MOF-BZN. c) The illustrations of structure and ion transport mechanism in MOF-BZN SSE. d) The cycling performance of the Li|MOF-BZN|LFP and Li|MOF-BZN|NCM811 pouch cells at 0.1 C and 30 °C. Reproduced with permission.[96] Copyright 2023, Wiley–VCH.

Kang's group has documented the development of anionic MOF-based SSEs utilizing UiO-66-NH_2 MOFs, wherein a trifluoromethanesulfonyl group is covalently linked to the MOF framework.[125] This SSE, referred to as UiOLiTFSI (**Figure 19a**), demonstrated a noteworthy σ of 2.1×10^{-4} S cm^{-1} and a t_{Li^+} of 0.84 at 25 °C. Moreover, the Li|PL/UiOLiTFSI|LFP cell utilizing the UiOLiTFSI/PVDF composite SSE, exhibited exceptional cycling stability at r.t. It displayed an initial discharge capacity of 152 mAh g^{-1} and capacity retention of 97.2% after 100 cycles at 0.2C. Notably, the cell still achieved capacity retention of 97% after 500 cycles at a high rate of 1 C (Figure 19b). However, we should note that, in the absence of liquid plasticizers and external Li salts, attaining a σ exceeding 10^{-4} S cm^{-1} at r.t. is a challenging task in most MOFs-based SSEs.[331] In 2023, Huang's group reported bilayer zwitterionic MOF SSEs, referred to as MOF-BZN, by grafting soft multicationic oligomers onto the pore walls of rigid anionic MOF channels (Figure 19c).[96] This design facilitated fast Li^+ transport while limiting the movement of anions. Remarkably, the bilayer zwitterionic MOFs SSE demonstrated a high σ of 8.8×10^{-4} S cm^{-1} at r.t., along with a high t_{Li^+} of 0.75, without the need for any liquid components or external Li salts. However, prior to use, the SSE was activated by treating it with a 1 M LiTFSI solution in acetonitrile, followed by washing and drying it at 120 °C under vacuum. Furthermore, the bilayer zwitterionic MOF SSEs exhibited a wide ESW of up to 4.9 V (vs Li^+/Li). Leveraging the MOF-BZN SSE, a significant energy density of 419.6 Wh kg^{-1}, calculated based on the total mass of anode, cathode, and electrolyte, was achieved for the full cell configuration (Li|MOF-BZN|NCM811), utilizing NCM811 as the cathode with a loading of 20.1 mg cm^{-2} and Li metal as the anode. Moreover,

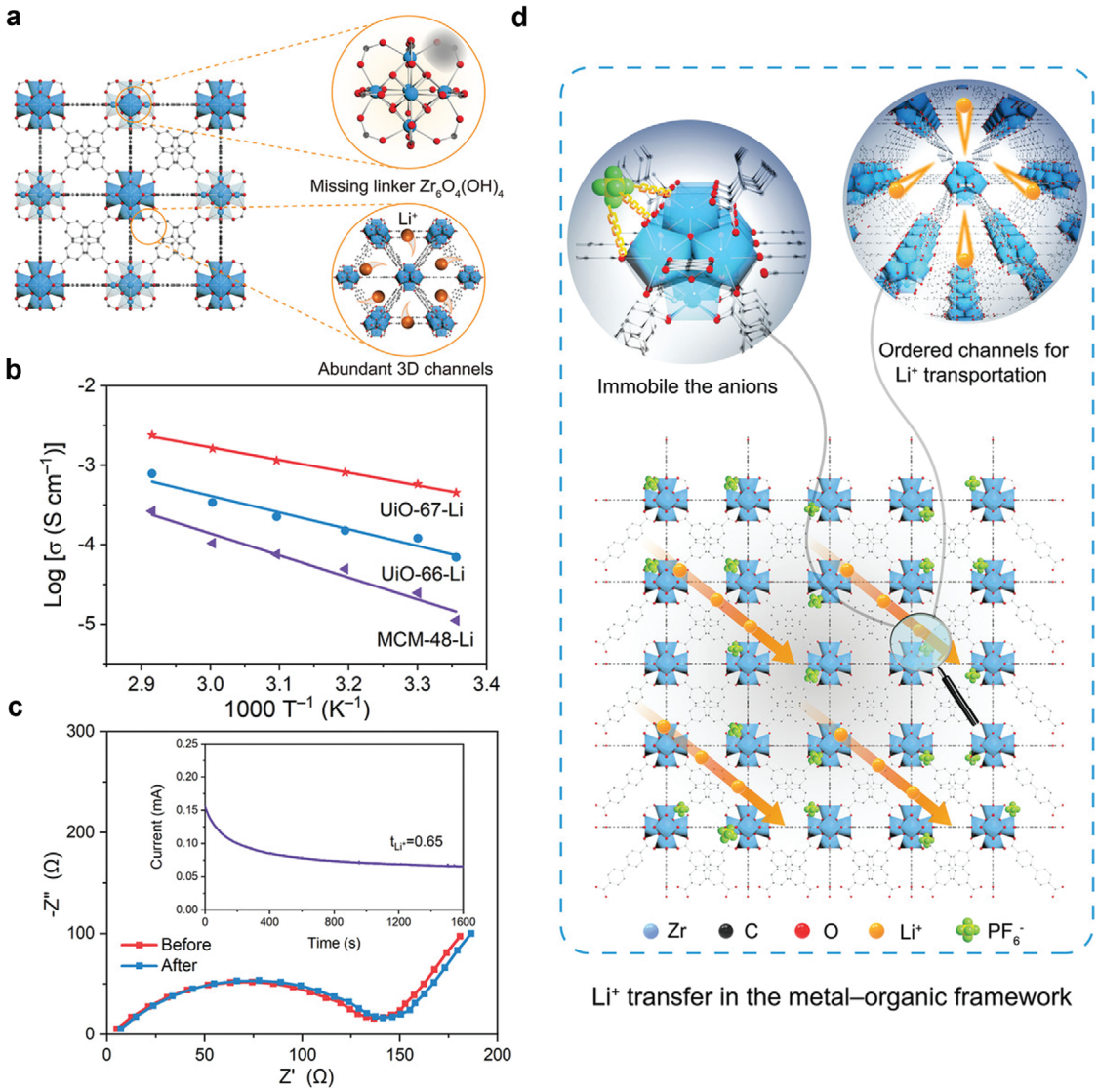

Figure 20. The fabrication and performance analysis of the UiO-67-Li SSE, along with the illustration of the Li^+ transport mechanism. a) The structure of UiO-67-Li SSE. b) Arrhenius plots of the σ of UiO-67-Li SSE. c) The chronoamperometry profile of a Li symmetric cell utilizing UiO-67-Li as the SSE, the inset shows the Nyquist plots obtained from EIS measurements conducted before and after polarization. d) Li^+ conduction mechanism occurring within the UiO-67-Li MOFs SSE. Reproduced with permission.[126] Copyright 2022, Wiley-VCH.

both the Li|MOF-BZN|LFP and Li|MOF-BZN|NCM811 pouch cells demonstrated stable cycling performance when operated at 0.1 C and 30 °C. (Figure 19d). The design of bilayer zwitterionic MOFs SSE represents a novel and promising strategy for fabricating advanced MOFs-based SSEs for advanced ASSLMBs with enhanced energy densities.

Xu's group reported an SSE based on UiO-67 MOFs with fast Li^+ transport (**Figure 20a**).[126] The SSE incorporating UiO-67-Li exhibited a notably higher σ of 6.4×10^{-4} S cm^{-1} at 25 °C compared to UiO-66-Li SSE, which showed a σ of 6.9×10^{-5} S cm^{-1} (Figure 20b). This enhanced σ is attributed to the larger pore size of UiO-67-Li, which facilitated rapid Li^+ conduction through the abundant 3D channels within the MOFs. Furthermore, UiO-67-Li SSE demonstrates a t_{Li^+} of 0.65 (Figure 20c). The mechanism underlying Li^+ transport can be explained by the presence of numerous well-organized channels for Li^+ transportation, while the anions are immobilized by the framework of the MOFs (Figure 20d).

3.3.2. COFs

COFs, another distinct type of PCPs constructed from organic molecules as nodes and junctions through reversible covalent reactions, are an important class of emerging SSEs. Since Yaghi's group reported the first boronic acid-based COFs formed by the self-condensation of boronic acid in 2005,[338] COFs gained increasing interest owing to highly defined nanoscale channels and spaces, high chemical/electrochemical/thermal stabilities, significant specific surface area, and highly regulated network

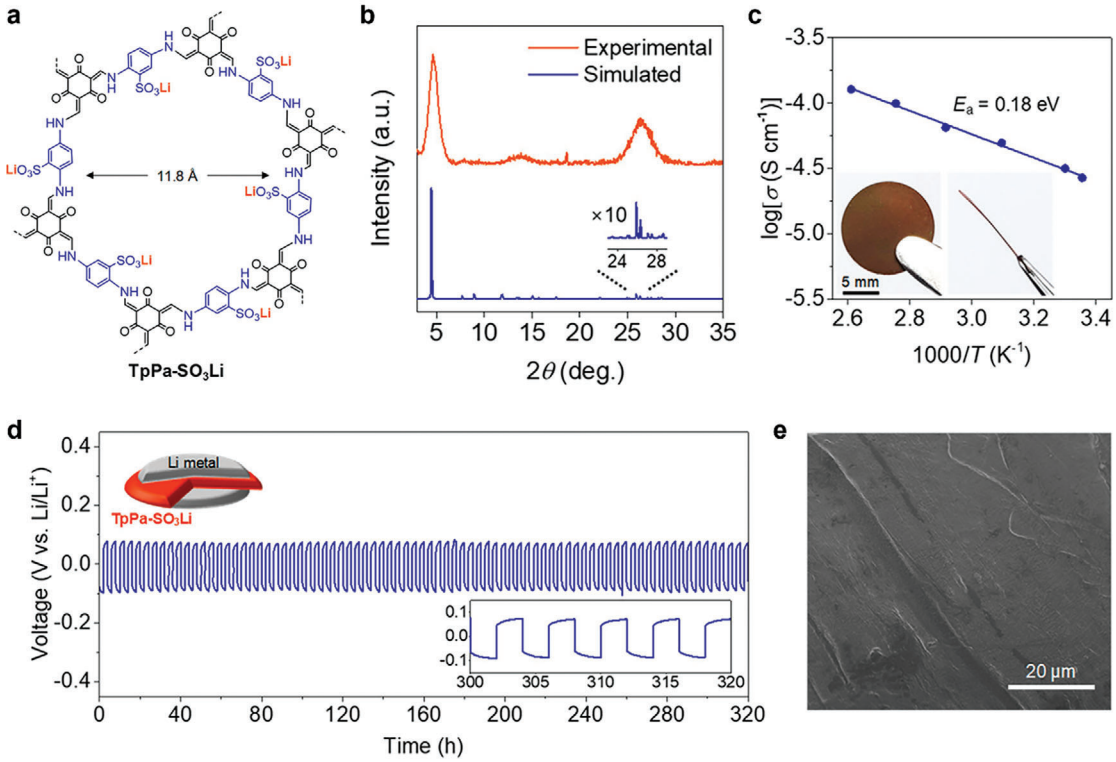

Figure 21. Representative COFs SSE, denoted as TpPa-SO_3Li. a) The chemical structure of TpPa-SO_3Li SSE. b) Powder X-ray diffraction (PXRD) pattern of the TpPa-SO_3Li. c, Arrhenius plots of the σ of TpPa-SO_3Li SSE. d) The cycling performance of the Li|TpPa-SO_3Li|Li symmetric cell at a current density of 0.01 mA cm^{-2} and r.t. over 320 h (4 h each cycle). e) The surface morphology of the Li metal was examined using SEM after undergoing the cycling test for 320 h. Reproduced with permission.[127] Copyright 2019, American Chemical Society.

structures.[339] COF-based materials have emerged as exceptional platforms for designing materials with diverse functions through manipulating linkers and linkage chemistry. Consequently, they have been widely explored and utilized in various applications.[340–342] Specifically, the fixed nanoscale channels and spaces formed by stacking covalent COFs frameworks offer great potential for applications such as molecular storage, release, and separation.[343,344] Moreover, the structural regularity of COFs renders them suitable for efficient carrier transport, thereby presenting significant potential in advanced batteries.[149,345,346] Indeed, COFs have received highlights due to their stable chemical/electrochemical/thermal properties, adjustable chemical design, high porosity, and large surface area, these characteristics make COFs appealing candidates for SSEs in advanced battery devices.[149,347] In 2015, the first reported ion-conductive covalent organic framework marked the beginning of a rapid development, driven by the introduction of spiroborate linkages.[348] iCOFs, incorporating ionic species within their frameworks, have demonstrated significant potential in energy devices, particularly as SSEs in LMBs.[98,349] In general, iCOFs as SSEs exhibit σ ranging from 10^{-5} to 10^{-4} S cm^{-1} at r.t., along with high electrochemical stability. While there are cases where COFs-based electrolytes have achieved high σ exceeding 10^{-3} S cm^{-1}, such as imidazolate iCOFs with an impressive σ of 7.2×10^{-3} S cm^{-1} at r.t., these are usually with 20 wt.% PC making them as QSSEs.[350] In this review, we focus on SSEs that do not contain any liquid components. In 2019, Lee's group synthesized a sulfonate-based iCOF as a single Li^+ conductor (**Figure 21a**).[127] Based on the powder X-ray diffraction (PXRD) pattern (Figure 21b), the iCOFs exhibited high crystallinity. This iCOF exhibited a σ of 2.7×10^{-5} S cm^{-1} at r.t. without the addition of external Li salts (Figure 21c). Furthermore, it demonstrated a t_{Li^+} of 0.9, indicating a single-ion conductive behavior. The Li|TpPa-SO_3Li|Li symmetric cell showed stable Li plating and stripping profiles at a current density of 0.01 mA cm^{-2} over 320 h (Figure 21d), and the clean morphology of the Li metal anode after cycling indicated that the TpPa-SO_3Li SSE possesses effective dendrite suppression ability (Figure 21e).

By employing a solvent-free in situ polymerization method and incorporating ether segments through grafting, Hou et al. synthesized the highly crystalline vinyl functionalized COF (denoted as V-COF).[351] The V-COF-based electrolyte exhibited a σ of 1.1×10^{-4} S cm^{-1} at 40 °C. Additionally, this SSE displayed a t_{Li^+} of 0.45 and a wide ESW of up to 5 V (vs. Li^+/Li). The rapid conduction of Li^+ can be attributed to the presence of one-dimensional nanochannels in the V-COFs, which facilitate efficient ion transport. Moreover, the rigid and electrochemically stable frameworks of the V-COFs contribute to enhancing the electrochemical stability of ether-based materials used in the electrolytes. When using the V-COF-based SSEs, the Li|SSE|Li symmetric cell demonstrated remarkable stability, with no significant degradation observed even after 600 h of operation at a current density of 0.1 mA cm^{-2} and 40 °C. The average polarization voltage of these cells was ≈125 mV. Furthermore, when incorporated into Li|SSE|LFP cells, the initial specific capacity was measured

at 136 mAh g^{-1} at a rate of 1 C and 40 °C. The cell exhibited a high capacity retention of 83.8% after 300 charge–discharge cycles, indicating good cycling stability and long-term performance.

In addition, cationic COFs can also be utilized as SSEs for batteries when combined with Li^+ from an external Li source. This combination enables cationic COFs to function as a conductive medium for Li^+, facilitating their transport within the battery system.[99] Li et al. fabricated a novel cationic COF, denoted as Im-COF-Br, through a Schiff base reaction using imidazolium-based monomers as building blocks.[131] The COF structure possesses adjustable anions and positively charged properties. Im-COF-TFSI, synthesized via Im-COF-Br through an ion exchange process. When combined with LiTFSI, the resulting SSE, denoted as Im-COF-TFSI@Li, exhibits a σ of 2.9×10^{-5} S cm^{-1} and a t_{Li^+} of 0.62 at 30 °C. The Li|Im-COF-TFSI@Li|Li symmetric cell displayed stable Li plating/stripping behavior for 300 h at a current density of 0.02 mA cm^{-2} and 80 °C, followed by 0.1 mA cm^{-2}. This indicates excellent compatibility between Im-COF-TFSI@Li SSE and Li metal, as well as the ability to inhibit the growth of Li dendrites. Furthermore, the Li|Im-COF-TFSI@Li|LFP cell exhibited an initial discharge capacity of 123.3 mAh g^{-1} and a capacity retention of 91.6% after 100 cycles at 0.1 C and 80 °C. Li et al. further developed an SSE based on defective 2D iCOFs with imidazolium functional groups, denoted as dCOF-ImTFSI-60@Li, through post-functionalization (**Figure 22a**).[129] This dCOF-ImTFSI-60@Li SSE exhibited a σ of 9.7×10^{-5} S cm^{-1} and a t_{Li^+} of 0.72 at 30 °C (Figure 22b). Moreover, this SSE demonstrated high thermal stability, allowing it to function within a wide temperature range up to 150 °C. When applied in ASSLMBs, the Li|dCOF-ImTFSI-60@Li|LFP cell demonstrated an initial capacity of 143.7 mAh g^{-1} at 0.1 C and 80 °C, and a capacity retention of 98.3% after 40 cycles (Figure 22c). These findings highlight the potential of COFs-based SSEs for enabling efficient Li^+ conduction at r.t. and above. However, we should note that σ over 10^{-4} S cm^{-1} at r.t. is required for practical applications in LMBs. Huang's group presented a novel approach to enhance the σ of SSEs by combining COFs with multi-cationic molecular chains, referred to as COF-MCMC (Figure 22d).[99] This design strategy improved Li^+ conduction in COF-MCMC by facilitating the dissociation of Li^+ from the coordinated sites while restricting the movement of anions. This effect is attributed to the Coulombic interaction between the multi-cationic molecular chains and anions. As a result, the COF-MCMC SSE exhibited a high σ of 4.9×10^{-4} S cm^{-1} and a t_{Li^+} of 0.71 at 30 °C (Figure 22e). Moreover, the Li|COF-MCMC|NCM811 cell displayed excellent cycling performance when operated at 0.2 C and 30 °C, demonstrating an initial discharge capacity of ≈200 mAh g^{-1} and a capacity retention of ≈96.5% after 100 cycles. (Figure 22f). These findings suggest that the incorporation of multi-cationic molecular chains into COFs can significantly enhance the σ and overall performance of the SSE systems.

Besides anionic or cationic COFs, zwitterionic COFs have also emerged as highly promising SSEs for LMBs, offering fast Li^+ conduction. Kang et al. reported an intriguing example where Zwitterionic COF was utilized as an SSE for ASSLMBs.[352] The SSE, denoted as Zwitt-COF, was formed by combining Zwitterionic COF with LiTFSI, demonstrating a high σ of 1.7×10^{-4} S cm^{-1} and a t_{Li^+} of 0.31 at r.t. By incorporating zwitterionic groups into the COF structure, theoretical simulations unveiled an intriguing phenomenon: the dissociation of strong ion pairs and subsequent reconstruction of the AA-stacking configuration. As a result, the adsorption of Li^+ onto Zwitt-COF triggered the formation of linear hexagonal ion channels within the SSE, enabling rapid transport of Li^+. Furthermore, the Zwitt-COF SSE demonstrated a wide ESW of 4.8 V (vs Li^+/Li). The Li|Zwitt-COF|Li symmetric cell exhibited stable Li plating/stripping profiles when subjected to a current density of 0.3 mA cm^{-2} for 100 h. Moreover, the rate performance of the Li|Zwitt-COF|LFP cell was evaluated across a range of rates, from 0.2 C to 2 C. Notably, at a rate of 0.2 C, the cell exhibited a discharge capacity of 162 mAh g^{-1}. Of greater significance, the cell showcased exceptional long-term stability, initially delivering a specific capacity of 60.5 mAh g^{-1} at 1 C, and impressively retaining 100% of its capacity after 200 cycles.

3.3.3. Single-Ion Conductive Polymer Electrolytes

Single-ion conductive polymer electrolytes (SICPEs) are currently being popularly researched due to their high t_{Li^+}≈1, which may alleviate the primary issues associated with LMBs, such as Li dendrite growth. Furthermore, SICPEs offer promising prospects for developing advanced electrolyte systems with enhanced ion transport properties, improved stability, and enhanced safety features.[353] Typically, conventional polymer electrolytes doped with Li salt function as binary-ion conductors, allowing both Li cations and counter-anions to move freely. The mobility of cations with Lewis basic sites in the polymeric host is closely interconnected, resulting in an accelerated movement of anions, approximately four times faster than the speed of Li^+ (**Figure 23a**). As a consequence, the transfer of Li^+ contributes only a small fraction, ≈20%, to the overall ionic current.[354] Moreover, the absence of electrode reactions for anions leads to the accumulation of anions at the interface between the electrode and electrolyte, causing cell polarization and limiting the battery's lifespan.

In contrast, the anions in SICPEs are immobilized within the polymer matrix, allowing Li transfer to predominantly carry the ionic current (Figure 23b, c) This characteristic eliminates concentration gradients and facilitates rapid charging and discharging, as demonstrated by Newman's simulations and the work of McCloskey et al., who also highlighted the potential for high power densities and fast charging by increasing the t_{Li^+} of the electrolyte.[106,358,359] Additionally, the Chazlviel model predicted that dendrite growth can be minimized in SICPEs due to the even plating and stripping of Li during the charging and discharging process.[360,361] It also been seen as an outstanding resistance to lithium dendrite growth in many SICPEs studies (Figure 23d).[357,362,363] Furthermore, SICPEs significantly enhance the electrochemical performance of batteries. Unlike binary ion-conducting electrolytes, which exhibit a relatively narrow ESW of 4–4.3 V (vs Li^+/Li),[183,364,365] SICPEs confine anion oxidation to the electrode|electrolyte interface, preventing it from occurring throughout the electrolyte. The strong electron-withdrawing capability of these stationary anions further lowers the electrolyte's highest occupied molecular orbital level, thereby improving its electrochemical stability.[366,367]

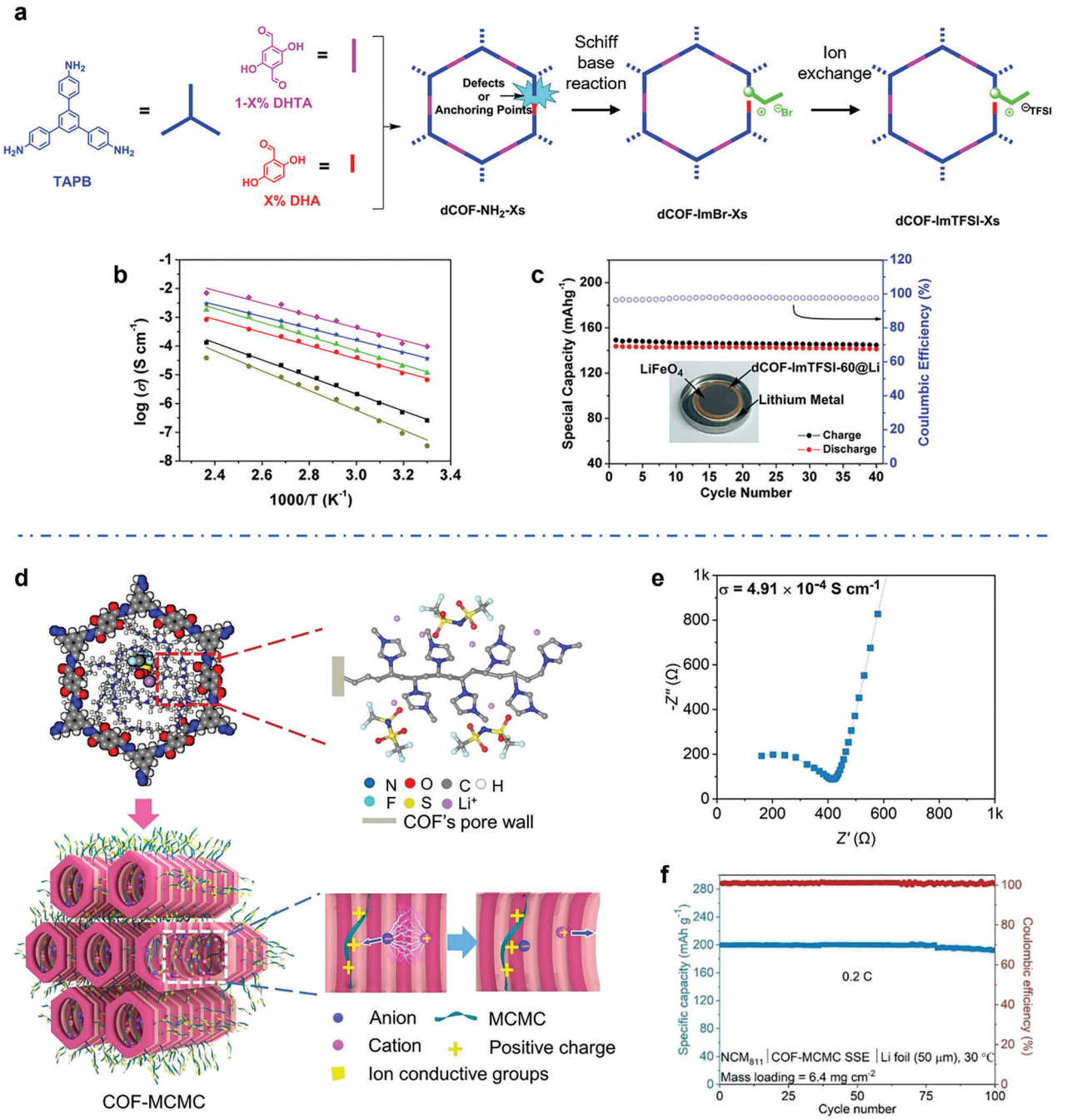

Figure 22. Representative COF SSE for ASSLMBs. a–c) dCOF-ImTFSI-60@Li. a) The synthesis route of dCOF-ImTFSI-Xs (X = 20, 40, and 60). b) Arrhenius plots of the σ of dCOF-ImTFSI-Xs based SSEs. The compounds dCOF-ImTFSI-20@Li, dCOF-ImTFSI-40@Li, and dCOF-ImTFSI-60@Li are represented by the colors green, blue, and magenta, respectively. c) The cycling performance of the Li|dCOF-ImTFSI-60@Li|LFP at 0.1 C and 80 °C. Reproduced with permission.[129] Copyright 2020, Wiley-VCH. KgaA. d–f) COF-MCMC. d) The schematic diagram of COF-MCMC's molecular structure and the ion transport pathway within the COFs. In this structure, MCMC molecules are bonded to the pore wall of the ACOF. e) The Nyquist plot of EIS measurement for COF-MCMC SSE at 30 °C. f) The cycling performance of the Li|COF-MCMC|NCM811 cell at 0.2 C and 30°C. Reproduced with permission.[99] Copyright 2023, Wiley-VCH.

Additionally, SICPEs can incorporate functional groups, such as cyano groups,[116] to enhance oxidation resistance. The SICPE, which incorporates lithium poly[(cyano)(4-styrenesulfonyl)imide] with cyano groups, exhibits an impressive ESW of 5.5 V vs Li^+/Li (Figure 23e). Additionally, its high t_{Li^+} with a value of 0.84, combined with a highly delocalized negative charged anion tethered to the polymer chain, promotes uniform Li deposition and effectively suppresses the formation of Li dendrites. As a result, the Li|SICPE|Li symmetric cell demonstrates excellent stability, allowing it to be operated steadily at a current

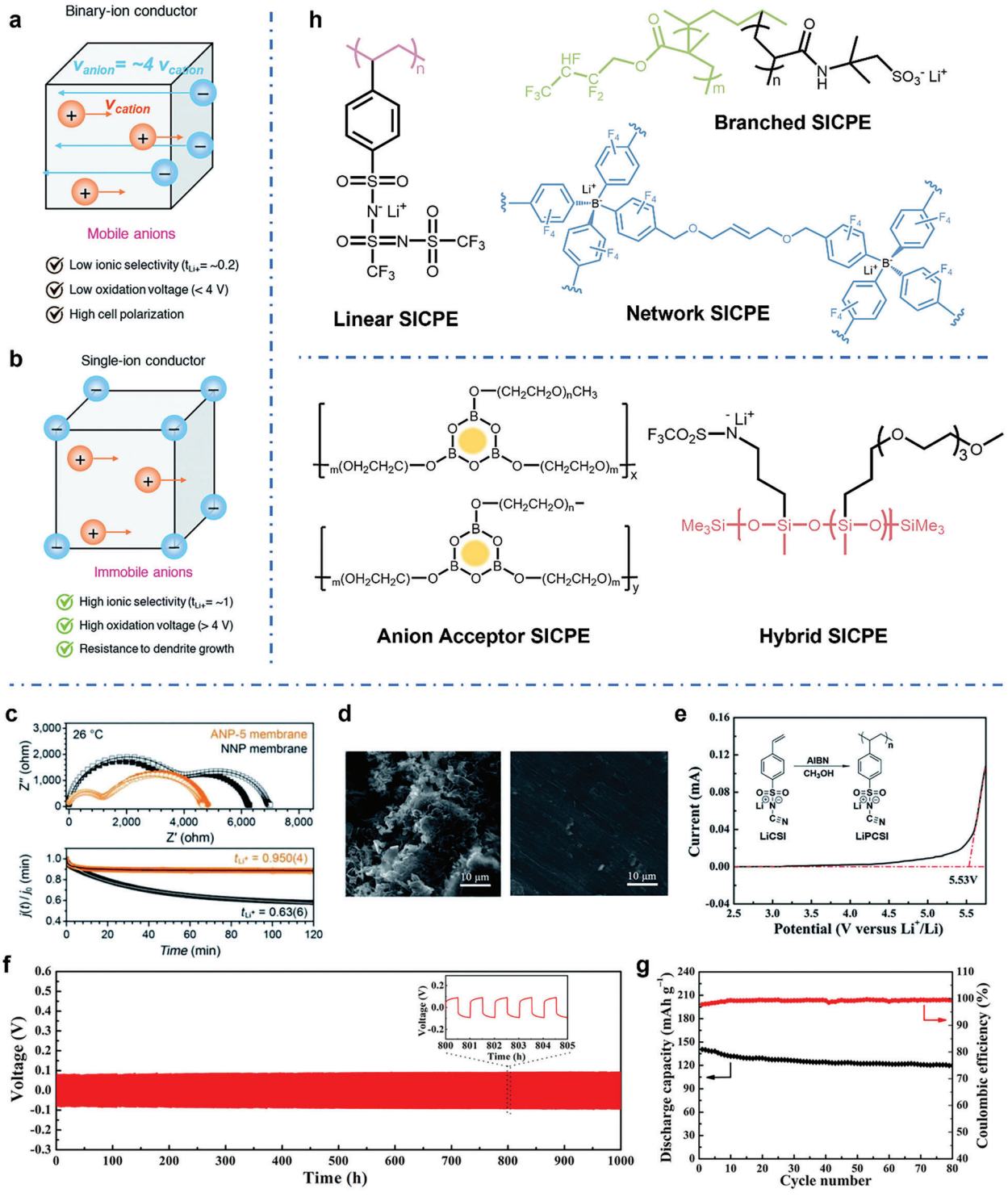

Figure 23. Single-ion conductive polymer electrolytes (SICPEs). a,b) Schematic illustration of binary-ion and single-ion conductors, respectively. Reproduced with permission.[355] Copyright 2021, Royal Society of Chemistry. c) Nyquist plot of EIS measurements and current decay curves for SICPE and binary-ion conducting electrolyte before and after polarization. Reproduced with permission.[356] Copyright 2020, Wiley-VCH. d) SEM images of the Li electrode surface from a dual-ion conductor cell (left) and SICPE cell (right) after Li plating/stripping test. Reproduced with permission.[357] Copyright 2018, Wiley-VCH. e–g) Electrochemical performance of a representative SICPE. e) Linear sweep voltammetry of linear SICPE from 2.5 to 5.8 V (vs Li^+/Li). f) Cycling performance of Li|SICPE|Li symmetric cell at a current density of 0.01 mA cm^{-2} and 60 °C. g) Cycling performance of Li|SICPE|LFP cell at a rate of 0.1 C and 60 °C.[116] Copyright 2020, American Chemical Society. h) Various polymer backbones for constructing SICPEs. Reproduced with permission.[355] Copyright 2021, Royal Society of Chemistry.

density of 0.01 mA cm^{-2} and 60 °C for a remarkable duration of 1,000 h (Figure 23f). Furthermore, the mean polarization voltage of the symmetric cell only experiences a marginal increase of 10 mV, indicating minimal degradation. Moreover, in the Li|SICPE|LFP cell configuration, the cell exhibited an initial discharge capacity of 141 mAh g^{-1} at 0.1 C and 60°C, along with a capacity retention of 85.1% after 80 cycles. (Figure 23g). These results highlight the SICPE's great potential for dendrite-free ASSLMBs, offering enhanced electrochemical performance without compromising safety. The improved electrochemical stability of SICPEs is attributed to several factors, including anion oxidation confinement, electron-withdrawing stationary anions, and resistance-enhancing functional groups. However, SICPEs exhibit a significant drawback in lower σ compared to traditional polymer electrolytes. The σ of solvent-free SICPEs are generally within the range of 10^{-7} to 10^{-5} S cm^{-1} at elevated temperatures,[310] which restricts their utility in high-power applications.

To optimize the performance of SICPEs, careful selection of anions is essential to minimize the anion-cation dissociation energy barrier. One approach to reducing the interaction strength is by enlarging the conjugation structure of the anionic parts or attaching strong electron-withdrawing groups adjacent to the anionic units, which increases the delocalization of negative charges, thereby weakening the interaction between anions and Li^+ and further enhancing Li^+ transport.[368] It has been shown that the metal affinities to Lewis bases increase in the following order: carboxylate > phosphate > N-sulfate anions > O-sulfate anions.[369] This suggests that carboxylate groups tend to slow down the Li^+ transport. Therefore, alternative anionic groups with lower metal affinities, such as phosphates or sulfates, may be more suitable for facilitating efficient Li^+ transport in SICPEs. However, the stability of the chosen anionic groups must also be considered for practical applications involving high-potential cathodes. In particular, carboxylate groups exhibit low stability above 4 V.[370] This limitation hinders their practical implementation in applications where high-potential cathodes are employed.

Various polymer backbones, including linear, branched, and network, have been designed to develop SICPEs (Figure 23h). Of course, linear polyethylene backbones with installed cationic groups are widely studied. The structure of the backbone plays a crucial role in determining ion-conducting and mechanical properties, with flexible backbones facilitating ion transport and rigid units ensuring mechanical strength.[354,371] Branched polymer backbones with side functional chains, e.g., flexible or polar molecular units, tethered to the linear backbone prevent the crystallization of polymer matrices, resulting in increased flexibility and ultimately high σ.[372,373] The utilization of network matrices in the development of SICPEs has also garnered considerable attention due to their ability to enhance mechanical properties and stability while reducing crystallinity. These network polymers consist of anionic group nodes interconnected through linear linkers via covalent bonds.[109,356,374,375] For instance, Shin et al. developed an anionic porous aromatic framework electrolyte consisting of weakly coordinating borate anion nodes and crosslinkable linkers via nucleophilic substitution, which exhibited t_{Li^+} and relatively high σ due to its interpenetrated diamondoid network structure.[356] In addition, some unconventional methods have been employed to immobilize anions in SICPEs, such as designing special macromolecules, e.g., calixarenes, that capture anions in electrolytes to slow their mobility, and grafting the organic anions onto inorganic backbones, e.g., polysiloxane, organic aluminate polymers, SiO_2, and Al_2O_3 (Figure 23h).[376–379] For instance, Mehta et al. incorporated boroxine rings, B_3O_3, as Lewis acid-based anion acceptors into a polymer host to reach relatively high t_{Li^+} of 0.62–0.88.[380] Siska et al. also successfully synthesized SICPEs by grafting organic blocks containing trifluoromethylsulfonamide and short oligoethers onto the polysiloxane backbone.[381] The resulting electrolytes displayed a σ of 1.2×10^{-6} S cm^{-1} at 25 °C.

An interesting example is a self-healing poly(ethylene-co-acrylic lithium (fluoro sulfonyl)imide) SICPE reported by Ahmed et al., denoted as PEALiFSI (**Figure 24a**).[382] Notably, the SICPE employed in this study does not include solvents and plasticizers, thereby ensuring enhanced safety without including organic solvents. This SSE demonstrated a high σ of 5.8×10^{-4} S cm^{-1} at 25 °C and a high t_{Li^+} of 0.91 (Figure 24b,c). This high σ can be attributed to two key factors. First, the self-healing property of the SSE contributes to generating a larger amorphous phase, facilitating enhanced Li^+ conduction. Second, the interaction between Li^+ and the acrylic(fluorosulfonyl)imide anion is weak, favoring the efficient Li^+ conduction. Additionally, when the self-healing SICPE was incorporated into the ASSLMB cells, the Li|PEALiFSI|LFP cell displayed notable cycling stability with an initial discharge capacity of approximately 159 mAh g^{-1} and a high-capacity retention of 95.6% even after 500 cycles at 0.1 C and 25 °C (Figure 24d). These findings highlight the potential of the self-healing SICPEs for enabling high-performance and durable ASSLMBs. These unconventional approaches demonstrate the potential of designing macromolecules and hybrid materials to develop high-performance SICPEs and ASSLMBs.

3.3.4. Crystalline Polymer Composites

In addition to the ceramic/polymer composites mentioned earlier, another noteworthy composite consists of blends of PCPs (such as MOFs and COFs) and polymers. As PCPs, such as MOFs and COFs, are rigid and brittle, interfacial contact resistance has been a critical issue, as with ceramic cases.[383] Thus, the fabrication of crystalline polymer composites has proven to be a direct and effective approach for enhancing electrochemical performance.[384,385] This unique composite has shown great potential in achieving high-performance SSEs that exhibit fast Li^+ conduction as well as high chemical and electrochemical stability. For instance, Guo's group reported a cationic MOF/PEO composite (denoted as P@CMOF), where the anions were immobilized by the cationic MOFs, leading to more free-moving Li^+ and faster Li^+ transport.[136] The P@CMOF SSE with an optimal MOF content of 12.5 vol% demonstrated the highest σ of 3.1×10^{-5} S cm^{-1} at 25 °C and a t_{Li^+} of 0.72. Furthermore, the SSE displayed a wide ESW of 5.0 V (vs Li^+/Li) due to the grafted NH_2 groups in the MOF, which prevented the oxidation of the ether oxygen in the polymer chains through hydrogen bonding. The property of immobilizing anions contributed to uniform Li^+ deposition, leading to dendrite-free performance in the SSE-based batteries. The Li|P@CMOF|Li symmetric cell showed stable Li plating/stripping behavior for 400 h at 0.1 mA cm^{-2}

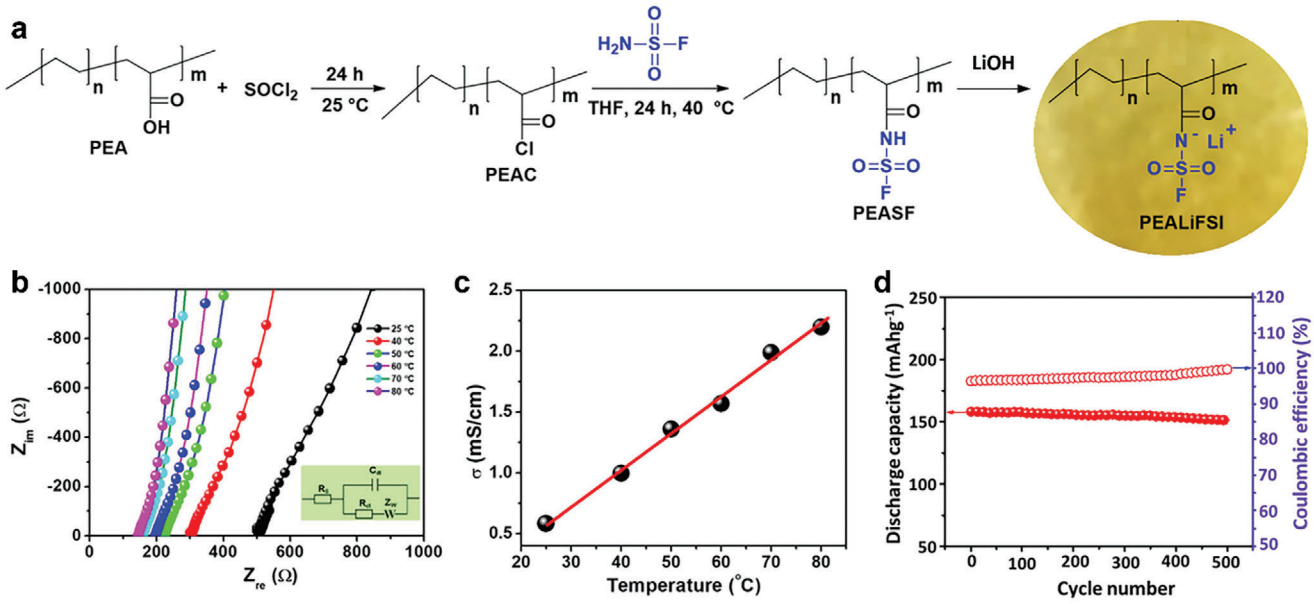

Figure 24. Representative SICPEs for ASSLMBs, denoted as PEALiFSI (poly(ethylene-co-acrylic lithium (fluoro sulfonyl)imide)). a) The synthesis route of the PEALiFSI SICPE. b) The Nyquist plots of EIS measurements of the PEALiFSI SICPE at different temperatures. c) The σ of PEALiFSI SICPE as a function of temperature. d) The cycling performance of the Li|PEALiFSI|LFP cell at 0.1 C and 25 °C. Reproduced with permission.[382] Copyright 2019, American Chemical Society.

and 200 h at 0.5 mA cm^{-2} without discernible dendrites. Moreover, the Li|P@CMOF|LFP cell demonstrated excellent cycling performance with a capacity retention of 85.4% after 300 cycles at 1 C and 60 °C. Wang et al. developed a composite SSE by covalently incorporating MOF nanoparticles into a flexible polymer matrix (**Figure 25**).[386] The synthesis of the SSE involved a one-pot photopolymerization process using vinyl-functionalized MOF (M-UiO-66-NH_2) nanoparticles, poly(ethylene glycol) diacrylate (PEGDA), a photoinitiator (1-hydroxycyclohexyl phenyl ketone) and LiTFSI salt as precursors (Figure 25a). The resulting composite SSE, referred to as HSPE-1-8, demonstrated a σ of 4.3×10^{-5} S cm^{-1} at 30 °C when the weight ratio of M-UiO-66-NH_2 to PEGDA was 1:8 (Figure 25b). Notably, the σ of HSPE-1-8 was more than five times higher than that of the SSE without vinyl-functionalized MOF. Furthermore, HSPE-1-8 SSE exhibited remarkable electrochemical stability and a wide ESW of up to 5.5 V (Figure 25c). Additionally, it demonstrated excellent interfacial compatibility with Li metal. The Li|HSPE-1-8|LFP cell, utilizing the HSPE-1-8 electrolyte, demonstrated excellent cycling stability, retaining a high discharge capacity of 153 mAh g^{-1} after 40 cycles at 0.5 C and 60 °C (Figure 25d). Moverover, the Li|HSPE-1-8|LFP cell displayed a satisfactory rate performance of up to 2 C when operated at 60 °C (Figure 25e). These findings highlight the potential of the MOF/polymer composite SSE for advanced ASSLMBs with high capacity and prolonged cycle life.

A notable advancement in the field of COFs/polymer composite SSE is the work of Wang's group. They developed a method for preparing COFs/PEG composite Li^+ conductors as SSEs.[139] The σ of this composite SSE reached 1.8×10^{-3} S cm^{-1} at 120 °C due to the presence of a fast Li^+ transport pathway provided by the PEG matrix, whereas the pure COFs fillers did not exhibit significant ion conduction (**Figure** 26a,b). Furthermore, the composite SSE displayed maintained σ even after heating at 90 °C for 48 h (Figure 26c). Manthiram's group developed an electrolyte-mediated iCOFs composite SSE using a 2 M dimethylacrylamide (DMA)@LiTFSI liquid electrolyte.[132] This solution was introduced into sulfonate COFs (LiCOF) and polymerized in situ to form a free-standing SSE membrane, called DMA@LiTFSI-mediated COFs (denoted as DLC). Unlike conventional SSEs based on solid polymers or pure iCOFs, the DLC SSEs demonstrated enhanced Li^+ transport by increased charge-carrier concentration within the iCOF channels (Figure 26d–f). This design also effectively decouples Li^+ from both COF walls and molecular chains. The resulting DLC SSEs exhibited satisfactory flexibility and manifested a high σ of 1.7×10^{-4} S cm^{-1} at r.t. (Figure 26g and 26h), along with a high t_{Li^+} of 0.85. When the DLC SSEs were implemented in the Li|DLC|LFP cells, the cell showcased excellent rate performance, maintaining stable operation up to a current density of 0.2 mA cm^{-2}, even under an elevated operating temperature of 45 °C (Figure 26i).

In another study conducted by Sun et al., they successfully fabricated a composite SSE by utilizing an ultra-thin COFs/aramid (Kevlar) membrane.[387] This hetero-layered membrane, synthesized through a bottom-up spin layer-by-layer assembly technology, possessed a thickness of 7.1 µm. The composite SSE exhibited excellent mechanical strength and achieved a high σ of 1.6×10^{-4} S cm^{-1} at 30°C, thanks to the strong chemical and mechanical interactions between aramid and the guanidinium-based cationic COF with $TFSI^-$ counterion. By employing this COF/Kevlar composite SSE, noteworthy outcomes were achieved in different cell configurations. The Li|SSE|Li symmetric cell exhibited a stable Li plating/stripping profile, with an overpotential of ≈250 mV, under an impressive current density of 0.5 mA cm^{-2} and at r.t. for 500 h (250 cycles). Meanwhile, the Li|SSE|LFP cell

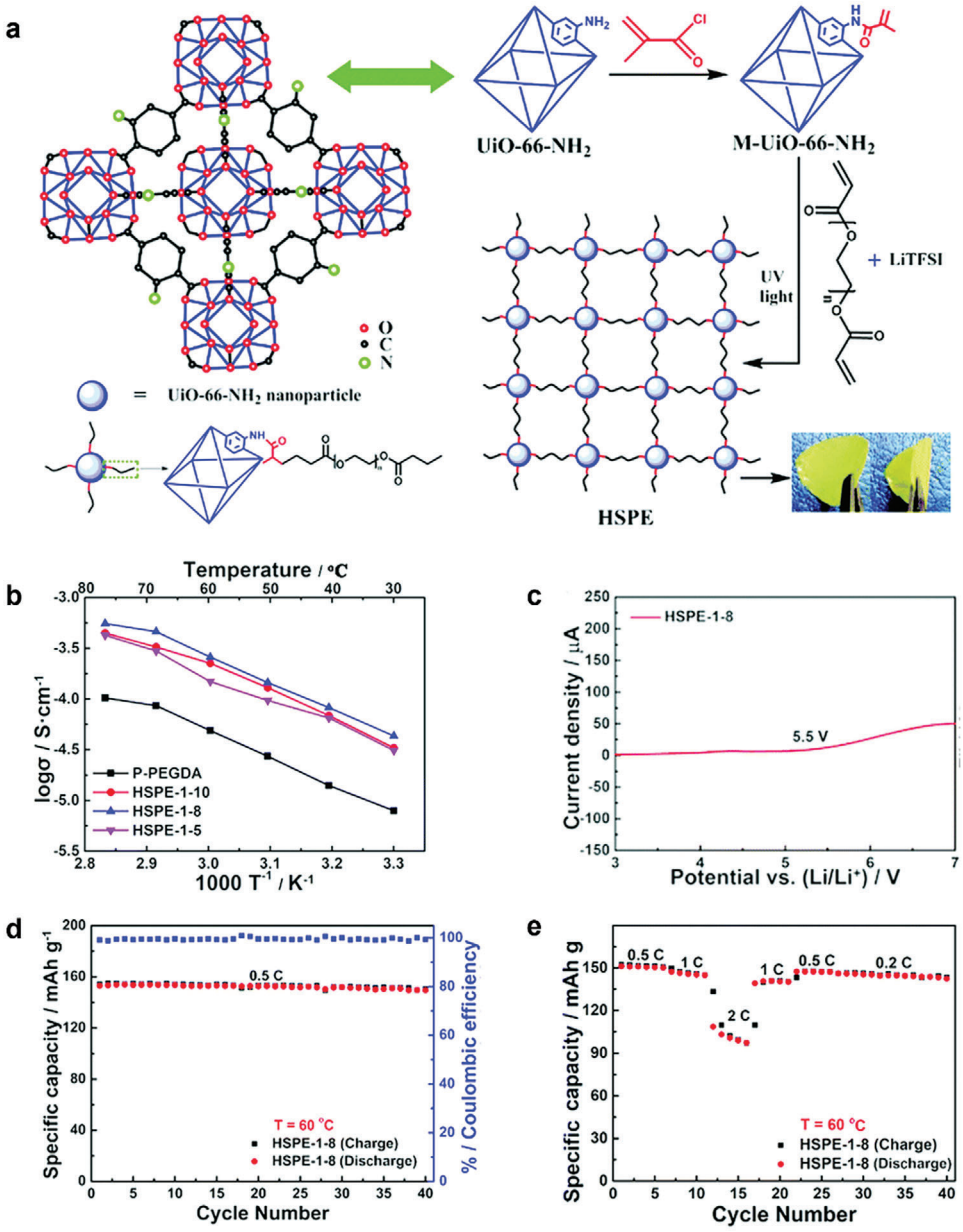

Figure 25. The covalently linked MOF-PEGDA-based composite SSE for ASSLMBs. a) The synthesis route of the composite SSE. b) Arrhenius plots of the σ of P-PEGDA and HSPEs SSEs. c) The ESW of the HSPE-1-8 composite SSE. d) The cycling performance of the Li|HSPE-1-8|LFP cell utilizing the HSPE-1-8 composite SSE at 0.5 C and 60 °C. e) The rate performance (0.2, 0.5, 1, and 2 C) of the LFP|HSPE-1-8|Li cells at 60 °C. Reproduced with permission.[386] Copyright 2018, Royal Society of Chemistry.

showcased an initial discharge capacity of 129 mAh g^{-1} and a capacity retention of 84.4% after 300 cycles at 0.2 C and r.t. Furthermore, the cell demonstrated favorable rate performance, with capacities of 112 mAh g^{-1} and 80 mAh g^{-1} at 0.5 C and 1 C rates, respectively. The development of COFs/polymer composite SSEs has experienced rapid growth in recent years following the discovery of iCOFs. This approach holds great potential for advancing the field of SSEs and improving their electrochemical performance. Below we summarize a comparison of electrolyte properties, including the σ, t_{Li^+} and ESW (vs. Li^+/Li), and battery performances equipped with them (**Table 2**).

3.3.5. Polymer Composites with Electrochemically Active Materials

The development of composite electrolytes that combine polymers with electrochemically active materials marks notable progress in energy storage technologies, especially within LMBs.[388] These composites harness the complementary properties of their constituent materials to improve overall performance. Incorporating polymers such as PEO and PVDF with active materials enhances σ, which is crucial for efficient ion transport within the electrolyte, while this integration impedes electron transport between the electrolytes and the electrodes.

Table 2. Comparison of electrolyte properties and battery performances equipped with them.

SSE type	Composition	σ [S cm^{-1}]	t_{Li+}	ESW (V, vs Li+/Li)	Cell configuration	Cycling condition/initial capacity [mAh g^{-1}]/capacity retention	Refs.
Polymer	Styrene-based PEO side-chain copolymer (Polymer host/Li salt)	1.6×10^{-5}	0.13	4.8	Li|SSE|NMC622	3.0–4.3 V, 175, 57%@100 cycles 0.1 C	[240]
	LiFSI/PEO (Polymer host/Li salt)	3.3×10^{-4} #	0.14	5.3	Li|LiFSI/PEO|LFP	2.75–3.8 V, 146, 98.6%@20 cycles 0.2 C	[241]
	NPE-V_2 (Cross-linked PIL host/Li salt)	3.2×10^{-5}	0.47	5.1	Li|SSE|LFP	2.5–4.0 V, 155, 99.5%@100 cycles 0.1 C	[251]
	PDADMA FSI/LiFSI (PIL-in-salt)	7.0×10^{-5}	0.56	>5.0	Li|PDADMA FSI/LiFSI|NMC	3.0–4.3 V, 188, 67.6%@50 cycles 0.1 C (first two cycles at 0.05 C)	[113]
	PEO_8–LiPCSI (Single-ion conductive polymer)	7.3×10^{-5} #	0.84	5.5	Li| PEO_8–LiPCSI |LFP	2.8–3.7 V, 141, 85.1%@80 cycles 0.1 C	[116]
	PEALiFSI (Single-ion conductive polymer)	5.8×10^{-4}	0.91	>4.0	Li|PEALiFSI|LFP	2.5–4.0 V, 159, 95.6%@500 cycles 0.1 C	[382]
Oxide	LAGP (NASICON-type)	5.0×10^{-4}	≈1	>3.9	Li|LAGP|LFP	2.7–3.9 V, 96, 37.5%@50 cycles 0.05 C	[266]
	LLZO (Garnet-type)	1.3×10^{-3}	≈1	>4.0	Li|LLZO|LCO	3.0–4.05 V, 94, 88.3%@100 cycles 0.05 C	[270]
	LLZT:LTO = 4:1 wt (LLZT: Ta-substituted garnet-type)	5.0×10^{-4}	≈1	>4.5	Li|LLZT-4LTO|NCM622@UiO66	2.8–4.5 V, 173, 86.3%@200 cycles 0.2 C	[272]
	Ta–LLZO (Ta-doped garnet-type)	5.1×10^{-4}	≈1	>4.2	Li|Ta–LLZO| NCM111	2.85–4.2 V, 3.2, 95%@1,000 cycles 0.5 C	[273]
Sulfide	LGPS (Sulfide)	2.8×10^{-3}	≈1	>4.1	Li|LGPS|LFP	2.5–4.1 V, 22, 0@60 cycles 0.1 C	[280]
	LGPS (Sulfide)	2.8×10^{-3}	≈1	>4.1	Li|PCE-LGPS-PCE|LFP	2.5–4.1 V, 131, 91.6@120 cycles 0.5 C	[280]
	Li_6PS_5I-20Sn (Sn-substituted sulfide)	3.5×10^{-4}	≈1	>4.2	Li|LGPS/LPSI-20Sn|LCO@LNO	2.8–4.2 V, 113, 88.5%@50 cycles 0.1 C	[284]
	98%(LPS)-2%La_2O_3 (La_2O_3 doped sulfide)	2.4×10^{-4}	≈1	5.0	Li|LGPS/98(LPS)-2La_2O_3|LCO	2.0–3.8 V, 118.5, 75.8%@100 cycles 0.1 C	[285]
MOF	UiOLiTFSI (Anionic MOFs with Li salt)	2.1×10^{-4}	0.84	4.5	Li|PL/UiOLiTFSI|LFP	2.7–4.0 V, 152, 97.2%@100 cycles 0.2 C	[125]
	UiO-66-based (MOFs with Li salt)	5.1×10^{-4}	0.65	5.4	Li|SSE|LFP	2.5–4.0 V, 154.6, 95.75%@200 cycles 0.2 C	[337]
	UiO-66-LiSS (Anionic MOFs)	6.0×10^{-5}	0.90	5.2	Li|UiO-66-LiSS|LFP	2.5–4.2 V, 127, 88.1%@100 cycles 0.2 C	[97]

(*Continued*)

Table 2. (Continued)

SSE type	Composition	σ [S cm^{-1}]	t_{Li+}	ESW (V, vs Li+/Li)	Cell configuration	Cycling condition/initial capacity [mAh g^{-1}]/capacity retention	Refs.
COF	V-COF (COFs with Li salt)	1.1×10^{-4}	0.45	5.0	Li|SSE|LFP	2.5–4.0 V, 136, 83.8%@300 cycles 1 C	[351]
	COF-MCMC (COFs with multi-cationic chains)	4.9×10^{-4} ^	0.71	4.8	Li|COF-MCMC|NCM811	3.0–4.3 V, 200, 96.5%@100 cycles 0.2 C	[99]
	dCOF-ImTFSI-60@Li (iCOFs with Li salt)	9.7×10^{-5} ^	0.72	5.3	Li|dCOF-ImTFSI-60@Li|LFP	2.5–4.0 V, 143.7, 98.3%@40 cycles 0.1 C	[129]
	Im-COF-TFSI@Li (iCOFs with Li salt)	2.9×10^{-5} ^	0.62	4.2	Li|Im-COF-TFSI@Li|LFP	2.5–4.0 V, 123.3, 91.6%@100 cycles 0.1 C	[131]
	Zwitt-COF (zwitterionic COFs with Li salt)	1.7×10^{-4}	0.13	4.8	Li|Zwitt-COF|LFP	2.0–4.2 V, 60.5, 100%@200 cycles 1 C	[352]
Composite	LLTO/$BiTiO_3$/PVDF (Oxide/polymer)	8.2×10^{-4}	0.57	4.8	Li| LLTO/$BaTiO_3$/PVDF |NCM811	2.8–4.3 V, 172.1, 57.1%@1,500 cycles 1 C	[134]
	LLTO/PEO (Oxide/polymer)	1.6×10^{-4}	0.48	4.7	Li|LLTO/PEO|LFP	2.5–3.8 V, 135, 79%@300 cycles 2 C	[315]
	LAGP/PEO (Oxide/polymer)	1.7×10^{-4}	0.56	4.5	Li|LAGP/PEO|LFP	2.5–3.8 V, 148.7, 93.3%@300 cycles 0.3 C	[316]
	LLZTO/PAN (Oxide/polymer)	1.1×10^{-4} #	0.66	4.4	Li|LLZTO/PAN|LFP	2.7–4.0 V, 167, 89.6%@100 cycles 0.1 C	[133]
	LGPS-PEO/PEG (Sulfide/polymer)	9.8×10^{-4}	0.68	5.1	Li|PEO/PEG-3LGPS|LFP	2.5–4.0 V, ~157, 91%@~140 cycles 0.5 C	[141]
	P@CMOF (MOF/polymer)	3.1×10^{-5}	0.72	5.0	Li|P@CMOF|LFP	2.8–3.8 V, ~110, 85.4%@300 cycles 1 C	[136]
	HSPE-1-8 (MOF/polymer)	4.3×10^{-5} ^	N.A.	5.5	Li|HSPE-1-8|LFP	2.5–4.0 V, 140, 86.4%@ ~85 cycles 0.2 C	[136]
	DLC (COF/polymer)	1.7×10^{-4}	0.85	>4.5	Li|DLC|LFP	2.8–3.8 V, 122, 90.2%@130 cycles 0.5 C	[132]
	COF/Kevlar (COF/polymer)	1.6×10^{-4} ^	0.32	4.2	Li|SSE|LFP	2.5–3.8 V, 129, 84.4%@300 cycles 0.2 C	[387]
	DMTHA-Si-Li/p(BVIm-TFSI) (COFs/polymer)	1.5×10^{-3}	0.80	5.1	Li| DMTHA-Si-Li/p(BVIm-TFSI)|LFP	2.5–4.0 V, 141.5, 87%@800 cycles 1 C	[103]

*σ measured at ^30 °C and #60°C. Note that the σ in refs. [93] and [326] were measured at 80 and 40 °C, respectively. Otherwise at or near r.t. The initial capacity in ref. [273] referred to areal capacity, which is measured in mAh cm^{-2}; LCO@LNO in ref. [284] indicates LiNbO*x*-coated LCO; The value "154.6" in ref. [337] represents the highest discharge capacity achieved during the cycling test.

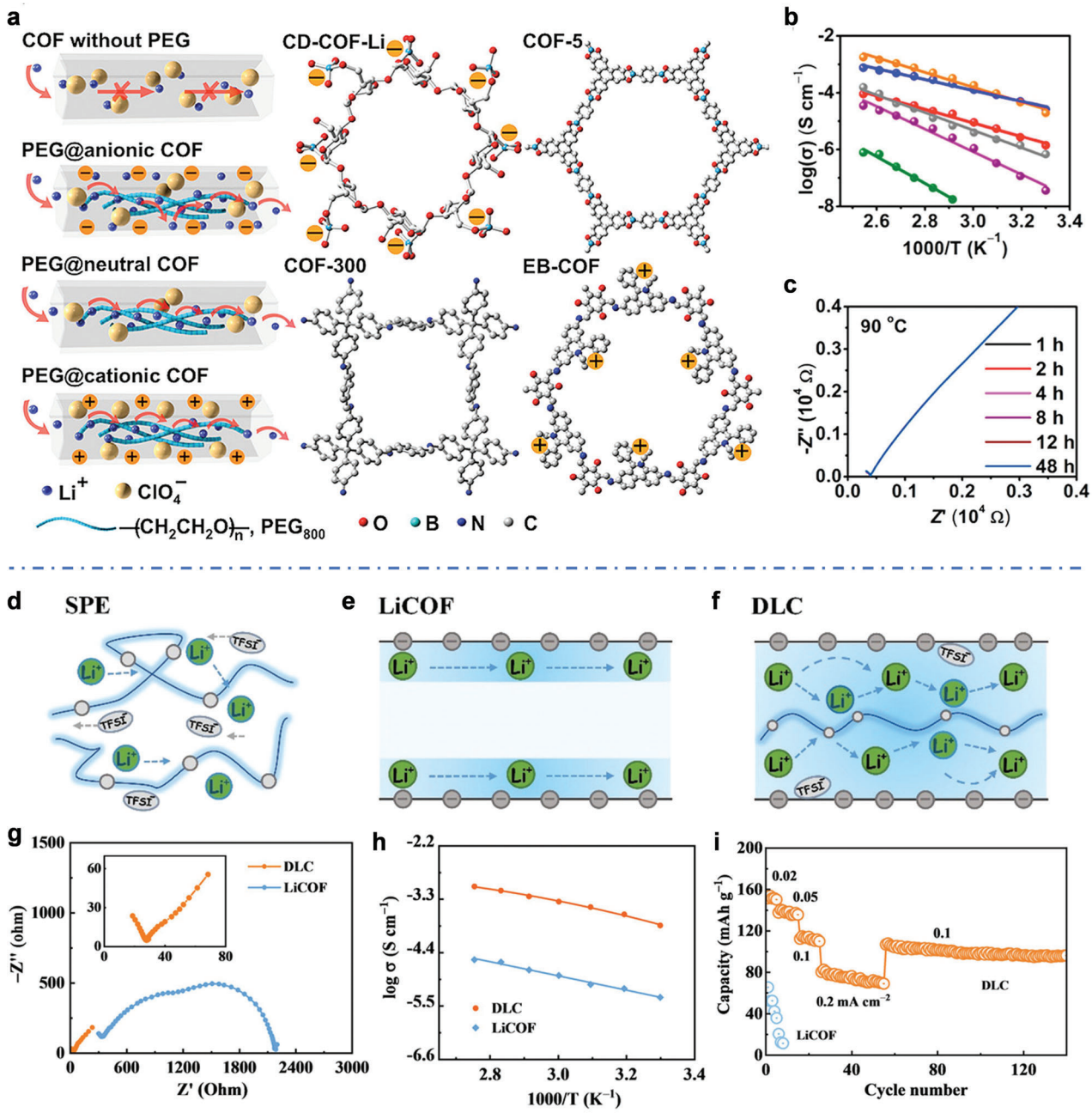

Figure 26. Representative COFs composite SSEs. a–c) COFs/PEG composites. a) The schematic illustrations of Li^+ transport in COFs/PEG composite SSE. b) Arrhenius plots of the σ of the COFs/PEG composite SSEs. σ of PEG-Li^+@EB-COF-ClO_4, PEG-Li^+@CD-COF-Li, PEG-Li^+@COF-300, PEG/Li^+@EB-COF-ClO_4, PEG-Li^+@COF-5, and Li^+@CD-COF-Li are shown in orange, blue, red, gray, purple, and green dots and lines, respectively. c) The stability of the impedance spectrum of PEGLi^+@EB-COF-ClO_4 at 90 °C for 48 h. Reproduced with permission.[139] Copyright 2019, American Chemical Society. d–i) DMA@LiTFSI-mediated COFs (DLC). d–f) Illustration of Li^+ transport in conventional solid polymer electrolytes (denote as SPE), sulfonate iCOFs (denoted as LiCOF), and DLC, respectively. g) The Nyquist plots of EIS measurements of the DLC and LiCOF SSEs at r.t. h) Arrhenius plots of the σ of LiCOF and DLC SSEs. i) Rate performance of the Li|DLC|LFP cells utilizing the LiCOF and DLC SSEs at 45 °C. Reproduced with permission.[132] Copyright 2022, Wiley-VCH.

Zou et al. introduced an SSE configuration that features ceramic materials $Li_{1.5}Al_{0.5}Ti_{1.5}(PO_4)_3$, LiV_3O_8, and $Li_4Ti_5O_{12}$ positioned between two solid electronic separators.[389] This arrangement effectively shields the ionic conductors using materials that are ionic-conductive yet electronic-insulative. As a result, the design demonstrated an impressive capacity retention of 87% after 400 cycles in full cells containing $LiNi_{0.8}Mn_{0.1}Co_{0.1}O_2$ cathodes. Peng et al. highlighted the promise of $Li_{0.95}Na_{0.05}FePO_4$ as a highly effective SSE owing to its excellent σ and stability in conjunction with Li metal anodes.[390] They developed composite SSE

based on $Li_{0.95}Na_{0.05}FePO_4$ to improve electronic insulation and enhance interfacial stability. The composite SSE containing 50 wt% $Li_{0.95}Na_{0.05}FePO_4$ displayed a σ of 3.6×10^{-4} S cm^{-1} at 25 °C and exhibited favorable compatibility with both Li metal anodes and cathodes. Additionally, spinel $Li_4Ti_5O_{12}$ was incorporated into PVDF to develop a composite solid electrolyte for the first time.[391] The resulting membrane, which comprised 80 wt% $Li_4Ti_5O_{12}$, exhibited an impressive σ of 2.9×10^{-4} S cm^{-1} at 35 °C, while also effectively preventing electronic conduction. Researchers can customize the electrochemical properties of these composites by choosing specific polymers and active materials, enabling them to fulfill specific application requirements, including enhanced interfacial stability, high energy density, and rapid charging capabilities.

4. Outlook: Toward Balanced and Improved SSEs for LMBs

This section discusses the failure mechanisms encountered in ASSLMBs, stemming from charge transfer issues at the interface between the electrolyte and electrode. We identify and explore the four primary types of failure: electric, mechanical, chemical, and electrochemical. We delve into these failure types through representative case studies to provide a comprehensive understanding. In addition, we discussed the impact of cathode degradation on the performance of ASSLMB cells. Given the growing research interest in comprehending the electrode|electrolyte interface issues in ASSLMBs, we also show how advanced characterization techniques can shed light on these failure mechanisms. Furthermore, we present solutions to prevent those failures, from the perspective of SSEs. These solutions entail the development of SSEs with high mechanical strength, and σ and t_{Li^+} to suppress the growth of Li dendrites, exceptional chemical stability, and a wide ESW for sustained cell capacity by preventing oxidation during charge and discharge processes. Additionally, we examined the critical challenges associated with SSEs for LMBs, including the reversibility of Li plating/stripping during cycling, as well as the risk of thermal runaway. Moving forward, we shift our attention to the potential of composite SSEs with balanced properties, aiming to achieve high-safety, high-energy-density, and cycling stability in ASSLMBs. We approach this topic comprehensively, considering materials design, battery device integration, and practical applicability. We conduct an in-depth analysis of the accomplishments and challenges associated with current composite SSEs, while offering potential solutions for addressing these challenges. Lastly, we emphasize the importance of computational studies in understanding the intricate link between SSE properties and structural design, thereby achieving SSEs with balanced characteristics. We investigate a variety of computational methods, including density functional theory (DFT), molecular dynamics (MD), and machine learning (ML). Notable examples of their applications in SSE research are showcased. While we highlight the challenges associated with employing computational techniques to analyze composite SSEs, we also delve into the promising potential of ML algorithms in overcoming these obstacles. Finally, we broaden our discussion to encompass the potential and challenges of SSEs for ASS Li–S and lithium–oxygen (Li–O_2) batteries.

4.1. Failure Mechanisms and Solutions

We emphasize the significance of understanding the failure mechanisms in achieving high-energy-density and high-safety in ASSLMBs. The failure processes related to the electrode|electrolyte interface can be categorized into four types: mechanical, electric, electrochemical, and chemical failures (**Figure 27**).[392] Here, we analyze the causes behind the four types of failure and discuss potential solutions. Furthermore, we relate advanced in situ and ex situ characterization techniques to those failures to better understand the mechanisms and explore effective solutions.

Mechanical failures in active ASSLMBs occur due to volume expansion of the Li anode during plating and contraction during stripping processes. These volume changes cause fluctuations and instability at the interfaces between the Li anode and SSE, potentially resulting in contact loss or delamination at the electrode|electrolyte interface.[392,393] The interface experiences volumetric changes resulting from Li deposition and dissolution, which cannot be absorbed or mitigated by SSEs. Instead, these changes are spatially confined by the interfacial contact between the anode materials and the SSEs. Consequently, a substantial amount of stress is generated, posing the risk of mechanical damage to the interface.[394–396] Furthermore, The significant volume expansion during Li plating can induce the formation of additional cracks, thereby hastening the pulverization of Li.[397] The initiation of cracks near the plated Li anode is primarily attributed to the locally concentrated stress field generated by the electroplating of Li within interfacial defects.[398,399] These defects, such as voids, impurities, and high roughness, are commonly found on the surface of SSEs as a result of manufacturing processes and cyclic plating/stripping.[400,401] Voids present in SSEs, including oxides, sulfides, MOFs, COFs, and their composites, are known to have significant contact resistance among SSEs and high contact resistance at the electrode|electrolyte interfaces. This, in turn, hinders the transport of Li^+, destabilizes the interface, and poses a potential risk for battery failure. To enhance the Li^+ transport within SSEs and improve interface stability, reducing voids in SSEs and at the interface is an efficient approach. Addressing these issues makes it possible to enable the development of high-performance ALLMBs. This topic is extensively discussed in "Section 2.2 Interfacial contact". During the electrodeposition of Li at the interface between the Li anode and SSE, the interfacial defects are initially filled owing to their capacity to enhance Li nucleation and facilitate a high local Li^+ flux. Upon filling these defects with deposited Li, even a minor overpotential during subsequent plating can generate substantial mechanical stress, leading to Griffith-like cracks within the SSEs.[402–404] Huang's group introduced an innovative experimental setup, integrating an in situ atomic force microscope and an environmental TEM, to study the real-time growth of individual Li whiskers (primary morphologies of Li dendrites) and measure their stress levels.[405] They observed a remarkable growth stress of Li dendrites, reaching up to 130 MPa, significantly surpassing the stresses observed in bulk Li. Furthermore, the measured yield strength of Li whiskers reached an impressive value of 244 MPa. These findings offer important quantitative benchmarks for developing strategies to suppress Li dendrite growth in ASSLMBs. The chemo-mechanical model proposed by Chiang's

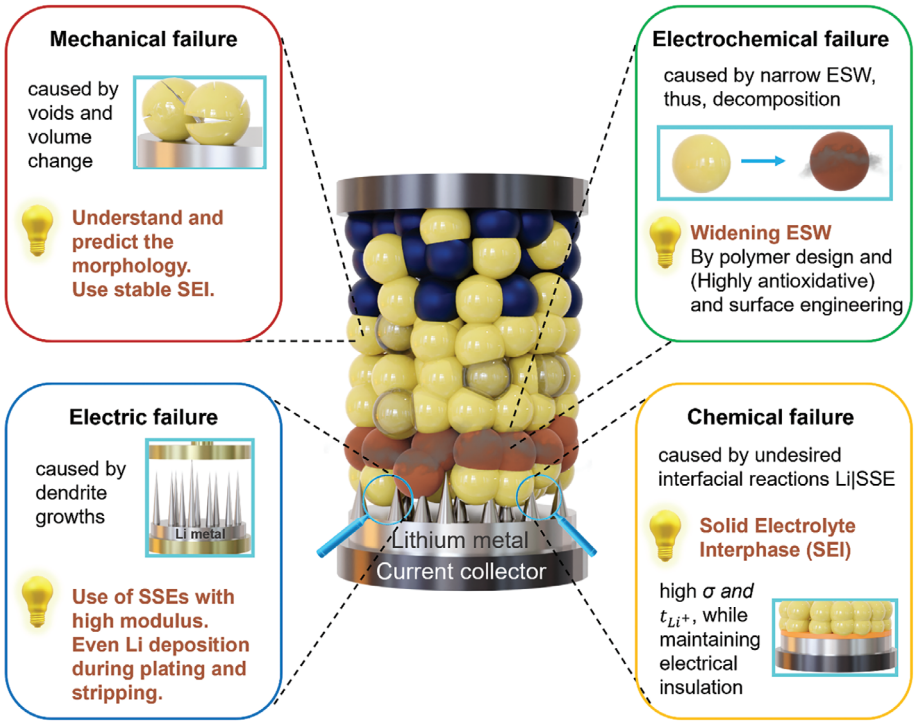

Figure 27. Four failure mechanisms in ASSLMBs and SSE designs to avoid these failures. The failures experienced by ASSLMBs can be categorized into four types based on their mechanisms: mechanical, electric, electrochemical, and chemical failures. To address these failures, various solutions regarding the SSE perspective are available, ranging from materials design and structure design to surface chemistry and surface engineering.

group was formulated to assess the stresses arising in a sharp flaw during the electrodeposition of Li metal.[215] This model enables the understanding of Li metal propagation in brittle ceramic SSEs, such as LPS and LLZTO, across a wide range of surface conditions, encompassing polished single crystals and polycrystals with microscopic pores and grain boundaries. The findings of the study revealed that the dominant failure mechanism in brittle SSEs exhibits characteristics akin to Griffith-like behavior. In 2023, Xiong et al. developed a modified electro-chemo-mechanical model by incorporating the Butler-Volmer equation and damage mechanics.[406] This model provides a deeper understanding of the mechanical failure mechanisms in SSEs and sheds light on the interplay between interfacial defect geometry, internal defect quantity, and position. The study highlights that stress-induced damage originates from the top of interfacial defects, and internal voids influence its propagation. These voids play a secondary regulatory role by directing the damage pathway and acting as internal sources within the SSEs. For example, by employing multiphysics simulation, Liu et al. examined the electro-chemo-mechanical failure of LAGP SSE caused by the continuous electrodeposition of Li within interfacial defects.[407]

To address the mechanical failure issues caused by Li metal electrodeposition at interfacial and internal defects, several strategies have been developed.[408,409] These strategies include interfacial modification techniques, such as fine polishing, which helps improve the interface between the electrode and electrolyte. Additionally, improved manufacturing processes have been implemented to prevent internal defects within the SSEs. These strategies aim to enhance the structural integrity and performance of SSEs, thereby mitigating the risk of mechanical failure. For example, Botros et al. utilized field-assisted sintering technology to achieve a theoretical density of 93% and fine-grained structure in an LLZO SSE.[410] The resulting stable Li|LLZO interface enabled stable operation of a Li|LLZO|Li symmetric cell for more than 100 h at a maximum current density of 0.049 mA cm^{-2}. Additionally, the reactivity of the Li anode towards SSEs significantly impacts the mechanical degradation of the ASSLMBs. The formation and evolution of the interphase layer between Li and SSEs plays a crucial role. During interphase growth, Li insertion and interfacial transformation cause volumetric expansion and internal stress within SSEs, leading to mechanical damage and increased resistance.[411] The properties of the chemically or electrochemically formed interphase also affect mechanical integrity. SSEs that chemically react with Li metal to form mixed ionic-electronic conducting interphases are prone to mechanical degradation, disabling batteries during cyclic charging and discharging process.[402] Kang's group discovered that LAGP undergoes a chemical reaction with Li metal, forming an interphase comprising stoichiometrically modified LAGP and Li-related oxides (such as Li_2CO_3) that act as a mixed ionic-electronic conductor, with electronic conductivity being dominant.[412] The mechanical integrity of the LAGP SSE is significantly affected by the chemically formed interphase, causing the pulverization of LAGP pellets and the repeated formation of microcracks on the interphase side. Moreover, the electrochemical reactions that occur with the chemically formed interphase during cell operation can further deteriorate the mechanical properties of the SSE, ultimately resulting in cell failure. By manipulating the properties of SSEs to

create stable artificial interphases, it is possible to prevent the accumulation of stress and reduce mechanical failures in cells.[413]

Researchers have utilized advanced characterization techniques to study and understand these mechanical failure mechanisms. For instance, Sun et al. employed in situ and in operando synchrotron X-ray tomography to record the morphological and compositional evolution of the electrode/electrolyte interface during battery cycling.[414] The electrolyte investigated in their work is sulfide-type $Li_{10}SnP_2S_{12}$. Similarly, McDowell's group utilized in situ X-ray computed tomography to investigate the evolution of mechanical damage in SSEs of LAGP type resulting from interphase growth during the charge/discharge cycles of the battery.[415] These advanced characterization techniques provide valuable insights into the morphological and compositional changes occurring at the electrode|electrolyte interface during battery operation. Thus, to achieve mechanical stability, it is crucial to implement comprehensive protective strategies such as incorporating soft interlayers and ensuring the SSEs are free from surface defects. These strategies enable stress relaxation and contribute to maintaining the mechanical integrity of the system.[392] Additionally, the utilization of advanced characterization techniques contributes to the development of durable interfaces, effectively mitigating mechanical failures in ASSLMBs. These efforts collectively facilitate the design of more robust and reliable battery systems.

Electric failure primarily pertains to the Li^+ plating and stripping process, which is closely linked to the electrical characteristics of the LMBs. Major consequence of this electric failure is the occurrence of short circuits caused by the Li dendrite growth.[416] Based on the Monroe and Newman model, the growth of dendrites can be theoretically suppressed if the shear modulus of SSEs exceeds 1.8 times the shear modulus of Li metal, which is ≈2–4 GPa.[203,204] However, among the various SSE types, polymer SSEs exhibit limited capability in inhibiting the penetration of Li dendrites within the SSEs due to their low shear modulus, even at low current densities. For instance, when using PEO SSEs, a Li|PEO/LiTFSI|Li symmetric cell experienced a short circuit within 68 h of cycling under a current density of 0.2 mA cm^{-2} and a capacity of 0.1 mAh cm^{-2}.[155] Polymers usually have stronger mechanical properties when they have higher molecular weight.[417] However, the ideal direction of suppressing dendrites using polymer-based SSEs is to make a composite with mechanically strong fillers.[418] An illustrative example is the work of Luo's group, where they reported a PEO-based SSE, incorporating 2D vermiculite sheets with a high Young's modulus of 175 GPa, thus having a significantly higher tensile modulus of 13.1 MPa compared to the 6.8 MPa of regular PEO SSE.[419] The Li|SSE|Li symmetric cell employing the vermiculite-modified PEO SSE exhibited stable Li plating/stripping behavior without short-circuiting over an extended operation period of more than 60 days at a current density of 0.05 mA cm^{-2}. The increased tensile modulus played a crucial role in delaying the nucleation of Li dendrites, ultimately enhancing the SSE's ability to impede the growth of Li dendrites.[420,421] Indeed, inorganic ceramics, MOFs, and COFs, and their composites, having high mechanical strength, are preferred to prevent electric failures. As an example, the garnet-type LLZO has been theoretically predicted to be highly effective in preventing the formation of Li dendrites. This is primarily due to its exceptional shear modulus of ≈55 GPa and an extremely high t_{Li^+} of unity.[422,423] Wu's group presented a single-ion MOFs-based SSE developed by integrating flexible anionic chains within static rigid porous frameworks.[424] This MOFs-based SSE demonstrated an impressive Young's modulus of 14.5 GPa, highlighting its significant potential in effectively preventing the formation of Li dendrites. COF-5, a pioneering example of COFs, was synthesized by the co-condensation reaction of 1,4-benzenediboronic acid and 2,3,6,7,10,11-hexahydroxytriphenylene.[222] COF-5 displays a remarkable Young's modulus within the range of 15 to 20 GPa. This substantial mechanical strength enables COF-5 to effectively hinder the growth of Li dendrites. Composite method has proven to be effective in enhancing the mechanical properties of soft polymers while maintaining good interfacial contact between SSEs and electrodes. Fan et al. reported the development of a ceramic/polymer SSE by combining bulk LLZTO with PEO.[425] This SSE exhibited an exceptionally high average Young's modulus of 75.5 GPa, indicating its superior mechanical strength. It is expected that this ceramic/polymer SSE can prevent the formation of Li dendrites.

Besides simply increasing modulus of the SSEs, having even Li deposition at the interfaces between Li and SSEs, as well as retarding dendrite growth speed, can also prevent electric failures.[215,104] Surprisingly, this phenomenon occurs regardless of the SSE's shear modulus.[426] The non-uniform Li|SSE interface promotes Li dendrite formation due to the localized high current density and concentrated electric field at Li protrusions.[422,427] Consequently, during subsequent charging, Li selectively accumulates at these specific locations. For example, impurity particles or defects at the Li|SSE interface in polymer SSEs act as critical sites for the Li dendrite deposition.[428,429] In garnet-type or certain sulfide SSEs, dendrite growth occurs at grain boundaries, voids, pores, and cracks.[215] Unexpectedly, Li dendrites can still form at polished Li|SSE interfaces, altered grain boundaries, and single-crystalline SSE surfaces. The inhomogeneous Li|SSE interface alone cannot fully explain Li dendrite growth. SSEs with high electrical conductivity facilitate to Li dendrite growth in grains and grain boundaries.[430] High electronic conductivity, as demonstrated by Wang's group, leads to dendrite formation in representative oxide-type LLZO and sulfide-type LPS SSEs.[431] Therefore, designing SSEs with minimal electronic conductivity is an effective strategy to mitigate the formation of metallic Li dendrites. The mechanism of Li dendrites at the Li|SSE interface requires further investigation.

State-of-the-art characterization techniques, including a range of in situ imaging techniques, are crucial for understanding the mechanisms of Li dendrite formation and growth. These techniques include in situ optical-based imaging techniques such as optical microscopy and Raman spectroscopy, as well as electron-based imaging techniques, including scanning electron microscopy (SEM), transmission electron microscopy (TEM), and cryo-electron microscopy (cryo-EM).[432] Among these techniques, in situ optical microscopy is widely utilized due to its accessibility and ability to observe dendrite growth in real-time. However, when compared to in situ optical microscopy, in situ SEM offers significantly higher spatial resolution, making it particularly suitable for studying the intricacies of Li dendrite growth. By employing in situ SEM, researchers can directly visualize Li dendrites' nucleation, growth, and morphological

evolution at a highly detailed level. This technique facilitates the observation of dendrite formation, identification of potential failure mechanisms, and exploration of the effects of various parameters on dendrite growth, such as current density, temperature, and electrolyte composition.[433] For instance, in a notable example from 2021, Lu's group employed in situ optical microscopy in combination with cryo-TEM to observe the nucleation and growth of Li inside LPS SSE.[434] Based on their findings, they proposed that the formation of Li dendrites within the SSE, causing cracking and failure, precedes the dendrite formation at the Li|SSE interface. These advanced characterization techniques enable a comprehensive understanding of battery failure mechanisms resulting from Li dendrite growth. This knowledge plays a crucial role in the design and development of SSEs for high-performance ASSLMBs.

Electrochemical failure is observed when SSEs cannot withstand higher voltages due to their limited ESWs. Additionally, unexpected reactions between the cathode and SSE can result in the formation of new interphases, negatively impacting battery performance or even leading to battery failure. Besides them, various factors, including electrode degradation, electrolyte decomposition, and interface instability, can cause electrochemical failure in ASSLMBs.[435] For example, Zhang's group showed that the redox decomposition of $Li_7P_3S_{11}$ and the subsequent formation of irreversible side products, including Li_2S and S, can contribute to the charge resistance at the interface.[436] The redox reactions of LPS took place over a wide electrochemical window of 0.5–3.5 V (vs Li^+/Li), generating a number of side products. As decomposition products are generated and accumulated, the interfacial resistance increased, and the polarization effect intensified. This led to the formation of an insulative layer at the electrode|electrolyte interface, causing a rapid decline in capacity. Another notable instance is the research conducted by Chiang's group, which explored the redox behavior of β-LPS SSE across a wide voltage range of 0–5.0 V (vs Li^+/Li).[437] During electrochemical oxidation, β-LPS underwent an irreversible decomposition process, resulting in the formation of an interphase rich in oxidized sulfur species, including P_2S_5. The irreversibility of this reaction was due to the electronically insulating characteristic of the resulting reaction products. Conversely, electrochemical reduction of β-LPS led to decomposition into components where both sulfur and phosphorus undergo reduction, with the overall extent of the reaction being several times greater than that observed during oxidation. Notably, the interphase formed during reduction stands out for its reversibility, distinguishing it from the interphase formed during oxidation. These findings provided valuable insights into the underlying reasons for the higher impedance encountered at the SSE|cathode interface in ASSLMBs utilizing β-LPS-based SSEs. To effectively mitigate electrochemical failure in ASSLMBs, a notable approach is to enhance the electrochemical stability of SSEs by incorporating them into composites. These composites offer wide ESWs while maintaining high σ, enabling stable electrode|electrolyte interfaces. For example, Hu's group reported on an oxide/polymer composite SSE consisting of 3D garnet-type $Li_{6.4}La_3Zr_2Al_{0.2}O_{12}$ nanofiber fillers embedded in a PEO matrix.[184] This composite demonstrated an impressive electrochemical window of 0–6 V (vs. Li^+/Li) while maintaining a high σ of 2.5×10^{-4} S cm^{-1} at r.t. The combination of a wide ESW, high σ, inhibition of Li dendrites growth, and a stable Li|SSE interface enabled the Li|SSE|Li symmetric cell to exhibit stable Li stripping/plating. Specifically, the cell exhibited stable Li stripping/plating for a duration of 500 h at a current density of 0.2 mA cm^{-2} and over 300 h at a current density of 0.5 mA cm^{-2} at r.t. Another strategy involves designing SSEs with a multilayered structure to enhance the ESW and address interfacial instability issues. For instance, Guo's group reported a multilayered SSE composed of LAGP, antioxidative PAN, and reduction-tolerant PEGDA.[183] This SSE exhibited a wide electrochemical window of 0–5 V (vs Li^+/Li) while maintaining a σ of 3.7×10^{-4} S cm^{-1} at r.t. During the assembly of the Li|SSE|NCM811 configuration, the use of PAN in contact with the cathode and PEGDA in contact with the Li metal ensures stable electrode|electrolyte interfaces, thus preventing side reactions that could arise from direct contact between LAGP and the Li anode. This design facilitates fast Li^+ transport and takes advantage of the wide ESW of the SSE. Consequently, the cell demonstrates exceptional cycling performance at 0.2 C with a remarkable initial capacity of 184 mA h g^{-1} and an impressive capacity retention of 94.4% after 175 cycles. As discussed earlier, PCPs, such as COFs-based materials, have emerged as promising candidates for SSEs in ASSLMBs, offering wide ESW exceeding 5.0 V (vs. Li+/Li). For example, a holistically oriented quinolyl-linked COFs film exhibited an impressive ESW of up to 5.6 V (vs. Li^+/Li), along with a σ of 1.5×10^{-4} S cm^{-1} at 60 °C and excellent mechanical strength characterized by a Young's modulus of 10.5 GPa.[181] These findings demonstrate the significant potential of COFs-based SSEs for high-energy-density ASSLMBs when combined with suitable cathode materials. However, further research is needed to thoroughly investigate the solid-solid Li|PCPs interface, which holds promise as a crucial research direction for next-generation ASSLMBs.

Chemical failure can occur when undesired interfacial reactions between the electrode and electrolyte materials happen. This is particularly relevant as Li anode exhibit high reactivity with the most SSEs.[438] The chemically formed interphase layer between SSE and Li metal plays a critical role in the performance of ASSLMBs. The desired interphase layer is thermodynamically stable, exhibits high σ, and is electronically insulating.[439] Such an interphase layer can reduce the decomposition of SSEs and facilitate rapid Li^+ transport, enabling batteries with high-energy-density and long lifespan during practical operations. However, attaining a stable interphase possessing both high σ and electronic insulation proves challenging for most SSEs, primarily because the strong thermodynamic driving force compels Li metal to undergo reactions with the SSEs.[392] The formation of an interphase at the interface between Li anode and SSE, which exhibits negligible electrical conductivity but low σ, leads to slow Li^+ transport and increased interface resistance. This, in turn, negatively impacts the performance of the cell, including cycling stability. For example. Wenzel et al. investigated the interaction between phosphorus-based sulfide SSEs such as argyrodite Li_6PS_5X (X = Cl, Br, and I) and Li metal.[440] A combination of experimental and theoretical calculations confirmed the formation of decomposition products, including Li_2S, Li_3P, and LiX (X = Cl, Br, and I). These decomposition products are insulating materials that exhibit relative stability when in contact with Li metal, enabling the interphase to self-passivate. However, the drawback of these materials is their low σ, leading to increased interfacial resistance. This higher resistance can

have a detrimental impact on the overall performance of the cell. By investigating the Li|Li_6PS_5Cl interface using quantum mechanics-based reactive molecular dynamics, Cheng et al. observed its instability and rapid decomposition, leading to the formation of multiple phases.[441] The resulting decomposition products, including Li_3P, Li_2S, LiCl, and potentially LiP, exhibit significantly lower σ than the original Li_6PS_5Cl. This decrease in σ adversely affects the transport properties of the entire system. Consequently, the cell performance is compromised, and in some cases, it can lead to failure. To address these issues, a promising approach to improving stability is constructing a multifunctional layer at the Li|SSE interface that exhibits high σ while maintaining electrical insulation. Li's group introduced a nanostructured lithium fluoride (LiF) and lithium–zinc (Li–Zn) alloy component (referred to as LiF@Li–Zn) between LAGP SSE and Li using in-situ conversion reactions.[442] This nano layer possesses electrical insulation properties while retaining high σ. The incorporation of the multifunctional layer at the Li|LAGP interface not only promotes stability but also reduces interface resistance. Moreover, it effectively mitigates side reactions that arise from the intrinsic instability of LAGP when in contact with metallic Li. This multifunctional layer enables Li|LAGP|Li symmetric cells to exhibit stable Li plating/stripping behavior for more than 1,000 h at a current density of 0.1 mA cm^{-2}. Additionally, these cells demonstrate superior cycling performance, even when subjected to a remarkable current density of 0.5 mA cm^{-2}.

In addition, the presence of mixed ionic-electronic conducting interphases at the Li|SSE interface can lead to the rapid decomposition of the SSE, ultimately resulting in cell failure. These mixed interphases are characterized by their ability to facilitate both ionic and electronic charge transfer across the interface. Highly ionic conductive SSEs, such as NASICON-type LAGP, perovskite-type LLTO, and sulfide-type LGPS, are known to exhibit such mixed interphases.[443] As an example, the LGPS undergoes decomposition upon contact with Li metal, primarily due to its favorable decomposition energy of −1.2 eV per atom.[165] The predicted decomposition products are Li_2S, Li_3P, and Li–Ge alloys. Li_2S is an insulator, Li_3P is an ionic conductor, and Li-Ge alloys act as electronic conductors.[444] The existence of Li–Ge phases increased in local electronic conductivity, causing continuous degradation of the LGPS surface. This degradation process results in an increase in cell resistance and a decrease in cell cyclability, ultimately affecting the overall performance of the cell. To address this issue, a viable solution is to incorporate a thin and stable barrier layer between the reactive SSE and the Li metal in ASSLMBs. This barrier layer should possess high σ, excellent electronic insulation, thermodynamic stability with both Li metal and SEs, and mechanical ductility for effective Li|SSE contact. The barrier layer effectively prevents undesirable side reactions by satisfying these requirements while maintaining the SE's high σ.[63] In a study by Zhang et al., a chemically stable interface was achieved by applying a protective layer of LiH_2PO_4 on the Li metal surface using an in situ approach.[445] This interface re-engineering strategy effectively prevents the migration of mixed ionic-electronic reactants into the LGPS and improves the kinetics of reactions at the interface. The incorporation of the LiH_2PO_4 protective layer enables a stable Li|LGPS interface. As a result, the Li|LGPS|Li symmetric cell exhibited stable operation for over 950 h at a current density of 0.1 mA cm^{-2}, with a consistently low overpotential of 50 mV. Additionally, the Li|LGPS|LCO cell demonstrated an initial discharge capacity of 131.1 mAh g^{-1} and a capacity retention of 86.7% over 500 cycles at a rate of 0.1 C. These results highlight the effectiveness of the protective layer in improving the stability of Li|SSE interface and the performance of ASSLMBs. Indeed, the "building barrier layer" strategy can also be applied to LMBs equipped with liquid electrolytes. Our group utilized a silicate COFs as SEI for LMBs.[163] The COFs protective layer formed on the surface of the Li metal anode served dual purposes: facilitating rapid transport of Li^+ while effectively suppressing dendrite formation. By implementing this strategy, the LMB cell equipped with a LCO cathode achieved an impressive maximum reversible capacity of 188 mAh g^{-1} at a rate of 0.25 C. Moreover, the cell exhibited exceptional cycling stability, with a capacity decrease of less than 3% over the course of 100 cycles.

Advanced characterization techniques are crucial in acquiring a deeper understanding of and mitigating these chemical failure mechanisms. For example, Wenzel et al. conducted in situ X-ray photoelectron spectroscopy and time-resolved electrochemical measurements to understand the chemical reactions occurring at the interface between the LGPS SSE and Li metal anode.[444] These techniques allowed for a detailed examination of the chemical reaction processes at the Li|LGPS interface and provided valuable insights into the mechanisms involved. With the aid of these characterization techniques, the researchers confirmed that the predicted decomposition products at the interface indeed consist of Li_2S, Li_3P, and Li–Ge alloys, aligning with the theoretical calculations. Our group employed in situ OM to observe the growth of Li dendrites. Through the utilization of in situ OM, we acquired valuable insights into the complex growth patterns and features of Li dendrites throughout various battery operating stages. This comprehensive understanding enabled us to identify potential methods to mitigate dendrite formation and enhance the overall performance of the LMBs.[163] In summary, achieving a stable Li|SSE interface is crucial to prevent chemical failures in active ASSLMBs during practical use. This requires the design of SSEs with high chemical stability and advanced structural features at the Li|SSE interface. Moreover, advanced characterization techniques and complementary methods such as electrochemical impedance spectroscopy and in situ measurements enable a comprehensive understanding of the chemical failure mechanisms in ASSLMBs. These techniques are vital in designing effective strategies to mitigate chemical degradation and enhance battery performance.[64,446,447] Characterization techniques are essential to gain a comprehensive understanding of the underlying mechanisms and develop effective strategies to mitigate electrochemical failure. These techniques provide valuable insights into the underlying processes and contribute to a more comprehensive understanding of battery performance and failure modes. Thus, interested readers are suggested to read the cited papers for further study.[63,448–451]

Cathode degradation significantly impacts cell performance, as the compatibility of suitable cathodes with Li metal anodes is crucial for enhancing the overall energy density of LMBs.[452,453] Understanding the mechanisms of cathode degradation is essential for designing high-performance ASSLMB systems. It is well established that cathode degradation in ASSLMBs significantly increases the interfacial resistance at the cathode|SSE

interface.[454] As this interfacial resistance rises, the transport of Li^+ at the cathode|SSE interface becomes impeded, leading to diminished electrochemical performance characterized by low Coulombic efficiency (CE) and reduced capacity. Ni-rich layered oxide cathodes with high Ni content ($LiNi_xMn_yCo_{1-x-y}O_2$, x>0.8) are particularly promising due to their high specific capacity, exceeding 200 mAh g^{-1}.[390,455] Park et al. explored the mechanisms underlying capacity decay in Ni-rich cathodes, placing particular emphasis on the internal particle structure.[456] They discovered that the primary cause of deterioration in these cathodes was mechanical degradation associated with the formation of microcracks. This mechanical failure not only contributed to additional chemical and structural degradation but also heightened the susceptibility of the internal areas of the secondary particles to electrolyte attack. Therefore, safeguarding the internal structure of the particles from electrolyte attack by mitigating microcrack formation is an effective strategy for ensuring the practical use of high-energy Ni-rich cathodes with long-term stability.

The fabrication of composite cathodes, often referred to as catholytes, which consist of active materials and SSEs, is an effective and widely adopted approach to reduce interfacial resistance between the cathode and SSEs.[457] The degradation of composite cathodes is more complex due to the electrochemical-mechanical coupling failure mechanisms involved.[458] For example, Yuan et al. proposed a 3D electrochemical–mechanical coupled model to study the failure mechanism of the composite cathode went through the electrochemical and physics processes.[459] The irregular distribution of primary particles within the NCM111 secondary particle induces anisotropic Li diffusion and variations in volume. Consequently, this leads to substantial nonuniformity Li concentration and stress distributions, especially at the boundaries of the primary particles, ultimately resulting in the development of internal cracks within the particles. When equipped with LLZO SSE, the cell experiences capacity decay due to increased interfacial resistance resulting from lamination, which occurs as the particle volume shrinks under the constraints imposed by the rigid structure.

Advanced characterization tools are essential for gaining insights into the mechanisms of cathode degradation.[460,461] For example, Meng's group conducted a study utilizing a combination of multiscale imaging analysis and computational modeling to explore the degradation mechanisms of the NCM811 cathodes during cycling.[462] They showcased the effectiveness of plasma-focused ion beam-scanning electron microscopy technology for achieving 3D imaging and quantitative analysis of the NCM811 cathodes. The data obtained from this imaging technique serves as a foundation for conducting relevant statistical analyses and developing computational models. By integrating these models, the research provides valuable quantitative insights into how the structure of the thick electrode evolves during the cycling process.

4.2. Li Plating/Stripping Coulombic Efficiency in SSEs

Typically, attaining high Li plating/stripping CE continues to be a challenge in SSEs. Li plating/stripping CE is influenced by the loss of Li at the negative electrode during each cycle, which primarily arises from two sources: Li^+ trapped in the SEI and the presence of "dead Li".[416] By minimizing the loss of Li^+ within the SEI and reducing the quantity of dead Li, it is possible to enhance the CE of Li plating/stripping processes significantly. Several factors contribute to the low CE of Li plating/stripping in SSEs. In certain SSEs, limited σ impedes the movement of Li^+, adversely affecting the reversibility of the plating and stripping processes. This limitation ultimately results in reduced CE. Furthermore, high interfacial resistance between the SSEs and the electrodes restricts the movement of Li^+ at the electrode|electrolyte interfaces. This restriction diminishes the reversibility of Li plating and stripping, further lowering the CE. In addition, the undesirable formation and growth of Li dendrites within SSEs generate "dead Li". The accumulation of "dead Li", resulting from irreversible stripping and plating processes during cycling, significantly decreases CE.[463] Therefore, preventing dendrite growth is critical for enhancing Li plating and stripping efficiency. It is widely recognized that the highly reactive nature of Li metal can result in ongoing reactions with organic liquid electrolytes, leading to the formation of a thick SEI during cycling.[464] This reaction not only consumes a significant amount of Li from the anode but also depletes the liquid electrolyte. Similarly, the chemical stability of SSEs is also a critical factor influencing the CE of Li plating/stripping. Chen et al. investigated a garnet-type oxide SSE, LLZTO, which exhibits notable stability in contact with Li metal.[465] Consequently, the ASSLMB cell utilizing an LFP cathode achieved an impressive initial CE of 96.80% at a rate of 0.1 C. This performance significantly surpasses the initial CE of 79.35% recorded for LMBs employing a liquid electrolyte (1 M $LiPF_6$ in a 1:1 v/v mixture of ethylene carbonate and dimethyl carbonate). Moreover, the electrochemical stability of SSEs significantly influences the CE of Li plating/stripping. For example, Zhang's group showed that the redox decomposition of $Li_7P_3S_{11}$ and the subsequent formation of irreversible side products, including Li_2S and S, can contribute to the charge resistance at the interface.[436] The redox reactions of $Li_7P_3S_{11}$ took place over a wide electrochemical window of 0.5–3.5 V (vs. Li^+/Li), generating several side products. As decomposition products are generated and accumulated, the interfacial resistance increases, and the polarization effect intensifies. This leads to the formation of an insulative layer at the electrode|electrolyte interface, causing a rapid decline in capacity. Additionally, impediments to Li^+ movement at the electrode|electrolyte interface adversely affect the reversibility of the plating/stripping processes, ultimately resulting in reduced Li plating/stripping CE.

4.3. Thermal Runaway of the ASSLMBs with SSEs

Although SSEs demonstrate greater intrinsic thermal stability compared to liquid electrolytes, ASSLMBs continue to face considerable safety challenges due to the potential for thermal runaway.[466–468] This risk becomes more pronounced as the energy density of LMBs increases.[469] Thermal runaway in ASSLMBs is primarily linked to the processes of heat generation and release, influenced by multiple factors. One significant concern is the decompose behavior of SSEs under high-temperature conditions. As temperatures rise, SSEs can decompose or melt, particularly in polymer-based electrolytes, which may lead to internal short circuits.[201] This short-circuiting not only generates heat but can also trigger thermal runaway in the battery

system. Furthermore, the decomposition products of certain electrolytes can react with Li metal, releasing heat and potentially flammable gases. For instance, when PEO decomposes, it produces byproducts such as alcohols and water that react with Li to generate hydrogen gas, increasing the risk of thermal runaway.[470] In the case of in situ polymerized PDOL SSE, thermal decomposition occurs at temperatures above 110 °C, releasing formaldehyde gas, which further enhances the threat of thermal runaway.[79] Sulfide-based SSEs also pose challenges due to their relative thermal instability compared to oxides.[471] For example, during the heating of Li_3PS_4, the formation of the $Li_4P_2S_6$ phase occurs, and sublimation of sulfur can be observed at ≈660 °C.[472] Such decomposition reactions can release heat and interact with Li metal, further contributing to the risk of thermal runaway in ASSLMBs.

In addition, undesirable side reactions between SSEs and electrodes can induce heat generation and gas production. These ongoing exothermic reactions lead to heat accumulation, which raises the temperature within the batteries.[466] Elevated temperatures, in turn, can accelerate the chemical interactions between the SSE and the electrodes, creating a feedback loop that exacerbates the situation. As a result, thermal runaway may occur when the rate of heat dissipation falls significantly short of the rate of heat generation. Although ceramic-based SSEs, such as sulfides, demonstrate comparatively high thermal stability and nonflammability, their limited chemical stability can still contribute to thermal runaway issues in LMBs.[467] For instance, Zhang's group explored the mechanisms underlying thermal runaway in ASSLMBs that utilize Li_6PS_5Cl SSEs.[473] They employed characterization techniques, including extended-volume accelerating rate calorimetry and differential scanning calorimetry. Their research identified that a passivation layer of LiCl forms through the reaction between the SSE and Li metal, which initially restricts any further reactions at 178 °C, thus preventing thermal runaway at 0% state-of-charge. However, the melting of Li compromises this passivation layer, facilitating ongoing reactions between the SSE and Li. This persistent chemical interaction results in heat accumulation, significantly increasing the risk of thermal runaway in ASSLMBs. Furthermore, the formation and growth of Li dendrites can lead to internal short circuits within ASSLMBs, resulting in heat generation and potential thermal runaway.[474,475] SSEs with high mechanical strength are expected to effectively inhibit dendrite growth. Recently, a single-crystal COF membrane was reported to have a Young's modulus of 73.4 ± 11.6 GPa,[223] demonstrating significant potential for COF-based materials in blocking dendrite formation due to their superior mechanical properties. Therefore, to mitigate the risk of thermal runaway in ASSLMBs, SSEs should possess certain characteristics, including high thermal stability, high chemical stability, wide ESWs, and effective suppression of Li dendrites. Additionally, the development of advanced detection tools can effectively monitor thermal runaway in ASSLMBs, thereby enhancing safety in practical applications.

4.4. Composite SSEs

To make SSEs with balanced properties in all aspects, the composite method, combining the advantages of high-performing fillers and flexible matrix, is the most practical and promising way. Although remarkable progress has been made on composite SSEs in LMBs, there is still a long way to go before practical industrial implementation. These challenges encompass various aspects, including materials design, integration into batteries, and adapting manufacturing processes to accommodate SSEs. It is crucial to pay greater attention to these bottlenecks and ensure compatibility with the existing mature battery production system, which is primarily based on liquid electrolytes. First, further efforts are required to improve the composite electrolytes' insufficient σ at r.t. The polymer matrix, which often takes the form of polymer–Li salts systems, in composite SSEs accounts for partial ion transport. It significantly lowers σ and ion transport kinetics of the bulk composite SSE.[476,477] The σ of polymer matrices and the transport behavior of the composite SSE determine whether the bulk σ can reach a value that meets the working requirements, 10^{-4} S cm^{-1}. Thus, designing polymer matrices with higher σ, embedding 3D continuous conductive ceramics, or nano-scale fillers with aligned Li^+ conductive channels in the composite SSE are promising directions.[478] Second, reducing the high interfacial reactivity and resistance deserves attention to enhance interfacial stability under battery operating conditions and ensure long-term cycling.[479] Although the high flexibility and processability of the polymer matrices contribute to the smooth contact at the interfaces, the rough surfaces of electrodes and most electrolytes still render a considerable issue.[480] For this, in situ polymerization, featuring the liquid precursor converted into solid polymer on the surface of both anode and cathode electrode, is regarded as a promising approach to achieve excellent interface contact.[78,481] Additionally, high reactivity of metallic Li may deteriorate the interfacial chemical stability by reacting with the residual solvents or protuberant inorganic ceramics fillers, e.g., sulfide and NASICON-type LAGP, which can cause side products at the interface and sluggish the carrier transport. Therefore, improving interface compatibility between electrode and electrolyte via modifying Li metal electrode or enhancing the intrinsic chemical stability of composite electrolytes is an effective strategy to ensure durable long-term battery cycling.[482] Finally, identifying the right balance between mechanical properties and electrochemical performance is also essential in commercializing composite SSEs. Composite SSEs with high thickness usually demonstrate high mechanical strength and enhanced processability, enabling the production of a large-area membrane.[483] However, large thicknesses will significantly increase the proportion of non-capacity components in batteries and sacrifice the high-energy density of solid-state LMBs. The commercial Celgard separator in the liquid electrolyte system is about 10 µm thick.[484] Unfortunately, composite SSEs with similar thickness show great challenges in large-scale production, and the mechanical strength is insufficient to withstand the external pressure required to maintain the operation of solid-state LMBs. Thus, it is necessary to reduce the thickness of the composite SSEs while improving their mechanical strength.

Such successfully developed SSEs with a σ and a wide ESW can be ideal next-generation SSEs for LMBs with a high-energy density that can be paired with high-voltage cathodes. When a cell's operating voltage exceeds the ESW of SSEs, it forms new interphases due to undesirable redox reactions between the electrodes and electrolyte. These interphases play a crucial role in

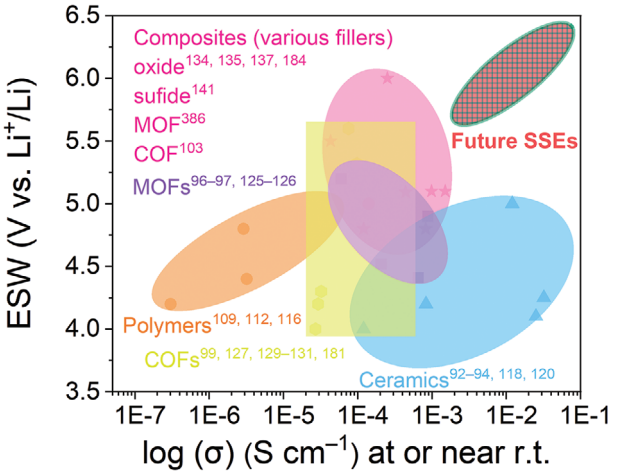

Figure 28. Comparison of the σ and ESWs (vs. Li^+/Li) of various SSEs, including conventional polymers,[109,112,116] ceramics,[92–94,118,120] MOFs,[96,97,125,126] COFs,[99,127,129–131,181] and composites.[103,134,135,137,141,184,386]

determining the cell's performance and stability. Here, we summarize a comparison of the σ and ESW (vs Li^+/Li) observed in a selection of representative composite SSEs and show the target area for the next-generation ASSLMBs that can endure highly demanding energy output. Other SSE types, including polymers, ceramics, MOFs, and COFs, were also evaluated for comparison (**Figure 28**). Polymer SSEs typically exhibit σ ranging from 10^{-7} to 10^{-4} S cm^{-1} at r.t., with ESWs typically in the 4.2–5.0 V (vs Li^+/Li). Among the various types of single SSEs, inorganic ceramics demonstrate the highest σ. For instance, sulfide-type SSEs exhibit σ in the range of 10^{-3} to 10^{-2} S cm^{-1} at r.t. However, the ESWs of most sulfides do not exceed 5.0 V (vs Li^+/Li). On the other hand, PCPs, including MOFs and COFs, exhibit σ in the range of 10^{-5} to 10^{-4} S cm^{-1} at r.t., while maintaining wide ESWs ranging from 4.0 V to 5.6 V (vs Li^+/Li). Composite SSEs, composed of different types of fillers (such as oxides, sulfides, MOFs, and COFs) embedded in a polymer matrix, offer a wide range of σ varying from 10^{-5} to 10^{-3} S cm^{-1} at r.t., with the majority falling within the range of 10^{-4}–10^{-3} S cm^{-1}. These composites also have exceptional ESWs ranging from 4.8 to 6.0 V (vs Li^+/Li), providing a desirable balance between conductivity and stability for SSE applications. Moreover, we highlight the performance targets that future SSEs should aim to achieve to endure the demanding environments of high-energy-density batteries. Overall, composite SSEs offer a balanced and high-performing combination of σ and electrochemical stability.

4.5. Computational Study

When designing composite SSEs with desired properties, an essential prerequisite is understanding the ion transport mechanisms thoroughly; however, the modes of ion motions and their associated pathways in composite SSEs are still under debate.[485] Specifically, the complexity of composite SSE systems may arise from the multi-phase interactions near boundaries and space charge redistributions at the interfaces, which can hardly be fully described by the current experimental characterizations.[486] Thus, many computational approaches, such as DFT calculations and MD simulations, have become indispensable tools for predicting intrinsic material structure-property relationships (**Figure 29**). These methods are expected to provide a deeper understanding of the elusive ion transport mechanism in composite SSEs. DFT simulations have become a linchpin, especially in investigating the energetics of novel composite electrolytes for solid-state batteries. In the study of Li sulfonated COFs, (TpPa-SO_3Li, DFT has been adopted in elucidating Li^+ conduction behaviors.[127] The calculated migration barriers revealed a preference for axial Li^+ migration over planar pathways, Similarly, Zhou's group utilized DFT calculations to investigate the energy barriers for the transport of $TFSI^-$ through MOF channels longitudinally and laterally (Figure 29a).[142] A higher energy barrier was observed for lateral diffusion through the rigid MOF frameworks. This highlights the MOF channels' ability to hinder $TFSI^-$ transport within channels through spatial constraints.

In addition to DFT, MD simulation is a valuable tool for providing dynamical information of electrolyte materials during electrochemical processes at atomic and molecular scales.[311] For instance, Yi Cui's group demonstrated the use of MD to understand the enhanced σ in composite SSEs with aligned polymer chains (Figure 29b).[207] The simulations captured preferential Li^+ diffusion pathways along the alignment direction with a modified OPLS-AA (OPLS: optimized potentials for liquid simulations; AA: all-atom) force field.[490] However, these classical MD models, governed by conventional interatomic potentials, are not always available nor precisely calibrated for new composite electrolyte systems.[491] On the other hand, ab initio MD (AIMD), whose force evaluations are usually based on DFT calculations, are comparatively more suitable for real-time simulations of ion motions for novel SSE materials.[492,493] Nevertheless, the primary drawback of AIMD lies in their substantial computational expense. Consequently, this technique is still constrained to small supercells comprising only a few hundred atoms and is limited to a relatively short physical timescale, typically ranging from tens of picoseconds to a few nanoseconds.[494] To balance accuracy, applicability, and computational cost, MD enabled by ML force fields (MLFF) has gradually emerged as a potential game changer.[495,496] In a recent example, MD with deep-learning potential was adopted for developing a new sulfide solid-state electrolyte. This ML-assisted MD is 100–1000 times faster than AIMD, while accommodating a system size ten times larger than that achievable with AIMD.[497] In the context of large-scale atomistic simulations of composite SSEs, MLFF shows great promise to develop a universally accurate polarizable interatomic potential (Figure 29c).[487] This is essential for uncovering the properties and mechanisms associated with the complex variety of chemical elements, phase components, and interfaces.

ML techniques have also been effectively employed for identifying suitable SSE materials via making robust predictions on key parameters such as σ,[498] electrochemical stability,[499] and mechanical properties.[488,500,501] By training ML models on extensive datasets,[502] researchers expedite material screening and selection, as demonstrated in the search for high-performance solid Li^+ conductors.[498,500,503] Notably, most of the existing ML-related research on SSEs is still concentrated on pure inorganic ceramics (Figure 29d)[488,500] and polymer electrolytes (Figure 29e).[489,504] The difficulty in exploring composite SSEs with ML may lie

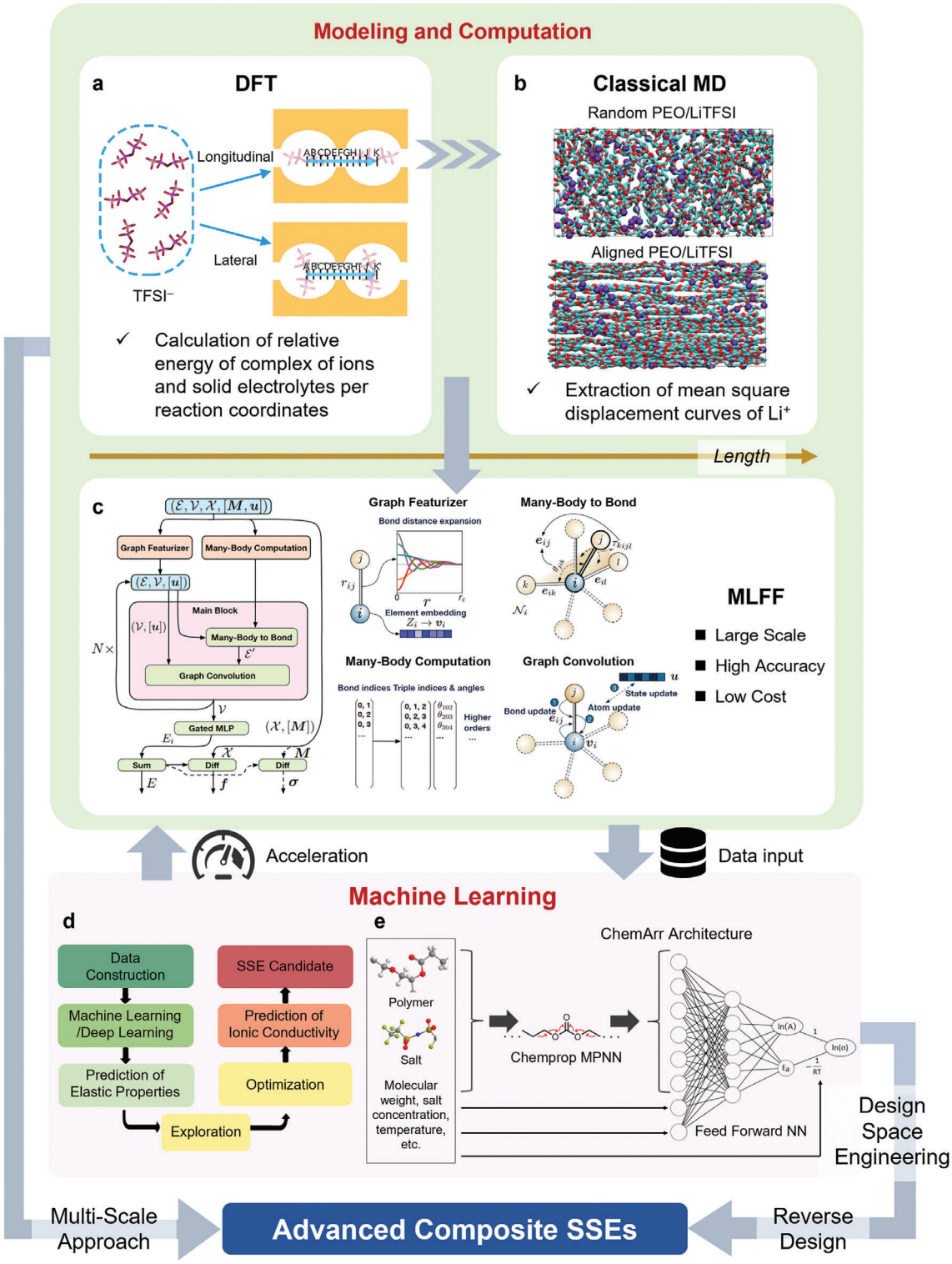

Figure 29. A proposed workflow that combines multi-scale models and ML techniques for designing new composite SSEs. a) Density functional theory (DFT) calculations of $TFSI^-$ transport in MOF channels. Reproduced with permission.[142] Copyright 2018, Elsevier. b) Molecular dynamics (MD) simulations of Li^+ transport in electrolyte systems, with the corresponding mean square displacement (MSD) curves plotted as functions of time. Reproduced with permission.[207] Copyright 2019, Springer Nature. c) Schematic architecture of the many-body graph potential. Reproduced with permission.[487] Copyright 2022, Springer Nature. d) Flowchart of machine learning (ML) processes to predict elastic properties and ionic conductivities of garnet-type SSEs. Reproduced with permission.[488] Copyright 2023, American Chemical Society. e) Diagram of ChemArr architecture containing a message passing neural network (MPNN). Reproduced with permission.[489] Copyright 2023, American Chemical Society.

in establishing a comprehensive design space. Unlike single-type SSEs, the design space for composite SSEs is not simply an intersection or union of individual components' parameters due to diverse component interfaces and distinct ion transport mechanisms. To summarize this section, composite SSEs offer a promising pathway to overcome inherent shortcomings in existing SSEs. However, their complex composition and interfaces pose significant challenges in mechanistic investigations and materials design. ML-assisted multiscale modeling from the electronic level to the atomic level should be of great importance in understanding microscopic properties within composite SSEs, such as ion migration, interface formation, and microstructure evolution. In parallel, developing ML algorithms for promoting global exploration and reverse design of composite electrolyte materials should also be significant in advancing research in composite SSEs.

4.6. All-solid-State Li–S and Li–O_2 Batteries

Batteries utilizing Li metal anodes have shown considerable promise for achieving elevated energy densities.[505] In addition to LMBs, alternative technologies, such as Li–S and Li–O_2 batteries, are emerging as strong contenders for next-generation energy storage solutions that are both high in energy density and low in cost.[506–509] Nevertheless, liquid-based Li–S batteries face notable obstacles primarily due to the shuttling effect of soluble Li polysulfides that move between the anode and cathode.[510,511] This migration leads to diminished CE and accelerates capacity degradation over cycling. ASS (all-solid-state) Li–S that incorporate SSEs instead of liquid electrolytes represent a promising approach to mitigate this issue.[37,512] Although polymer-based SSEs, such as PEO and PAN, offer benefits like flexibility, high chemical stability, and cost-effectiveness, their low σ at r.t. and limited capability to suppress dendrite growth restrict their broader application in ASS Li–S batteries.[513] Furthermore, the solubility of Li polysulfides in conventional polymers continues to be problematic.[514] For example, PEO exhibits a high solubility for Li polysulfides due to its high Gutmann donor number of 22 for ethylene oxide units, which indicates significant solvent properties.[515] To address the polysulfide shuttling issue in PEO-based ASS Li–S batteries, Goodenough's group reported a strategy involving the introduction of a PVDF layer on the sulfur cathode.[516] The low Gutmann donor number and weak solvent properties of PVDF render long-chain polysulfides insoluble and unstable within this material. By mitigating the polysulfide shuttling problem, this approach significantly enhances the electrochemical performance of the batteries. The high interfacial resistance between oxide-based SSEs and electrodes, attributed to the inherent rigidity of oxides, represents a significant drawback that limits the broader application of these materials in ASS Li–S batteries.[517] In contrast, ASS Li–S batteries utilizing sulfide-based SSEs demonstrate high energy density due to the absence of the polysulfide shuttling effect.[277] However, their practical use is hindered by the poor chemical and electrochemical stability of sulfides. Creating polymer-ceramic composites is an effective strategy to address both interfacial issues and polysulfide shuttling simultaneously. For instance, Cheng et al. reported a composite electrolyte composed of garnet-type oxide $Li_{6.28}La_3Al_{0.24}Zr_2O_{12}$ nanofibers integrated into a PEO polymer matrix.[518] The incorporation of $Li_{6.28}La_3Al_{0.24}Zr_2O_{12}$ not only enhances the mechanical properties and dendrite suppression of the PEO-based composite SSE but also improves the inhibition of polysulfide diffusion throughout the cycling process. MOFs or COFs, along with their composites, offer considerable promise for enhancing the performance of ASS Li–S batteries. For instance, a study by Li et al. introduced a 3D composite SSE that integrates ordered MOF fillers within a PEO matrix.[519] The presence of the ordered MOF structure not only promotes ion transport but also creates well-defined micropores and multiple barriers that effectively inhibit the shuttling of Li polysulfides. This design leads to significant improvements in both the rate performance and cycling stability of the ASS Li–S batteries. To advance the future development of ASS Li–S batteries, it is essential not only to design SSEs with attributes such as high σ, excellent compatibility with electrodes, and effective suppression of polysulfide shuttling, but also to develop advanced characterization techniques and theoretical calculations.

Li–O_2 batteries represent a promising energy storage technology due to their exceptionally high theoretical energy density of 3,458 Wh kg^{-1}, low manufacturing costs, and open system design.[520–522] ASS Li–O_2 batteries that incorporate SSEs significantly enhance safety and are regarded as one of the most promising configurations for Li metal anodes.[523] In the development of ASS Li–O_2 batteries, various types of SSEs have been explored for practical applications, including polymers,[524–526] inorganic ceramics (such as oxides and halides),[527–530] PCPs like MOFs and COFs,[126,224,531] as well as composite materials.[532–534] However, the advancement of ASS Li–O_2 batteries, which aim for high energy density and durability, is currently limited by the availability of effective SSEs. The SSEs used in these systems often exhibit several limitations, including high interfacial resistance with electrodes, inadequate σ, and poor stability under practical operating conditions. Cycling performance poses a major challenge for the wider application of ASS Li–O_2 batteries, as many systems struggle to achieve more than 1,000 cycles, resulting in substantial capacity loss over time; only a limited number of studies have reported successful long-term performance.[535] Additionally, the operation of ASS Li–O_2 batteries as open systems that draw oxygen from the surrounding environment introduces risks of contamination. The ingress of substances like water can lead to safety concerns and potential battery failure due to adverse reactions with the Li anodes.[536,537] Looking ahead, the future of ASS Li–O_2 batteries should prioritize advancements in high-performance SSEs, the development of sophisticated characterization techniques, and the creation of electrocatalysts with improved catalytic efficiency and stability. Furthermore, effective battery management strategies, including thermal management, will be essential for enhancing cycling stability and ensuring safety in practical applications.

4.7. Conclusion

In summary, in this review, starting from the introduction of Li-based batteries, we conducted a comprehensive analysis of the advantages of LMBs compared to traditional LIBs and Li–S batteries. While LMBs have made significant progress, the primary

objective in current LMB research is to achieve a gravimetric energy density exceeding 500 Wh kg^{-1} and a volumetric energy density surpassing 1500 Wh L^{-1} to meet the needs of highly demanding and large-scale electronic devices. SSEs, as crucial components of ASSLMBs, demonstrate outstanding potential in realizing these goals while offering superior safety. We evaluated the properties of SSEs based on six criteria: ionic conductivity, Li^+ transference number, interfacial contact, manufacturing cost, electrochemical stability, and dendrite suppression. We comprehensively analyzed different types of SSEs, including oxides, sulfides, polymers, MOFs, COFs, and their composites, highlighting their distinct advantages and disadvantages. In addition, we conducted a comprehensive review of recent breakthroughs in the field of SSEs and identified the critical bottlenecks that researchers have encountered in SSE development. Based on our analysis, we provided valuable insights and recommendations for future directions in SSE research. Additionally, we offered notable examples of these SSEs in the past five years and analyzed their application in ASSLMBs. By thoroughly examining the properties and performance of various SSEs, we provided a comprehensive understanding of their potential for enabling high-energy-density LMBs.

In our research, we analyzed the four main types of failure (electric, mechanical, chemical, and electrochemical) in ASSLMBs and proposed solutions. We also discussed the impact of the cathode degradation on cell performance, as well as future directions for overcoming these challenges. The issues of Li plating/stripping reversibility, along with thermal runaway, in ASSLMBs have been extensively examined. Additionally, we explored advanced characterization techniques for understanding solid-solid electrode|electrolyte interfaces and emphasized the emerging trend in SSEs towards developing composites with balanced properties. However, we acknowledged the difficulties associated with composite SSEs, particularly in achieving high-energy density, safety, and long-term durability in ASSLMBs, and proposed ideas for future advancements in this field. Although significant progress has been made in understanding the Li^+ transport mechanism in SSEs through computational tools such as density functional theory, molecular dynamics, and machine learning, there are still gaps in our understanding, particularly for complex composite structures and components with distinct properties. Further research is needed to clarify the Li^+ transport mechanism and the interactions between electrodes and electrolytes in SSEs. Lastly, while advancements have been made in the design of SSEs for ASSLMBs, there are still considerable challenges to address. Ongoing research and innovation are required to improve safety, achieve higher energy density, enable fast charging, and ensure long cycling life in ASSLMBs. Additionally, alternative solid-state battery technologies utilizing Li metal anodes, such as Li–S and Li–O_2 batteries, also show significant promise.

Acknowledgements

J.H. and C.L. contributed equally to this work. This work was supported by the Research Grants Council of the Hong Kong SAR Government (Early Career Scheme, #26309420, General Research Fund, #16306921 and #16306022, and Collaborative Research Fund, #C6011-20G), the Department of Chemical and Biomolecular Engineering, HKUST (startup funding) and the 30 for 30 Research Initiative Scheme, VPRDO, HKUST. Z.L.X. acknowledges the support from RCDSE at PolyU (project No. 1-BBDC).

Conflict of Interest

The authors declare no conflict of interest.

Keywords

Composites, Inorganic ceramics, Lithium metal batteries, Porous crystalline polymers, Solid-state electrolytes

Received: June 25, 2024
Revised: September 30, 2024
Published online:

[1] M. Li, J. Lu, Z. Chen, K. Amine, *Adv. Mater.* **2018**, *30*, 1800561.
[2] J. Xie, Y.-C. Lu, *Nat. Commun.* **2020**, *11*, 2499.
[3] J. T. Frith, M. J. Lacey, U. Ulissi, *Nat. Commun.* **2023**, *14*, 420.
[4] C. D. Quilty, D. Wu, W. Li, D. C. Bock, L. Wang, L. M. Housel, A. Abraham, K. J. Takeuchi, A. C. Marschilok, E. S. Takeuchi, *Chem. Rev.* **2023**, *123*, 1327.
[5] W. M. Seong, K.-Y. Park, M. H. Lee, S. Moon, K. Oh, H. Park, S. Lee, K. Kang, *Energy Environ. Sci.* **2018**, *11*, 970.
[6] E. Fan, L. Li, Z. Wang, J. Lin, Y. Huang, Y. Yao, R. Chen, F. Wu, *Chem. Rev.* **2020**, *120*, 7020.
[7] A. N. Kay Lup, in *Handbook of Smart Materials Technologies, and Devices: Applications of Industry 4.0*, (Eds.: C. M. Hussain, P. Di Sia), Springer International Publishing, Cham **2022**, pp. 2337–2365.
[8] G. G. Eshetu, H. Zhang, X. Judez, H. Adenusi, M. Armand, S. Passerini, E. Figgemeier, *Nat. Commun.* **2021**, *12*, 5459.
[9] P. Xiao, X. Yun, Y. Chen, X. Guo, P. Gao, G. Zhou, C. Zheng, *Chem. Soc. Rev.* **2023**, *52*, 5255.
[10] L.-Z. Fan, H. He, C.-W. Nan, *Nat. Rev. Mater.* **2021**, *6*, 1003.
[11] Y. Tang, T. Li, W. Zhao, C. Ming, F. Huang, *J. Power Sources* **2022**, *536*, 231479.
[12] C. Bao, C. Zheng, M. Wu, Y. Zhang, J. Jin, H. Chen, Z. Wen, *Adv. Energy Mater.* **2023**, *13*, 2204028.
[13] J.-H. Kim, J.-M. Kim, S.-K. Cho, N.-Y. Kim, S.-Y. Lee, *Nat. Commun.* **2022**, *13*, 2541.
[14] C. Niu, D. Liu, J. A. Lochala, C. S. Anderson, X. Cao, M. E. Gross, W. Xu, J.-G. Zhang, M. S. Whittingham, J. Xiao, J. Liu, *Nat. Energy* **2021**, *6*, 723.
[15] S. Chang, J. Fang, K. Liu, Z. Shen, L. Zhu, X. Jin, X. Zhang, C. Hu, H. Zhang, A.-D. Li, *Adv. Energy Mater.* **2023**, *13*, 2204002.
[16] H. Chen, X. Zhang, S. Li, Y. Zheng, *ACS Energy Lett.* **2023**, *8*, 619.
[17] Z. Li, I. Sami, J. Yang, J. Li, R. V. Kumar, M. Chhowalla, *Nat. Energy* **2023**, *8*, 84.
[18] W. Xue, Z. Shi, L. Suo, C. Wang, Z. Wang, H. Wang, K. P. So, A. Maurano, D. Yu, Y. Chen, L. Qie, F. H. Richter, J. Janek, Z. Zhu, G. Xu, J. Kong, J. Li, *Nat. Energy* **2019**, *4*, 374.
[19] D. Wang, C. Han, F. Mo, Q. Yang, Y. Zhao, Q. Li, G. Liang, B. Dong, C. Zhi, *Energy Storage Mater.* **2020**, *28*, 264.
[20] S. Xia, X. Wu, Z. Zhang, Y. Cui, W. Liu, *Chem* **2019**, *5*, 753.
[21] M. Winter, B. Barnett, K. Xu, *Chem. Rev.* **2018**, *118*, 11433.
[22] G. Zhou, H. Chen, Y. Cui, *Nat. Energy* **2022**, *7*, 312.
[23] R. Carter, C. T. Love, *Joule* **2022**, *6*, 2447.
[24] J. Xiao, F. Shi, T. Glossmann, C. Burnett, Z. Liu, *Nat. Energy* **2023**, *8*, 329.
[25] S.-J. Tan, W.-P. Wang, Y.-F. Tian, S. Xin, Y.-G. Guo, *Adv. Funct. Mater.* **2021**, *31*, 2105253.

[26] H. Wang, Z. Yu, X. Kong, S. C. Kim, D. T. Boyle, J. Qin, Z. Bao, Y. Cui, *Joule* **2022**, *6*, 588.
[27] Y.-S. Hu, *Nat. Energy* **2016**, *1*, 16042.
[28] S. Randau, D. A. Weber, O. Kötz, R. Koerver, P. Braun, A. Weber, E. Ivers-Tiffée, T. Adermann, J. Kulisch, W. G. Zeier, F. H. Richter, J. Janek, *Nat. Energy* **2020**, *5*, 259.
[29] J. Sung, J. Heo, D.-H. Kim, S. Jo, Y.-C. Ha, D. Kim, S. Ahn, J.-W. Park, *Mater. Chem. Front.* **2024**, *8*, 1861.
[30] E. C. Evarts, *Nature* **2015**, *526*, S93.
[31] X.-B. Cheng, C.-Z. Zhao, Y.-X. Yao, H. Liu, Q. Zhang, *Chem* **2019**, *5*, 74.
[32] P. P. Paul, E. J. McShane, A. M. Colclasure, N. Balsara, D. E. Brown, C. Cao, B.-R. Chen, P. R. Chinnam, Y. Cui, E. J. Dufek, D. P. Finegan, S. Gillard, W. Huang, Z. M. Konz, R. Kostecki, F. Liu, S. Lubner, R. Prasher, M. B. Preefer, J. Qian, M.-T. F. Rodrigues, M. Schnabel, S.-B. Son, V. Srinivasan, H.-G. Steinrück, T. R. Tanim, M. F. Toney, W. Tong, F. Usseglio-Viretta, J. Wan, et al., *Adv. Energy Mater.* **2021**, *11*, 2100372.
[33] G. Cui, *Matter* **2020**, *2*, 805.
[34] C. Niu, H. Lee, S. Chen, Q. Li, J. Du, W. Xu, J.-G. Zhang, M. S. Whittingham, J. Xiao, J. Liu, *Nat. Energy* **2019**, *4*, 551.
[35] J. Liu, Z. Bao, Y. Cui, E. J. Dufek, J. B. Goodenough, P. Khalifah, Q. Li, B. Y. Liaw, P. Liu, A. Manthiram, Y. S. Meng, V. R. Subramanian, M. F. Toney, V. V. Viswanathan, M. S. Whittingham, J. Xiao, W. Xu, J. Yang, X.-Q. Yang, J.-G. Zhang, *Nat. Energy* **2019**, *4*, 180.
[36] M. Jiang, D. L. Danilov, R.-A. Eichel, P. H. L. Notten, *Adv. Energy Mater.* **2021**, *11*, 2103005.
[37] X. Yang, J. Luo, X. Sun, *Chem. Soc. Rev.* **2020**, *49*, 2140.
[38] H. Li, Y. Tao, C. Zhang, D. Liu, J. Luo, W. Fan, Y. Xu, Y. Li, C. You, Z.-Z. Pan, M. Ye, Z. Chen, Z. Dong, D.-W. Wang, F. Kang, J. Lu, Q.-H. Yang, *Adv. Energy Mater.* **2018**, *8*, 1703438.
[39] P. Albertus, V. Anandan, C. Ban, N. Balsara, I. Belharouak, J. Buettner-Garrett, Z. Chen, C. Daniel, M. Doeff, N. J. Dudney, B. Dunn, S. J. Harris, S. Herle, E. Herbert, S. Kalnaus, J. A. Libera, D. Lu, S. Martin, B. D. McCloskey, M. T. McDowell, Y. S. Meng, J. Nanda, J. Sakamoto, E. C. Self, S. Tepavcevic, E. Wachsman, C. Wang, A. S. Westover, J. Xiao, T. Yersak, *ACS Energy Lett.* **2021**, *6*, 1399.
[40] Y. Jie, X. Ren, R. Cao, W. Cai, S. Jiao, *Adv. Funct. Mater.* **2020**, *30*, 1910777.
[41] Y.-K. Liu, C.-Z. Zhao, J. Du, X.-Q. Zhang, A.-B. Chen, Q. Zhang, *Small* **2023**, *19*, 2205315.
[42] Y. Zhao, J. Guo, *InfoMat* **2020**, *2*, 866.
[43] X. Fan, C. Wang, *Chem. Soc. Rev.* **2021**, *50*, 10486.
[44] J. Zhang, X. Yao, R. K. Misra, Q. Cai, Y. Zhao, *J. Mater. Sci. Technol.* **2020**, *44*, 237.
[45] V. L. Martins, *Curr. Opin. Electrochem.* **2023**, *38*, 101241.
[46] Q. Liu, L. Wang, *Adv. Energy Mater.* **2023**, *13*, 2301742.
[47] X. He, D. Bresser, S. Passerini, F. Baakes, U. Krewer, J. Lopez, C. T. Mallia, Y. Shao-Horn, I. Cekic-Laskovic, S. Wiemers-Meyer, F. A. Soto, V. Ponce, J. M. Seminario, P. B. Balbuena, H. Jia, W. Xu, Y. Xu, C. Wang, B. Horstmann, R. Amine, C.-C. Su, J. Shi, K. Amine, M. Winter, A. Latz, R. Kostecki, *Nat. Rev. Mater.* **2021**, *6*, 1036.
[48] B. Horstmann, J. Shi, R. Amine, M. Werres, X. He, H. Jia, F. Hausen, I. Cekic-Laskovic, S. Wiemers-Meyer, J. Lopez, D. Galvez-Aranda, F. Baakes, D. Bresser, C.-C. Su, Y. Xu, W. Xu, P. Jakes, R.-A. Eichel, E. Figgemeier, U. Krewer, J. M. Seminario, P. B. Balbuena, C. Wang, S. Passerini, Y. Shao-Horn, M. Winter, K. Amine, R. Kostecki, A. Latz, *Energy Environ. Sci.* **2021**, *14*, 5289.
[49] Z. Li, R. Yu, S. Weng, Q. Zhang, X. Wang, X. Guo, *Nat. Commun.* **2023**, *14*, 482.
[50] Y. Xie, L. Feng, D. Li, Y. Tang, C. Zhu, M. Wang, J. Xu, *Colloids Surf. A* **2023**, *670*, 131487.
[51] P. Jaumaux, J. Wu, D. Shanmukaraj, Y. Wang, D. Zhou, B. Sun, F. Kang, B. Li, M. Armand, G. Wang, *Adv. Funct. Mater.* **2021**, *31*, 2008644.
[52] Z. Chang, H. Yang, X. Zhu, P. He, H. Zhou, *Nat. Commun.* **2022**, *13*, 1510.
[53] Z. Wang, J. Liu, M. Wang, X. Shen, T. Qian, C. Yan, *Nanoscale Adv.* **2020**, *2*, 1828.
[54] Y. Liu, L. Hou, Y. Jiao, P. Wu, *ACS Appl. Mater. Interfaces* **2021**, *13*, 13319.
[55] M. Balaish, J. C. Gonzalez-Rosillo, K. J. Kim, Y. Zhu, Z. D. Hood, J. L. M. Rupp, *Nat. Energy* **2021**, *6*, 227.
[56] W. Ren, C. Ding, X. Fu, Y. Huang, *Energy Storage Mater.* **2021**, *34*, 515.
[57] S. Liang, W. Yan, X. Wu, Y. Zhang, Y. Zhu, H. Wang, Y. Wu, *Solid State Ionics* **2018**, *318*, 2.
[58] X. Liu, H. Jia, H. Li, *Energy Storage Mater.* **2024**, *67*, 103263.
[59] K. Yoon, S. Lee, K. Oh, K. Kang, *Adv. Mater.* **2022**, *34*, 2104666.
[60] F. Duffner, N. Kronemeyer, J. Tübke, J. Leker, M. Winter, R. Schmuch, *Nat. Energy* **2021**, *6*, 123.
[61] G. Xu, X. Shangguan, S. Dong, X. Zhou, G. Cui, *Angew. Chem., Int. Ed.* **2020**, *59*, 3400.
[62] D.-H. Liu, Z. Bai, M. Li, A. Yu, D. Luo, W. Liu, L. Yang, J. Lu, K. Amine, Z. Chen, *Chem. Soc. Rev.* **2020**, *49*, 5407.
[63] A. Banerjee, X. Wang, C. Fang, E. A. Wu, Y. S. Meng, *Chem. Rev.* **2020**, *120*, 6878.
[64] D. H. S. Tan, A. Banerjee, Z. Chen, Y. S. Meng, *Nat. Nanotechnol.* **2020**, *15*, 170.
[65] W. Zhao, J. Yi, P. He, H. Zhou, *Electrochem. Energy Rev.* **2019**, *2*, 574.
[66] K. Qin, K. Holguin, M. Mohammadiroudbari, J. Huang, E. Y. S. Kim, R. Hall, C. Luo, *Adv. Funct. Mater.* **2021**, *31*, 2009694.
[67] J. Huang, F. Li, M. Wu, H. Wang, S. Qi, G. Jiang, X. Li, J. Ma, *Sci. China: Chem.* **2022**, *65*, 840.
[68] P. Ding, Z. Lin, X. Guo, L. Wu, Y. Wang, H. Guo, L. Li, H. Yu, *Mater. Today* **2021**, *51*, 449.
[69] J. Wu, L. Shen, Z. Zhang, G. Liu, Z. Wang, D. Zhou, H. Wan, X. Xu, X. Yao, *Electrochem. Energy Rev.* **2021**, *4*, 101.
[70] K. J. Kim, M. Balaish, M. Wadaguchi, L. Kong, J. L. M. Rupp, *Adv. Energy Mater.* **2021**, *11*, 2002689.
[71] N. Zhao, W. Khokhar, Z. Bi, C. Shi, X. Guo, L.-Z. Fan, C.-W. Nan, *Joule* **2019**, *3*, 1190.
[72] K. Tuo, C. Sun, S. Liu, *Electrochem. Energy Rev.* **2023**, *6*, 17.
[73] J. Mindemark, M. J. Lacey, T. Bowden, D. Brandell, *Prog. Polym. Sci.* **2018**, *81*, 114.
[74] S. Huo, L. Sheng, W. Xue, L. Wang, H. Xu, H. Zhang, X. He, *InfoMat* **2023**, *5*, e12394.
[75] Y. Wu, Y. Li, Y. Wang, Q. Liu, Q. Chen, M. Chen, *J. Energy Chem.* **2022**, *64*, 62.
[76] H. Yang, M. Jing, L. Wang, H. Xu, X. Yan, X. He, *Nano-Micro Lett.* **2024**, *16*, 127.
[77] H. Liu, X. Sun, X.-B. Cheng, C. Guo, F. Yu, W. Bao, T. Wang, J. Li, Q. Zhang, *Adv. Energy Mater.* **2022**, *12*, 2202518.
[78] Q. Zhao, X. Liu, S. Stalin, K. Khan, L. A. Archer, *Nat. Energy* **2019**, *4*, 365.
[79] W. Li, J. Gao, H. Tian, X. Li, S. He, J. Li, W. Wang, L. Li, H. Li, J. Qiu, W. Zhou, *Angew. Chem., Int. Ed.* **2022**, *61*, 202114805.
[80] S.-J. Yang, H. Yuan, N. Yao, J.-K. Hu, X.-L. Wang, R. Wen, J. Liu, J.-Q. Huang, *Adv. Mater.* **2024**, *36*, 2405086.
[81] X. Huang, T. Li, W. Fan, R. Xiao, X.-B. Cheng, *Adv. Energy Mater.* **2024**, *14*, 2303850.
[82] R. Murugan, V. Thangadurai, W. Weppner, *Angew. Chem., Int. Ed.* **2007**, *46*, 7778.
[83] J. Xiao, B. Zhang, J. Liu, X. He, Z. Xiao, H. Qin, T. Liu, K. Amine, X. Ou, *Nano Energy* **2024**, *127*, 109730.
[84] S. Wang, J. Wang, J. Liu, H. Song, Y. Liu, P. Wang, P. He, J. Xu, H. Zhou, *J. Mater. Chem. A* **2018**, *6*, 21248.
[85] Y. Zhu, X. He, Y. Mo, *ACS Appl. Mater. Interfaces* **2015**, *7*, 23685.

[86] J. Zhang, C. Zheng, L. Li, Y. Xia, H. Huang, Y. Gan, C. Liang, X. He, X. Tao, W. Zhang, *Adv. Energy Mater.* **2020**, *10*, 1903311.
[87] S. Liu, L. Zhou, J. Han, K. Wen, S. Guan, C. Xue, Z. Zhang, B. Xu, Y. Lin, Y. Shen, L. Li, C.-W. Nan, *Adv. Energy Mater.* **2022**, *12*, 2200660.
[88] J. Hu, S. Yang, Y. Pei, X. Wang, Y. Liao, S. Li, A. Yue, J.-Q. Huang, H. Yuan, *Particuology* **2024**, *86*, 55.
[89] S. Wang, Y. Zhang, X. Zhang, T. Liu, Y.-H. Lin, Y. Shen, L. Li, C.-W. Nan, *ACS Appl. Mater. Interfaces* **2018**, *10*, 42279.
[90] Y.-L. Liao, J.-K. Hu, Z.-H. Fu, C.-Z. Zhao, Y. Lu, S. Li, S.-J. Yang, S. Sun, X.-L. Wang, J. Liu, J.-Q. Huang, H. Yuan, *J. Energy Chem.* **2023**, *80*, 458.
[91] C. Wang, J. Liang, Y. Zhao, M. Zheng, X. Li, X. Sun, *Energy Environ. Sci.* **2021**, *14*, 2577.
[92] N. Kamaya, K. Homma, Y. Yamakawa, M. Hirayama, R. Kanno, M. Yonemura, T. Kamiyama, Y. Kato, S. Hama, K. Kawamoto, A. Mitsui, *Nat. Mater.* **2011**, *10*, 682.
[93] Y. Kato, S. Hori, T. Saito, K. Suzuki, M. Hirayama, A. Mitsui, M. Yonemura, H. Iba, R. Kanno, *Nat. Energy* **2016**, *1*, 16030.
[94] Y. Li, S. Song, H. Kim, K. Nomoto, H. Kim, X. Sun, S. Hori, K. Suzuki, N. Matsui, M. Hirayama, T. Mizoguchi, T. Saito, T. Kamiyama, R. Kanno, *Science* **2023**, *381*, 50.
[95] Y. Liu, L. Chen, L. Yang, T. Lan, H. Wang, C. Hu, X. Han, Q. Liu, J. Chen, Z. Feng, X. Cui, Q. Fang, H. Wang, L. Li, Y. Li, H. Xing, S. Yang, D. Zhao, J. Li, *Green Energy Environ.* **2024**, *9*, 217.
[96] Y. Ouyang, W. Gong, Q. Zhang, J. Wang, S. Guo, Y. Xiao, D. Li, C. Wang, X. Sun, C. Wang, S. Huang, *Adv. Mater.* **2023**, *35*, 2304685.
[97] H. Yang, B. Liu, J. Bright, S. Kasani, J. Yang, X. Zhang, N. Wu, *ACS Appl. Energy Mater.* **2020**, *3*, 4007.
[98] X. Liang, Y. Tian, Y. Yuan, Y. Kim, *Adv. Mater.* **2021**, *33*, 2105647.
[99] W. Gong, Y. Ouyang, S. Guo, Y. Xiao, Q. Zeng, D. Li, Y. Xie, Q. Zhang, S. Huang, *Angew. Chem., Int. Ed.* **2023**, *62*, 202302505.
[100] W. Li, S. Han, C. Xiao, J. Yan, B. Wu, P. Wen, J. Lin, M. Chen, X. Lin, *Angew. Chem., Int. Ed.* **2024**, *63*, 202410392.
[101] J. Wang, S. Guo, Z. Li, W. Kou, J. Zhu, J. Dang, Y. Zhang, W. Wu, *Chem. Eng. J.* **2022**, *450*, 137994.
[102] J.-K. Hu, Y.-C. Gao, S.-J. Yang, X.-L. Wang, X. Chen, Y.-L. Liao, S. Li, J. Liu, H. Yuan, J.-Q. Huang, *Adv. Funct. Mater.* **2024**, *34*, 2311633.
[103] J. Huang, L. Cheng, Z. Zhang, C. Li, K.-T. Bang, A. Liem, H. Luo, C. Hu, Y. M. Lee, Y. Lu, Y. Wang, Y. Kim, *Adv. Energy Mater.* **2024**, 2400762.
[104] T. Famprikis, P. Canepa, J. A. Dawson, M. S. Islam, C. Masquelier, *Nat. Mater.* **2019**, *18*, 1278.
[105] H. Yang, N. Wu, *Energy Sci. Eng.* **2022**, *10*, 1643.
[106] K. M. Diederichsen, E. J. McShane, B. D. McCloskey, *ACS Energy Lett.* **2017**, *2*, 2563.
[107] Y. Zhao, L. Wang, Y. Zhou, Z. Liang, N. Tavajohi, B. Li, T. Li, *Adv. Sci.* **2021**, *8*, 2003675.
[108] Z. Xue, D. He, X. Xie, *J. Mater. Chem. A* **2015**, *3*, 19218.
[109] J. Gao, J. Zhou, C. Wang, X. Ma, K. Jiang, E. Kim, C. Li, H. Liu, L. Xu, H. C. Shum, S.-P. Feng, D.-M. Shin, *Chem. Eng. J.* **2022**, *450*, 138407.
[110] D. Zhou, D. Shanmukaraj, A. Tkacheva, M. Armand, G. Wang, *Chem* **2019**, *5*, 2326.
[111] S. Han, P. Wen, H. Wang, Y. Zhou, Y. Gu, L. Zhang, Y. Shao-Horn, X. Lin, M. Chen, *Nat. Mater.* **2023**, *22*, 1515.
[112] D. G. Mackanic, W. Michaels, M. Lee, D. Feng, J. Lopez, J. Qin, Y. Cui, Z. Bao, *Adv. Energy Mater.* **2018**, *8*, 1800703.
[113] X. Wang, F. Chen, G. M. A. Girard, H. Zhu, D. R. MacFarlane, D. Mecerreyes, M. Armand, P. C. Howlett, M. Forsyth, *Joule* **2019**, *3*, 2687.
[114] M. Zhang, S. Yu, Y. Mai, S. Zhang, Y. Zhou, *Chem. Commun.* **2019**, *55*, 6715.
[115] F. Zhang, Y. Sun, Z. Wang, D. Fu, J. Li, J. Hu, J. Xu, X. Wu, *ACS Appl. Mater. Interfaces* **2020**, *12*, 23774.
[116] H. Yuan, J. Luan, Z. Yang, J. Zhang, Y. Wu, Z. Lu, H. Liu, *ACS Appl. Mater. Interfaces* **2020**, *12*, 7249.
[117] Y. Zhang, W. Lu, L. Cong, J. Liu, L. Sun, A. Mauger, C. M. Julien, H. Xie, J. Liu, *J. Power Sources* **2019**, *420*, 63.
[118] Z. Yao, K. Zhu, J. Zhang, J. Li, X. Li, J. Wang, K. Yan, J. Liu, *J. Electron. Mater.* **2022**, *51*, 736.
[119] K. Waetzig, A. Rost, C. Heubner, M. Coeler, K. Nikolowski, M. Wolter, J. Schilm, *J. Alloys Compd.* **2020**, *818*, 153237.
[120] J. Gai, E. Zhao, F. Ma, D. Sun, X. Ma, Y. Jin, Q. Wu, Y. Cui, *J. Eur. Ceram. Soc.* **2018**, *38*, 1673.
[121] T. Krauskopf, B. Mogwitz, H. Hartmann, D. K. Singh, W. G. Zeier, J. Janek, *Adv. Energy Mater.* **2020**, *10*, 2000945.
[122] S. Qin, X. Zhu, Y. Jiang, M. E. Ling, Z. Hu, J. Zhu, *Appl. Phys. Lett.* **2018**, 112.
[123] Y. Meesala, Y.-K. Liao, A. Jena, N.-H. Yang, W. K. Pang, S.-F. Hu, H. Chang, C.-E. Liu, S.-C. Liao, J.-M. Chen, X. Guo, R.-S. Liu, *J. Mater. Chem. A* **2019**, *7*, 8589.
[124] W. Arnold, V. Shreyas, S. Akter, Y. Li, S. Halacoglu, M. B. Kalutara Koralalage, X. Guo, D. Vithanage, W. Wei, G. Sumanasekera, J. B. Jasinski, B. Narayanan, H. Wang, *J. Phys. Chem. C* **2023**, *127*, 11801.
[125] F. Zhu, H. Bao, X. Wu, Y. Tao, C. Qin, Z. Su, Z. Kang, *ACS Appl. Mater. Interfaces* **2019**, *11*, 43206.
[126] X.-X. Wang, X.-W. Chi, M.-L. Li, D.-H. Guan, C.-L. Miao, J.-J. Xu, *Adv. Funct. Mater.* **2022**, *32*, 2113235.
[127] K. Jeong, S. Park, G. Y. Jung, S. H. Kim, Y.-H. Lee, S. K. Kwak, S.-Y. Lee, *J. Am. Chem. Soc.* **2019**, *141*, 5880.
[128] H. Chen, H. Tu, C. Hu, Y. Liu, D. Dong, Y. Sun, Y. Dai, S. Wang, H. Qian, Z. Lin, L. Chen, *J. Am. Chem. Soc.* **2018**, *140*, 896.
[129] Z. Li, Z.-W. Liu, Z. Li, T.-X. Wang, F. Zhao, X. Ding, W. Feng, B.-H. Han, *Adv. Funct. Mater.* **2020**, *30*, 1909267.
[130] X. Li, Q. Hou, W. Huang, H.-S. Xu, X. Wang, W. Yu, R. Li, K. Zhang, L. Wang, Z. Chen, K. Xie, K. P. Loh, *ACS Energy Lett.* **2020**, *5*, 3498.
[131] Z. Li, Z.-W. Liu, Z.-J. Mu, C. Cao, Z. Li, T.-X. Wang, Y. Li, X. Ding, B.-H. Han, W. Feng, *Mater. Chem. Front.* **2020**, *4*, 1164.
[132] D. Guo, D. B. Shinde, W. Shin, E. Abou-Hamad, A.-H. Emwas, Z. Lai, A. Manthiram, *Adv. Mater.* **2022**, *34*, 2201410.
[133] W.-P. Chen, H. Duan, J.-L. Shi, Y. Qian, J. Wan, X.-D. Zhang, H. Sheng, B. Guan, R. Wen, Y.-X. Yin, S. Xin, Y.-G. Guo, L.-J. Wan, *J. Am. Chem. Soc.* **2021**, *143*, 5717.
[134] P. Shi, J. Ma, M. Liu, S. Guo, Y. Huang, S. Wang, L. Zhang, L. Chen, K. Yang, X. Liu, Y. Li, X. An, D. Zhang, X. Cheng, Q. Li, W. Lv, G. Zhong, Y.-B. He, F. Kang, *Nat. Nanotechnol.* **2023**, *18*, 602.
[135] T. Jiang, P. He, G. Wang, Y. Shen, C.-W. Nan, L.-Z. Fan, *Adv. Energy Mater.* **2020**, *10*, 1903376.
[136] H. Huo, B. Wu, T. Zhang, X. Zheng, L. Ge, T. Xu, X. Guo, X. Sun, *Energy Storage Mater.* **2019**, *18*, 59.
[137] S. Hao, Q. Ran, Y. Xiao, L. Li, Y. Ji, J. Liu, Y. C. Yang, X. Liu, *Adv. Mater. Interfaces* **2022**, *9*, 2101486.
[138] J. Sun, C. He, X. Yao, A. Song, Y. Li, Q. Zhang, C. Hou, Q. Shi, H. Wang, *Adv. Funct. Mater.* **2021**, *31*, 2006381.
[139] Z. Guo, Y. Zhang, Y. Dong, J. Li, S. Li, P. Shao, X. Feng, B. Wang, *J. Am. Chem. Soc.* **2019**, *141*, 1923.
[140] M. Liu, X. Guan, H. Liu, X. Ma, Q. Wu, S. Ge, H. Zhang, J. Xu, *Chem. Eng. J.* **2022**, *445*, 136436.
[141] K. Pan, L. Zhang, W. Qian, X. Wu, K. Dong, H. Zhang, S. Zhang, *Adv. Mater.* **2020**, *32*, 2000399.
[142] S. Bai, Y. Sun, J. Yi, Y. He, Y. Qiao, H. Zhou, *Joule* **2018**, *2*, 2117.
[143] A. Nyman, M. Behm, G. Lindbergh, *Electrochim. Acta* **2008**, *53*, 6356.
[144] H. Zhao, L. Sheng, L. Wang, H. Xu, X. He, *Energy Storage Mater.* **2020**, *33*, 360.
[145] Y. Yang, S. Yang, X. Xue, X. Zhang, Q. Li, Y. Yao, X. Rui, H. Pan, Y. Yu, *Adv. Mater.* **2024**, *36*, 2308332.
[146] C. Wang, K. Fu, S. P. Kammampata, D. W. McOwen, A. J. Samson, L. Zhang, G. T. Hitz, A. M. Nolan, E. D. Wachsman, Y. Mo, V. Thangadurai, L. Hu, *Chem. Rev.* **2020**, *120*, 4257.
[147] J. Liu, W. Guo, H. Guo, C. Xu, L. Zhang, Y. Chen, F. Shen, X. Han, *Energy Fuels* **2022**, *36*, 8500.

[148] J. Li, F.-Q. Zhang, F. Li, Z. Wu, C. Ma, Q. Xu, P. Wang, X.-M. Zhang, *Chem. Commun.* **2020**, *56*, 2747.
[149] Z. Gao, Q. Liu, G. Zhao, Y. Sun, H. Guo, *J. Mater. Chem. A* **2022**, *10*, 7497.
[150] X. Han, Y. Gong, K. Fu, X. He, G. T. Hitz, J. Dai, A. Pearse, B. Liu, H. Wang, G. Rubloff, Y. Mo, V. Thangadurai, E. D. Wachsman, L. Hu, *Nat. Mater.* **2017**, *16*, 572.
[151] X. Huang, Y. Lu, Z. Song, K. Rui, Q. Wang, T. Xiu, M. E. Badding, Z. Wen, *Energy Storage Mater.* **2019**, *22*, 207.
[152] J.-M. Doux, H. Nguyen, D. H. S. Tan, A. Banerjee, X. Wang, E. A. Wu, C. Jo, H. Yang, Y. S. Meng, *Adv. Energy Mater.* **2020**, *10*, 1903253.
[153] X. Hu, Z. Zhang, X. Zhang, Y. Wang, X. Yang, X. Wang, M. Fayena-Greenstein, H. A. Yehezkel, S. Langford, D. Zhou, B. Li, G. Wang, D. Aurbach, *Nat. Rev. Mater.* **2024**.
[154] K. J. Kim, J. L. M. Rupp, *Energy Environ. Sci.* **2020**, *13*, 4930.
[155] H. Huo, Y. Chen, J. Luo, X. Yang, X. Guo, X. Sun, *Adv. Energy Mater.* **2019**, *9*, 1804004.
[156] R. Schmuch, R. Wagner, G. Hörpel, T. Placke, M. Winter, *Nat. Energy* **2018**, *3*, 267.
[157] J. Schnell, F. Tietz, C. Singer, A. Hofer, N. Billot, G. Reinhart, *Energy Environ. Sci.* **2019**, *12*, 1818.
[158] L. Hu, J. Wang, K. Wang, Z. Gu, Z. Xi, H. Li, F. Chen, Y. Wang, Z. Li, C. Ma, *Nat. Commun.* **2023**, *14*, 3807.
[159] W. Zaman, K. B. Hatzell, *Current Opin. Solid State Mater. Sci.* **2022**, *26*, 101003.
[160] D. Karabelli, K. P. Birke, M. Weeber, *Batteries* **2021**, *7*, 18.
[161] P. Albertus, S. Babinec, S. Litzelman, A. Newman, *Nat. Energy* **2018**, *3*, 16.
[162] W. Xu, X. Pei, C. S. Diercks, H. Lyu, Z. Ji, O. M. Yaghi, *J. Am. Chem. Soc.* **2019**, *141*, 17522.
[163] C. Li, D.-D. Wang, G. S. H. Poon Ho, Z. Zhang, J. Huang, K.-T. Bang, C. Y. Lau, S.-Y. Leu, Y. Wang, Y. Kim, *J. Am. Chem. Soc.* **2023**, *145*, 24603.
[164] W. D. Richards, L. J. Miara, Y. Wang, J. C. Kim, G. Ceder, *Chem. Mater.* **2016**, *28*, 266.
[165] Y. Zhu, X. He, Y. Mo, *J. Mater. Chem. A* **2016**, *4*, 3253.
[166] X.-X. Wang, L.-N. Song, L.-J. Zheng, D.-H. Guan, C.-L. Miao, J.-X. Li, J.-Y. Li, J.-J. Xu, *Angew. Chem., Int. Ed.* **2023**, *62*, e202308837.
[167] X. Shan, M. Morey, Z. Li, S. Zhao, S. Song, Z. Xiao, H. Feng, S. Gao, G. Li, A. P. Sokolov, E. Ryan, K. Xu, M. Tian, Y. He, H. Yang, P.-F. Cao, *ACS Energy Lett.* **2022**, *7*, 4342.
[168] J. Chai, Z. Liu, J. Ma, J. Wang, X. Liu, H. Liu, J. Zhang, G. Cui, L. Chen, *Adv. Sci.* **2017**, *4*, 1600377.
[169] Y. He, S. Chen, L. Nie, Z. Sun, X. Wu, W. Liu, *Nano Lett.* **2020**, *20*, 7136.
[170] E. M. Sorensen, S. J. Barry, H.-K. Jung, J. M. Rondinelli, J. T. Vaughey, K. R. Poeppelmeier, *Chem. Mater.* **2006**, *18*, 482.
[171] P. López-Aranguren, M. Reynaud, P. Głuchowski, A. Bustinza, M. Galceran, J. M. López del Amo, M. Armand, *ACS Energy Lett.* **2021**, *6*, 445.
[172] Q. Liu, Z. Geng, C. Han, Y. Fu, S. Li, Y.-B. He, F. Kang, B. Li, *J. Power Sources* **2018**, *389*, 120.
[173] Y. Benabed, M. Rioux, S. Rousselot, G. Hautier, M. Dollé, *Front. Energy Res.* **2021**, *9*, 682008.
[174] F. Han, Y. Zhu, X. He, Y. Mo, C. Wang, *Adv. Energy Mater.* **2016**, *6*, 1501590.
[175] J. Roh, J. Lyoo, S.-T. Hong, *ACS Appl. Energy Mater.* **2023**, *6*, 5446.
[176] Z. Liu, W. Fu, E. A. Payzant, X. Yu, Z. Wu, N. J. Dudney, J. Kiggans, K. Hong, A. J. Rondinone, C. Liang, *J. Am. Chem. Soc.* **2013**, *135*, 975.
[177] Z. Wang, Y. Jiang, J. Wu, Y. Jiang, S. Huang, B. Zhao, Z. Chen, J. Zhang, *Chem. Eng. J.* **2020**, *393*, 124706.
[178] D. H. S. Tan, E. A. Wu, H. Nguyen, Z. Chen, M. A. T. Marple, J.-M. Doux, X. Wang, H. Yang, A. Banerjee, Y. S. Meng, *ACS Energy Lett.* **2019**, *4*, 2418.
[179] R. Rajagopal, K.-S. Ryu, *Chem. Eng. J.* **2020**, *402*, 126179.
[180] Q. Zeng, J. Wang, X. Li, Y. Ouyang, W. He, D. Li, S. Guo, Y. Xiao, H. Deng, W. Gong, Q. Zhang, S. Huang, *ACS Energy Lett.* **2021**, *6*, 2434.
[181] C. Niu, W. Luo, C. Dai, C. Yu, Y. Xu, *Angew. Chem., Int. Ed.* **2021**, *60*, 24915.
[182] Y. Yang, S. Yao, Z. Liang, Y. Wen, Z. Liu, Y. Wu, J. Liu, M. Zhu, *ACS Energy Lett.* **2022**, *7*, 885.
[183] H. Duan, M. Fan, W.-P. Chen, J.-Y. Li, P.-F. Wang, W.-P. Wang, J.-L. Shi, Y.-X. Yin, L.-J. Wan, Y.-G. Guo, *Adv. Mater.* **2019**, *31*, 1807789.
[184] K. Fu, Y. Gong, J. Dai, A. Gong, X. Han, Y. Yao, C. Wang, Y. Wang, Y. Chen, C. Yan, Y. Li, E. D. Wachsman, L. Hu, *Proc. Natl. Acad. Sci. USA* **2016**, *113*, 7094.
[185] Y. Yao, Y. Cao, G. Li, C. Liu, Z. Jiang, F. Pan, J. Sun, *Trans. Tianjin Univ.* **2022**, *28*, 67.
[186] Y. Jing, Q. Lv, B. Wang, B. Wu, C. Li, S. Yang, D. Wang, H. Liu, S. Dou, *Energy Storage Mater.* **2024**, *65*, 103109.
[187] H. Wang, L. Sheng, G. Yasin, L. Wang, H. Xu, X. He, *Energy Storage Mater.* **2020**, *33*, 188.
[188] M. Kotobuki, H. Munakata, K. Kanamura, Y. Sato, T. Yoshida, *J. Electrochem. Soc.* **2010**, *157*, A1076.
[189] F. Han, T. Gao, Y. Zhu, K. J. Gaskell, C. Wang, *Adv. Mater.* **2015**, *27*, 3473.
[190] F. Liu, L. Gao, Z. Zhang, L. Zhang, N. Deng, Y. Zhao, W. Kang, *Energy Storage Mater.* **2024**, *64*, 103072.
[191] M. Feinauer, H. Euchner, M. Fichtner, M. A. Reddy, *ACS Appl. Energy Mater.* **2019**, *2*, 7196.
[192] S. Zhou, S. Zhong, Y. Dong, Z. Liu, L. Dong, B. Yuan, H. Xie, Y. Liu, L. Qiao, J. Han, W. He, *Adv. Funct. Mater.* **2023**, *33*, 2214432.
[193] Y. Yang, Q. Wu, Y. Cui, Y. Chen, S. Shi, R.-Z. Wang, H. Yan, *ACS Appl. Mater. Interfaces* **2016**, *8*, 25229.
[194] R. Du, Y. Wu, Y. Yang, T. Zhai, T. Zhou, Q. Shang, L. Zhu, C. Shang, Z. Guo, *Adv. Energy Mater.* **2021**, *11*, 2100154.
[195] C. N. Hong, A. B. Crom, J. I. Feldblyum, M. R. Lukatskaya, *Chem* **2023**, *9*, 798.
[196] X. Zhao, P. Pachfule, A. Thomas, *Chem. Soc. Rev.* **2021**, *50*, 6871.
[197] X. Zhang, F. Li, S. Yang, B. Song, R. Luo, R. Xiong, W. Xu, *SusMat* **2024**, *4*, 4.
[198] K. Park, J. B. Goodenough, *Adv. Energy Mater.* **2017**, *7*, 1700732.
[199] B. Li, Y. Chao, M. Li, Y. Xiao, R. Li, K. Yang, X. Cui, G. Xu, L. Li, C. Yang, Y. Yu, D. P. Wilkinson, J. Zhang, *Electrochem. Energy Rev.* **2023**, *6*, 7.
[200] Z. Wang, J. Xia, X. Ji, Y. Liu, J. Zhang, X. He, W. Zhang, H. Wan, C. Wang, *Nat. Energy* **2024**.
[201] S.-J. Yang, J.-K. Hu, F.-N. Jiang, H. Yuan, H. S. Park, J.-Q. Huang, *InfoMat* **2024**, *6*, e12512.
[202] D. Cao, X. Sun, Q. Li, A. Natan, P. Xiang, H. Zhu, *Matter* **2020**, *3*, 57.
[203] C. Monroe, J. Newman, *J. Electrochem. Soc.* **2005**, *152*, A396.
[204] Z. Zhao, W. Chen, S. Impeng, M. Li, R. Wang, Y. Liu, L. Zhang, L. Dong, J. Unruangsri, C. Peng, C. Wang, S. Namuangruk, S.-Y. Lee, Y. Wang, H. Lu, Jia Guo, *J. Mater. Chem. A* **2020**, *8*, 3459.
[205] R. Khurana, J. L. Schaefer, L. A. Archer, G. W. Coates, *J. Am. Chem. Soc.* **2014**, *136*, 7395.
[206] G. Yang, M. L. Lehmann, S. Zhao, B. Li, S. Ge, P.-F. Cao, F. M. Delnick, A. P. Sokolov, T. Saito, J. Nanda, *Energy Storage Mater.* **2021**, *35*, 431.
[207] J. Wan, J. Xie, X. Kong, Z. Liu, K. Liu, F. Shi, A. Pei, H. Chen, W. Chen, J. Chen, X. Zhang, L. Zong, J. Wang, L.-Q. Chen, J. Qin, Y Cui, *Nat. Nanotechnol.* **2019**, *14*, 705.
[208] J. E. Ni, E. D. Case, J. S. Sakamoto, E. Rangasamy, J. B. Wolfenstine, *J. Mater. Sci.* **2012**, *47*, 7978.
[209] Y. Shen, Y. Zhang, S. Han, J. Wang, Z. Peng, L. Chen, *Joule* **2018**, *2*, 1674.

[210] H. Liu, X.-B. Cheng, J.-Q. Huang, H. Yuan, Y. Lu, C. Yan, G.-L. Zhu, R. Xu, C.-Z. Zhao, L.-P. Hou, C. He, S. Kaskel, Q. Zhang, *ACS Energy Lett.* **2020**, *5*, 833.
[211] X. Ke, Y. Wang, L. Dai, C. Yuan, *Energy Storage Mater.* **2020**, *33*, 309.
[212] Q. Lv, Y. Jiang, B. Wang, Y. Chen, F. Jin, B. Wu, H. Ren, N. Zhang, R. Xu, Y. Li, T. Zhang, Y. Zhou, D. Wang, H. Liu, S. Dou, *Cell Rep. Phys. Sci.* **2022**, *3*, 100706.
[213] R. Sudo, Y. Nakata, K. Ishiguro, M. Matsui, A. Hirano, Y. Takeda, O. Yamamoto, N. Imanishi, *Solid State Ionics* **2014**, *262*, 151.
[214] J. Kasemchainan, S. Zekoll, D. Spencer Jolly, Z. Ning, G. O. Hartley, J. Marrow, P. G. Bruce, *Nat. Mater.* **2019**, *18*, 1105.
[215] L. Porz, T. Swamy, B. W. Sheldon, D. Rettenwander, T. Frömling, H. L. Thaman, S. Berendts, R. Uecker, W. C. Carter, Y.-M. Chiang, *Adv. Energy Mater.* **2017**, *7*, 1701003.
[216] J.-F. Wu, B.-W. Pu, D. Wang, S.-Q. Shi, N. Zhao, X. Guo, X. Guo, *ACS Appl. Mater. Interfaces* **2019**, *11*, 898.
[217] F. Han, J. Yue, X. Zhu, C. Wang, *Adv. Energy Mater.* **2018**, *8*, 1703644.
[218] K. Kerman, A. Luntz, V. Viswanathan, Y.-M. Chiang, Z. Chen, *J. Electrochem. Soc.* **2017**, *164*, A1731.
[219] Z. Wang, Z. Du, Y. Liu, C. E. Knapp, Y. Dai, J. Li, W. Zhang, R. Chen, F. Guo, W. Zong, X. Gao, J. Zhu, C. Wei, G. He, *eScience* **2023**, 100189.
[220] L. Yue, X. Wang, L. Chen, D. Shen, Z. Shao, H. Wu, S. Xiao, W. Liang, Y. Yu, Y. Li, *Energy Environ. Sci.* **2024**, *17*, 1117.
[221] Z.-J. Zheng, Q. Su, Q. Zhang, X.-C. Hu, Y.-X. Yin, R. Wen, H. Ye, Z.-B. Wang, Y.-G. Guo, *Nano Energy* **2019**, *64*, 103910.
[222] J. He, A. Bhargav, A. Manthiram, *Angew. Chem., Int. Ed.* **2022**, *61*, e202116586.
[223] Y. Yang, B. Liang, J. Kreie, M. Hambsch, Z. Liang, C. Wang, S. Huang, X. Dong, L. Gong, C. Liang, D. Lou, Z. Zhou, J. Lu, Y. Yang, X. Zhuang, H. Qi, U. Kaiser, S. C. B. Mannsfeld, W. Liu, A. Gölzhäuser, Z. Zheng, *Nature* **2024**.
[224] X.-X. Wang, X.-W. Chi, M.-L. Li, D.-H. Guan, C.-L. Miao, J.-J. Xu, *Chem* **2023**, *9*, 394.
[225] X.-X. Zeng, Y.-X. Yin, N.-W. Li, W.-C. Du, Y.-G. Guo, L.-J. Wan, *J. Am. Chem. Soc.* **2016**, *138*, 15825.
[226] W. He, H. Ding, X. Chen, W. Yang, *J. Membr. Sci.* **2023**, *665*, 121095.
[227] D. Lu, R. Li, M. M. Rahman, P. Yu, L. Lv, S. Yang, Y. Huang, C. Sun, S. Zhang, H. Zhang, J. Zhang, X. Xiao, T. Deng, L. Fan, L. Chen, J. Wang, E. Hu, C. Wang, X. Fan, *Nature* **2024**, *627*, 101.
[228] Z. Zhang, W.-Q. Han, *Nano-Micro Lett.* **2023**, *16*, 24.
[229] H. Liu, Y. Liang, C. Wang, D. Li, X. Yan, C.-W. Nan, L.-Z. Fan, *Adv. Mater.* **2023**, *35*, 2206013.
[230] R. Pacios, A. Villaverde, M. Martínez-Ibañez, M. Casas-Cabanas, F. Aguesse, A. Kvasha, *Adv. Energy Mater.* **2023**, *13*, 2301018.
[231] K. Boukayouht, L. Bazzi, S. El Hankari, *Coord. Chem. Rev.* **2023**, *478*, 214986.
[232] H. Li, A. Dilipkumar, S. Abubakar, D. Zhao, *Chem. Soc. Rev.* **2023**, *52*, 6294.
[233] D. Fenton, *Polymer* **1973**, *14*, 589.
[234] M. B. Armand, J. M Chabagno, M. J. Duclot, *Fast Ion Transport in Solids* (Eds: P. Vashista, J. N. Mundy, G. K. Shenoy), North-Holland, Amsterdam **1979**, p. 131.
[235] S. N. Banitaba, D. Semnani, E. Heydari-Soureshjani, B. Rezaei, A. A. Ensafi, *Solid State Ionics* **2020**, *347*, 115252.
[236] Y. Wang, S. Chen, Z. Li, C. Peng, Y. Li, W. Feng, *Energy Storage Mater.* **2022**, *45*, 474.
[237] B. Zhang, Y. Liu, X. Pan, J. Liu, K. Doyle-Davis, L. Sun, J. Liu, X. Jiao, J. Jie, H. Xie, X. Sun, *Nano Energy* **2020**, *72*, 104690.
[238] G. Xi, M. Xiao, S. Wang, D. Han, Y. Li, Y. Meng, *Adv. Funct. Mater.* **2021**, *31*, 2007598.
[239] W.-S. Young, J. N. L. Albert, A. B. Schantz, T. H. Epps III, *Macromolecules* **2011**, *44*, 8116.
[240] A. J. Butzelaar, P. Röring, T. P. Mach, M. Hoffmann, F. Jeschull, M. Wilhelm, M. Winter, G. Brunklaus, P. Théato, *ACS Appl. Mater. Interfaces* **2021**, *13*, 39257.
[241] H. Zhang, C. Liu, L. Zheng, F. Xu, W. Feng, H. Li, X. Huang, M. Armand, J. Nie, Z. Zhou, *Electrochim. Acta* **2014**, *133*, 529.
[242] Y. Li, L. Zhang, Z. Sun, G. Gao, S. Lu, M. Zhu, Y. Zhang, Z. Jia, C. Xiao, H. Bu, K. Xi, S. Ding, *J. Mater. Chem. A* **2020**, *8*, 9579.
[243] R. Xu, X.-Q. Zhang, X.-B. Cheng, H.-J. Peng, C.-Z. Zhao, C. Yan, J.-Q. Huang, *Adv. Funct. Mater.* **2018**, *28*, 1705838.
[244] J. Jie, Y. Liu, L. Cong, B. Zhang, W. Lu, X. Zhang, J. Liu, H. Xie, L. Sun, *J. Energy Chem.* **2020**, *49*, 80.
[245] S.-Y. Zhang, Q. Zhuang, M. Zhang, H. Wang, Z. Gao, J.-K. Sun, J. Yuan, *Chem. Soc. Rev.* **2020**, *49*, 1726.
[246] J. Yuan, D. Mecerreyes, M. Antonietti, *Prog. Polym. Sci.* **2013**, *38*, 1009.
[247] Q. Li, F. Yan, J. Texter, *Chem. Rev.* **2024**, *124*, 3813.
[248] Y. Wan, Z. Qiu, J. Yuan, J. Yang, J. Li, C. F. Guo, *J. Phys. D: Appl. Phys.* **2024**, *57*, 093002.
[249] X. Ma, J. Yu, Y. Hu, J. Texter, F. Yan, *Ind. Chem. Mater.* **2023**, *1*, 39.
[250] Y. Li, Z. Sun, L. Shi, S. Lu, Z. Sun, Y. Shi, H. Wu, Y. Zhang, S. Ding, *Chem. Eng. J.* **2019**, *375*, 121925.
[251] L. Dong, X. Zeng, J. Fu, L. Chen, J. Zhou, S. Dai, L. Shi, *Chem. Eng. J.* **2021**, *423*, 130209.
[252] F. Chen, X. Wang, M. Armand, M. Forsyth, *Nat. Mater.* **2022**, *21*, 1175.
[253] X. Hu, B. Hu, C. Niu, J. Yao, M. Liu, H. Tao, Y. Huang, S. Kang, K. Geng, N. Li, *Nat. Energy* **2024**.
[254] L. Jia, J. Zhu, X. Zhang, B. Guo, Y. Du, X. Zhuang, *Electrochem. Energy Rev.* **2024**, *7*, 12.
[255] W. Feng, Y. Zhao, Y. Xia, *Adv. Mater.* **2024**, *36*, 2306111.
[256] S. Liu, W. Liu, D. Ba, Y. Zhao, Y. Ye, Y. Li, J. Liu, *Adv. Mater.* **2023**, *35*, 2110423.
[257] J. B. Bates, N. J. Dudney, G. R. Gruzalski, R. A. Zuhr, A. Choudhury, C. F. Luck, J. D. Robertson, *Solid State Ionics* **1992**, *53*, 647.
[258] N. J. Dudney, J. B. Bates, R. A. Zuhr, C. F. Luck, J. D. Robertson, *Solid State Ionics* **1992**, *53*, 655.
[259] Y. Inaguma, C. Liquan, M. Itoh, T. Nakamura, T. Uchida, H. Ikuta, M. Wakihara, *Solid State Commun.* **1993**, *86*, 689.
[260] J. Fu, *Solid State Ionics* **1997**, *96*, 195.
[261] J. Fu, *Solid State Ionics* **1997**, *104*, 191.
[262] V. Epp, Q. Ma, E.-M. Hammer, F. Tietz, M. Wilkening, *Phys. Chem. Chem. Phys.* **2015**, *17*, 32115.
[263] B. Lang, B. Ziebarth, C. Elsässer, *Chem. Mater.* **2015**, *27*, 5040.
[264] M. Weiss, D. A. Weber, A. Senyshyn, J. Janek, W. G. Zeier, *ACS Appl. Mater. Interfaces* **2018**, *10*, 10935.
[265] L. Yang, Y. Song, H. Liu, Z. Wang, K. Yang, Q. Zhao, Y. Cui, J. Wen, W. Luo, F. Pan, *Small Methods* **2020**, *4*, 1900751.
[266] Y. Meesala, C.-Y. Chen, A. Jena, Y.-K. Liao, S.-F. Hu, H. Chang, R.-S. Liu, *J. Phys. Chem. C* **2018**, *122*, 14383.
[267] X. He, Y. Zhu, Y. Mo, *Nat. Commun.* **2017**, *8*, 15893.
[268] X. Huang, J. Su, Z. Song, T. Xiu, J. Jin, M. E. Badding, Z. Wen, *Ceram. Int.* **2021**, *47*, 2123.
[269] R. Wei, S. Chen, T. Gao, W. Liu, *Nano Select* **2021**, *2*, 2256.
[270] F. Han, J. Yue, C. Chen, N. Zhao, X. Fan, Z. Ma, T. Gao, F. Wang, X. Guo, C. Wang, *Joule* **2018**, *2*, 497.
[271] C. Wang, C. Wang, M. Li, S. Zhang, C. Zhang, S. Chou, J. Mao, Z. Guo, *Mater. Today* **2024**, *72*, 235.
[272] C. Zheng, Y. Lu, J. Su, Z. Song, T. Xiu, J. Jin, M. E. Badding, Z. Wen, *Small Methods* **2022**, *6*, 2200667.
[273] S. Kim, J.-S. Kim, L. Miara, Y. Wang, S.-K. Jung, S. Y. Park, Z. Song, H. Kim, M. Badding, J. Chang, V. Roev, G. Yoon, R. Kim, J.-H. Kim, K. Yoon, D. Im, K. Kang, *Nat. Commun.* **2022**, *13*, 1883.
[274] J. Lau, R. H. DeBlock, D. M. Butts, D. S. Ashby, C. S. Choi, B. S. Dunn, *Adv. Energy Mater.* **2018**, *8*, 1800933.
[275] J.-C. Wang, L.-L. Zhao, N. Zhang, P.-F. Wang, T.-F. Yi, *Nano Energy* **2024**, *123*, 109361.

[276] Z. Zhang, L. Gao, X. Sun, N. Deng, Y. Zhao, W. Kang, *Energy Storage Mater.* **2024**, 103422.
[277] J. Wu, S. Liu, F. Han, X. Yao, C. Wang, *Adv. Mater.* **2021**, *33*, 2000751.
[278] B. Tao, C. Ren, H. Li, B. Liu, X. Jia, X. Dong, S. Zhang, H. Chang, *Adv. Funct. Mater.* **2022**, *32*, 2203551.
[279] A. Kuhn, V. Duppel, B. V. Lotsch, *Energy Environ. Sci.* **2013**, *6*, 3548.
[280] C. Wang, K. R. Adair, J. Liang, X. Li, Y. Sun, X. Li, J. Wang, Q. Sun, F. Zhao, X. Lin, R. Li, H. Huang, L. Zhang, R. Yang, S. Lu, X. Sun, *Adv. Funct. Mater.* **2019**, *29*, 1900392.
[281] S. Li, S.-J. Yang, G.-X. Liu, J.-K. Hu, Y.-L. Liao, X.-L. Wang, R. Wen, H. Yuan, J.-Q. Huang, Q. Zhang, *Adv. Mater.* **2024**, *36*, 2307768.
[282] Y. Seino, T. Ota, K. Takada, A. Hayashi, M. Tatsumisago, *Energy Environ. Sci.* **2014**, *7*, 627.
[283] L. Zhou, K.-H. Park, X. Sun, F. Lalère, T. Adermann, P. Hartmann, L. F. Nazar, *ACS Energy Lett.* **2019**, *4*, 265.
[284] F. Zhao, J. Liang, C. Yu, Q. Sun, X. Li, K. Adair, C. Wang, Y. Zhao, S. Zhang, W. Li, S. Deng, R. Li, Y. Huang, H. Huang, L. Zhang, S. Zhao, S. Lu, X. Sun, *Adv. Energy Mater.* **2020**, *10*, 1903422.
[285] N. Zhang, L. Wang, Q. Diao, K. Zhu, H. Li, C. Li, X. Liu, Q. Xu, *J. Electrochem. Soc.* **2022**, *169*, 020544.
[286] Y. Ni, C. Huang, H. Liu, Y. Liang, L.-Z. Fan, *Adv. Funct. Mater.* **2022**, *32*, 2205998.
[287] Y. Morino, H. Sano, T. Takahashi, N. Miyashita, A. Sakuda, A. Hayashi, *J. Phys. Chem. C* **2023**, *127*, 13616.
[288] B. Pang, Y. Gan, Y. Xia, H. Huang, X. He, W. Zhang, *Front. Chem.* **2022**, *10*, 837978.
[289] X. Li, Z. Ren, M. Norouzi Banis, S. Deng, Y. Zhao, Q. Sun, C. Wang, X. Yang, W. Li, J. Liang, X. Li, Y. Sun, K. Adair, R. Li, Y. Hu, T.-K. Sham, H. Huang, L. Zhang, S. Lu, J. Luo, X. Sun, *ACS Energy Lett.* **2019**, *4*, 2480.
[290] X. Li, J. Liang, X. Yang, K. R. Adair, C. Wang, F. Zhao, X. Sun, *Energy Environ. Sci.* **2020**, *13*, 1429.
[291] T. Asano, A. Sakai, S. Ouchi, M. Sakaida, A. Miyazaki, S. Hasegawa, *Adv. Mater.* **2018**, *30*, 1803075.
[292] B. Helm, R. Schlem, B. Wankmiller, A. Banik, A. Gautam, J. Ruhl, C. Li, M. R. Hansen, W. G. Zeier, *Chem. Mater.* **2021**, *33*, 4773.
[293] J. Liang, X. Li, S. Wang, K. R. Adair, W. Li, Y. Zhao, C. Wang, Y. Hu, L. Zhang, S. Zhao, S. Lu, H. Huang, R. Li, Y. Mo, X. Sun, *J. Am. Chem. Soc.* **2020**, *142*, 7012.
[294] Z. Liu, S. Ma, J. Liu, S. Xiong, Y. Ma, H. Chen, *ACS Energy Lett.* **2021**, *6*, 298.
[295] Y.-C. Yin, J.-T. Yang, J.-D. Luo, G.-X. Lu, Z. Huang, J.-P. Wang, P. Li, F. Li, Y.-C. Wu, T. Tian, Y.-F. Meng, H.-S. Mo, Y.-H. Song, J.-N. Yang, L.-Z. Feng, T. Ma, W. Wen, K. Gong, L.-J. Wang, H.-X. Ju, Y. Xiao, Z. Li, X. Tao, H.-B. Yao, *Nature* **2023**, *616*, 77.
[296] Y. Ye, J. Geng, D. Zuo, K. Niu, D. Chen, J. Lin, X. Chen, H. J. Woo, Y. Zhu, J. Wan, *ACS Nano* **2024**, *18*, 18368.
[297] A. Manthiram, X. Yu, S. Wang, *Nat. Rev. Mater.* **2017**, *2*, 16103.
[298] Z. Wu, X. Li, C. Zheng, Z. Fan, W. Zhang, H. Huang, Y. Gan, Y. Xia, X. He, X. Tao, J. Zhang, *Electrochem. Energy Rev.* **2023**, *6*, 10.
[299] K.-H. Park, K. Kaup, A. Assoud, Q. Zhang, X. Wu, L. F. Nazar, *ACS Energy Lett.* **2020**, *5*, 533.
[300] C. Wang, J. Liang, J. T. Kim, X. Sun, *Sci. Adv.* **2022**, *8*, eadc9516.
[301] Y. Nikodimos, W.-N. Su, B. J. Hwang, *Adv. Energy Mater.* **2023**, *13*, 2202854.
[302] T. Sun, Q. Liang, S. Wang, J. Liao, *Small* **2024**, *20*, 2308297.
[303] K. Daems, P. Yadav, K. B. Dermenci, J. Van Mierlo, M. Berecibar, *Renewable Sustainable Energy Rev.* **2024**, *191*, 114136.
[304] R. Whba, M. S. Su'ait, F. Whba, A. Ahmad, *J. Power Sources* **2024**, *606*, 234539.
[305] L. Hu, X. Gao, H. Wang, Y. Song, Y. Zhu, Z. Tao, B. Yuan, R. Hu, *Small* **2024**, *20*, 2312251.
[306] X. Yu, A. Manthiram, *Energy Storage Mater.* **2021**, *34*, 282.
[307] Z. Shen, Y. Cheng, S. Sun, X. Ke, L. Liu, Z. Shi, *Carbon Energy* **2021**, *3*, 482.
[308] J. A. Isaac, D. Devaux, R. Bouchet, *Nat. Mater.* **2022**, *21*, 1412.
[309] Y. Liu, B. Xu, W. Zhang, L. Li, Y. Lin, C. Nan, *Small* **2020**, *16*, 1902813.
[310] J. Lopez, D. G. Mackanic, Y. Cui, Z. Bao, *Nat. Rev. Mater.* **2019**, *4*, 312.
[311] T. T. Vu, H. J. Cheon, S. Y. Shin, G. Jeong, E. Wi, M. Chang, *Energy Storage Mater.* **2023**, *61*, 102876.
[312] Q. Zhao, S. Stalin, C.-Z. Zhao, L. A. Archer, *Nat. Rev. Mater.* **2020**, *5*, 229.
[313] P. Yang, X. Gao, X. Tian, C. Shu, Y. Yi, P. Liu, T. Wang, L. Qu, B. Tian, M. Li, W. Tang, B. Yang, J. B. Goodenough, *ACS Energy Lett.* **2020**, *5*, 1681.
[314] S. Song, Y. Wu, W. Tang, F. Deng, J. Yao, Z. Liu, R. Hu, A. Z. Wen, L. Lu, N. Hu, *ACS Sustainable Chem. Eng.* **2019**, *7*, 7163.
[315] K. Liu, R. Zhang, J. Sun, M. Wu, T. Zhao, *ACS Appl. Mater. Interfaces* **2019**, *11*, 46930.
[316] X. Wang, H. Zhai, B. Qie, Q. Cheng, A. Li, J. Borovilas, B. Xu, C. Shi, T. Jin, X. Liao, Y. Li, X. He, S. Du, Y. Fu, M. Dontigny, K. Zaghib, Y. YangY. Li, X. He, S. Du, Y. Fu, M. Dontigny, K. Zaghib, Y. Yang, *Nano Energy* **2019**, *60*, 205.
[317] Y. Qiao, X. Yin, T. Zhu, H. Li, C. Tang, *Prog. Polym. Sci.* **2018**, *80*, 153.
[318] J.-F. Liu, Z.-Y. Wu, F. J. Stadler, Y.-F. Huang, *Angew. Chem., Int. Ed.* **2023**, *62*, e202300243.
[319] Y. Ji, L. Dong, J. Liu, H. Xie, S. Zhong, C. Yang, J. Han, W. He, *Energy Environ. Sci.* **2024**, *17*, 4078.
[320] C. Xue, S. Guan, B. Hu, X. Wang, C. Xin, S. Liu, J. Yu, K. Wen, L. Li, C.-W. Nan, *Energy Storage Mater.* **2022**, *46*, 452.
[321] S. Zekoll, C. Marriner-Edwards, A. K. O. Hekselman, J. Kasemchainan, C. Kuss, D. E. J. Armstrong, D. Cai, R. J. Wallace, F. H. Richter, J. H. J. Thijssen, P. G. Bruce, *Energy Environ. Sci.* **2018**, *11*, 185.
[322] X. Wang, S. Huang, Y. Peng, Y. Min, Q. Xu, *ChemSusChem* **2024**, *17*, 202301262.
[323] X. Yang, J. Liu, N. Pei, Z. Chen, R. Li, L. Fu, P. Zhang, J. Zhao, *Nano-Micro Lett.* **2023**, *15*, 74.
[324] L. Chen, K. Ding, K. Li, Z. Li, X. Zhang, Q. Zheng, Y.-P. Cai, Y.-Q. Lan, *EnergyChem* **2022**, *4*, 100073.
[325] H.-C. Zhou, J. R. Long, O. M. Yaghi, *Chem. Rev.* **2012**, *112*, 673.
[326] Y. Xie, X. Wu, Y. Shi, Y. Peng, H. Zhou, X. Wu, J. Ma, J. Jin, Y. Pi, H. Pang, *Small* **2024**, *20*, 2305548.
[327] H. Furukawa, K. E. Cordova, M. O'Keeffe, O. M. Yaghi, *Science* **2013**, *341*, 1230444.
[328] C. Cong, H. Ma, *Small* **2023**, *19*, 2207547.
[329] S. Xie, Z. Zhou, X. Zhang, J. Fransaer, *Chem. Soc. Rev.* **2023**, *52*, 4292.
[330] C. Liu, L. Deng, X. Li, T. Wu, W. Zhang, H. Cui, H. Yang, *Electrochem. Commun.* **2023**, *150*, 107491.
[331] R. Zhao, Y. Wu, Z. Liang, L. Gao, W. Xia, Y. Zhao, R. Zou, *Energy Environ. Sci.* **2020**, *13*, 2386.
[332] X. Tang, C. Liu, H. Wang, L.-P. Lv, W. Sun, Y. Wang, *Coord. Chem. Rev.* **2023**, *494*, 215361.
[333] H. Wang, S. Duan, Y. Zheng, L. Qian, C. Liao, L. Dong, H. Guo, C. Ma, W. Yan, J. Zhang, *eTransportation* **2024**, *20*, 100311.
[334] E. M. Miner, S. S. Park, M. Dincă, *J. Am. Chem. Soc.* **2019**, *141*, 4422.
[335] H. Zhang, X. Li, J. Hou, L. Jiang, H. Wang, *Chem. Soc. Rev.* **2022**, *51*, 2224.
[336] J. Lu, X. Hu, K. M. Ung, Y. Zhu, X. Zhang, H. Wang, *Acc. Mater. Res.* **2022**, *3*, 735.
[337] W. Shang, Y. Chen, J. Han, P. Ouyang, C. Fang, J. Du, *ACS Appl. Energy Mater.* **2020**, *3*, 12351.
[338] A. P. Côté, A. I. Benin, N. W. Ockwig, M. O'Keeffe, A. J. Matzger, O. M. Yaghi, *Science* **2005**, *310*, 1166.

[339] K. T. Tan, S. Ghosh, Z. Wang, F. Wen, D. Rodríguez-San-Miguel, J. Feng, N. Huang, W. Wang, F. Zamora, X. Feng, A. Thomas, D. Jiang, A. Thomas, D. Jiang, *Nat. Rev. Methods Primers* **2023**, *3*, 1.
[340] S. Kandambeth, K. Dey, R. Banerjee, *J. Am. Chem. Soc.* **2019**, *141*, 1807.
[341] N. Arora, C. Flores, M. C. Senarathna, C. M. Thompson, R. A. Smaldone, *CCS Chemistry* **2024**, *6*, 57.
[342] M. Liu, Q. Xu, G. Zeng, *Angew. Chem., Int. Ed.* **2024**, *63*, 202404886.
[343] X. Guan, F. Chen, Q. Fang, S. Qiu, *Chem. Soc. Rev.* **2020**, *49*, 1357.
[344] Z. Wang, S. Zhang, Y. Chen, Z. Zhang, S. Ma, *Chem. Soc. Rev.* **2020**, *49*, 708.
[345] X. Ni, J. Zhou, K. Long, P. Qing, T. Naren, S. Huang, W. Liu, Q. Zhao, Y. Qian, T. Qian, C. Yan, L. Chen, C. Yan, L. Chen, *Energy Storage Mater.* **2024**, *67*, 103295.
[346] Q. Zhang, P. Zhi, J. Zhang, S. Duan, X. Yao, S. Liu, Z. Sun, S. C. Jun, N. Zhao, L. Dai, L. Wang, X. Wu, Z. He, Q. Zhang, *Adv. Mater.* **2024**, *36*, 2313152.
[347] Y. Zhu, Q. Bai, S. Ouyang, Y. Jin, W. Zhang, *ChemSusChem* **2024**, *17*, 202301118.
[348] Y. Du, H. Yang, J. M. Whiteley, S. Wan, Y. Jin, S.-H. Lee, W. Zhang, *Angew. Chem., Int. Ed.* **2016**, *55*, 1737.
[349] J. Zou, K. Fan, Y. Chen, W. Hu, C. Wang, *Coord. Chem. Rev.* **2022**, *458*, 214431.
[350] Y. Hu, N. Dunlap, S. Wan, S. Lu, S. Huang, I. Sellinger, M. Ortiz, Y. Jin, S.-h. Lee, W. Zhang, *J. Am. Chem. Soc.* **2019**, *141*, 7518.
[351] Z. Hou, S. Xia, C. Niu, Y. Pang, H. Sun, Z. Li, Y. Xu, S. Zheng, *Carbon Energy* **2022**, *4*, 506.
[352] T. W. Kang, J.-H. Lee, J. Lee, J. H. Park, J.-H. Shin, J.-M. Ju, H. Lee, S. U. Lee, J.-H. Kim, *Adv. Mater.* **2023**, *35*, 2301308.
[353] J. Zhu, Z. Zhang, S. Zhao, A. S. Westover, I. Belharouak, P.-F. Cao, *Adv. Energy Mater.* **2021**, *11*, 2003836.
[354] R. Bouchet, S. Maria, R. Meziane, A. Aboulaich, L. Lienafa, J.-P. Bonnet, T. N. T. Phan, D. Bertin, D. Gigmes, D. Devaux, R. Denoyel, M. Armand, *Nat. Mater.* **2013**, *12*, 452.
[355] J. Gao, C. Wang, D.-W. Han, D.-M. Shin, *Chem. Sci.* **2021**, *12*, 13248.
[356] D.-M. Shin, J. E. Bachman, M. K. Taylor, J. Kamcev, J. G. Park, M. E. Ziebel, E. Velasquez, N. N. Jarenwattananon, G. K. Sethi, Y. Cui, J. R. Long, *Adv. Mater.* **2020**, *32*, 1905771.
[357] K. Deng, J. Qin, S. Wang, S. Ren, D. Han, M. Xiao, Y. Meng, *Small* **2018**, *14*, 1801420.
[358] M. Doyle, T. F. Fuller, J. Newman, *Electrochim. Acta* **1994**, *39*, 2073.
[359] K. E. Thomas, S. E. Sloop, J. B. Kerr, J. Newman, *J. Power Sources* **2000**, *89*, 132.
[360] C. Brissot, M. Rosso, J. N. Chazalviel, S. Lascaud, *J. Power Sources* **1999**, *81*, 925.
[361] M. Rosso, C. Brissot, A. Teyssot, M. Dollé, L. Sannier, J.-M. Tarascon, R. Bouchet, S. Lascaud, *Electrochim. Acta* **2006**, *51*, 5334.
[362] C. Li, B. Qin, Y. Zhang, A. Varzi, S. Passerini, J. Wang, J. Dong, D. Zeng, Z. Liu, H. Cheng, *Adv. Energy Mater.* **2019**, *9*, 1803422.
[363] T. K. L. Nguyen, G. Lopez, C. Iojoiu, R. Bouchet, B. Ameduri, *J. Power Sources* **2021**, *498*, 229920.
[364] W. Zhou, Z. Wang, Y. Pu, Y. Li, S. Xin, X. Li, J. Chen, J. B. Goodenough, *Adv. Mater.* **2019**, *31*, 1805574.
[365] X. Yang, M. Jiang, X. Gao, D. Bao, Q. Sun, N. Holmes, H. Duan, S. Mukherjee, K. Adair, C. Zhao, J. Liang, W. Li, J. Li, Y. Liu, H. Huang, L. Zhang, S. Lu, Q. Lu, R. Li, C. V. Singh, X. Sun, *Energy Environ. Sci.* **2020**, *13*, 1318.
[366] J. Kalhoff, G. G. Eshetu, D. Bresser, S. Passerini, *ChemSusChem* **2015**, *8*, 2154.
[367] Y.-K. Han, Y. Moon, K. Lee, Y. S. Huh, *Curr. Appl. Phys.* **2014**, *14*, 897.
[368] Z. Shao, P. Jannasch, *Polym. Chem.* **2017**, *8*, 785.
[369] M. Remko, P. T. van Duijnen, C.-W. von der Lieth, *J. Mol. Struct.: Theochem.* **2007**, *814*, 119.
[370] H. Zhang, C. Li, M. Piszcz, E. Coya, T. Rojo, L. M. Rodriguez-Martinez, M. Armand, Z. Zhou, *Chem. Soc. Rev.* **2017**, *46*, 797.
[371] C. Cao, Y. Li, Y. Feng, P. Long, H. An, C. Qin, J. Han, S. Li, W. Feng, *J. Mater. Chem. A* **2017**, *5*, 22519.
[372] Y. Ding, X. Shen, J. Zeng, X. Wang, L. Peng, P. Zhang, J. Zhao, *Solid State Ionics* **2018**, *323*, 16.
[373] L. Porcarelli, A. S. Shaplov, M. Salsamendi, J. R. Nair, Y. S. Vygodskii, D. Mecerreyes, C. Gerbaldi, *ACS Appl. Mater. Interfaces* **2016**, *8*, 10350.
[374] Z. Yu, D. G. Mackanic, W. Michaels, M. Lee, A. Pei, D. Feng, Q. Zhang, Y. Tsao, C. V. Amanchukwu, X. Yan, H. Wang, S. Chen, K. Liu, J. Kang, J. Qin, Y. Cui, Z. Bao, *Joule* **2019**, *3*, 2761.
[375] M. L. Aubrey, J. C. Axelson, K. E. Engler, J. R. Long, *Macromolecules* **2021**, *54*, 7582.
[376] S. Liang, U. H. Choi, W. Liu, J. Runt, R. H. Colby, *Chem. Mater.* **2012**, *24*, 2316.
[377] H. Zhao, Z. Jia, W. Yuan, H. Hu, Y. Fu, G. L. Baker, G. Liu, *ACS Appl. Mater. Interfaces* **2015**, *7*, 19335.
[378] N. Lago, O. Garcia-Calvo, J. M. Lopez del Amo, T. Rojo, M. Armand, *ChemSusChem* **2015**, *8*, 3039.
[379] M. Meyer, C. Vechambre, L. Viau, A. Mehdi, O. Fontaine, E. Mourad, S. Monge, J.-M. Chenal, L. Chazeau, A. Vioux, *J. Mater. Chem. A* **2014**, *2*, 12162.
[380] M. A. Mehta, T. Fujinami, T. Inoue, *J. Power Sources* **1999**, *81*, 724.
[381] D. P. Siska, D. F. Shriver, *Chem. Mater.* **2001**, *13*, 4698.
[382] F. Ahmed, I. Choi, M. M. Rahman, H. Jang, T. Ryu, S. Yoon, L. Jin, Y. Jin, W. Kim, *ACS Appl. Mater. Interfaces* **2019**, *11*, 34930.
[383] E. Ploetz, H. Engelke, U. Lächelt, S. Wuttke, *Adv. Funct. Mater.* **2020**, *30*, 1909062.
[384] A.-G. Nguyen, C.-J. Park, *J. Membr. Sci.* **2023**, *675*, 121552.
[385] Z.-J. Zheng, H. Ye, Z.-P. Guo, *Energy Environ. Sci.* **2021**, *14*, 1835.
[386] Z. Wang, S. Wang, A. Wang, X. Liu, J. Chen, Q. Zeng, L. Zhang, W. Liu, L. Zhang, *J. Mater. Chem. A* **2018**, *6*, 17227.
[387] W. Sun, J. Zhang, M. Xie, D. Lu, Z. Zhao, Y. Li, Z. Cheng, S. Zhang, H. Chen, *Nano Lett.* **2020**, *20*, 8120.
[388] Y. Xu, X. Xiong, J. Peng, Q. Zhou, W. Wu, W. Gao, Y. Peng, T. Wang, F. Wang, Y. Wu, *J. Mater. Chem. A* **2024**, *12*, 26848.
[389] P. Zou, C. Wang, Y. He, H. L. Xin, *Energy Environ. Sci.* **2023**, *16*, 5871.
[390] B. Peng, Z. Liu, Q. Zhou, X. Xiong, S. Xia, X. Yuan, F. Wang, K. I. Ozoemena, L. Liu, L. Fu, Y. Wu, *Adv. Mater.* **2024**, *36*, 2307142.
[391] Q. Zhou, X. Yang, X. Xiong, Q. Zhang, B. Peng, Y. Chen, Z. Wang, L. Fu, Y. Wu, *Adv. Energy Mater.* **2022**, *12*, 2201991.
[392] J. Liu, H. Yuan, H. Liu, C.-Z. Zhao, Y. Lu, X.-B. Cheng, J.-Q. Huang, Q. Zhang, *Adv. Energy Mater.* **2022**, *12*, 2100748.
[393] Y. Tang, L. Zhang, J. Chen, H. Sun, T. Yang, Q. Liu, Q. Huang, T. Zhu, J. Huang, *Energy Environ. Sci.* **2021**, *14*, 602.
[394] J. A. Lewis, J. Tippens, F. J. Q. Cortes, M. T. McDowell, *Trends Chem.* **2019**, *1*, 845.
[395] X. Gao, P. He, J. Ren, J. Xu, *Energy Storage Mater.* **2019**, *18*, 23.
[396] Y.-X. Song, Y. Shi, J. Wan, S.-Y. Lang, X.-C. Hu, H.-J. Yan, B. Liu, Y.-G. Guo, R. Wen, L.-J. Wan, *Energy Environ. Sci.* **2019**, *12*, 2496.
[397] Y. Lu, X. Huang, Z. Song, K. Rui, Q. Wang, S. Gu, J. Yang, T. Xiu, M. E. Badding, Z. Wen, *Energy Storage Mater.* **2018**, *15*, 282.
[398] Z. Ning, D. S. Jolly, G. Li, R. De Meyere, S. D. Pu, Y. Chen, J. Kasemchainan, J. Ihli, C. Gong, B. Liu, D. L. R. Melvin, A. Bonnin, O. Magdysyuk, P. Adamson, G. O. Hartley, C. W. Monroe, T. James Marrow, P. G. Bruce, *Nat. Mater.* **2021**, *20*, 1121.
[399] W. Wang, J. Wang, C. Lin, H. Ruan, *Adv. Funct. Mater.* **2023**, *33*, 2303484.
[400] M. Yang, Y. Liu, A. M. Nolan, Y. Mo, *Adv. Mater.* **2021**, *33*, 2008081.
[401] B. S. Vishnugopi, K. G. Naik, H. Kawakami, N. Ikeda, Y. Mizuno, R. Iwamura, T. Kotaka, K. Aotani, Y. Tabuchi, P. P. Mukherjee, *Adv. Energy Mater.* **2023**, *13*, 2203671.

[402] Q. Tu, T. Shi, S. Chakravarthy, G. Ceder, *Matter* **2021**, *4*, 3248.
[403] X. Xu, Y. Liu, O. O. Kapitanova, Z. Song, J. Sun, S. Xiong, *Adv. Mater.* **2022**, *34*, 2207232.
[404] H. Wang, H. Gao, X. Chen, J. Zhu, W. Li, Z. Gong, Y. Li, M.-S. Wang, Y. Yang, *Adv. Energy Mater.* **2021**, *11*, 2102148.
[405] L. Zhang, T. Yang, C. Du, Q. Liu, Y. Tang, J. Zhao, B. Wang, T. Chen, Y. Sun, P. Jia, H. Li, L. Geng, J. Chen, H. Ye, Z. Wang, Y. Li, H. Sun, X. Li, Q. Dai, Y. Tang, Q. Peng, T. Shen, S. Zhang, T. Zhu, J. Huang, *Nat. Nanotechnol.* **2020**, *15*, 94.
[406] S. Xiong, X. Xu, X. Jiao, Y. Wang, O. O. Kapitanova, Z. Song, Y. Liu, *Adv. Energy Mater.* **2023**, *13*, 2203614.
[407] Y. Liu, X. Xu, X. Jiao, O. O. Kapitanova, Z. Song, S. Xiong, *Adv. Mater.* **2023**, *35*, 2301152.
[408] Q. Tu, L. Barroso-Luque, T. Shi, G. Ceder, *Cell Rep. Phys. Sci.* **2020**, *1*, 100106.
[409] F. P. McGrogan, T. Swamy, S. R. Bishop, E. Eggleton, L. Porz, X. Chen, Y.-M. Chiang, K. J. Van Vliet, *Adv. Energy Mater.* **2017**, *7*, 1602011.
[410] M. Botros, R. Djenadic, O. Clemens, M. Möller, H. Hahn, *J. Power Sources* **2016**, *309*, 108.
[411] J. Zhu, J. Zhao, Y. Xiang, M. Lin, H. Wang, B. Zheng, H. He, Q. Wu, J. Y. Huang, Y. Yang, *Chem. Mater.* **2020**, *32*, 4998.
[412] H. Chung, B. Kang, *Chem. Mater.* **2017**, *29*, 8611.
[413] R. Xu, X.-B. Cheng, C. Yan, X.-Q. Zhang, Y. Xiao, C.-Z. Zhao, J.-Q. Huang, Q. Zhang, *Matter* **2019**, *1*, 317.
[414] F. Sun, K. Dong, M. Osenberg, A. Hilger, S. Risse, Y. Lu, P. H. Kamm, M. Klaus, H. Markötter, F. García-Moreno, T. Arlt, I. Manke, *J. Mater. Chem. A* **2018**, *6*, 22489.
[415] J. Tippens, J. C. Miers, A. Afshar, J. A. Lewis, F. J. Q. Cortes, H. Qiao, T. S. Marchese, C. V. Di Leo, C. Saldana, M. T. McDowell, *ACS Energy Lett.* **2019**, *4*, 1475.
[416] L. Su, A. Manthiram, *Small Struct.* **2022**, *3*, 2200114.
[417] G. M. Stone, S. A. Mullin, A. A. Teran, D. T. Hallinan, A. M. Minor, A. Hexemer, N. P. Balsara, *J. Electrochem. Soc.* **2012**, *159*, A222.
[418] L. Wu, Y. Wang, X. Guo, P. Ding, Z. Lin, H. Yu, *SusMat* **2022**, *2*, 264.
[419] W. Tang, S. Tang, C. Zhang, Q. Ma, Q. Xiang, Y.-W. Yang, J. Luo, *Adv. Energy Mater.* **2018**, *8*, 1800866.
[420] S.-O. Tung, S. Ho, M. Yang, R. Zhang, N. A. Kotov, *Nat. Commun.* **2015**, *6*, 6152.
[421] S. Choudhury, S. Stalin, D. Vu, A. Warren, Y. Deng, P. Biswal, L. A. Archer, *Nat. Commun.* **2019**, *10*, 4398.
[422] C.-L. Tsai, V. Roddatis, C. V. Chandran, Q. Ma, S. Uhlenbruck, M. Bram, P. Heitjans, O. Guillon, *ACS Appl. Mater. Interfaces* **2016**, *8*, 10617.
[423] H. Huo, J. Liang, N. Zhao, X. Li, X. Lin, Y. Zhao, K. Adair, R. Li, X. Guo, X. Sun, *ACS Energy Lett.* **2020**, *5*, 2156.
[424] Y. Xu, L. Gao, Q. Liu, Q. Liu, Z. Chen, W. Zhao, X. Kong, H. B. Wu, *Energy Storage Mater.* **2023**, *54*, 854.
[425] R. Fan, W. Liao, S. Fan, D. Chen, J. Tang, Y. Yang, C. Liu, *Adv. Sci.* **2022**, *9*, 2104506.
[426] S. A. Pervez, P. Ganjeh-Anzabi, U. Farooq, M. Trifkovic, E. P. L. Roberts, V. Thangadurai, *Adv. Mater. Interfaces* **2019**, *6*, 1900186.
[427] B. S. Vishnugopi, M. B. Dixit, F. Hao, B. Shyam, J. B. Cook, K. B. Hatzell, P. P. Mukherjee, *Adv. Energy Mater.* **2022**, *12*, 2102825.
[428] K. J. Harry, X. Liao, D. Y. Parkinson, A. M. Minor, N. P. Balsara, *J. Electrochem. Soc.* **2015**, *162*, A2699.
[429] Z. Li, J. Fu, S. Zheng, D. Li, X. Guo, *Small* **2022**, *18*, 2200891.
[430] C. Zhu, T. Fuchs, S. A. L. Weber, F. H. Richter, G. Glasser, F. Weber, H.-J. Butt, J. Janek, R. Berger, *Nat. Commun.* **2023**, *14*, 1300.
[431] F. Han, A. S. Westover, J. Yue, X. Fan, F. Wang, M. Chi, D. N. Leonard, N. J. Dudney, H. Wang, C. Wang, *Nat. Energy* **2019**, *4*, 187.
[432] T. Foroozan, S. Sharifi-Asl, R. Shahbazian-Yassar, *J. Power Sources* **2020**, *461*, 228135.
[433] M. Golozar, A. Paolella, H. Demers, S. Bessette, M. Lagacé, P. Bouchard, A. Guerfi, R. Gauvin, K. Zaghib, *Commun. Chem.* **2019**, *2*, 131.
[434] M. Sun, T. Liu, Y. Yuan, M. Ling, N. Xu, Y. Liu, L. Yan, H. Li, C. Liu, Y. Lu, Y. Shi, Y. He, Y. Guo, X. Tao, C. Liang, J. Lu, *ACS Energy Lett.* **2021**, *6*, 451.
[435] Y. Pang, J. Pan, J. Yang, S. Zheng, C. Wang, *Electrochem. Energy Rev.* **2021**, *4*, 169.
[436] G.-L. Zhu, C.-Z. Zhao, H. Yuan, B.-C. Zhao, L.-P. Hou, X.-B. Cheng, H.-X. Nan, Y. Lu, J. Zhang, J.-Q. Huang, Q.-B. Liu, C.-X. He, Q. Zhang, *Energy Storage Mater.* **2020**, *31*, 267.
[437] T. Swamy, X. Chen, Y.-M. Chiang, *Chem. Mater.* **2019**, *31*, 707.
[438] Y. Lu, C.-Z. Zhao, H. Yuan, X.-B. Cheng, J.-Q. Huang, Q. Zhang, *Adv. Funct. Mater.* **2021**, *31*, 2009925.
[439] S. Wang, H. Xu, W. Li, A. Dolocan, A. Manthiram, *J. Am. Chem. Soc.* **2018**, *140*, 250.
[440] S. Wenzel, S. J. Sedlmaier, C. Dietrich, W. G. Zeier, J. Janek, *Solid State Ionics* **2018**, *318*, 102.
[441] T. Cheng, B. V. Merinov, S. Morozov, W. A. GoddardIII, *ACS Energy Lett.* **2017**, *2*, 1454.
[442] J. Yu, Q. Liu, X. Hu, S. Wang, J. Wu, B. Liang, C. Han, F. Kang, B. Li, *Energy Storage Mater.* **2022**, *46*, 68.
[443] L. Xu, S. Tang, Y. Cheng, K. Wang, J. Liang, C. Liu, Y.-C. Cao, F. Wei, L. Mai, *Joule* **2018**, *2*, 1991.
[444] S. Wenzel, S. Randau, T. Leichtweiß, D. A. Weber, J. Sann, W. G. Zeier, J. Janek, *Chem. Mater.* **2016**, *28*, 2400.
[445] Z. Zhang, S. Chen, J. Yang, J. Wang, L. Yao, X. Yao, P. Cui, X. Xu, *ACS Appl. Mater. Interfaces* **2018**, *10*, 2556.
[446] Y. Chu, Y. Shen, F. Guo, X. Zhao, Q. Dong, Q. Zhang, W. Li, H. Chen, Z. Luo, L. Chen, *Electrochem. Energy Rev.* **2020**, *3*, 187.
[447] X. Liu, L. Zhang, H. Yu, J. Wang, J. Li, K. Yang, Y. Zhao, H. Wang, B. Wu, N. P. Brandon, S. Yang, *Adv. Energy Mater.* **2022**, *12*, 2200889.
[448] Y. Nomura, K. Yamamoto, *Adv. Energy Mater.* **2023**, *13*, 2203883.
[449] R. F. Ziesche, T. M. M. Heenan, P. Kumari, J. Williams, W. Li, M. E. Curd, T. L. Burnett, I. Robinson, D. J. L. Brett, M. J. Ehrhardt, P. D. Quinn, L. B. Mehdi, P. J. Withers, M. M. Britton, N. D. Browning, P. R. Shearing, *Adv. Energy Mater.* **2023**, *13*, 2300103.
[450] L. Zhang, H. Fan, Y. Dang, Q. Zhuang, H. Arandiyan, Y. Wang, N. Cheng, H. Sun, H. H. Pérez Garza, R. Zheng, Z. Wang, S. S. Mofarah, P. Koshy, S. K. Bhargava, Y. Cui, Z. Shao, Y. Liu, *Mater. Horiz.* **2023**, *10*, 1479.
[451] Z. Lin, O. Sheng, X. Cai, D. Duan, K. Yue, J. Nai, Y. Wang, T. Liu, X. Tao, Y. Liu, *J. Energy Chem.* **2023**, *81*, 358.
[452] X. Yang, Y. Huang, J. Li, W. Huang, W. Yang, C. Wu, S. Tang, F. Ren, Z. Gong, N. Zhou, Y. Yang, *Energy Mater.* **2023**, *3*, 300029.
[453] L. Liu, M. Li, L. Chu, B. Jiang, R. Lin, X. Zhu, G. Cao, *Prog. Mater. Sci.* **2020**, *111*, 100655.
[454] S. Jeong, V.-C. Ho, O. Kwon, Y. Park, J. Mun, *Energy Mater.* **2023**, *3*, 300048.
[455] X. Wang, Y.-L. Ding, Y.-P. Deng, Z. Chen, *Adv. Energy Mater.* **2020**, *10*, 1903864.
[456] N.-Y. Park, G.-T. Park, S.-B. Kim, W. Jung, B.-C. Park, Y.-K. Sun, *ACS Energy Lett.* **2022**, *7*, 2362.
[457] L. Li, H. Duan, J. Li, L. Zhang, Y. Deng, G. Chen, *Adv. Energy Mater.* **2021**, *11*, 2003154.
[458] Y. Song, B. Bhargava, D. M. Stewart, A. A. Talin, G. W. Rubloff, P. Albertus, *Joule* **2023**, *7*, 652.
[459] C. Yuan, W. Lu, J. Xu, *Energy Storage Mater.* **2023**, *60*, 102834.
[460] R. Chen, C. L. A. Leung, C. Huang, *Adv. Funct. Mater.* **2024**, 2308165.
[461] L. de Biasi, B. Schwarz, T. Brezesinski, P. Hartmann, J. Janek, H. Ehrenberg, *Adv. Mater.* **2019**, *31*, 1900985.
[462] M. Zhang, M. Chouchane, S. A. Shojaee, B. Winiarski, Z. Liu, L. Li, R. Pelapur, A. Shodiev, W. Yao, J.-M. Doux, S. Wang, Y. Li, C. Liu, H. Lemmens, A. A. Franco, Y. S. Meng, *Joule* **2023**, *7*, 201.

[463] H. Sun, Q. Liu, J. Chen, Y. Li, H. Ye, J. Zhao, L. Geng, Q. Dai, T. Yang, H. Li, Z. Wang, L. Zhang, Y. Tang, J. Huang, *ACS Nano* **2021**, *15*, 19070.
[464] G. M. Hobold, J. Lopez, R. Guo, N. Minafra, A. Banerjee, Y. Shirley Meng, Y. Shao-Horn, B. M. Gallant, *Nat. Energy* **2021**, *6*, 951.
[465] S. Chen, J. Zhang, L. Nie, X. Hu, Y. Huang, Y. Yu, W. Liu, *Adv. Mater.* **2021**, *33*, 2002325.
[466] Q.-K. Zhang, X.-Q. Zhang, H. Yuan, J.-Q. Huang, *Small Science* **2021**, *1*, 2100058.
[467] X. Rui, D. Ren, X. Liu, X. Wang, K. Wang, Y. Lu, L. Li, P. Wang, G. Zhu, Y. Mao, X. Feng, L. Lu, H. Wang, M. Ouyang, *Energy Environ. Sci.* **2023**, *16*, 3552.
[468] A. M. Bates, Y. Preger, L. Torres-Castro, K. L. Harrison, S. J. Harris, J. Hewson, *Joule* **2022**, *6*, 742.
[469] S.-J. Yang, F.-N. Jiang, J.-K. Hu, H. Yuan, X.-B. Cheng, S. Kaskel, Q. Zhang, J.-Q. Huang, *Electron* **2023**, *1*, e8.
[470] H. Zhang, J. Xue, Y. Qin, J. Chen, J. Wang, X. Yu, B. Zhang, Y. Zou, Y.-H. Hong, Z. Li, Y. Qiao, S.-G. Sun, *Small* **2024**, 2406110.
[471] S. Wang, Y. Wu, H. Li, L. Chen, F. Wu, *InfoMat* **2022**, *4*, e12316.
[472] H. Stöffler, T. Zinkevich, M. Yavuz, A.-L. Hansen, M. Knapp, J. Bednarčík, S. Randau, F. H. Richter, J. Janek, H. Ehrenberg, S. Indris, *J. Phys. Chem. C* **2019**, *123*, 10280.
[473] S.-J. Yang, J.-K. Hu, F.-N. Jiang, X.-B. Cheng, S. Sun, H.-J. Hsu, D. Ren, C.-Z. Zhao, H. Yuan, M. Ouyang, L.-Z. Fan, J.-Q. Huang, Q. Zhang, *eTransportation* **2023**, *18*, 100279.
[474] F.-N. Jiang, X.-B. Cheng, S.-J. Yang, J. Xie, H. Yuan, L. Liu, J.-Q. Huang, Q. Zhang, *Adv. Mater.* **2023**, *35*, 2209114.
[475] X. Yao, X. Lu, Y. Zhou, T. Šamořil, J. Bi, M. G. Masteghin, H. Zhang, L. Askew, J. Kim, F. Xiong, J. Wang, D. C. Cox, T. Sui, I. Gilmore, S. R. P. Silva, L. Mai, G. Hinds, P. R. Shearing, J. Park, Y. Zhao, *Energy Environ. Sci.* **2023**, *16*, 2167.
[476] D. Lin, W. Liu, Y. Liu, H. R. Lee, P.-C. Hsu, K. Liu, Y. Cui, *Nano Lett.* **2016**, *16*, 459.
[477] P.-J. Alarco, Y. Abu-Lebdeh, A. Abouimrane, M. Armand, *Nat. Mater.* **2004**, *3*, 476.
[478] W. Liu, N. Liu, J. Sun, P.-C. Hsu, Y. Li, H.-W. Lee, Y. Cui, *Nano Lett.* **2015**, *15*, 2740.
[479] Y. Xiao, Y. Wang, S.-H. Bo, J. C. Kim, L. J. Miara, G. Ceder, *Nat. Rev. Mater.* **2020**, *5*, 105.
[480] D. Chen, M. Zhu, P. Kang, T. Zhu, H. Yuan, J. Lan, X. Yang, G. Sui, *Adv. Sci.* **2022**, *9*, 2103663.
[481] F.-Q. Liu, W.-P. Wang, Y.-X. Yin, S.-F. Zhang, J.-L. Shi, L. Wang, X.-D. Zhang, Y. Zheng, J.-J. Zhou, L. Li, Y.-G. Guo, *Sci. Adv.* **2018**, *4*, eaat5383.
[482] J. A. Lewis, F. J. Q. Cortes, M. G. Boebinger, J. Tippens, T. S. Marchese, N. Kondekar, X. Liu, M. Chi, M. T. McDowell, *ACS Energy Lett.* **2019**, *4*, 591.
[483] X. Cheng, J. Pan, Y. Zhao, M. Liao, H. Peng, *Adv. Energy Mater.* **2018**, *8*, 1702184.
[484] J. Wu, Z. Rao, Z. Cheng, L. Yuan, Z. Li, Y. Huang, *Adv. Energy Mater.* **2019**, *9*, 1902767.
[485] Y. Horowitz, M. Lifshitz, A. Greenbaum, Y. Feldman, S. Greenbaum, A. P. Sokolov, D. Golodnitsky, *J. Electrochem. Soc.* **2020**, *167*, 160514.
[486] Z. Li, H.-M. Huang, J.-K. Zhu, J.-F. Wu, H. Yang, L. Wei, X. Guo, *ACS Appl. Mater. Interfaces* **2019**, *11*, 784.
[487] C. Chen, S. P. Ong, *Nat. Comput. Sci.* **2022**, *2*, 718.
[488] J. Sun, S. Kang, J. Kim, K. Min, *ACS Appl. Mater. Interfaces* **2023**, *15*, 5049.
[489] G. Bradford, J. Lopez, J. Ruza, M. A. Stolberg, R. Osterude, J. A. Johnson, R. Gomez-Bombarelli, Y. Shao-Horn, *ACS Cent. Sci.* **2023**, *9*, 206.
[490] W. L. Jorgensen, D. S. Maxwell, J. Tirado-Rives, *J. Am. Chem. Soc.* **1996**, *118*, 11225.
[491] Y. Zheng, Y. Yao, J. Ou, M. Li, D. Luo, H. Dou, Z. Li, K. Amine, A. Yu, Z. Chen, *Chem. Soc. Rev.* **2020**, *49*, 8790.
[492] A. M. Nolan, Y. Zhu, X. He, Q. Bai, Y. Mo, *Joule* **2018**, *2*, 2016.
[493] K. Zhang, B. Zhang, M. Weng, J. Zheng, S. Li, F. Pan, *Phys. Chem. Chem. Phys.* **2019**, *21*, 9883.
[494] X. He, Y. Zhu, A. Epstein, Y. Mo, *npj Comput. Mater.* **2018**, *4*, 18.
[495] Y. Zhou, Y. Ouyang, Y. Zhang, Q. Li, J. Wang, *J. Phys. Chem. Lett.* **2023**, *14*, 2308.
[496] O. T. Unke, S. Chmiela, H. E. Sauceda, M. Gastegger, I. Poltavsky, K. T. Schütt, A. Tkatchenko, K.-R. Müller, *Chem. Rev.* **2021**, *121*, 10142.
[497] P. Lu, Y. Xia, G. Sun, D. Wu, S. Wu, W. Yan, X. Zhu, J. Lu, Q. Niu, S. Shi, Z. Sha, L. Chen, H. Li, F. Wu, *Nat. Commun.* **2023**, *14*, 4077.
[498] Z. Lu, P. Adeli, C.-H. Yim, M. Jiang, J. Rempel, Z. W. Chen, S. Yadav, P. Mercier, Y. Abu-Lebdeh, C. V. Singh, *ACS Appl. Energy Mater.* **2022**, *5*, 8042.
[499] S. J. Honrao, X. Yang, B. Radhakrishnan, S. Kuwata, H. Komatsu, A. Ohma, M. Sierhuis, J. W. Lawson, *Sci. Rep.* **2021**, *11*, 16484.
[500] Z. Ahmad, T. Xie, C. Maheshwari, J. C. Grossman, V. Viswanathan, *ACS Cent. Sci.* **2018**, *4*, 996.
[501] Y. Ren, K. Zhang, Y. Zhou, Y. Cao, *ACS Appl. Mater. Interfaces* **2022**, *14*, 30658.
[502] A. Jain, S. P. Ong, G. Hautier, W. Chen, W. D. Richards, S. Dacek, S. Cholia, D. Gunter, D. Skinner, G. Ceder, K. A. Persson, *APL Mater.* **2013**, *1*, 011002.
[503] A. D. Sendek, E. D. Cubuk, E. R. Antoniuk, G. Cheon, Y. Cui, E. J. Reed, *Chem. Mater.* **2019**, *31*, 342.
[504] T. Xie, A. France-Lanord, Y. Wang, J. Lopez, M. A. Stolberg, M. Hill, G. M. Leverick, R. Gomez-Bombarelli, J. A. Johnson, Y. Shao-Horn, J. C. Grossman, *Nat. Commun.* **2022**, *13*, 3415.
[505] S. Xia, Z. Lin, B. Peng, X. Yuan, J. Du, X. Yuan, L. Liu, L. Fu, R. Holze, Y. Wu, *Energy Environ. Sci.* **2024**, *17*, 5461.
[506] Y. Liu, P. He, H. Zhou, *Adv. Energy Mater.* **2018**, *8*, 1701602.
[507] L.-P. Hou, H. Yuan, C.-Z. Zhao, L. Xu, G.-L. Zhu, H.-X. Nan, X.-B. Cheng, Q.-B. Liu, C.-X. He, J.-Q. Huang, Q. Zhang, *Energy Storage Mater.* **2020**, *25*, 436.
[508] M. Li, K. Pan, W. Wang, S. Xing, Y. Dou, Z. Zhang, Z. Zhou, *Batteries Supercaps* **2023**, *6*, 202300230.
[509] T. Wang, J. He, X.-B. Cheng, J. Zhu, B. Lu, Y. Wu, *ACS Energy Lett.* **2023**, *8*, 116.
[510] J. Liu, Y. Zhou, T. Yan, X.-P. Gao, *Adv. Funct. Mater.* **2024**, *34*, 2309625.
[511] Z. Li, S. Zhou, X. Wu, B. Zhang, X. Yu, F. Pei, H.-G. Liao, Y. Qiao, H. Zhou, S.-G. Sun, *Adv. Funct. Mater.* **2023**, *33*, 2211774.
[512] F. Liang, S. Wang, Q. Liang, A. Zhong, C. Yang, J. Qian, H. Song, R. Chen, *Adv. Energy Mater.* **2024**, *14*, 2401959.
[513] M. Jiang, Z. Zhang, B. Tang, T. Dong, H. Xu, H. Zhang, X. Lu, G. Cui, *J. Energy Chem.* **2021**, *58*, 300.
[514] S. Li, W. Zhang, J. Zheng, M. Lv, H. Song, L. Du, *Adv. Energy Mater.* **2021**, *11*, 2000779.
[515] X. Gao, X. Zheng, Y. Tsao, P. Zhang, X. Xiao, Y. Ye, J. Li, Y. Yang, R. Xu, Z. Bao, Y. Cui, *J. Am. Chem. Soc.* **2021**, *143*, 18188.
[516] R. Fang, H. Xu, B. Xu, X. Li, Y. Li, J. B. Goodenough, *Adv. Funct. Mater.* **2021**, *31*, 2001812.
[517] J. Yue, M. Yan, Y.-X. Yin, Y.-G. Guo, *Adv. Funct. Mater.* **2018**, *28*, 1707533.
[518] H. Cheng, C. Yan, L. Chang, M. Dirican, R. Orenstein, X. Zhang, *ACS Appl. Energy Mater.* **2024**, *7*, 3071.
[519] J. Li, F. Xie, W. Pang, Q. Liang, X. Yang, L. Zhang, *Sci. Adv.* **2024**, *10*, eadl3925.
[520] C. Xia, C. Y. Kwok, L. F. Nazar, *Science* **2018**, *361*, 777.
[521] X. Sun, Y. Song, Q. Liu, X. Zhang, H. An, N. Sun, Y. Shi, C. Fu, H. Huo, Y. Xie, Y. Tong, F. Kong, J. Wang, *Sci. Adv.* **2022**, *8*, eabq6261.
[522] Z. Li, S. Weng, X. Wu, C. Song, X. Yu, H. Zhang, S. Zhou, X. Wang, X. Wang, Y. Qiao, S.-G. Sun, *Next Energy* **2023**, *1*, 100036.

[523] M. Kim, H. Lee, H. J. Kwon, S.-M. Bak, C. Jaye, D. A. Fischer, G. Yoon, J. O. Park, D.-H. Seo, S. B. Ma, D. Im, *Sci. Adv.* **2022**, *8*, eabm8584.
[524] M. Balaish, E. Peled, D. Golodnitsky, Y. Ein-Eli, *Angew. Chem., Int. Ed.* **2015**, *54*, 436.
[525] W. Yu, C. Xue, B. Hu, B. Xu, L. Li, C.-W. Nan, *Energy Storage Mater.* **2020**, *27*, 244.
[526] J. Yi, S. Guo, P. He, H. Zhou, *Energy Environ. Sci.* **2017**, *10*, 860.
[527] X. B. Zhu, T. S. Zhao, Z. H. Wei, P. Tan, G. Zhao, *Energy Environ. Sci.* **2015**, *8*, 2782.
[528] Z. Gu, X. Xin, Z. Xu, J. He, J. Wu, Y. Sun, X. Yao, *Adv. Funct. Mater.* **2023**, *33*, 2301583.
[529] Y. Ding, Y. Li, Z.-S. Wu, *Battery Energy* **2023**, *2*, 20220014.
[530] C. Zhao, J. Liang, X. Li, N. Holmes, C. Wang, J. Wang, F. Zhao, S. Li, Q. Sun, X. Yang, J. Liang, X. Lin, W. Li, R. Li, S. Zhao, H. Huang, L. Zhang, S. Lu, X. Sun, *Nano Energy* **2020**, *75*, 105036.
[531] H. Wang, X. Wang, M. Li, L. Zheng, D. Guan, X. Huang, J. Xu, J. Yu, *Adv. Mater.* **2020**, *32*, 2002559.
[532] Z. Gu, X. Xin, J. Yang, D. Guo, S. Yang, J. Wu, Y. Sun, X. Yao, *ACS Appl. Energy Mater.* **2022**, *5*, 9149.
[533] A. Kondori, M. Esmaeilirad, A. M. Harzandi, R. Amine, M. T. Saray, L. Yu, T. Liu, J. Wen, N. Shan, H.-H. Wang, A. T. Ngo, P. C. Redfern, C. S. Johnson, K. Amine, R. Shahbazian-Yassar, L. A. Curtiss, M. Asadi, *Science* **2023**, *379*, 499.
[534] H.-F. Wang, X.-X. Wang, F. Li, J.-J. Xu, *Small Sci.* **2022**, *2*, 2200005.
[535] T. Lu, Y. Qian, K. Liu, C. Wu, X. Li, J. Xiao, X. Zeng, Y. Zhang, S.-L. Chou, *Adv. Energy Mater.* **2024**, *14*, 2400766.
[536] Z. Li, C. Song, P. Dai, X. Wu, S. Zhou, Y. Qiao, L. Huang, S.-G. Sun, *Nano Lett.* **2022**, *22*, 815.
[537] Z. Li, Y.-E. Liu, S. Weng, X. Wu, X. Yu, H. Luo, X. Wang, X. Wang, Y. Qiao, S.-G. Sun, *Energy Storage Mater.* **2023**, *58*, 94.

Jun Huang is currently a postdoctoral fellow in the Chemical and Biological Engineering department at The Hong Kong University of Science and Technology, where he received his Ph.D. under the supervision of Prof. Yoonseob Kim. He completed his undergraduate studies at the School of Materials Science and Engineering, Nanchang University, and pursued his master's degree at Harbin Institute of Technology. His current research focuses on the application of COFs (Covalent Organic Frameworks) materials in the field of batteries, specifically exploring the use of COFs as solid-state electrolytes in lithium metal batteries.

Chen Li is currently a postdoctoral researcher in the Chemical and Biological Engineering department at the Hong Kong University of Science and Technology. She graduated from Hohai University with a bachelor's degree and was recommended for admission to Shanghai Jiao Tong University for her master's degree. She completed her Ph.D. at the Hong Kong University of Science and Technology under the supervision of Prof. Yoonseob Kim, where she focused on the application of redox-active covalent organic frameworks (COFs) in the energy and environmental fields, specifically investigating their use as solid-state electrolytes and solid electrolyte interfaces in lithium metal batteries.

Yoonseob Kim is an assistant professor in the Department of Chemical and Biological Engineering at Hong Kong University of Science and Technology. He studied Chemical Engineering at Hanyang University, Korea (2010), and received his Ph.D. from the Department of Chemical Engineering at the University of Michigan, Ann Arbor, in 2016. Subsequently, he worked at the Department of Chemistry, Massachusetts Institute of Technology, as a postdoctoral associate from 2016 to 2019. His research group at the HKUST synthesizes porous crystalline polymers and applies them to energy applications. His group especially focuses on solid electrolytes from COFs for lithium metal batteries.